Real-time Synchrotron X-ray Radiography of Nucleation, Growth and Phase Selection of Fe-rich Intermetallic Compounds in Al Alloy Solidification



Shikang Feng

Linacre College

University of Oxford

A thesis submitted for the degree of

Doctor of Philosophy

Trinity 2019

Real-time Synchrotron X-ray Radiography of Nucleation, Growth and Phase Selection of Fe-rich Intermetallic Compounds in Al Alloy Solidification

Shikang Feng, Linacre College

Doctor of Philosophy, Trinity 2019

Abstract

In-situ synchrotron X-ray radiography has been used to study the dynamics of nucleation, growth and other temperature related phenomena of Fe-rich and analogous faceted IMCs. Measurements from radiographs have been combined with post-solidification microscopy.

A method was developed to estimate the temperature at any time and any position in the radiography field of view and applied to obtain tip temperatures of 203 secondary Fe-rich IMCs growing in an Al-Cu-Fe alloy. The cooling rate and grain refiner additions affected the IMC tip temperature, phase selection and the final population, primarily by affecting the inter-dendritic liquid channel tortuosity. Adding grain refiners and using a higher cooling rate delayed the growth of secondary IMCs to lower temperatures.

The formation dynamics of Fe-rich IMCs were investigated at different cooling rates, thermal gradients and inoculation conditions (no inoculation, TiB_2 and TiC) in a hypereutectic Al-Fe alloy that formed $Al_{13}Fe_4$ as a primary phase. Without inoculation, IMCs formed on the oxide of sample surface; with inoculants, IMC formation in the melt was increased. When a thermal gradient was imposed/increased,

the IMC number density and average formation rate decreased, and it was inferred that their formation temperature also decreased. A conceptual model for IMC nucleation was proposed.

Last, faceted growth of primary and secondary IMCs was studied in three model alloys: Al-Cu-Fe, Al-Fe and Al-Pt-Er that formed primary Pt-rich IMCs related to the Fe-rich IMCs while providing stronger X-ray absorption imaging contrast. Time-resolved radiography measurements suggested that growth of both secondary IMCs in constrained liquid and primary IMCs in non-constrained liquid, were governed by solute diffusion effects in the liquid. Repeated formation of twin plane re-entrant (TPRE) corners facilitated preferential anisotropic growth and resulted in IMC platelets with a high aspect ratio of up to 10. In contrast, the formation of layered twins perpendicular to the preferential growth direction, promoted crystals with a much lower aspect ratio. The findings suggest that if "modifying" elements could be added to poison the TPRE mechanism of IMC growth, layered twins might be promoted to obtain IMCs with a lower, more uniform aspect ratio. In this scenario, the usual embrittling effects of high-aspect ratio, platelet IMCs may be reduced.

Declaration of Originality

The work described in this thesis was carried out by the author in the Department of Materials, University of Oxford, under the supervision of Prof. Patrick Grant and Dr. Enzo Liotti. This thesis is submitted for the degree of Doctor of Philosophy at University of Oxford. I hereby declare that all of the work in this thesis is original and my own, except as specified in Acknowledgements or in the text, and that no part of the thesis has been submitted for a degree at this or any other university.

Acknowledgements

I am sincerely grateful to my supervisors Prof. Patrick Grant and Dr. Enzo Liotti for their guidance and support throughout the entire project. I really enjoyed all the discussions that we have had. Without them my DPhil would not be possible.

I would like to show my gratitude to Prof. Ragnvald Mathiesen for providing me with access to his state-of-art laboratory apparatus, and all his support and patience through my experiments and afterwards.

I wish to thank Dr. Christopher Gourlay and Yi Cui from Imperial College London for the collaborated EBSD work on my intermetallic compounds.

A special thank you to Dr. Andrew Lui, Robin Vincent and Gideon Ring for their help in building the solidification rig and suggestions on my trivial technical matters.

I would like to thank Dr. Thomas Connolley and Dr. Matthew Wilson for their contribution as team members of our synchrotron campaign.

A special thanks to the beamline scientists at ID19, ESRF and Psiche, SOLEIL for the support and guidance throughout the synchrotron beamtime.

I would also like to thank my colleague Dr. Junfu Bu for always being available for a warm chat.

Finally I must thank my parents and my younger brother for their constant encouragement and support.

Contents

1 Introduction **1**

1.1 The aluminium industry 1

1.2 Fe and Fe-rich intermetallics in Al alloys 3

1.3 Project objectives 6

1.4 Thesis structure 7

2 Literature Review **9**

2.1 Nucleation of Fe-rich IMCs 9

2.1.1 Heterogeneous nucleation 10

2.1.2 Nucleants for Fe-rich IMCs 17

2.1.2.1 TiB_2 and TiC 17

2.1.2.2 Oxides 19

2.1.2.3 AlP particles 22

2.1.2.4 Primary Al dendrites 23

2.1.2.5 Other inclusions 25

2.2 Faceted growth of Fe-rich IMCs 25

2.2.1 Faceted crystal growth 25

2.2.2 Experimental studies of Fe-rich IMC growth 28

2.2.3 Modification of faceted growth 33

2.2.3.1 Growth modifier 33

2.2.3.2 Fragmentation 36

2.3 Phase selection of Fe-rich IMCs 37
2.3.1 Fe-rich IMCs in Al alloys 37
2.3.1.1 Fe-rich IMCs in Al-Si-Fe based system 37
2.3.1.2 Fe-rich IMCs in Al-Cu-Fe system 43
2.3.2 Modification of Fe-rich IMC phase selection 48
2.3.2.1 Neutralisers 48
2.3.2.2 Cooling rate 52
2.4 Summary 54

3 Experimental Methods **56**

3.1 Design of experiments 57
3.1.1 Nucleation and growth of primary IMCs in *binary* system . 58
3.1.2 Nucleation and growth of primary IMCs in *ternary* system 59
3.2 Alloy and sample preparation 61
3.2.1 Al-Cu-Fe 61
3.2.2 Al-Fe 62
3.2.3 Al-Pt-Er 64
3.3 *In-situ* X-ray radiography 65
3.3.1 Solidification rigs 66
3.3.2 Experimental set-up 68
3.4 Data processing and data analysis 73
3.4.1 Image processing 74
3.4.2 Data analysis 79
3.4.2.1 Tip temperature estimation for secondary Fe-rich IMCs 80
3.4.2.2 Estimation of branching points in interdendritic channels 82
3.4.2.3 Formation of primary IMCs 84

3.4.2.4 Estimation of formation temperature of primary IMCs . . . 84
3.4.2.5 Estimation of formation undercooling for primary IMCs . . . 86
3.4.2.6 Measurement of IMC growth . . . 88
3.5 Electron microscopy . . . 88
3.5.1 SEM/EDX . . . 89
3.5.2 TEM . . . 89
3.5.3 EBSD . . . 90

4 Tip Temperature and Phase Selection of Secondary Fe-rich IMCs 91
4.1 Introduction . . . 91
4.2 Results . . . 92
4.2.1 IMC tip temperature . . . 92
4.2.2 IMC identification . . . 94
4.3 Discussion . . . 98
4.3.1 IMC phase selection . . . 98
4.3.2 Inter-dendritic channel tortuosity . . . 99
4.4 Summary . . . 104

5 Crystal formation and inoculation of primary Fe-rich IMCs 105
5.1 Introduction . . . 105
5.2 Results . . . 106
5.3 Discussion . . . 112
5.3.1 Nucleants for IMCs . . . 112
5.3.2 IMC nucleation . . . 114
5.3.2.1 Size of UZ and magnitude of available undercooling 117
5.3.2.2 Cooling rate and time . . . 119
5.3.3 IMC formation undercooling . . . 125

5.4 Summary 127

6 Growth of faceted IMC crystals **129**

6.1 Introduction 129

6.2 Results and Discussion 130

6.2.1 Growth of secondary IMCs 130

6.2.2 Growth of primary IMCs 133

6.2.3 Twinning 136

6.3 Summary 145

7 Conclusions **148**

8 A look to the future **151**

8.1 Multi-element mapping using synchrotron X-ray fluorescence . . . 152

8.1.1 Experimental set-up 152

8.1.2 Preliminary results 152

8.2 Multi-element mapping using laboratory X-ray transmission . . . 153

8.2.1 Experimental set-up 153

8.2.2 Data processing 156

8.2.3 Results 157

8.3 Further work 160

Bibliography **162**

List of Figures

1.1 Production and consumption of Al in the world, data from [3]. . . 2

1.2 Global consumption of Al by industrial sector in 2015, data from [3]. 3

1.3 Al-rich side of the Al-Fe binary phase diagram [25]. 5

1.4 Optical image showing a micro-crack initiating from an Fe-rich IMC needle in fatigue testing of a cast Al-Si alloy [16]. 5

1.5 Decrease of ductility with increasing Fe concentration due to needle-like Fe-rich IMCs (inset) in die cast Al-Si-Mg alloys [14]. 6

2.1 Schematic of nucleation of a spherical solid cap on a liquid-foreign substrate interface, reproduced after [30]. 11

2.2 The probability of finding a cluster of critical size as a function of undercooling [32]. 12

2.3 Heterogeneous nucleation rate in pure Al melt as a function of absolute temperature for contact $\theta = \pi/4$, based on data from [30]. 13

2.4 Simulated distribution of activated nucleants as a function of undercooling at a constant cooling rate, after [30]. 16

2.5 A graph showing the regimes of heterogeneous nucleation behaviour as a function of undercooling and contact angle for a given nucleant size, after [36]. 17

2.6 Secondary electron image showing a crack along the β-Fe IMCs [42]. 20

2.7 Backscattered electron image of (a) α-Fe and β-Fe IMCs on the surface of α-Al_2O_3, and (b) β-Fe IMCs on the surface of $MgAl_2O_4$ [43]. 21
2.8 β-Fe IMCs on the surface of γ-Al_2O_3 [44]. 22
2.9 Radiography image showing β-Fe IMCs in an Al-9.5Si-3Cu-1.2Fe alloy [49]. 24
2.10 Interface free energy as a function of occupied fraction of surface sites, after [58]. 26
2.11 A schematic showing growth of a Ge crystal with one {111} twin, creating three re-entrant grooves as preferential sites for atom attachment for growth along $\langle 11\overline{2} \rangle$ directions [62]. 28
2.12 A schematic showing growth of a Ge crystal with two {111} twin, creating 6 re-entrant grooves as preferential sites for atom attachment for growth along $\langle 11\overline{2} \rangle$ directions [62]. 28
2.13 (a) HRTEM image of β-AlFeSi IMCs along [100] zone axis, showing the presence of periodic faults and twins on (001) [74]. (b) HRTEM image showing the small steps on the faceted boundary of β-AlFeSi IMCs [73]. 29
2.14 Radiography images of a growing β-AlFeSi IMC at (a) 564°C, (b) 558°C, and (c) 531°C. "P" in (c) indicates the presence of porosity [78]. 30
2.15 Two types of IMC-IMC interations: (a-c) impingement and (d-f) potential branching [50]. 31
2.16 Radiograph sequences showing growth of two IMCs with (a) hexagonal shape at 0.5 Ks^{-1} and (b) star shape at fastest cooling when power regulation was switched off in an Al-8.6Si-2Cu-1.2Fe (wt.%) alloy [81]. 33

2.17 A secondary electron image of a deep-etched sample used in the radiography experiments, showing a three-armed star-shaped IMC [81]. 34
2.18 Synchrotron X-ray radiograph sequence showing fragmentation of a primary Al_2Cu IMC (highlighted by dashed ellipse) induced by a pulsating cavity bubble [99]. 36
2.19 Liquidus projection of ternary Al-Si-Fe phase diagram at Al-rich corner [106]. 38
2.20 Thermodynamic calculation of solidification sequence in Al-0.5Si-0.5Mg-0.2Fe based on equilibrium condition [107]. 39
2.21 TEM image of needle shaped Al_3Fe particles on the grain boundaries of a DC cast Al-0.25Fe-0.13Si alloy ingot, with diffraction pattern along [110] zone axis [111]. 40
2.22 (a) Bright field TEM image of an α'-AlFeSi extracted from an ingot of 6063 Al alloy with 0.1 wt.%Fe solidified at 0.06 °C/s and homogenised at 585 °C for 2400 ks. (b) Selected area diffraction pattern from [001] zone axis [114]. 40
2.23 (a) Bright field TEM image of a needle β-AlFeSi extracted from ingot of 6063 Al alloy with 0.1 wt.%Fe solidified at 0.06 °C/s. (b) Selected area diffraction pattern from [001] zone axis [114]. 41
2.24 Bright field TEM image of a Chinese-script α-AlFeSi in a directionally resolidified 6xxx alloy with selected area diffraction pattern from [111] zone axis [77]. 42
2.25 Liquidus projection of ternary Al-Cu-Fe phase diagram at Al-rich corner [156]. 45
2.26 Backscattered electron image showing needle-like Al_7Cu_2Fe (β-Fe) in Al-4.5Cu-0.3Fe (wt.%) [46]. 47

2.27 Different morphologies of Fe-rich IMCs in (a) Al-7Si-0.38Mg-0.2Fe, (b) Al-7Si-0.38Mg-0.2Fe-0.07Mn, (c) Al-7Si-0.38Mg-0.2Fe-0.13Mn, and (d) Al-7Si-0.38Mg-0.2Fe-0.2Mn [179]. 50
2.28 Optical micrographs showing the morphologies of Al_2Cu, Al_7Cu_2Fe and Mn-bearing IMCs in cast (a) Al-4.5Cu-0.3Fe-0.29Mn, (b) Al-4.5Cu-0.3Fe-0.66Mn (arrow 1: Al_2Cu, arrow 2: Al_7Cu_2Fe, arrow 3: Mn-bearing) [146]. 51
2.29 Optical micrographs showing Chinese script α-IMCs in (a) Al-11.7Si-0.6Cu-2.4Fe-2.4Co [183], and (b) Al-7Si-0.3Mg-1Fe-1Co [177]. 52
2.30 Distribution of Fe-rich IMCs in Al-7.5Si-0.65Fe-0.3Cu-0.2Mn at cooling rates of (a) 0.1°C/s, and (b) 1°C/s [116]. 54
2.31 Microstructure of Al-4.7Cu-0.3Fe-0.2Si-0.2Mn at (a) 1°C/s, and (b) 4°C/s. Notice the decrease in the amount of Al_7Cu_2Fe (β(FeCu)) and the formation of $Al_{32}(Cu,Fe,Mn)_8(Al,Si)_4Si_2$ (α(MnFe)) at increasing cooling rate [166]. 54

3.1 A diagram summarising the relationship between the *in-situ* experimental campaigns, their principal focus, the alloy used and post-solidification microscopy. 57
3.2 Linear absorption coefficient as a function of photon energy for $Al_{24}Pt_9Er_4$ (phase of interest in the work), the liquid matrix and Al_3Er, which was the other primary phase in the alloy. 60
3.3 Photos of the author preparing samples for (a) laboratory X-ray radiography experiments at NTNU, and (b) synchrotron experiments at ID19, ESRF. Encapsulated samples are shown in the zoomed-in images. 62
3.4 A schematic showing how foil samples were sectioned from a bulk Al-Cu-Fe ingot. 63

3.5 A schematic showing the casting arrangement and how foil samples were sectioned from the bulk Al-Fe ingot. The as-cast ingot was chopped as indicated by the yellow dashed lines, and sliced using wire electro-discharge machining (wire EDM) to produce foil samples. 64

3.6 A schematic showing how foil samples were sectioned from a bulk Al-Pt-Er ingot. The as-cast ingot was cut by water jet as indicated by the yellow dashed lines, and sectioned using a diamond wheel blade to produce foil samples. 65

3.7 Schematic of experimental configurations for (a) synchrotron radiography experiments where gravity was parallel to the sample surface, and the incident X-ray was a parallel beam, and (b) laboratory radiography experiments where gravity was perpendicular to the sample surface, and the incident X-ray was a cone beam. . 65

3.8 A photo of a sample being mounted onto the first-generation Bridgman solidification rig. 66

3.9 A photo of the second-generation Bridgman solidification rig for *in-situ* synchrotron X-ray radiography experiments. The front plate has been removed to show the interior. 68

3.10 (a) A photo of the author adjusting the set-up of the laboratory apparatus for *in-situ* X-ray radiography of solidification at NTNU, Norway. (b) A photo of the XRMON-GF apparatus. 70

3.11 An example of cooling curves of the two heaters during a typical solidification experiment. A constant temperature difference was maintained between the two heaters while cooling both heater at a constant cooling rate to achieve directional solidification. 72

3.12 An example of image processing sequence for radiographic images from NTNU for Al-Fe. (a) Raw image. (b) Image after flat field correction. (c) Image after Wiener (11×11 pixels) filtering for noise reduction. (d) Image after normalisation of pixel intensity range. . 75
3.13 An example of image processing sequence for radiographic images from DLS for Al-Cu-Fe. (a) Raw image. (b) Image after flat field correction. (c) Image after de-banding codes were applied. (d) Final image after Wiener filtering (5×5 pixels) for noise reduction and normalisation of pixel intensity range. 76
3.14 An example of image processing sequence for radiographic images from ESRF for Al-Fe. (a) Raw image. (b) Image after flat field correction. (c) Image after Wiener filtering (5×5 pixels) for noise reduction. (d) Final image after subtraction with the image 15 frames before it and normalisation of pixel intensity range to further enhance the image quality and the visibility of the IMCs. . . 77
3.15 An example of image processing sequence for radiographic images from ESRF for Al-Pt-Er. (a) Raw image. (b) Image after geometrical correction was performed by resizing (a) along the horizontal axis to correct the distorted image pixel due to the 45° sample-beam angle. (c) Image after flat field correction. (d) Final image after Gaussian filtering (3×3 pixels) for noise reduction and normalisation of pixel intensity range. 78
3.16 An example of image processing sequence for radiographic images from SOLEIL for Al-Pt-Er. (a) Raw image. (b) Image after geometrical correction. (c) Image after flat field correction. (d) Final image after Gaussian filtering (5×5 pixels) for noise reduction and normalisation of pixel intensity range. 79

3.17 A diagram summarising the measurements and data analysis, relating to the overall research objectives and the different alloys. . 80
3.18 Radiographs of 0.8Fe at 0.2 Ks^{-1} and a schematic showing how the temperature field was estimated. 81
3.19 An example showing the key steps of the procedure to estimate the number of inter-dendritic channel branching points. (a) A radiograph of 0.8Fe-GR at the frame just before IMCs appeared. (b) Image after skeletonisation that thinned the inter-dendritic channels to single pixel inter-connected lines, superimposed on the radiograph. (c) Branching points were counted from (b) and superimposed on the image. 83
3.20 (a) A radiography image (subtracted from the image 8 frames before it) of AF-B at 1 Ks^{-1}, 8 $K\,mm^{-1}$, showing the eutectic front near the middle of the field of view. Green markers were manually added frame by frame to track the position of this eutectic front. (b) A 3D scatter plot of time when eutectic appeared ($t = 0$ was set when primary IMC first appeared in the field of view) as a function of position (x, y), with a 2D surface best-fit, $R^2 = 0.999$. 85
3.21 A schematic of the hypereutectic side of the Al-Fe phase diagram to illustrate the estimation of instantaneous liquidus temperature. C_0 is the initial alloy composition, C_E is the eutectic composition, and C_L^* is the instantaneous liquid composition when the nth IMC was forming. T_{L0}, T_E and T_L^* are the corresponding equilibrium (liquidus) temperature at C_0, C_E and C_L^* respectively. N is the total number of IMCs formed in the field of view in an experiment. 87

4.1 Radiograph sequences of IMC growth at a cooling rate of 0.2 Ks^{-1} in (a) 0.8Fe and (b) 0.8Fe-GR, with zoomed-in images showing the IMC tips. Time $t = 0$ was set when the α-Al dendrite tips first appeared at the bottom of the field of view. 93

4.2 IMC tip temperature at different cooling rates for 1.5Fe, 0.8Fe, 1.5Fe-GR and 0.8Fe-GR. 94

4.3 Secondary electron images of: (a) 1.5Fe showing presence of IMC A (in red ellipse), and IMC B (see inset image for detailed morphology) at $1\,Ks^{-1}$, with green arrow indicating the orientation of the primary α-Al dendrites, (b) a composite IMC particle with IMC A in the centre and IMC B around the edge in 1.5Fe at $0.2\,Ks^{-1}$, (c) IMC A particle with small regions near the edge transformed into IMC B in 1.5Fe-GR at $0.2\,Ks^{-1}$, and (d) 1.5Fe-GR at $2\,Ks^{-1}$ showing presence of IMC B only (IMC A: $Al_6(Fe,Cu)$; IMC B: Al_7Cu_2Fe). 96

4.4 Bright field TEM images of (a) Al_7Cu_2Fe (dark needles) and (c) $Al_6(Fe,Cu)$ (yellow squares indicate the positions where HR-TEM images were acquired); HR-TEM images of (b) Al_7Cu_2Fe with FFT pattern along [010] direction and (d) $Al_6(Fe,Cu)$ with FFT pattern along $[1\bar{1}0]$ direction. 97

4.5 IMC tip temperature at different cooling rates for 1.5Fe, 0.8Fe, 1.5Fe-GR and 0.8Fe-GR, with labels indicating different IMC phase populations and literature values of $Al_6(Fe,Cu)$ [159] and Al_7Cu_2Fe [46] formation temperatures determined by thermal analysis. . . . 100

4.6 Radiographs showing inter-dendritic channel morphology in: (a) 1.5Fe and (b) 1.5Fe-GR at 1 Ks^{-1}. Yellow lines highlight a path in the inter-dendritic channel from bottom to top. The image height is 1 mm and the inter-dendritic channel length highlighted are 1.02 mm and 1.31 mm respectively. 101

4.7 Radiographs of IMCs in 1.5Fe-GR at a cooling rate of: (a) 0.2 Ks^{-1} and (b) 1 Ks^{-1}. 102

4.8 Estimation of inter-dendritic channel branches per unit area (mm^{-2}) in 0.8Fe, 0.8Fe-GR, 1.5Fe and 1.5Fe-GR at different cooling rates. 103

5.1 Radiography sequences showing primary IMC formation in near isothermal, horizontal solidification of alloys (a) AF, (b) AF-B and (c) AF-C, all at a cooling rate of 2 Ks^{-1}. 106

5.2 (a) Total IMC density (total number of IMCs divided by the volume of the field of view) and (b) average formation rate (total IMC density divided by the duration of IMC formation) in alloys AF, AF-B and AF-C at 0.5 - 2 Ks^{-1} in near isothermal, horizontal solidification. The solid lines in (b) indicate a linear best-fit to highlight the trend. 107

5.3 Radiographic sequences showing primary IMC formation in directional, vertical solidification at 2 Ks^{-1} of (a) AF and (b) AF-B at a thermal gradient of 5 $K\,mm^{-1}$, and (c) AF-B at 8 $K\,mm^{-1}$. Each image was obtained by subtracting frame f_n with frame f_{n-15}. In AF-B, settling of IMCs was frequently observed, and the yellow circles in (b) and (c) highlight the white "shadow" left behind by the settling IMCs upon image subtraction. (d) Corresponding evolution of the number of IMCs in the field of view, and (e) evolution of formation rate as a function of time. Dashed lines in (e) indicate the average formation rate. For each experiment, $t = 0$ was set when the first IMC appeared in the field of view. 109

5.4 (a) Total IMC density (total number of time-resolved IMC formation events divided by the volume of the field of view) and (b) average formation rate in AF and AF-B at a thermal gradient of 5 $K\,mm^{-1}$ and AF-B at a thermal gradient of 8 $K\,mm^{-1}$, at cooling rates of 0.5 to 4 Ks^{-1} in directional, bottom-to-top solidification. The solid lines in (b) indicate a linear best-fit to highlight the trend. 110

5.5 (a) IMC density as a function of thermal gradient for alloy AF-B. (b) Average IMC formation rate as a function of thermal gradient for alloy AF-B. 110

5.6 Estimated formation temperature of primary IMCs as a function of cooling rate for AF and AF-B at $5\,\mathrm{K\,mm^{-1}}$ and AF-B at $8\,\mathrm{K\,mm^{-1}}$. For each box plot, the red line denotes the median of the IMC formation temperature, the black circle denotes the mean, the top and bottom edges of the box indicate the 75% and 25% percentile, and the top and bottom whiskers indicate the 95% and 5% percentile. Solid lines with the same colour code represents a linear best-fit of the median formation temperature. The data set comprises 1893 measurements. 111

5.7 Number fraction of mobile primary IMCs as a function of cooling rate for AF and AF-B at $5\,\mathrm{K\,mm^{-1}}$ and AF-B at $8\,\mathrm{K\,mm^{-1}}$. . . . 113

5.8 (a) A schematic of the liquid composition in front of a growing IMC. C_0 is the bulk liquid composition. (b) A schematic of the undercooled zone (UZ) in front of a growing IMC at isothermal condition, and thermal gradient of $G1$ and $G2$ ($G2 > G1$). T_L is the equilibrium liquidus temperature as a result of the liquid composition profile in (a). T_{L0} is the bulk liquidus. (c) Resultant available undercooling from (b), at isothermal condition, $G1$ and $G2$. UZ_{G1} and UZ_{G2} denote the extent of UZ at $G1$ and $G2$ respectively. ΔT_{maxISO}, ΔT_{maxG1} and ΔT_{maxG2} are the maximum available undercooling at isothermal condition, $G1$ and $G2$ respectively. 115

5.9 (a) A schematic illustrating the size of the undercooled region (UZ) as a function of thermal gradient. (b) A schematic illustrating the maximum available undercooling (ΔT_{maxG}) as a function of thermal gradient. 119

5.10 (a) A schematic of liquid composition profiles in front of a growing IMC at cooling rate $\dot{T}_1$ and $\dot{T}_2$ ($\dot{T}_2 > \dot{T}_1$)). (b) A schematic of equilibrium liquidus temperature profiles and the undercooled zones (UZ) at $\dot{T}_1$ and $\dot{T}_2$, at a thermal gradient of G_1. (c) Resultant distribution of available undercooling at $\dot{T}_1$ and $\dot{T}_2$, at G_1. The black dashed line indicates the undercooling required by the most potent nucleants to catalyse nucleation. 123

5.11 A schematic illustrating the translation of UZ with time, at two different cooling rates $\dot{T}_1$ and $\dot{T}_2$ ($\dot{T}_2 > \dot{T}_1$), at a thermal gradient of $G1$. The red dashed line in each graph indicates the boundary between the mushy zone (a mixture of solid and liquid) and full liquid. 124

5.12 Histograms showing the distribution of estimated formation undercooling of primary IMCs for each of the 12 experimental conditions. The term formation undercooling refers to the actual undercooling at which an IMC forms on any potent nucleant. Each histogram was averaged against the number of repeat experiments. A box plot is superimposed at the top of each histogram to show the median undercooling (red line), the 25% and 75% percentile (green box), and the 5% and 95% percentile (the whiskers). 125

6.1 Radiograph sequences of IMC growth at a cooling rate of 0.2 Ks^{-1} in (a) 0.8Fe and (b) 0.8Fe-GR, with zoomed-in images showing the IMC tips. Time $t = 0$ was set when IMCs first appeared at the bottom of the field of view. 131

6.2 (a) Evolution of length of 6 long IMCs in 0.8Fe at 0.2 Ks^{-1}. (b) Evolution of length of 15 short IMCs in 0.8Fe-GR at 0.2 Ks^{-1}. The red rectangles highlight the difference in the length scale. (c) Velocity evolution of the long IMCs in 0.8Fe. (d) Velocity evolution of the short IMCs in 0.8Fe-GR. 132

6.3 (a) An example radiograph showing primary Fe-rich IMCs in solidifying Al-3Fe (wt%) at 0.5 Ks^{-1}. The yellow rectangle indicates the field of view of the radiograph sequence in (b). (b) A radiograph sequence showing growth of a faceted Fe-rich crystal. $t = 0$ was set at the beginning of the size measurement. 134

6.4 (a) Evolution of length and width with time for the IMC in Fig. 6.3(b). (b) Growth velocity of the length and width. $t = 0$ was set at the beginning of the size measurement. The inset shows detail of the growth velocity of the width at $0 < t < 20$ s. 135

6.5 (a) A radiograph sequence of growth of a primary $Al_{13}Fe_4$ crystal, showing suspected twinning. (b) A secondary electron image of a twinned $Al_{13}Fe_4$ crystal in the solidified Al-Fe sample from synchrotron experiments. The dashed lines indicate the twin planes, which in this case are perpendicular to the paper, and the yellow arrows denote the re-entrant corners at the twin boundary. (c) An IPF-X map of the crystal in (b), showing four different orientations. (d) Pole figures of the crystal in (b). (e) Unit cell wire frames that illustrate the four different orientations. 136

6.6 (a) A radiograph of a typical twinned primary $Al_{24}Pt_9Er_4$ crystal. (b) A secondary electron image of a twinned $Al_{24}Pt_9Er_4$ crystal in the solidified Al-Pt-Er sample from synchrotron experiments. The yellow dash line indicates the twin plane, which is perpendicular to the paper, and the yellow arrow denotes the re-entrant corner. (c) The Kikuchi pattern of area 1 in (b). (d) The Kikuchi pattern of area 2 in (b). (e) Superimposed Euler angle map, pole figures, and unit cell wire frames for the $Al_{24}Pt_9Er_4$ crystal, indexed as a triclinic structure. (f) Superimposed Euler angle map, pole figures, and unit cell wire frames for the same $Al_{24}Pt_9Er_4$ crystal, indexed as a monoclinic structure. 138

6.7 (a) A radiograph sequence of growth of an elongated $Al_{13}Fe_4$ crystal at 0.5 Ks^{-1}, showing repeated suspected twin platelets and re-entrant corners. $t = 0$ was set at the beginning of the size measurement. Inset images with red frames provided a zoomed-in view. The green dashed lines at $t = 28$ s highlight the boundaries between the suspected twin platelets. (b) Evolution of the length and width. The IMC grew out of the field of view after $t = 28$ s. (c) Evolution of growth velocities along the length and width. The time when a new plate appeared at the re-entrant corners ($t = 4$ s, $t = 12$ s, $t = 16$ s and $t = 21$ s) is labelled. 139

6.8 (a) A radiograph sequence showing growth of a primary $Al_{13}Fe_4$ crystal containing layered platelets perpendicular to its preferential growth direction at 0.5 Ks^{-1}. The yellow dashed line at $t = 10$ s highlights the boundary between two suspected twin platelets, and the circle highlights a new thin plate growing between the two platelets. The dashed rectangle at $t = 72$ highlights a thin IMC plate that overgrew the other platelets of the crystal but eventually was stopped by a pre-existing crystal above it. (b) Evolution of the length and width of the crystal. (c) Evolution of growth velocities of the crystal. 142

6.9 (a) A radiograph sequence showing growth of a primary $Al_{13}Fe_4$ crystal containing layered platelets at 0.5 Ks^{-1}. The green dashed lines at $t = 50$ s highlight the boundaries between the microscopic twin platelets, and the green arrow denotes a re-entrant corner. (b) Evolution of crystal length and width. (c) Evolution of growth velocities. 144

6.10 (a) A radiograph sequence showing growth of a primary $Al_{24}Pt_9Er_4$ crystal, comprising layered twin platelets, in an Al-Pt-Er alloy at 0.5 Ks^{-1}. (b) Evolution of the length and width of the crystal in (a). (c) Evolution of the length and width growth velocity of the IMC crystal. 145

8.1 A schematic of simultaneous radiography-fluorescence set-up. . . . 153

8.2 (a) A radiograph of a solidifying Al-Pt-Er alloy at 0.1 Ks^{-1}. (b) Simultaneous HEXITEC fluorescence map of the Er distribution. (c) Simultaneous HEXITEC fluorescence map of the Pt distribution. The red square in (a) indicates the field of view of the HEXITEC maps. 154

8.3 A photo of the laboratory NSI apparatus and set-up for solid-sate HEXITEC mapping. 155

8.4 An example spectrum of $\ln(\frac{I_0}{I})$ as a function of photon energy from one pixel of the HEXITEC. h_{Er} and h_{Pt} are the sizes of the Er and Pt K-edges in the spectrum. The green and blue curves are the best-fit curves of the Er and Pt edges respectively. 157

8.5 (a) A radiograph of an Al-Pt-Er alloy as prepared by arc melting, using the NSI apparatus. The red square indicates the field of view in the HEXITEC in (b) and (c). (b) Qualitative HEXITIC map of Er. (c) Qualitative HEXITEC map of Pt. 158

8.6 Linear absorption coefficients of Al, Er and Pt as a function of photon energy. 159

8.7 A map of $\frac{c_{Pt}}{c_{Er}}$ ratio for the Al-Pt-Er alloy, using the same data as Fig. 8.5b and 8.5c. 160

Chapter 1

Introduction

1.1 The aluminium industry

Al and Al alloys are extensively used in modern life, from beverage cans and packaging foil to vehicles and aircrafts. Fig 1.1 summarises the global Al production and consumption from 2000 to 2014. In these 14 years, the world Al production increased from 24707 kt to 54091 kt, whilst the Al consumption increased from 24067 kt to 54126 kt. Fig. 1.2 shows the Al consumption by industrial sector in 2015. Transport industry accounted for 27% of the total Al consumption, followed by construction (25%). The extensive usage of Al alloys in transport and construction is because of their combination of lightweight, good specific mechanical properties and excellent corrosion resistance. Here the automotive industry is taken as an example to illustrate the advantage of using Al alloys. Replacement of dense steel parts by Al can achieve up to 50% weight saving [1]. By using a full Al body, the Audi A8 realised a direct weight saving of 194 kg. Every 100 kg weight reduction in personal vehicles can lead to a lifetime fuel saving of around 800 litres and a lifetime greenhouse gas saving of over 20 kg of CO_2 [2]. Thus, application of Al alloys has been strongly driven by the potential economic and environmental benefits.

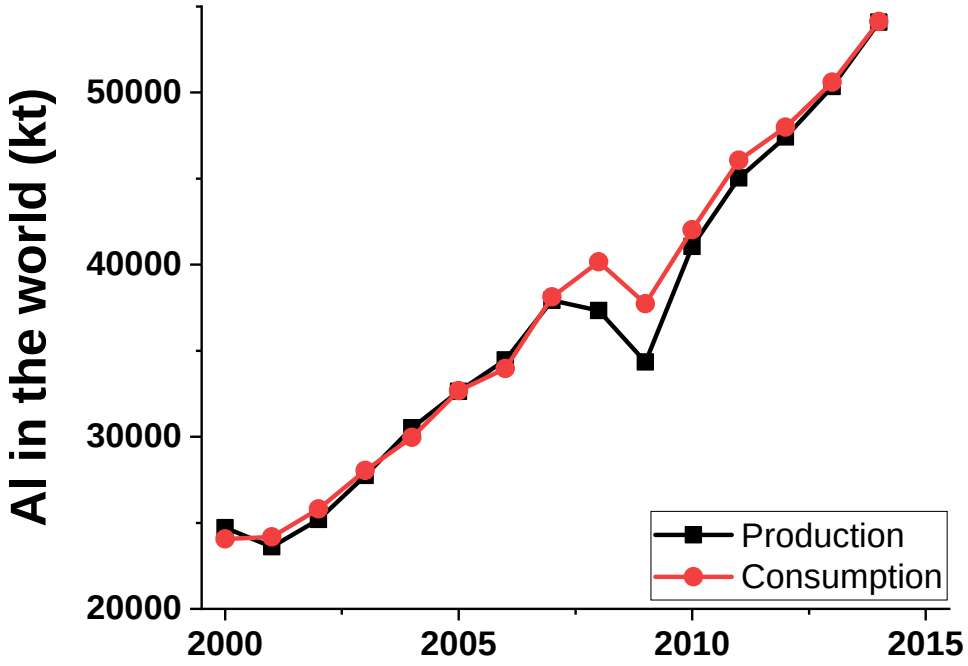


Figure 1.1: Production and consumption of Al in the world, data from [3].

Al alloys can be produced by either primary or secondary production. Primary production produces virgin Al via the Bayer process [4] in which bauxite is converted into alumina, followed by Hall-Heroult electrolytic reduction process [5] in which the alumina is reduced into aluminium liquid at temperatures above 950°C. The primary production route is expensive because it is energy-consuming to split Al from O [6, 7]. An average energy of 66 MJ is required to produce 1 kg of Al via primary production, and over 80% of the energy is consumed as electricity in Hall-Heroult electrolytic reduction process [8]. In 2009, for example, the greenhouse gas emission associated with global Al cycle was 0.45 Gt, and primary production processes took up over 90% of the emission, accounting for approximately 1% of global greenhouse gas emissions [9]. Secondary Al is produced by recycling and remelting Al scrap from a mixture of end-of-life Al alloys with different compositions. The recycling process is much less expensive

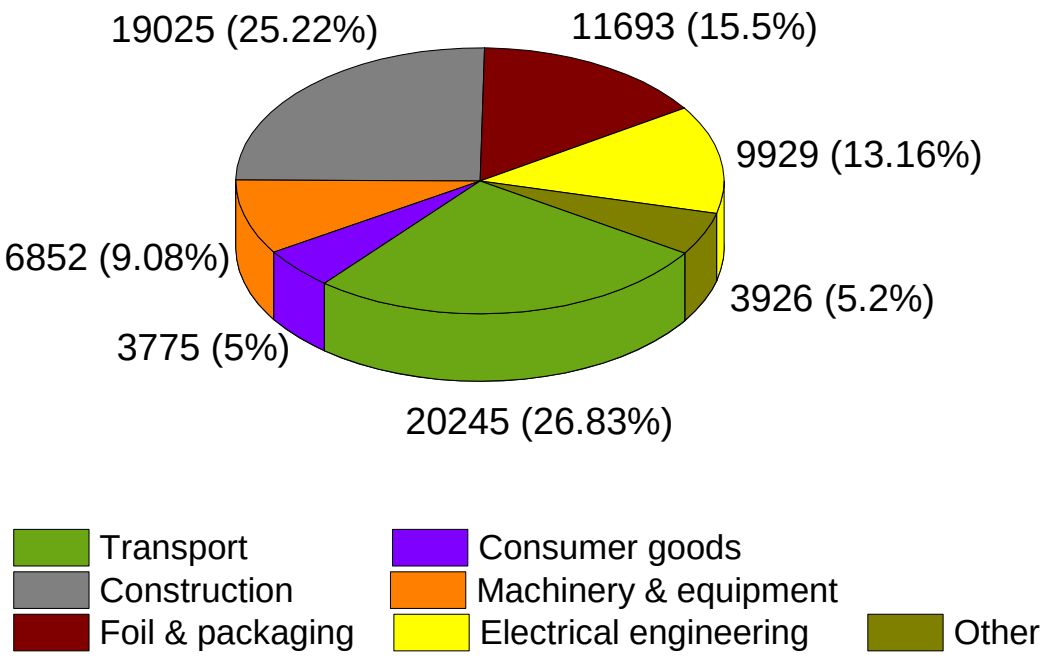


Figure 1.2: Global consumption of Al by industrial sector in 2015, data from [3].

and energy-intensive, saving up to 95% of energy and over 90% of greenhouse gas emission [9]. Faced with increasing global warming, increasing recycling of Al and other metals has been identified as an important mitigation factor by the Inter-governmental Panel on Climate Change (IPCC) to reduce greenhouse gas emissions.

1.2 Fe and Fe-rich intermetallics in Al alloys

While Al recycling enables dramatic reduction in emission and energy consumption, more extensive recycling of end-of-life Al alloys is hindered by the accumulation of impurities, Fe in particular. Controlled additions of Fe may promote fine dispersions of secondary Fe-rich intermetallic compounds (IMCs) that increase the strength of alloys [10]. However in most cases, Fe is picked up unintention-

ally as an impurity through the alloy production and manufacturing processes, particularly during recycling. During recycling, alloy scrap with different Fe concentrations are mixed and remelted, and the Fe concentration increases with increasing remelting cycles. It is technically challenging and so far uneconomical to remove the Fe impurities from the Al scrap.

Given the high solubility in liquid Al (2.5 wt.% at 700°C and 5 wt.% at 800°C) but low solubility (0.04 wt.%) in solid Al [11] as shown in Fig. 1.3, Fe impurities lead to precipitation of often highly faceted IMCs e.g. β-Al_5FeSi, during solidification. Al-Si based alloys and Al-Cu based alloys are two major alloy systems where a considerable number of issues caused by faceted Fe-rich IMCs have been reported. The faceted morphology of these Fe-rich IMCs degrade the mechanical properties (e.g. ductility) [12–15], fatigue life (Fig. 1.4) [13, 16] and corrosion resistance [17, 18]. Fig. 1.5 shows decreasing ductility with increasing Fe concentration in die cast Al-Si-Mg alloys as a result of needle-like (in 2D) Fe-rich IMCs [14]. The elongation of the alloy dropped from 20 % to 5 % as the Fe concentration increased from 0.2 wt.% to 2.5 wt.%. A similar decrease in ductility with increasing Fe concentration caused by needle-like Fe-rich IMCs was also reported in a squeeze-cast Al-Cu-Mn alloy [15]. In addition, these Fe-rich IMCs have also been widely reported to increase the alloy susceptibility to various solidification defects, such as porosity [19–22] and hot tearing [23, 24].

Given the detrimental effect of the faceted Fe-rich IMCs, the strategy extensively adapted by Al industry is post-solidification heat treatment to re-dissolve the IMCs and to re-precipitate the Fe in less harmful forms [26–29]. However, necking and fragmentation of the Fe-rich IMCs may occur only at high solution treatment temperatures and long holding times, which add cost and time. In order to avoid the formation of harmful Fe-rich IMCs and loss of performance, recycled Al scrap requires the addition of virgin Al produced by primary production to dilute the Fe impurities. Thus, the cost of recycling increases with

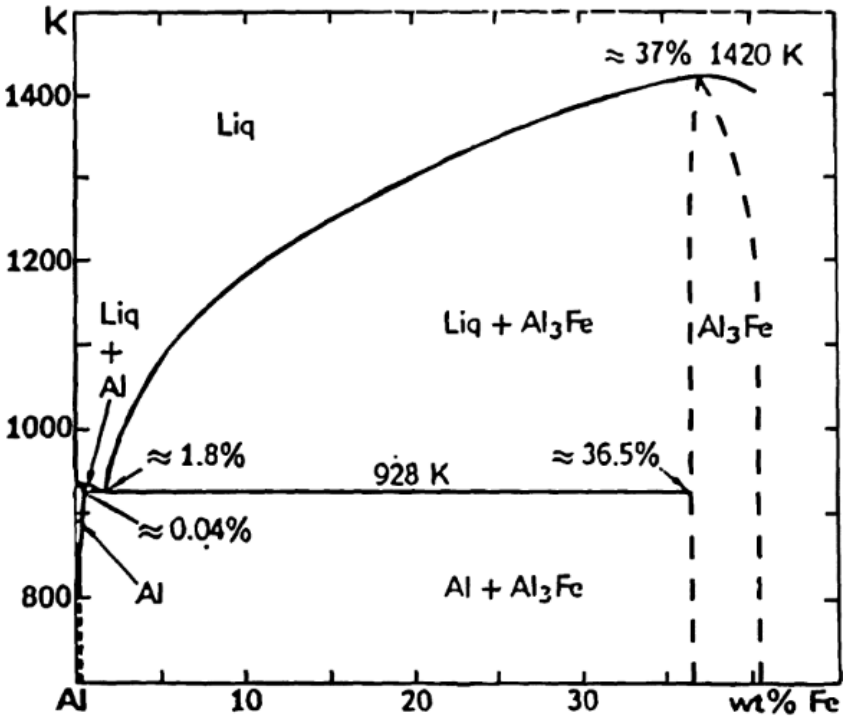


Figure 1.3: Al-rich side of the Al-Fe binary phase diagram [25].

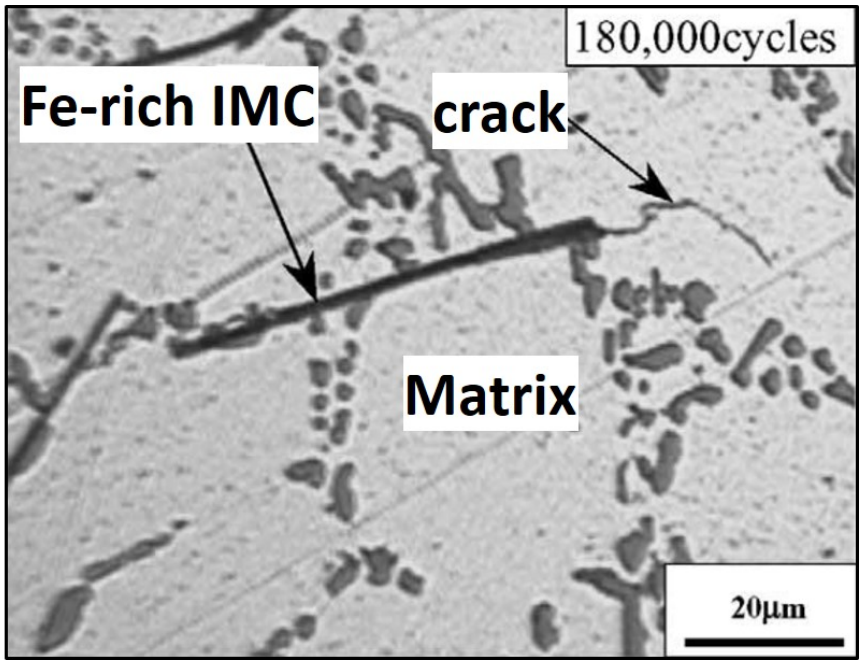


Figure 1.4: Optical image showing a micro-crack initiating from an Fe-rich IMC needle in fatigue testing of a cast Al-Si alloy [16].

remelting cycles.

In order to improve the recyclability of Al alloys to further meet the goal of re-

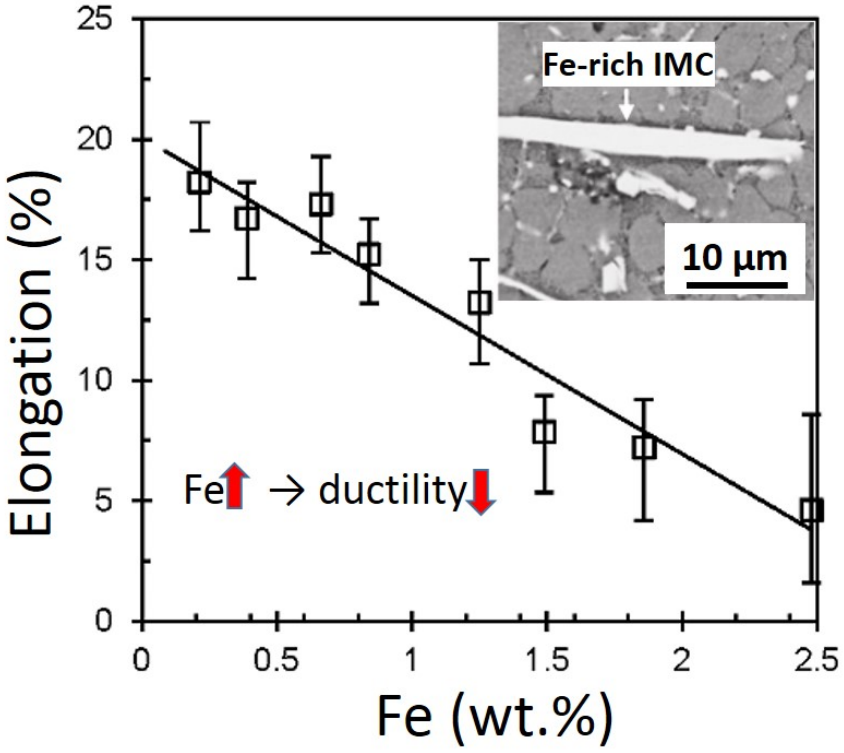


Figure 1.5: Decrease of ductility with increasing Fe concentration due to needle-like Fe-rich IMCs (inset) in die cast Al-Si-Mg alloys [14].

ducing emission and energy consumption, an alternative strategy is to control the morphology, size and distribution of Fe-rich IMCs during the solidification stage, so that more Fe can be tolerated in the alloys while maintaining the mechanical properties. To successfully control or modify the Fe-rich IMCs, their nucleation, growth and phase selection behaviour during solidification must be understood.

1.3 Project objectives

This project investigates the *dynamics* of nucleation, growth and phase selection of Fe-rich IMCs during the solidification of different Al model alloys under different conditions, by using *in-situ* X-ray radiography in combination with post-solidification microscopy. With this knowledge, it may be possible to manage IMC morphology, size and distribution by a better control of the nucleation, growth and phase selection, producing a more Fe-tolerant Al alloy processing route. The

main objectives are:

1. To investigate the nucleation of Fe-rich IMCs as a function of solidification conditions, namely cooling rate and thermal gradient, and inoculant additions.

2. To study the growth of Fe-rich IMCs and other similar faceted IMC crystals, and to explore the key controlling factors of their growth behaviour.

3. To study temperature-related phenomena, namely IMC formation temperature, formation undercooling and growth temperature as a function of solidification conditions and inoculant additions.

1.4 Thesis structure

This thesis is organised as follows:

Chapter 2 This chapter reviews the relevant literature regarding the nucleation, faceted growth and phase selection of Fe-rich IMCs, and studies on other closely related IMCs in Al alloys.

Chapter 3 This chapter describes the materials studied and methodologies employed, with a particular emphasis on *in-situ* X-ray radiography techniques.

Chapter 4 This chapter analyses data from synchrotron X-ray radiography investigation of the tip temperature and phase selection of secondary Fe-rich IMCs in model Al-Cu-Fe alloys, and discusses these results.

Chapter 5 This chapter investigates the nucleation of primary Fe-rich IMCs in a model hypereutectic Al-Fe alloy, using *in-situ* X-ray radiography both at synchrotrons and on a laboratory radiography arrangement.

Chapter 6 This chapter investigates *in-situ* X-ray radiography studies of faceted growth of primary and secondary IMCs in three model Al alloys: secondary Fe-rich IMCs in Al-Cu-Fe; primary Fe-rich IMCs in hypereutectic Al-Fe; and primary Pt-rich IMCs in an Al-Pt-Er model alloy as an analogue to Fe-rich IMCs.

Chapter 7 This chapter contains the conclusions of this work.

Chapter 8 This chapter describes ideas for future work.

Bibliography

Chapter 2

Literature Review

This chapter is a review of literature regarding the nucleation, faceted growth and phase selection of Fe-rich IMCs and other closely related faceted crystals in Al alloys. As mentioned in the introduction, the Al-Si based alloys and Al-Cu based alloys are two major systems where a large number of issues caused by faceted Fe-rich IMCs have been reported and the focus of most studies.

2.1 Nucleation of Fe-rich IMCs

When a system is cooled to its freezing temperature, an equilibrium will be reached, in which the Gibbs free energy of the liquid G_l^m equals that of the solid G_s^m [30]. As the temperature drops further, G_l^m will become higher than G_s^m, indicating a tendency for the liquid to transform into solid. However, an energy barrier must be overcome, which is associated with the creation of new solid-liquid interface before nucleation of the solid can occur. Therefore thermodynamically, a driving force is needed, which requires the liquid to be undercooled below equilibrium to compensate for the extra interfacial energy during the nucleation process. Meanwhile, kinetics must also be considered, which relate to the practicalities or rate with which the solid nuclei can form. Primarily, this relates to atomic-scale diffusion processes and the possibility of forming a nucleus of suf-

ficient size not to re-dissolve. Thus for nucleation to occur, both thermodynamic and kinetic criteria must be satisfied [30].

A full account of the nucleation theory and all the nucleation models is certainly beyond the scope of this work. The first part of this section will discuss the classical heterogeneous nucleation theory and the most widely accepted model for heterogeneous crystal nucleation, termed the free growth model [31], which by implication should apply to Fe-rich IMCs. The second part will review research papers relating more specifically to nucleation of Fe-rich IMCs.

2.1.1 Heterogeneous nucleation

Heterogeneous nucleation occurs when the solidification process initiates on a foreign surface in the melt [30]. The foreign surface can be the mould surface, oxides or other foreign particles in the melt, which are either trapped in unintentionally as impurities, or added deliberately to promote nucleation in an attempt to control the final microstructure. For example, it is common in the Al industry and particularly in the direct chill (DC) casting process to add 0.1-1 wt.% of Al-3Ti-1B or Al-5Ti-1B (wt.%) as "grain refiners" into liquid Al immediately before casting. These refiner alloys contain TiB_2 and Al_3Ti that refine the grain structure by promoting the formation of grains through a high nucleation density. Grain growth over large distances is inhibited as grains soon impinge on one another, and a refined, equiaxed structure results. [30].

Nucleation on a foreign substrate that has good chemical and structural matching with the solid phase can reduce the interfacial energy and hence the energy barrier. The concept is illustrated in Figure 2.1 , assuming that the nucleus is in a spherical cap shape. The relationships between the contact angle θ and the surface energies shown in Figure 2.1 is given by the Laplace-Young equation:

$$\gamma_{fl} = \gamma_{fs} + \gamma_{sl} cos\theta \tag{2.1}$$

where γ_{fl}, γ_{fs} and γ_{sl} are the interfacial energies (or the surface tensions) of the substrate-liquid, substrate-solid and solid-liquid interfaces, respectively.

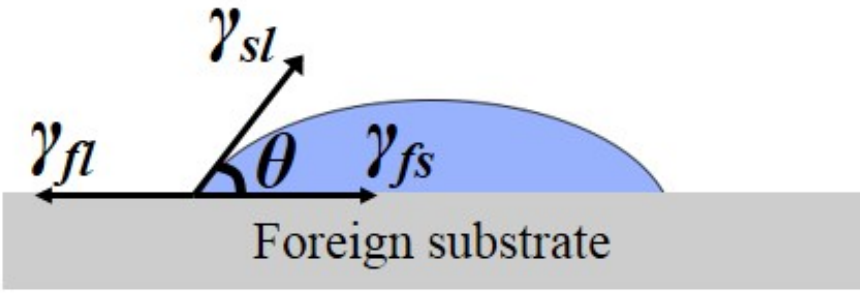


Figure 2.1: Schematic of nucleation of a spherical solid cap on a liquid-foreign substrate interface, reproduced after [30].

With the presence of the foreign substrate, the energy barrier for nucleation is given by:

$$\triangle G^{heter} = \triangle G^{homo} f(\theta) = \frac{16\pi}{3} \frac{\gamma_{sl}^3}{\triangle S_V^2 \triangle T^2} f(\theta) \tag{2.2}$$

$\triangle S_V$ is the entropy change of fusion per unit volume and $\triangle T$ is the undercooling of the system. $f(\theta)$ is a geometric factor between 0 and 1, and is determined by the wetting of the solid nucleus on the foreign substrate:

$$f(\theta) = \frac{(2 + cos\theta)(1 - cos\theta)^2}{4} \tag{2.3}$$

When $\theta = \pi$, $f(\theta) = 1$, which indicates no wetting of the solid on the foreign substrate. In this case, the solid is an entire sphere, and it is therefore equivalent to homogeneous nucleation. On the contrary, $f(\theta) = 0$ when $\theta = 0$, which corresponds to a perfect wetting of the solid on the substrate. In this case, there is no nucleation barrier [32]. $\triangle G^{homo}$ in Equation 2.2 represents the energy barrier in homogeneous nucleation conditions, where solid nuclei (assuming a sphere morphology with radius of r) form directly in liquid. $\triangle G^{homo}$ is given by [32]:

$$\triangle G^{homo} = \frac{4}{3}\pi r^{*2} \gamma sl = \frac{16\pi}{3} \frac{\gamma_{sl}^3}{\triangle S_V^2 \triangle T^2} \tag{2.4}$$

where r^* is the critical size above which of a cluster of atoms becomes a stable solid nucleus.

The probability of find a cluster of size r^* during heterogeneous nucleation was given by:

$$\frac{n_c}{n_l} = exp(-\frac{\triangle G^{heter}}{k_B T}) = exp(-\frac{16\pi}{3}\frac{\gamma_{sl}^3}{\triangle S_V^2 \triangle T^2 k_B T} f(\theta)) \tag{2.5}$$

where n_c is the number density of clusters with the the size of $r = r^*$ at a given ΔT, n_l is the number density of atoms in the liquid, and and k_B is the Boltzmann constant. The graph in Fig. 2.2 shows the number density of number density of critical clusters as a function of undercooling. At small undercooling, the term in the exponential in Equation 2.5 is large and negative, suggesting that the probability of finding a critical-size cluster is low. At larger undercooling that is sufficient to overcome the interfacial energy, the probability of finding a cluster of critical size increases dramatically within a narrow undercooling (temperature) interval (Fig. 2.2).

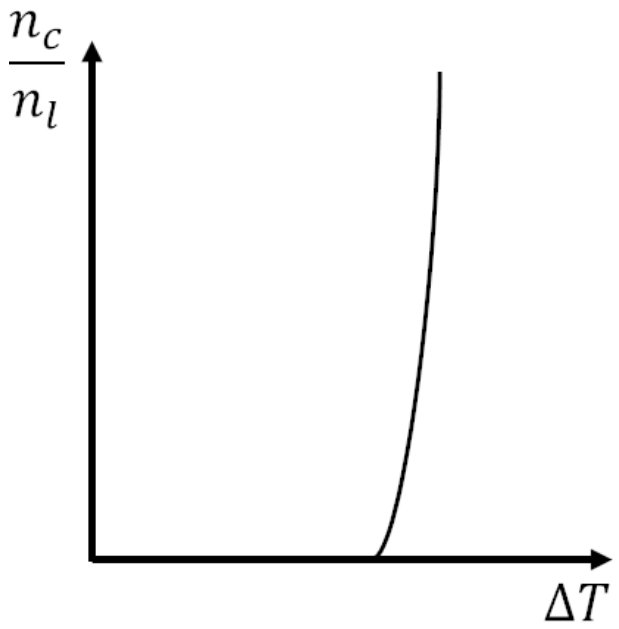


Figure 2.2: The probability of finding a cluster of critical size as a function of undercooling [32].

The nucleation rate depends on the probability of finding a critical-size cluster and the rate at which one or more atoms can jump onto the surface of the cluster for it to grow. The heterogeneous nucleation rate is given by:

$$I^{heter} = \nu_0 p_c n_p \, exp(-\frac{\triangle G^{heter}}{k_B T}) = I_0^{heter} \, exp(-\frac{16\pi}{3} \frac{\gamma_{sl}^3}{\triangle S_V^2 \triangle T^2 k_B T} f(\theta)) \qquad (2.6)$$

where ν_0 is the atomic vibration frequency, p_c is probability of capturing an atom on the surface of the cluster, and n_p is the number density of nucleation sites for heterogeneous nucleation with a wetting angle of θ, and was treated as identical to the number density foreign particles. Figure 2.3 illustrates the variation of heterogeneous nucleation rate as a function of temperature at contact angle of $\pi/4$.

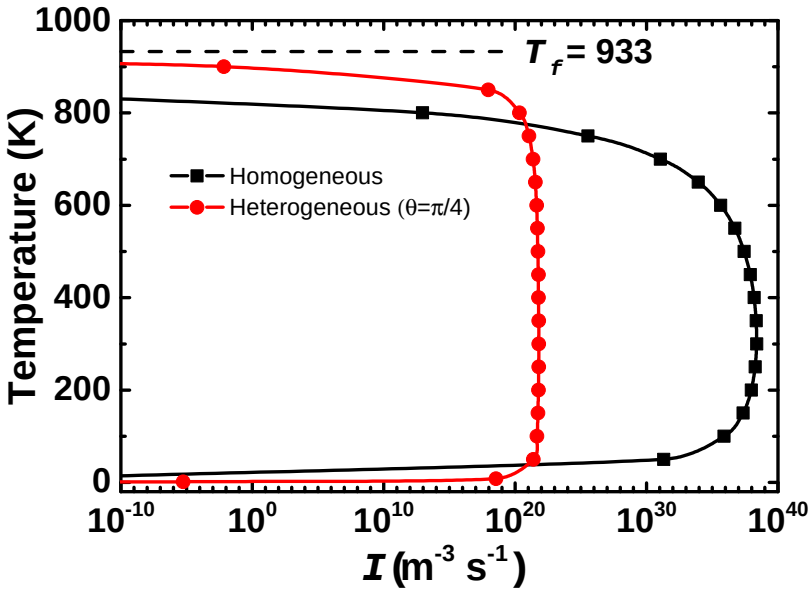


Figure 2.3: Heterogeneous nucleation rate in pure Al melt as a function of absolute temperature for contact $\theta = \pi/4$, based on data from [30].

The competition between $\triangle T$ and T in the exponential term in Equation 2.6 leads to a strong temperature dependence of the nucleation rate. The number of critical clusters increases with increasing thermodynamic driving force (i.e.

undercooling), while the diffusion rate of atoms increases with increasing temperature. At lower temperatures, there is a larger thermodynamic driving force due to larger undercooling, and therefore more critical clusters available. However, the mobility (i.e. diffusion) of atoms is limited. In contrast at higher temperatures, the mobility of atoms is higher, but the thermodynamic driving force (i.e. undercooling) is reduced. Thus, the overall nucleation rate is determined by a competition between the thermodynamic driving force and the kinetic constraints of the system. The competition of the two phenomena is illustrated in Figure 2.3.

Although classical heterogeneous nucleation predicts more realistic undercoolings than homogeneous nucleation for real casting conditions, there are limitations. First, theoretical difficulties arise with the spherical cap assumption when the catalytic efficiency of the nucleant is high, i.e. when θ, $f(\theta)$ and $\triangle G^{heter}$ are approaching zero [33–35]. At $\theta < 10°$, the solid nucleus falls below a monolayer of atoms, which makes it unreasonable to assume a spherical cap shape. Second, the theory assumes that the number of nucleation sites is identical to the total number of foreign particles and independent of the undercooling (see Equation 2.6). This implies that the number density of grains in the final casting solely depends on the number density of foreign particles (n_p) and the grain number density therefore remains the same regardless of solidification conditions. This prediction is contradictory to the observations in real castings, where the grain number density increases markedly with increasing cooling rate.

A major progress in the development of heterogeneous nucleation was presented by the free growth model [31] proposed in 2000. Regarding the first limitation of the classical heterogeneous nucleation theory, the free growth model assumes that the first solid layer is already formed on the face of a potent nucleant particle either above liquidus (by adsorption) or at very low undercooling, and the energy barrier of nucleation is dominated by the free growth of the solid

layer to initiate the grain. Regarding the second limitation of the classical theory, the free growth model says that the energy barrier, i.e. the critical undercooling for initiation of a stable nucleus by free growth is a function of the foreign particle size. In other words, the number of nucleation sites or potent nucleants is depended on the undercooling available in the melt rather than identical to the total number of foreign particles. Therefore, solid crystals forms preferentially on larger nucleant particles at lower undercooling and then on progressively smaller particles at increasing undercooling, according to:

$$\triangle T_{fg} = \frac{4\gamma_{sl}}{\triangle S_V \phi} \tag{2.7}$$

where ϕ is the diameter of the foreign substrate, which is assumed to be a circular disk. For each nucleant size ϕ_i, free growth takes place when $\triangle T \geq \triangle T_{fg}(\phi_i)$. Thus, a discrete distribution of nucleant sizes leads to a discrete distribution of activated nucleant number density n_i as a function of undercoolings $\triangle T_{fg}(\phi_i)$ (Figure 2.4). For numerical modelling purposes, the discrete distribution can be approximated by a continuous distribution of $dn/d(\triangle T)$, as indicated by the yellow line in Figure 2.4.

In 2005, Quested and Greer [36] explained the small-contact angle nucleation in Al alloy melt with TiB_2 inoculation, taking into account the initial formation of solid before activation of free growth. They have summarised regimes of heterogeneous nucleation behaviour as a function of undercooling and contact angle for a given nucleant (substrate) size, as shown in Figure 2.5.

In regime (i), the foreign substrate is too small for a nucleus to form assuming a spherical-cap model, and the heterogeneous nucleation in this case is therefore impossible. In regime (ii), the substrate is sufficiently large for a embryo to form via heterogeneous nucleation, and at the same time, however, small enough to restrict the further growth of the solid nucleus. The embryo in this case is believed to form rapidly on the foreign substrate at a small wetting angle

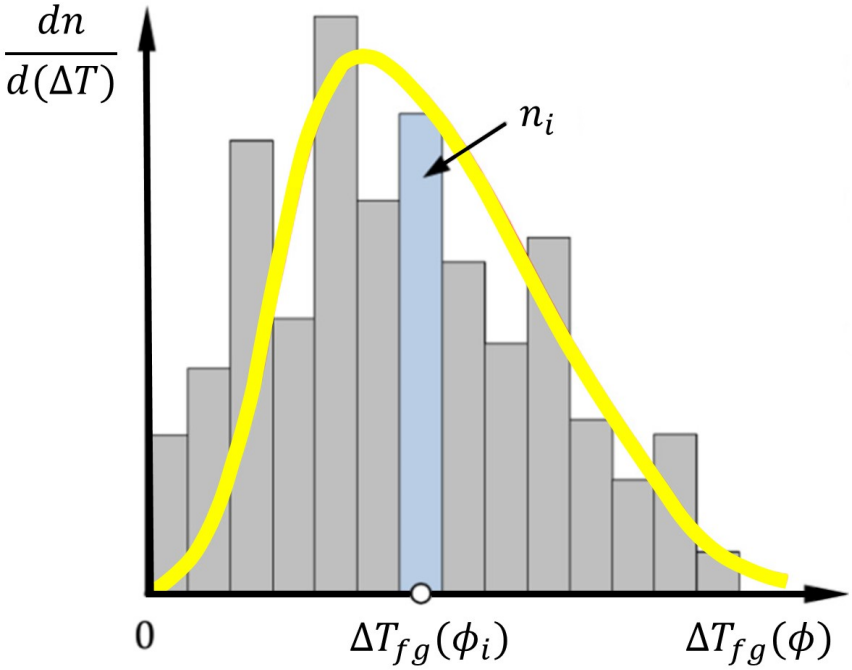


Figure 2.4: Simulated distribution of activated nucleants as a function of undercooling at a constant cooling rate, after [30].

(and undercooling). It then grows but the growth stops when the solid has spread over the area of the foreign substrate. To allow further growth of the embryo, the undercooling $\triangle T$ must increase beyond critical undercooling $\triangle T_{fg}$ of the given substrate to activate free growth. The rate-limiting step in this regime is the accumulation of undercooling to overcome the free growth barrier for the given substrate. In regime (iii), there is no barrier to free growth of the embryo, as $\triangle T > \triangle T_{fg}$. The rate-limiting step in this regime is therefore the initial formation of the embryo on the foreign substrate [36]. It should be noted that the free growth model mentioned above is based on an assumption of isothermal melt which means that nucleant particles of the same size (i.e. potency) become activated simultaneously and that the nucleation process is ceased due to recalescence, a temperature rise caused by release latent heat.

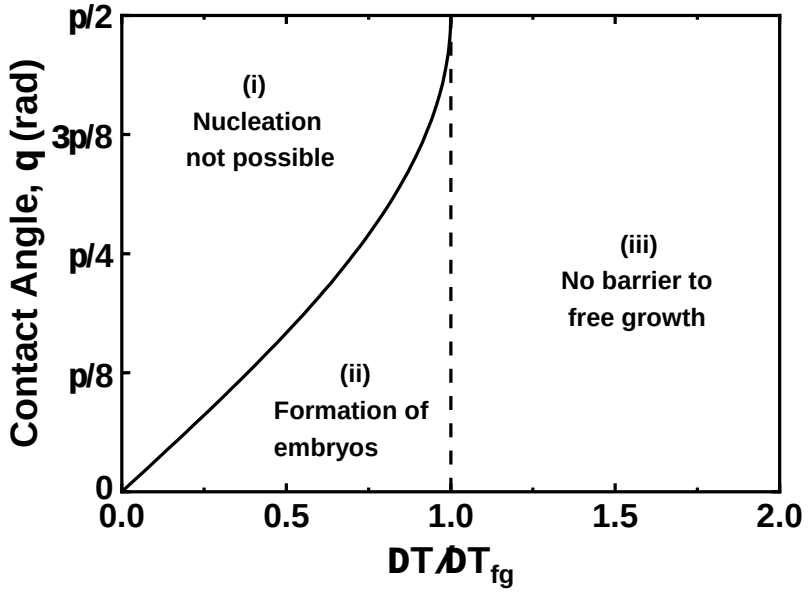


Figure 2.5: A graph showing the regimes of heterogeneous nucleation behaviour as a function of undercooling and contact angle for a given nucleant size, after [36].

2.1.2 Nucleants for Fe-rich IMCs

As opposed to primary α-Al (or other primary phases), relatively little attention has been given to understanding the nucleation mechanism of faceted Fe-rich IMCs, including β-Al_5FeSi which is considered particularly damaging but very commonly observed. Nonetheless, effort was spent to explore effective nucleants for β Fe-rich IMCs, in order to obtain a refined size and a more uniform distribution. Majority of these studies were based on post-solidification microscopy. Table 2.1 summarises the potential nucleants as reported in the literature.

2.1.2.1 TiB_2 and TiC

While TiB_2 is the most commonly used grain refiner for primary Al dendrites, Sha *et al.* [37], Lui *et al.* [39] and more recently Rakhmonov *et al.* [40, 41] suggested that TiB_2 through the addition of commercial Al-5Ti-1B grain refiners, might be associated with nucleation of secondary β-Al_5FeSi IMCs in Al-Si-Cu-Fe alloys, evidenced by consistent microscopic observation of TiB_2 particles in

Nucleant	Fe-rich IMC	Alloy system	Reference
TiB_2	β-Al_5FeSi	Al-Si-Fe, Al-Si-Cu-Fe	[37–41]
TiC	β-Al_5FeSi	Al-Si-Fe	[38]
α-Al_2O_3	β-Al_5FeSi	Al-Si-Mg-Fe	[42, 43]
γ-Al_2O_3	β-Al_5FeSi	Al-Si-Cu-Fe	[44, 45]
	β-Al_7Cu_2Fe	Al-Cu-Fe	[46]
MgO	β-Al_7Cu_2Fe	Al-Cu-Fe	[46]
$MgAl_2O_4$	β-Al_5FeSi	Al-Si-Mg-Fe	[43]
	β-Al_7Cu_2Fe	Al-Cu-Fe	[46]
AlP	β-Al_5FeSi	Al-Si-Fe, Al-Si-Cu-Fe	[47, 48]
Primary Al	β-Al_5FeSi	Al-Si-Cu-Fe	[49, 50]

Table 2.1: A summary of major potential nucleants as reported in the literature.

physical contact with the IMC platelet after extraction. However, an alternative interpretation of the observed co-location of the TiB_2 and IMCs may be simply due to physical impingement of growing IMCs with unused TiB_2 particles that are pushed into the inter-dendritic region by pre-formed α-Al dendrites in the final stage of solidification. Assuming TiB_2 promoted nucleation of β Fe-rich, another potential argument would be if the nucleation was facilitated by the Ti rich layer on the surface of the TiB_2 particle due to presence of excessive Ti from the Al-5Ti-1B master alloy. Instead of adding TiB_2 in the form of Al-5Ti-1B master alloy, Khalifa *et al.* [38] injected TiB_2 powders of $< 10\mu$m in Al-Si-Fe alloy melt. Similarly, frequent physical contact was observed.

In contrast with TiB_2, the other grain refiner used for primary Al, TiC has not received much attention regarding its effect on Fe-rich IMC nucleation. In the same study as mentioned above, Khalifa *et al.* [38] conducted parallel experiments by introducing different powder-form inoculants into separate alloy melts, including TiC, α-Al_2O_3, γ-Al_2O_3 and MgO. The potency of each type of inoculant was examined by quantifying the number fraction of particles in contact with β Fe-rich IMCs in each condition and found that the number fraction of particles in contact with the IMCs showed a weak relationship with type. It was concluded that nucleation of β Fe-rich IMCs was not largely affected by the type of particle

[38]. While the finding is potentially impactful, the results will be more helpful to the understanding of Fe-rich IMC nucleation if the size of the different particles in contact with the IMCs were known, i.e. if the particles showing physical contact with the IMCs were always the larger ones (which should be more potent according to the free growth model).

2.1.2.2 Oxides

Oxides inclusions are often inevitable during casting in Al industry. The major oxides that can form are α-Al_2O_3, γ-Al_2O_3, MgO (in high Mg-containing alloys) and $MgAl_2O_4$ (in medium Mg–containing alloys). A detailed account of the origins of the oxides is beyond the scope of this review and can be found in [51]. By means of metallography and thermal analysis, many researchers have reported observation of β Fe-rich IMCs physically associated with either oxide films or particles, whilst there has been argument regarding the "potency" of the different oxides. Some of the representative studies are reviewed here.

Cao and Campbell investigated the role of oxide films on the formation of the Fe-rich IMCs in Al-11.5Si-0.4Mg (wt.%) alloys with various Fe and Mn additions [42, 52]. Oxide films (known as bifilms) were found entrained in the melt, and two distinct surfaces were observed: dry inner surface and wetted exterior surface. They suggested that the wetted outer surface of the oxide films acted as preferred foreign substrate for nucleation and growth of the α- and β-IMCs (denoted as α- and β-Fe in the study). This was evidenced by the observation of crack-like defects through the IMCs (Figure 2.6), expected to originate from the dry, unbonded inner surfaces [42]. Miller *et al.* [43] further investigated the Fe-rich IMC nucleation on oxides films by adding α-Al_2O_3 and $MgAl_2O_4$ particles deliberately in an Al melt. The study verified the previous hypothesis by Cao and Campbell, and indicated that needle β-IMC phase was associated with both α-Al_2O_3 and $MgAl_2O_4$ particles (Figure 2.7). Narayanan *et al.* [44] studied the

nucleation behaviour of β-IMCs in commercial A319 alloys with additions of γ-Al_2O_3. They reported formation of β-IMCs on the γ-Al_2O_3 (Figure 2.8) under normal casting conditions (temperature of melt lower than 750 °C). However when the melt was superheated to temperatures higher than 850 °C, the γ-Al_2O_3 transformed into α-Al_2O_3, and the formation of β-IMCs was suppressed. They concluded that the γ-Al_2O_3 acted as a good nucleant for β-IMCs, while α-Al_2O_3 was not a favourable nucleation site for β-IMCs [44]. More recently, Orozco-Gonzalez et al. [53] reported similar observations that α-Al_2O_3 had no direct contact with the β-IMCs. While these findings may look contradictory, they might imply that there might exist other more important controlling factors (e.g. size) for the nucleating potency of the particles than their types.

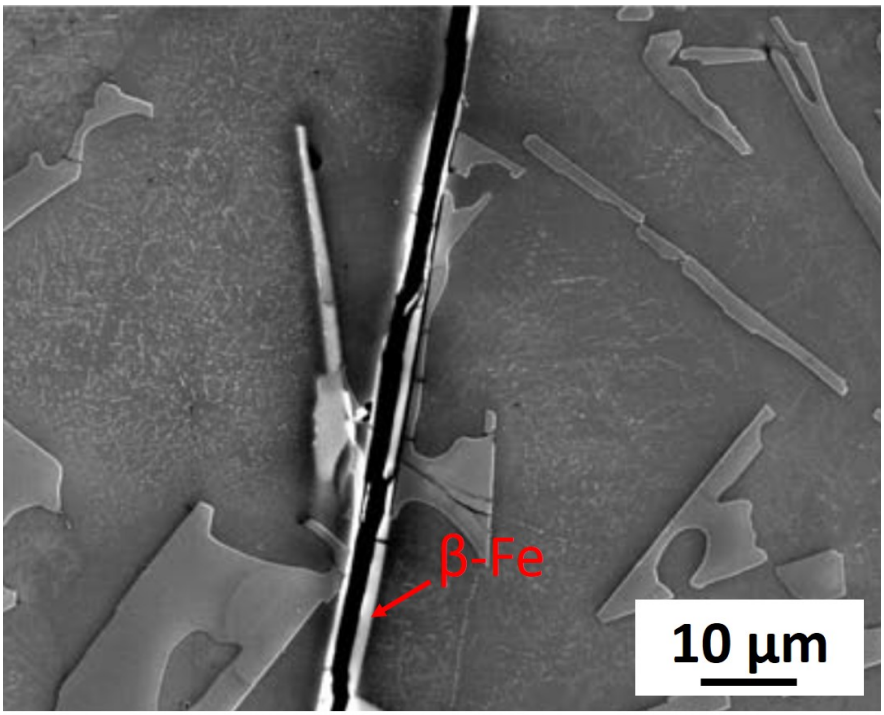


Figure 2.6: Secondary electron image showing a crack along the β-Fe IMCs [42].

In the past decade, *in-situ* X-ray radiography and tomography have increasingly been used to study Fe-rich IMCs for a better understanding of the dynamics. However, only a handful experiments were dedicated to investigating possible nucleants of these IMCs [45, 50]. An *in-situ* tomography study by Terzi *et al.* [45]

of Al-8Si-4Cu-0.8Fe (wt.%) at a cooling rate of 0.02°C/s revealed four IMC nucleation events from within a relatively small sample volume, all of which were β-IMCs formed on the surface of the specimen. They suggested that the γ-Al_2O_3 formed on the specimen surface had good potency for the nucleation of β-IMCs. However given only four β-IMC particles were involved, and also the insufficient time resolution (scans captured every 57 s), the repeatability and reliability of these observation remains doubtful.

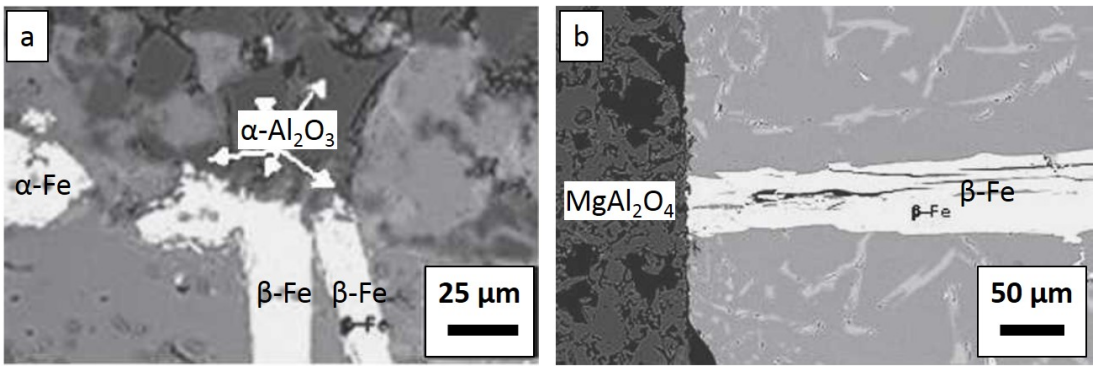


Figure 2.7: Backscattered electron image of (a) α-Fe and β-Fe IMCs on the surface of α-Al_2O_3, and (b) β-Fe IMCs on the surface of $MgAl_2O_4$ [43].

Apart from the Al-Si-Fe system reported above, another alloy system producing needle-like Fe-rich IMCs is Al-Cu-Fe. Based on microscopic investigation of needle-like Al_7Cu_2Fe (denoted as β-Fe in the study), Liu et al. [46] proposed three oxide films as potent nucleation sites, namely MgO, $MgAl_2O_4$ and γ-Al_2O_3. Further, a calculation of planar disregistry evaluated the lattice matching between potential nucleation substrates and β-IMC. In general, nucleation sites are believed to be more effective - more potent - when good crystallographic registry is achieved between the substrate crystal and the nucleus crystal. Table 2.2 lists the planar disregistry between β-IMC and different oxide substrates. δ denotes the planar disregistry, which should be lower than 12% for a potent nucleation site, assuming that the electronic bonding between the two phases is favourable [54]. $[uvw]_s$ and $[uvw]_n$ are low-index directions in the match planes of the substrate and the Fe-rich IMC nuclei, respectively. $d_{[uvw]s}$ and $d_{[uvw]n}$ are the interatomic

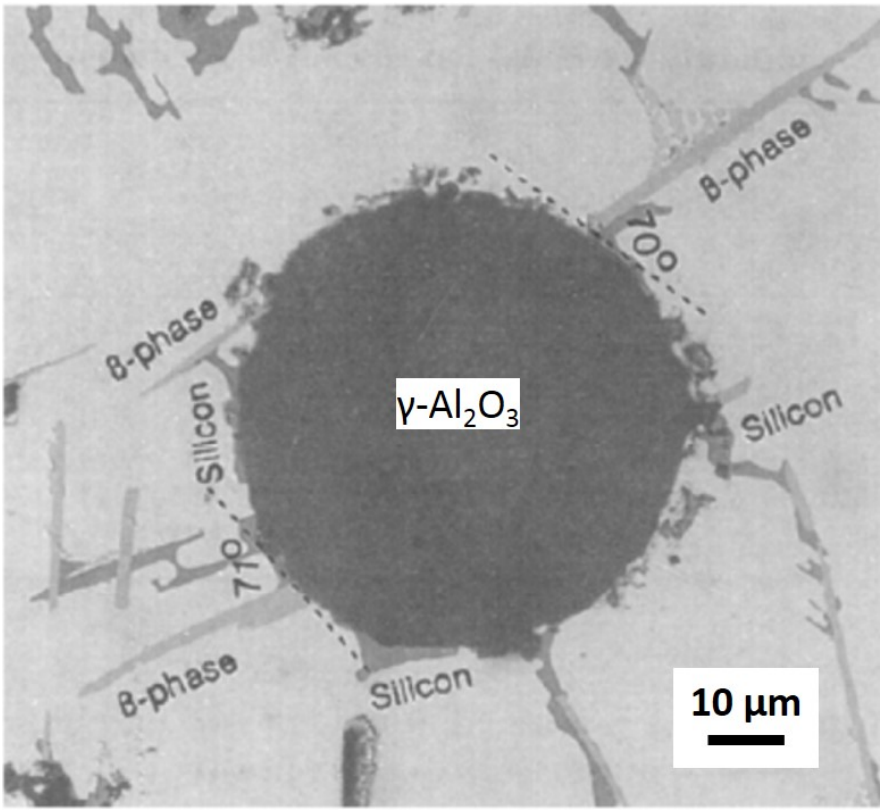


Figure 2.8: β-Fe IMCs on the surface of γ-Al_2O_3 [44].

spacing along $[uvw]_s$ and $[uvw]_n$, respectively. θ is the angle between $[uvw]_s$ and $[uvw]_n$. The good crystallographic registry suggested that these three oxides could be good substrates for β-IMC nucleation. However as discussed above for the Al-Si-Fe, this cannot rule out the possibility that other more important potency controlling factors might exist.

2.1.2.3 AlP particles

Sigworth [47] reported that addition of phosphorus can undesirably promote the nucleation of needle β-Al_5FeSi on AlP particles produced by reaction between P and Al. Similar effect of P additions have also been reported by Samuel and co-workers [48]. However, no further investigation has been reported regarding the mechanism of AlP promoting nucleation of β-Al_5FeSi. The effect of AlP was doubted by later researchers Lu and Dahle [55], and Khalifa *et al.* [56], who did not find either any increase in the number of β-Al_5FeSi on P addition, or any AlP

Substrate	**Match Planes**	$[uvw]_s$	$[uvw]_n$	$d_{[uvw]s}$ **(nm)**	$d_{[uvw]n}$ **(nm)**	θ	δ
MgO	(110)s //(110)n	[001]	$[\bar{1}10]$	5×0.423	2×0.896	0	7.94
		$[\bar{1}11]$	$[\bar{1}11]$	5×0.733	2×1.736	4.19	
		$[\bar{1}10]$	[001]	5×0.598	2×1.487	0	
$MgAl_2O_4$	(110)s //(110)n	[001]	$[\bar{1}10]$	5×0.808	4×0.896	0	5.72
		$[\bar{1}11]$	$[\bar{1}11]$	5×1.399	4×1.736	4.19	
		$[\bar{1}10]$	[001]	5×1.143	4×1.487	0	
γ-Al_2O_3	(110)s //(110)n	[001]	$[\bar{1}10]$	4×0.7859	3×0.896	0	7.18
		$[\bar{1}11]$	$[\bar{1}11]$	4×1.361	3×1.736	4.19	
		$[\bar{1}10]$	[001]	4×1.111	3×1.487	0	

Table 2.2: List of planar disregistry between Al_7Cu_2Fe and different oxide substrates [46].

particles in contact with β-Al_5FeSi. Khalifa *et al.* suggested that the nucleation of IMCs was very "system-dependent" and that the type of the nucleant was less important since IMCs that formed in the late stages of solidification were often metastable and probably formed at a relatively large undercooling. This is hardly a controversial statement in general terms but does not elucidate how β-Al_5FeSi nucleation and growth might be controlled, where presumably copious, efficient nucleation of β-Al_5FeSi is preferred, or the preferential nucleation of less damaging α-Al_8Fe_2Si.

2.1.2.4 Primary Al dendrites

Kim et al. [49] reported the formation of β-IMCs near the pre-developed α-Al dendrites network using real-time radiography of directional solidification of Al-9.5Si-3Cu-1.2Fe (wt.%) at 1 Hz (Figure 2.9). However due to the slow time resolution and only a handful IMCs, it cannot be clearly identified whether the β-IMCs tended to nucleate on the α-Al dendrites or they initially nucleated elsewhere i.e. heterogeneously on tiny substrates/particles in the melt and then became "sandwiched" between the growing, primary dendrites. The researchers further suggested that the β-IMC needles had a strong tendency to grow parallel to the α-Al dendrites, and is most likely due to the inevitable geometrical

constraint imposed by the primary Al dendrites, so that secondary IMCs are "forced" to grow in the extended inter-dendritic channels. More recently, a more systematic *in-situ* tomography study by Puncreobutr et al. [50] on isothermal solidification of Al-7.5Si-3.5Cu-0.6Fe (wt.%) suggested that the majority of the β-intermetallics ($\approx$66%) nucleated on/near the α-Al dendrites. Despite the use of both low-speed (72 s between scans) and high-speed (12 s between scans) acquisition, the observation of discrete nucleation events was still not possible. In other words, some of the reported apparent nucleation on primary α-Al could be unresolved impingement events of already nucleated β-IMCs. In contrast, other researchers [45, 57] reported that the β-IMCs nucleated independently of the primary α-Al. Distinguishing the difference is more difficult than might first be assumed because the IMCs are always present in low volume fractions less than 2% [24].

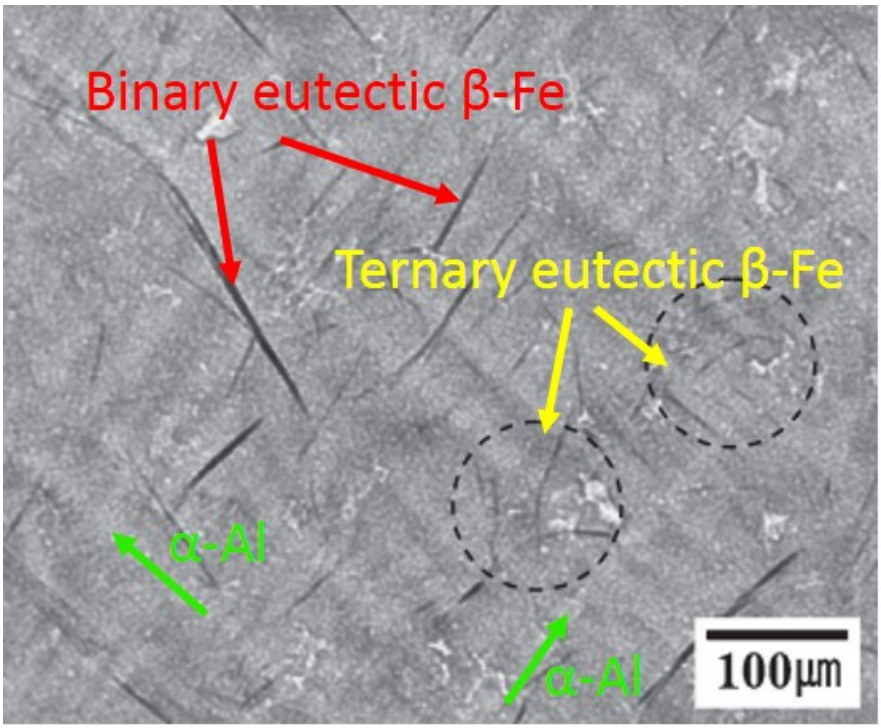


Figure 2.9: Radiography image showing β-Fe IMCs in an Al-9.5Si-3Cu-1.2Fe alloy [49].

2.1.2.5 Other inclusions

Khalifa et al. [38] observed direct physical contact between the Fe-rich IMCs and inclusions, such as CaO and SiC. They suggested that the inclusions were potent nucleants for Fe-rich IMCs. They further reported that the potency of the inclusions improved with increasing solute concentration up to a certain level, above which the nucleation sites became "poisoned" by the high solute concentration in the liquid, although this remains a hypothesis.

2.2 Faceted growth of Fe-rich IMCs

2.2.1 Faceted crystal growth

One of the most widely accepted growth theory accounting for both faceted crystal growth and non-faceted crystal growth is the interface morphology theory proposed by Jackson [58, 59], based on the concept of interface roughness and interface free energy minimisation. By assuming an initially flat surface, the change in the surface free energy upon adding atoms to fill up a fraction x of N possible sites on a crystal plane at equilibrium temperature T_E is given by:

$$\frac{\Delta G}{NkT_E} = \alpha x(1-x) + xlnx + (1-x)ln(1-x) \tag{2.8}$$

where $\alpha = \frac{\Delta H}{RT_E}\xi = \frac{\Delta S}{R}\xi$. ΔH is the latent heat of the phase transformation, ΔS is the entropy of fusion, R is the gas constant, and ξ ($\xi < 1$) is a factor dependent on the crystallography of the interface. In Fig. 2.10, Equation 2.8 is plotted for different α values.

For crystal surfaces with $\alpha < 2$, the minimum free energy is obtain when 50% of N sites are filled with atoms, i.e. the surface is atomically rough, which means a large number of sites are available for atom attachment. In comparison, for crystal surfaces with $\alpha > 2$ two minima are obtained when the N sites are

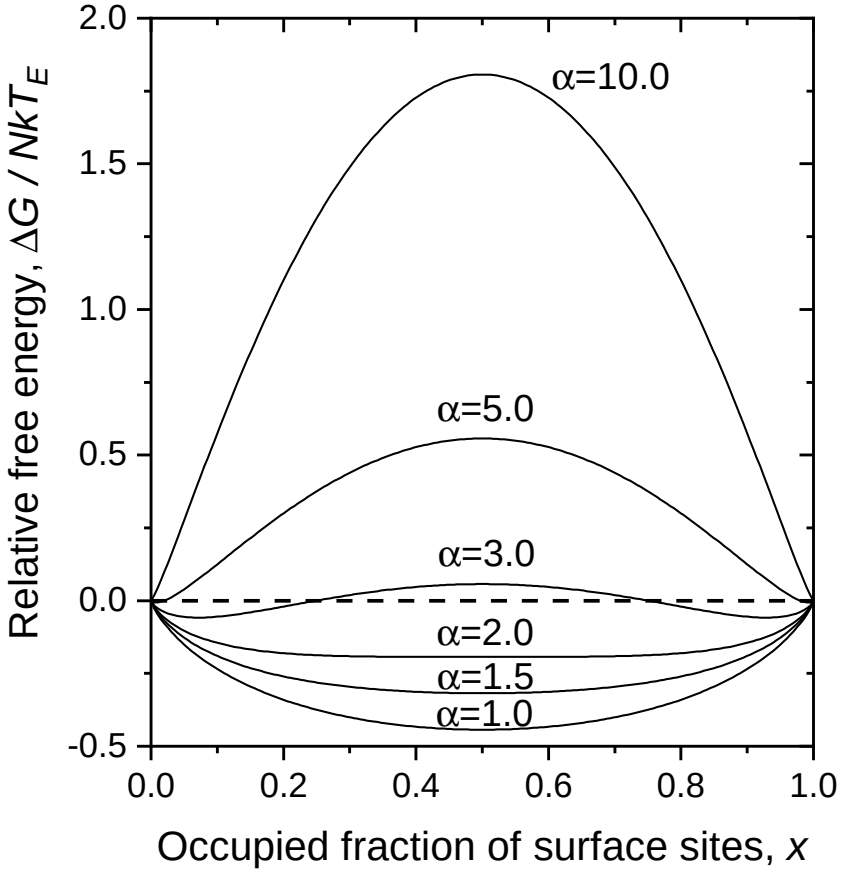


Figure 2.10: Interface free energy as a function of occupied fraction of surface sites, after [58].

nearly full or nearly empty, i.e. the surface is atomically smooth, which means few sites are available for atom attachment. Jackson further concluded that for a crystal with $\frac{\Delta S}{R} < 2$ (e.g. all metals), all the crystal planes, including the most closely-packed planes should be atomically rough (i.e. high growth rate), and the growth rate anisotropy of the crystal should be low. Crystals should therefore be non-faceted. In contrast for $\frac{\Delta S}{R} > 4$ (e.g. inorganic compounds), the most closely-pack face should be atomically smooth (i.e. low growth rate), while the less closely-packed faces should be rough, leading to anisotropic growth rate and microscopic facets.

Cahn *et al.* [60] correlated the non-faceted and faceted crystal surface morphologies to two growth mechanisms. They concluded that non-faceted crystals

should grow via a a continuous mechanism where new atoms can attach to the crystal surface at essentially any site. By comparison, faceted crystals should grow by a lateral mechanism, where the growth was realised by motion of a one-atom-high step across each facet and new atoms can only attach to the edge of the step. The crystal growth was therefore largely dependent on the formation of the steps.

In faceted semiconductor Ge and Si crystals, formation of these growth steps is believed to be facilitated by the frequently observed twinning phenomenon [61–72]. This is known as the twin plane re-entrant edge (TPRE) mechanism, proposed by Wagner [61] and Hamilton and Seidensticker [62]. The schematic in Fig. 2.11 illustrates the mechanism where there was one {111} twin (i.e one {111} twin plane) in a Ge crystal. Presence of the twin gives rise to three re-entrant grooves with an angle of 141° between the bounding planes. The three en-entrant grooves act as preferential sites for atom attachment, facilitating rapid growth along three $\langle 11\bar{2} \rangle$ directions (Fig. 2.11a). The rapid growth along these three preferential directions causes the re-entrant grooves to diminish. Rapid growth is stopped when the re-entrant grooves vanishes. In comparison, the schematic in Fig. 2.12 shows the growth of a Ge crystal where there are two {111} twin planes. In this case, there are six re-entrant grooves of 141°. As shown in Fig. 2.12b, formation of solid on each of the 141° re-entrant grooves (Type I) generates a new re-entrant groove of 109.5° (Type II). Different from the crystal in Fig. 2.11 which only possesses a single twin, this crystal with two twins now has self-perpetuating re-entrant grooves (i.e. preferential sites) for continued growth along the $\langle 11\bar{2} \rangle$ directions (Fig. 2.12c), giving rise to a highly anisotropic platelet morphology.

In contrast to semiconductors Ge and Si, growth mechanisms of Fe-rich and other faceted IMCs received less attention. It has been suggested that the same mechanism of TPRE may be followed during the growth of Fe-rich IMCs, based on frequent microscopy observation of twinning in the particles [73–75].

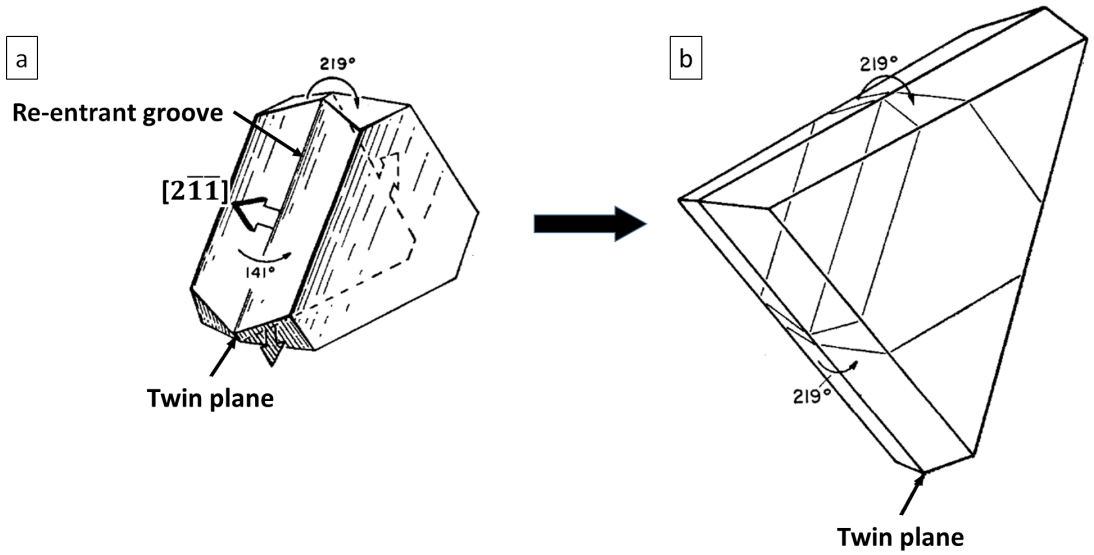


Figure 2.11: A schematic showing growth of a Ge crystal with one {111} twin, creating three re-entrant grooves as preferential sites for atom attachment for growth along $\langle 11\bar{2} \rangle$ directions [62].

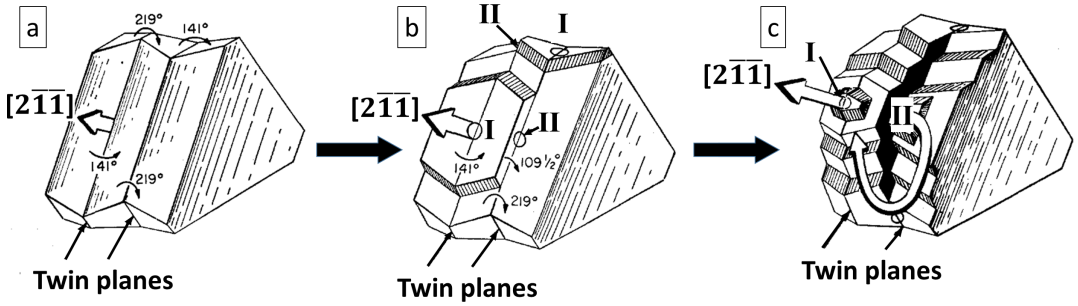


Figure 2.12: A schematic showing growth of a Ge crystal with two {111} twin, creating 6 re-entrant grooves as preferential sites for atom attachment for growth along $\langle 11\bar{2} \rangle$ directions [62].

2.2.2 Experimental studies of Fe-rich IMC growth

The primary tool to understand the growth of the faceted β Fe-rich IMCs has been post-solidification microscopy. The main facet (i.e the most closely-pack) which tends to grow (expand) is the (001) plane, as determined by Mulazimoglu et al. [74], Hansen et al. [76], and Sha et al. [57, 77]. Mulazimoglu et al. investigated the β-Al5FeSi phase using high resolution TEM (HRTEM) and proposed that the β-Al5FeSi crystal was highly faulted and contained multiple (001) growth twins (Figure 2.13a). Similarly, Hansen et al. observed streaks and twin spots

in the selected area diffraction patterns of β-Al5FeSi, indicating the presence of the twins. Mulazimoglu et al. [74] proposed that the growth of β-Al5FeSi followed the TPRE mechanism, where the (001) twins parallel to the growth direction tended to provide sites for atom attachment and therefore promote the growth of the β-Al5FeSi crystal into a faceted morphology. Further, Sha et al. [73] reported frequent observation of small steps on the (001) facet boundaries of β-Al5FeSi under HRTEM (Figure 2.13b). Those small steps, typically 2 nm in height, were also thought to provide low energy site for the adsorption of atoms in addition to the twin re-entrant grooves. However more extensive work is clearly needed, especially regarding the dynamics in order to examine the validity of this hypothesis and further to develop a more comprehensive understanding on growth of faceted IMCs.

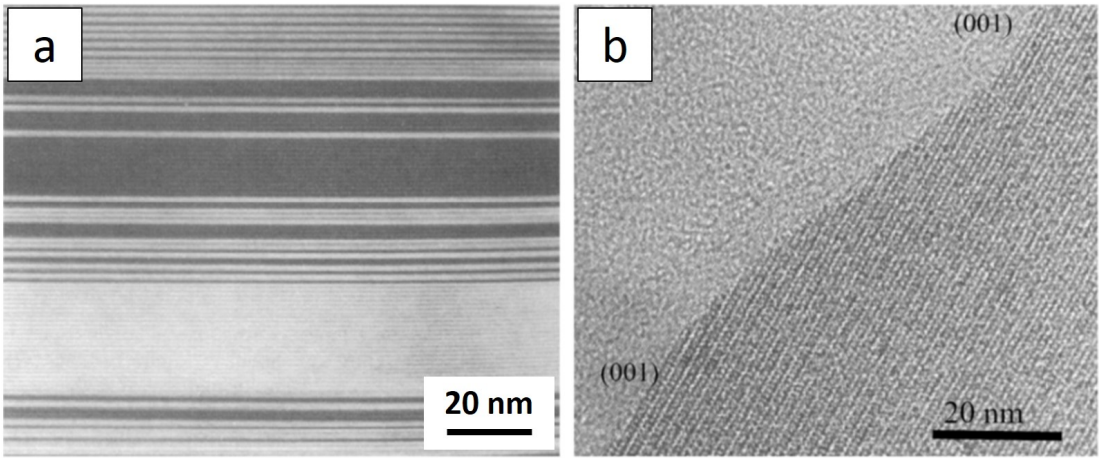


Figure 2.13: (a) HRTEM image of β-AlFeSi IMCs along [100] zone axis, showing the presence of periodic faults and twins on (001) [74]. (b) HRTEM image showing the small steps on the faceted boundary of β-AlFeSi IMCs [73].

With development of synchrotron techniques, *in-situ* synchrotron X-ray radiography [49, 78] and tomography [45, 50] studies have been conducted in an attempt to reveal the *dynamics* of β-IMCs growth. However, these studies were largely focused on reporting observations or measurements rather than providing links with existing microscopic findings above to explore the mechanisms of the observed growth behaviours. Using *in-situ* synchrotron radiography imaging at

2 Hz, Wang et al. studied the growth kinetics of four β-IMCs in Al-7.5Si-3.5Cu-0.8Fe (wt.%) at a cooling rate of 0.33°C/s [78]. Fig. 2.14 shows a radiograph sequence of growth of a needle-like (in 2D) IMC in the work. An initial rapid growth of the β-IMCs with instantaneous tip velocity up to 100 μm/s was observed, which was thought to be driven by the high Fe supersaturation in the interdendritic liquid channels. The growth velocity dropped to 10 μm/s towards the end of the growth, which was suggested to be a result of impingement. However, no evidence was reported for the Fe supersaturation at the initial stage of the growth or the impingement at the end of the growth. There was slight thickening of the IMCs towards the final stages of growth. However, due to the time and spatial resolution limit, convincing quantification of the thickening process was not possible.

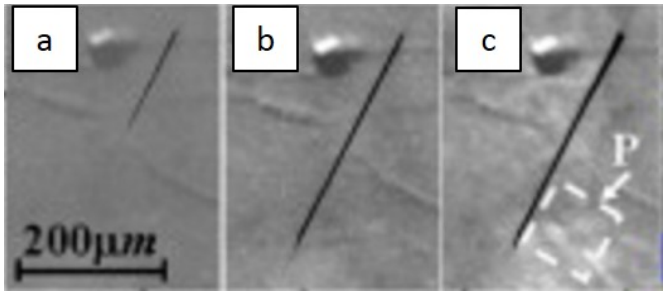


Figure 2.14: Radiography images of a growing β-AlFeSi IMC at (a) 564°C, (b) 558°C, and (c) 531°C. "P" in (c) indicates the presence of porosity [78].

Later on, a more systematic synchrotron tomographic study was carried out by Puncreobutr et al. [50] on a very similar composition Al-7.5Si-3.5Cu-0.6Fe (wt.%) alloy at 0.05°C/s. The study confirmed the initial rapid growth observed in [78] and showed that the β-IMCs grew initially at 30 μm/s, after which the growth velocity dropped exponentially towards zero. Furthermore, the authors also made an attempt in understanding the IMC-IMC interactions (Figure 2.15). Two types of interaction mechanisms were proposed, namely impingement (Figure 2.15a-c) and more interestingly branching (Figure 2.15d-f). The first interpretation of the observed "branching" could be that it was a real branching behaviour of one crys-

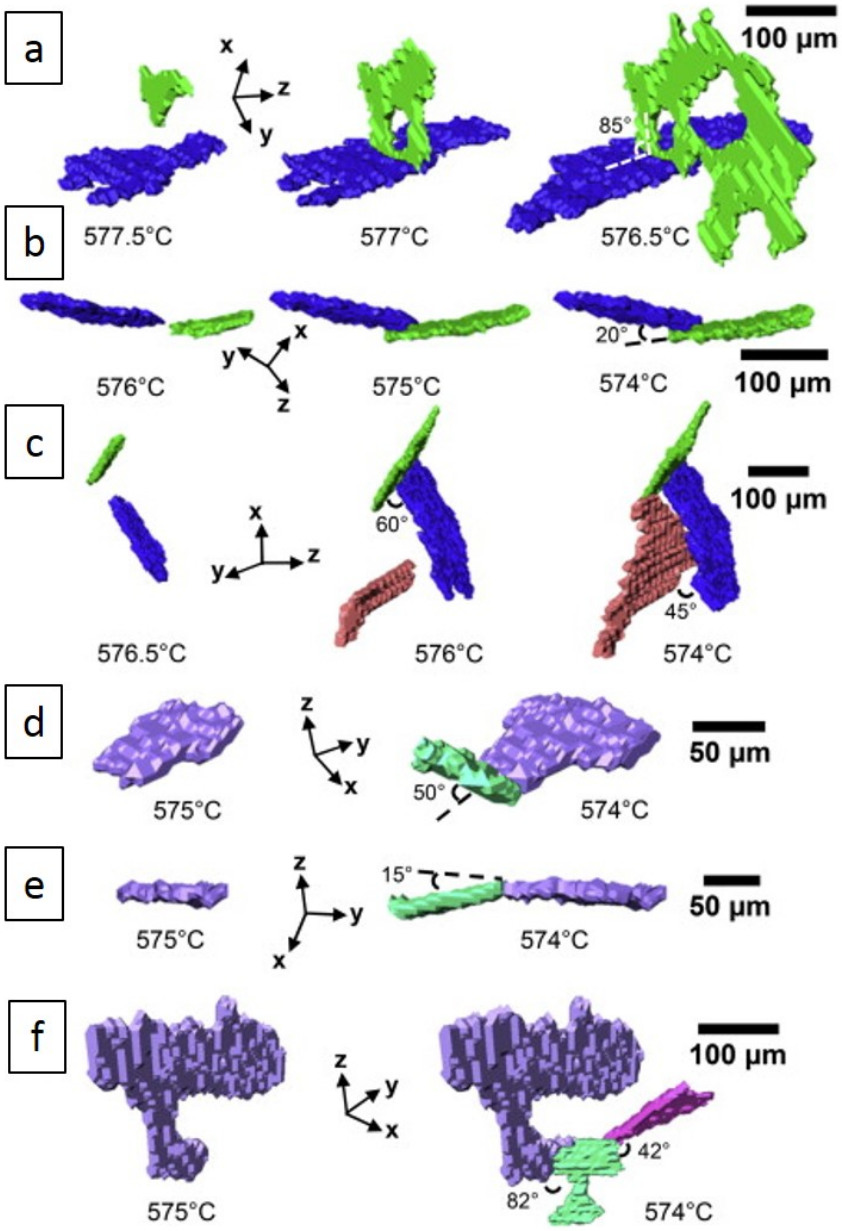


Figure 2.15: Two types of IMC-IMC interations: (a-c) impingement and (d-f) potential branching [50].

tal. In Ge and Si, branching behaviour was found to be associated with twinning [62, 68]. In $Al_{13}Fe_4$, it was also anticipated that branching of the IMC platelets was directly related to occurrence of twinning [75]. However given the limited temporal resolution (12 s in a high-speed mode), another interpretation is that the appeared "branching" could be unresolved impingement events between IMCs nucleating separately. This argument highlights the necessity of post-solidification

microscopy (e.g. EBSD) on synchrotron samples. The author has also explored the orientation relationships between the β-IMCs and the primary Al dendrites. The β-IMCs grew preferentially along the primary interdendritic channels. This observation was attributed to the intrinsic crystallographic relationships between the IMCs and the primary Al phase. However, it should not be excluded that the preferential growth of the IMCs could simply be a result of physical constraint from the surrounding Al dendrites. It should be recognised that the use of tomography imaging provides a 3-D view of the IMC morphology, which could potentially help with understanding the growth kinetics. However, due to lack of sufficient time and spatial resolution, growth kinetics remain largely obscure.

With recent development of more powerful laboratory microfocus X-ray tubes together with modern X-ray detectors, there has been a vast improvement in the performance of laboratory-based *in-situ* X-ray imaging techniques [79, 80]. In spite of source brilliance generally 10^{10} lower than typical 3rd generation synchrotron source (e.g. European Synchrotron Radiation Facility (ESRF)), laboratory systems offer the advantage of vertical X-ray beam, which allows a foil radiographic sample to be studied with its main surface horizontal so that gravity effects are minimised, e.g. reduced liquid convection, similar to micro-gravity conditions [80].

Laboratory-based *in-situ* X-ray radiography was conducted recently by Bjurenstedt *et al.* [81] to study the growth and morphology of primary α-Al(FeMnCr)Si IMCs in an Al-8.6Si-2Cu-1.2Fe (wt.%) alloy. Two basic morphologies were observed at increasing cooling rate, namely hexagonal (Fig. 2.16a) at 0.5 and 1 Ks^{-1} and star-shaped (Fig. 2.16b) at highest cooling rate by switching off the power regulation (*Reg.OFF*). The hexagonal shape at lower cooling rates was attributed to near-symmetrical growth along all the directions. In comparison, the star-shaped observed at the fastest cooling possessed a three-fold morphology. Further, growth of the star-shaped IMC was speculated to be related to

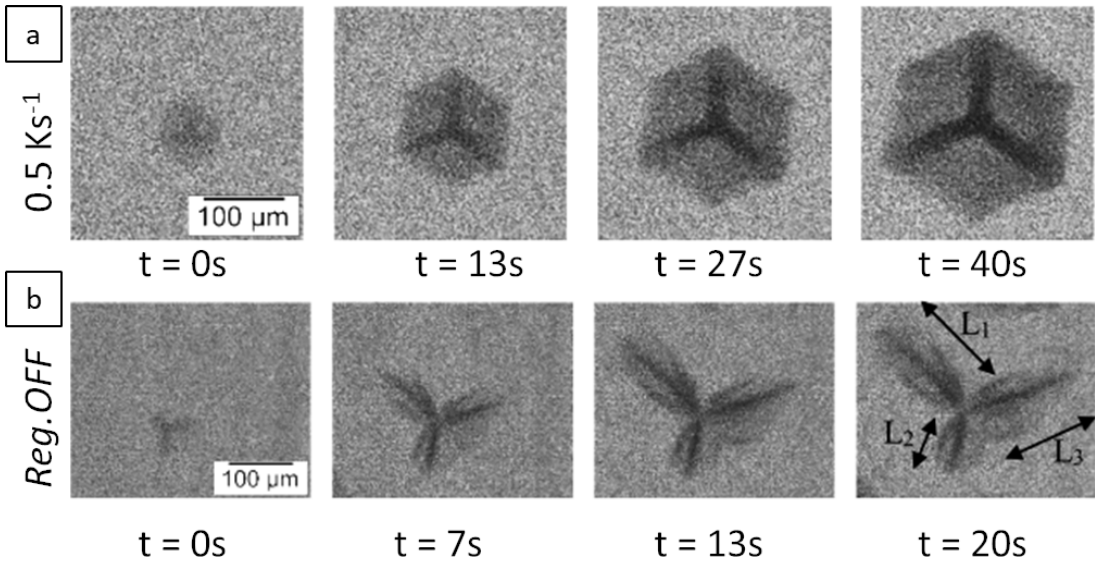


Figure 2.16: Radiograph sequences showing growth of two IMCs with (a) hexagonal shape at 0.5 Ks^{-1} and (b) star shape at fastest cooling when power regulation was switched off in an Al-8.6Si-2Cu-1.2Fe (wt.%) alloy [81].

twinning, with each elongated arm of the IMC not a single plane but appearing as split plates under SEM (Fig. 2.17). Judging from the SEM image, the observed three-fold star morphology could be attributed to three twined crystals growing outwards from one or an agglomerate of nucleant particles. In addition, it was also reported that the hexagonal crystals which formed at low cooling rates became elongated horizontally at $1Ks^{-1}$. However, this could be due to the thermal field that was not fully calibrated so that a small thermal gradient was present, promoting preferential growth along certain directions. There was no repeat experiment to validate the findings.

2.2.3 Modification of faceted growth

2.2.3.1 Growth modifier

While studying the faceted growth phenomena is the first step, controlling or modifying the growth of these faceted crystals into a more isotropic form could also be considered. In this respect, most studies have concerned modification of

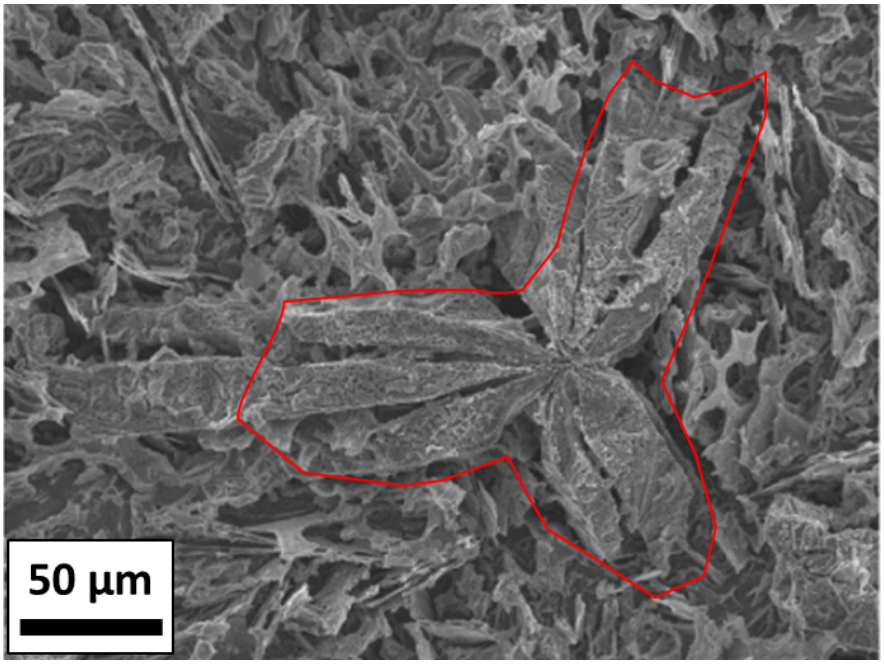


Figure 2.17: A secondary electron image of a deep-etched sample used in the radiography experiments, showing a three-armed star-shaped IMC [81].

Si growth in Al-Si alloys, and models have been proposed that explain the likely mechanisms of Si modification. Therefore in this part, modification of faceted Si growth will be reviewed, which may provide guidance to modification of faceted growth of Fe-rich IMCs.

Modification of Si growth has been realised by addition of "chemical modifiers", which include Na, Sr, Er, Eu, Y, La, Ce [66, 67, 70, 82–88]. Table 2.3 summaries the chemical modifiers and the reported concentrations of addition. Addition of modifiers is often accompanied by melt treatment to help to refine the morphology of Si from coarse platelet into fine fibrous or coralline form [83, 84, 89, 90], which contributes to a marked improvement in ductility [63, 84].

Two models were proposed to account for the observed effect of modification, namely the restricted TPRE mechanism [66] and the impurity induced twinning (IIT) mechanism [67, 93], both of which are well-accepted. These two models are not contradictory but complementary [83, 90] to explain that in modified Al-Si alloys the anisotropic growth of Si along the crystallographically preferential

Modifier	Level of addition (wt%)	Reference
Na	0.01-0.07	[66, 67]
Sr	0.015-0.04	[82, 83, 90]
Er	0.05-0.4	[84, 85]
Eu	0.05-0.06	[86, 89]
Y	0.07-1.09	[91, 92]
La	0.2-1.5	[87]
Ce	0.2-1.5	[87, 88]

Table 2.3: A summary of chemical modifiers for Si.

$\langle 11\bar{2} \rangle$ directions was restricted while {111} twins occurred more frequently, which resulted in thickening of Si crystals along the crystallographically unfavoured directions. More specifically, restricted TPRE occurs due to adsorption of modifiers on the re-entrant groove at the twin boundary, which poisons the low-energy re-entrants and deactivates the anisotropic TPRE growth mechanism. As Si builds up in the melt as solidification proceeds, stacking faults can easily occur when Si from the melt attaches onto the closely packed {111} planes due to a relatively small stacking fault energy of about 50-60 $\mathrm{mJ\,m^{-2}}$ [94], leading to formation of new twins. This promotes thickening of the crystal and gives rise to the formation of new re-entrant grooves, and the mechanism repeats.

The IIT mechanism is realised by adsorption of modifiers on lateral growth steps on {111} planes, which promotes stacking faults on the {111} planes and generates new twins. As a consequence, both mechanisms lead to suppression of anisotropic elongated Si platelet crystals and instead promote thickening of Si crystals over repeated twinning, and therefore promote more isotropic Si morphologies.

Although proposed for Si, the principle may be applied to modification of Fe-rich IMC growth by using carefully selected chemical modifiers, since the same TPRE growth mechanism was believed to be followed for Fe-rich IMCs [73–75].

2.2.3.2 Fragmentation

Many studies concern fragmentation of primary Al dendrites as a route to primary grain size refinement, for example, by application of external field [95, 96] or sudden alteration of the thermal field [97, 98]. In comparison, relatively little attention has been given to fragmentation of primary or secondary IMCs.

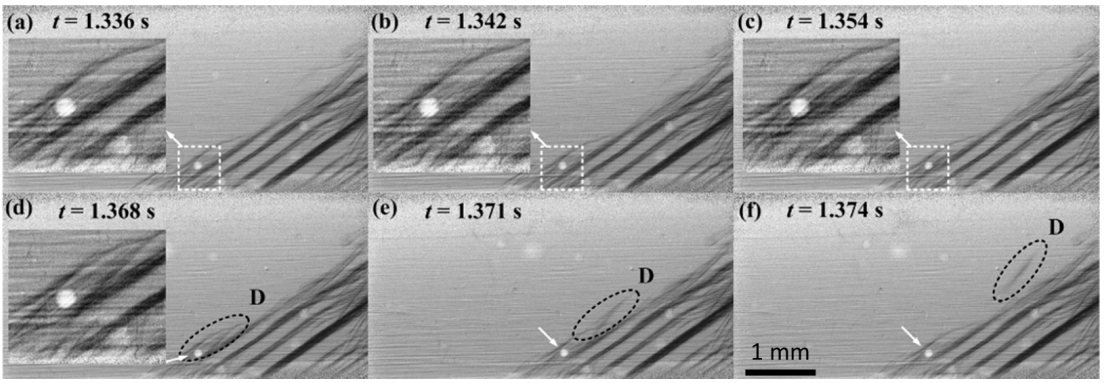


Figure 2.18: Synchrotron X-ray radiograph sequence showing fragmentation of a primary Al_2Cu IMC (highlighted by dashed ellipse) induced by a pulsating cavity bubble [99].

With high-speed synchrotron X-ray radiography at a temporal resolution up to 1000 Hz, Wang *et al.* [99] investigated the fragmentation of coarse primary Al_2Cu IMCs using ultrasonic melt processing (USMP) in a hypereutectic binary Al-35Cu (wt.%) alloy. When USMP (with a fixed frequency of 30 KHz) was applied to the alloy melt containing pre-developed coarse IMCs, some IMC fragments detached from the pre-formed IMC array and remelted (one representative IMC is denoted as 'D' in Fig. 2.18). Hence the researchers proposed that cavity bubbles (highlighted by arrow in Fig. 2.18) induced by USMP can break up the pre-formed IMCs. However as shown in the image sequence, the primary Al_2Cu IMC fragment ('D') floated up towards the top of the field of view, despite a greater density than the melt. This suggests the presence of strong convection currents in the alloy melt. Taking this into consideration, another possible cause of the IMC fragmentation may be strong liquid convection that altered the local liquid composition and led to a reduced local liquidus, which caused the

pre-formed IMCs to become thermodynamically unstable, and partially remelted and detached. Time-resolved solute concentration measurement based on the radiography images e.g. [96], would be very valuable to investigate solute transport effects in the liquid. Although the USMP experiments were not on Fe-rich IMCs, the findings may provide inspiration for future studies regarding the break-up of extended Fe-rich IMCs.

2.3 Phase selection of Fe-rich IMCs

Properties of cast Al (e.g. DC cast billets) depend significantly on the secondary phases, including their type, size, fraction, morphology and distribution, which of principal concern here are the Fe-rich IMCs. Due to the high liquid solubility and low equilibrium solid solubility of Fe in Al, Fe tends to combine with Al and other elements to form IMCs of various types either during solidification, or in the solid state (depending on time-temperature history). Before discussing the phase selection of Fe-rich IMCs in solidification, some important Fe-rich phases in Al-Si-Fe and Al-Cu-Fe systems will first be introduced.

2.3.1 Fe-rich IMCs in Al alloys

2.3.1.1 Fe-rich IMCs in Al-Si-Fe based system

Al alloys with presence of Si and Fe are extremely common, and Si is sometimes a useful alloying element to form metastable Mg_2Si precipitates for strengthening [100–102]. In equilibrium solidification of dilute Al-Si-Fe, three Fe-rich phases can form, namely θ-Al_3Fe, α-Al_8Fe_2Si and β-Al_5FeSi [57, 103–105], as indicated by the liquidus projection of ternary Al-Si-Fe phase diagram at Al-rich corner (Figure 2.19). These Fe-rich IMCs form in sequence by various eutectic and ternary peritectic reactions in equilibrium solidification of dilute Al-Si-Fe alloys [57]:

- $L \rightarrow Al_3Fe + \alpha$-Al
- $L + Al_3Fe \rightarrow \alpha$-AlFeSi $+ \alpha$-Al
- $L \rightarrow \alpha$-AlFeSi $+ \alpha$-Al
- $L + \alpha$-AlFeSi $\rightarrow \beta$-AlFeSi $+ \alpha$-Al
- $L \rightarrow \beta$-AlFeSi $+ \alpha$-Al
- $L \rightarrow \beta$-AlFeSi $+ \alpha$-Al $+$ Si

Figure 2.20 shows a thermodynamic calculation of solidification sequence in Al-0.5Si-0.5Mg-0.2Fe (wt.%) based on equilibrium condition. In addition, a series of structural variants of α-Al_8Fe_2Si and β-Al_5FeSi can form under non-equilibrium conditions, as summarised in Table 2.4.

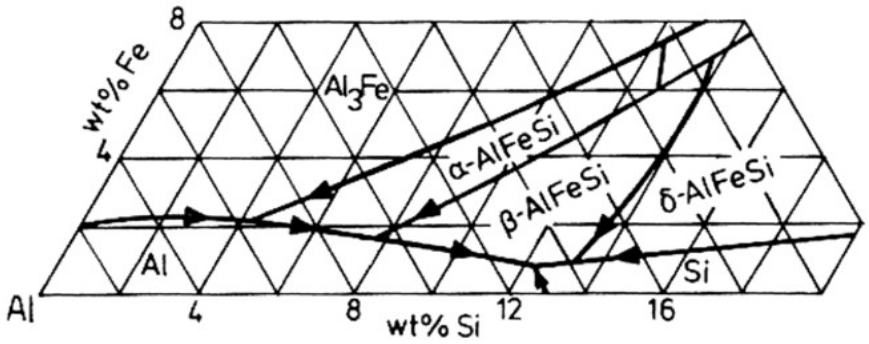


Figure 2.19: Liquidus projection of ternary Al-Si-Fe phase diagram at Al-rich corner [106].

Equilibrium θ-Al_3Fe In dilute Al-Si-Fe alloys, Al_3Fe (also reported as $Al_{13}Fe_4$ [103, 108, 109]) forms by a eutectic reaction with Al [57, 103]. Al_3Fe forming in the Al-Si-Fe system can dissolve a considerable amount of Si (1-6wt.%), depending on the alloy composition. Al_3Fe has a monoclinic crystal structure [110] and appears in a needle shape in 2-D micrographs. Figure 2.21 shows a typical TEM image of Al_3Fe needles on the grain boundaries of a DC cast Al-0.25Fe-0.13Si (wt.%) alloy ingot.

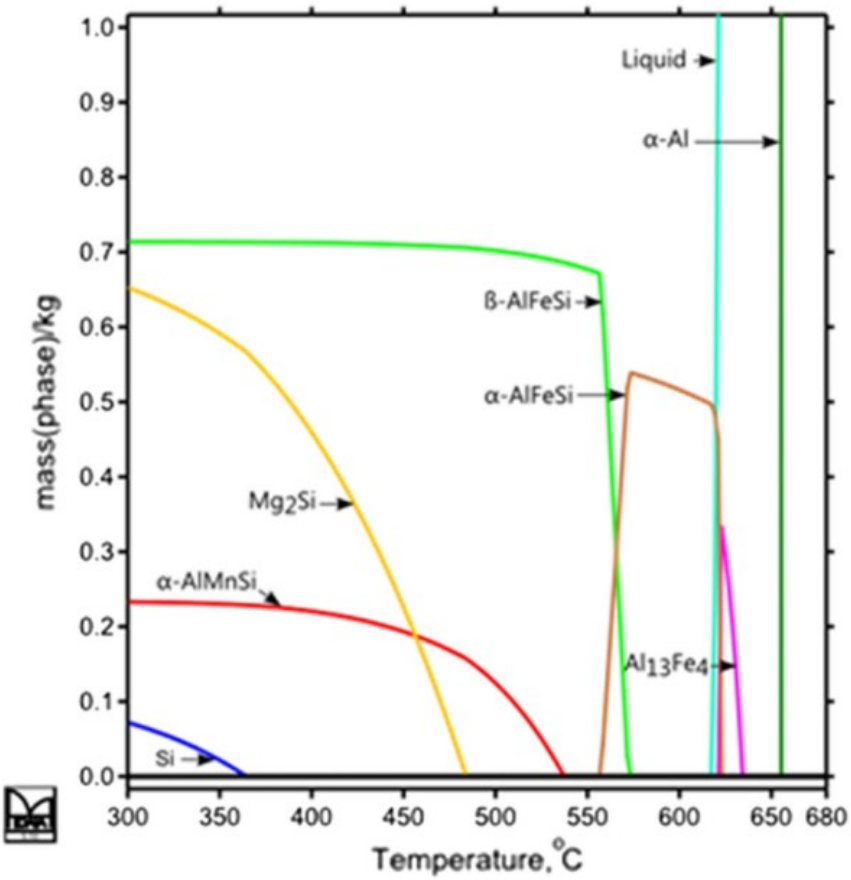


Figure 2.20: Thermodynamic calculation of solidification sequence in Al-0.5Si-0.5Mg-0.2Fe based on equilibrium condition [107].

Equilibrium α-AlFeSi The phase is also known as α'. In this review, α' will be used to distinguish it from another more frequently observed metastable AlFeSi phase (as will be discussed later). The stoichiometries of the α'-AlFeSi phase was reported by Mondolfo [108] as Al_8Fe_2Si. It adopts a hexagonal crystal structure in high purity Al-Si-Fe alloys, as determined by X-ray diffraction studies by Munson [112]. This was consistent with earlier work on single crystals performed by Robinson and Black [113] and further confirmed by Sun and Mondolfo [105]. Figure 2.22 shows a bright field TEM image together with the selected area diffraction pattern of an α'-AlFeSi particle extracted from an ingot of 6063 Al alloy with 0.1 wt.%Fe after solidification at 0.06 °C/s and homogenisation at 585 °C for 667 hours.

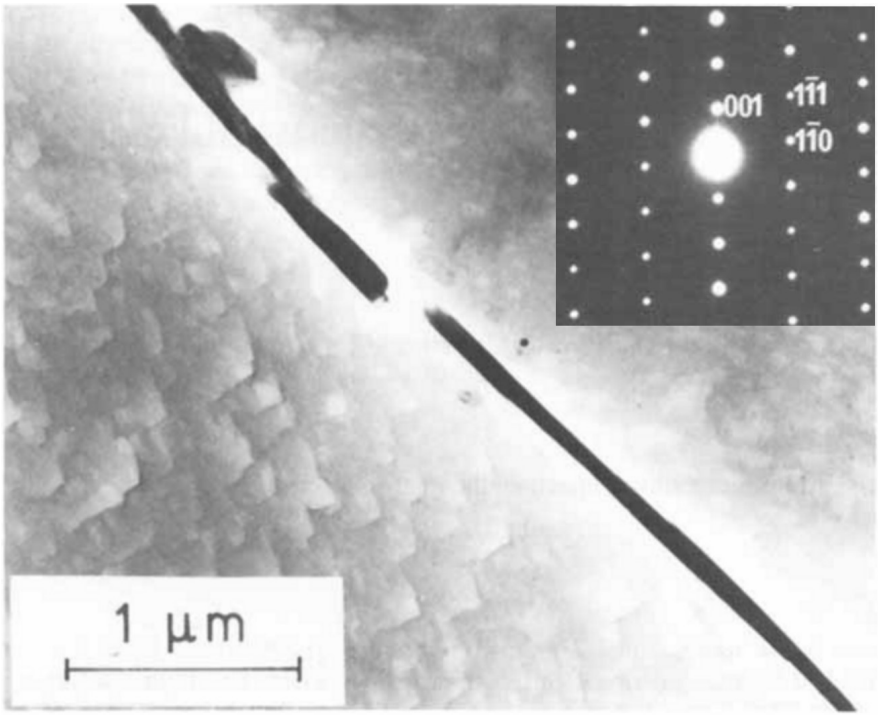


Figure 2.21: TEM image of needle shaped Al_3Fe particles on the grain boundaries of a DC cast Al-0.25Fe-0.13Si alloy ingot, with diffraction pattern along [110] zone axis [111].

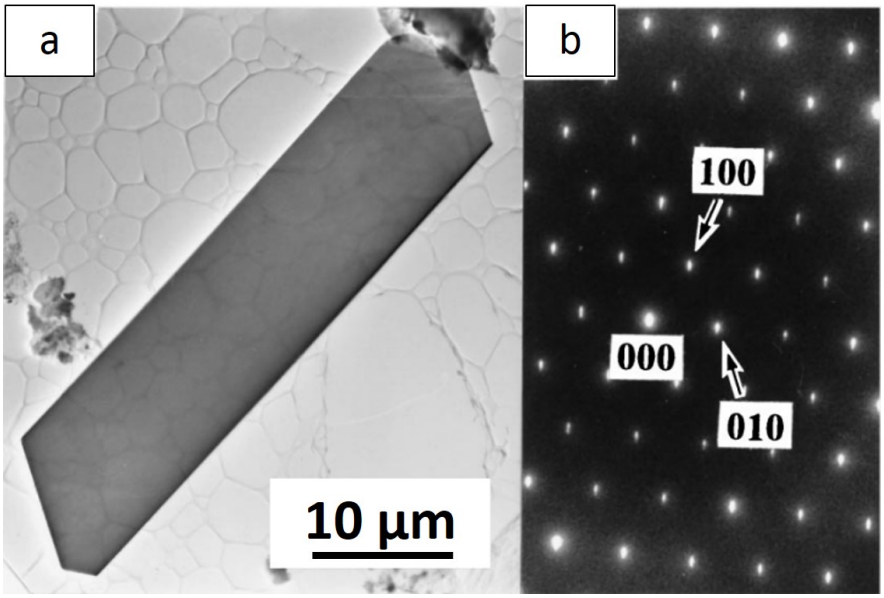


Figure 2.22: (a) Bright field TEM image of an α'-AlFeSi extracted from an ingot of 6063 Al alloy with 0.1 wt.%Fe solidified at 0.06 °C/s and homogenised at 585 °C for 2400 ks. (b) Selected area diffraction pattern from [001] zone axis [114].

Equilibrium β-AlFeSi The stoichiometries of the β-AlFeSi phase was reported by Mondolfo [108] as Al_5FeSi. β-AlFeSi has a monoclinic crystal structure, as determined by Phragmen [115]. It is considered a particularly harmful intermetallic phase in commercial Al alloys due to the faceted morphology, and has been extensively studied [13, 22, 24, 38, 45, 49, 50, 55, 73, 74, 76–78, 116–129]. Figure 2.23 shows a bright field TEM image and corresponding selected area diffraction pattern of a needle shaped β-AlFeSi extracted from an ingot of 6063 Al alloy with 0.1 wt.%Fe solidified at 0.06 °C/s. The β-AlFeSi is highly faceted, and was reported to contain multiple (001) growth twins along the growth direction by Mulazimoglu et al. [74], as has been discussed in section 2.2.2.

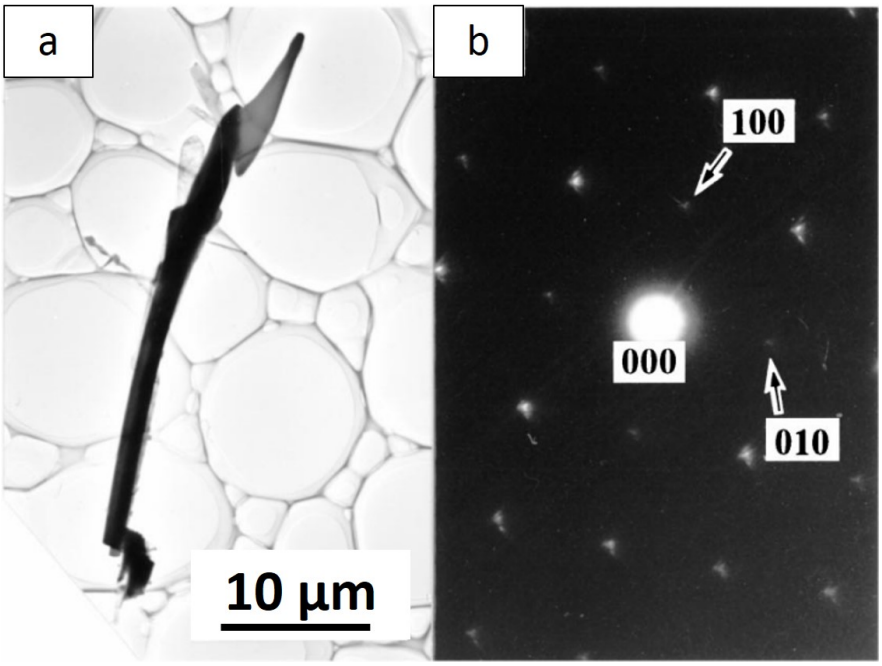


Figure 2.23: (a) Bright field TEM image of a needle β-AlFeSi extracted from ingot of 6063 Al alloy with 0.1 wt.%Fe solidified at 0.06 °C/s. (b) Selected area diffraction pattern from [001] zone axis [114].

Metastable structural variants of α-AlFeSi α- and β-AlFeSi can adopt a series of crystal structures under non-equilibrium solidification conditions, as summarised in Table 2.4. As pointed out above, equilibrium hexagonal α-AlFeSi is only stable in Al-Si-Fe with high purity. The presence of other alloying ele-

ments, such as Cu, Mn, Cr, V, W and Mo tends to destabilise the equilibrium phase and promote formation of a metastable cubic form of the α-AlFeSi, which is commonly denoted as α [11] and also know as c-AlFeSi in the literature [115]. The cubic α-AlFeSi was first observed by Phragmen [115] and then reported by Cooper [130], but was incorrectly proposed as an equilibrium phase by both. The cubic phase was frequently reported in the DC cast billets (cooling rate range: 1°C/s - 20°C/s [107]) of dilute Al-Si-Fe alloys, particularly in the rapidly cooled outer zone of the billets [106, 131–133]. The cubic α-AlFeSi has been reported to have a dendritic or so-called Chinese script morphology in 2-D section [38, 77, 121, 134–140], as shown in Figure 2.24. Apart from the metastable cubic structure, various other metastable structures of α-AlFeSi have been reported, namely monoclinic α_v [132], monoclinic α_T [106, 132, 141], orthorhombic α'' [106, 131, 142], monoclinic q_2 [142], and rhombohedral α_R [143]. However since these metastable structures are not commonly observed in the phase selection of Al-Si-Fe system, they will not be discussed in detail in this review.

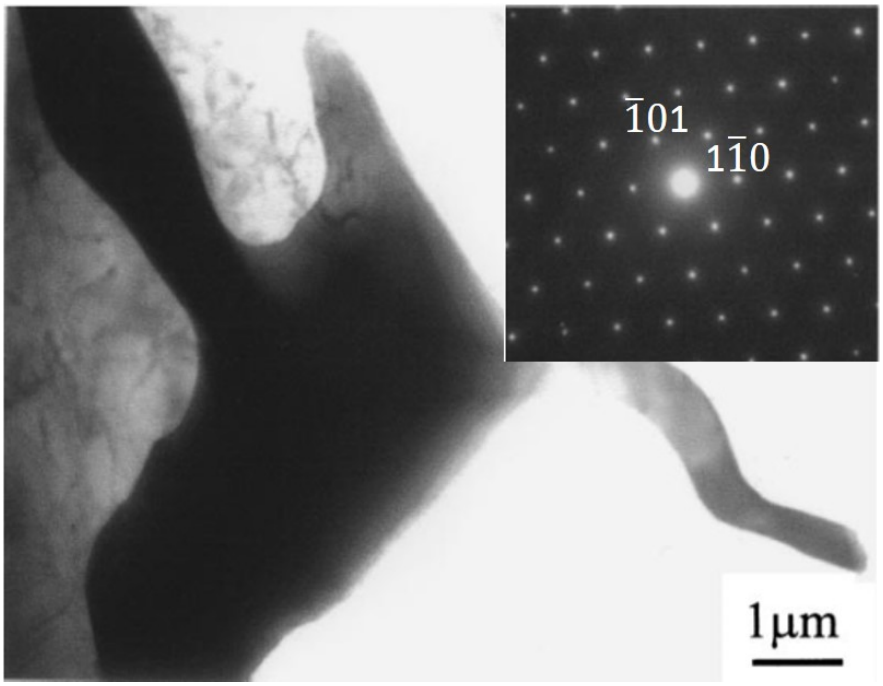


Figure 2.24: Bright field TEM image of a Chinese-script α-AlFeSi in a directionally resolidified 6xxx alloy with selected area diffraction pattern from [111] zone axis [77].

Metastable monoclinic β'-AlFeSi The β' particles were found by Westengen [131] in DC cast AA1050. The c-aixs of the monoclinic β' is 4.16 nm in length, which is quite similar to that of the β phase. In addition, the β' phase showed presence of twin boundaries, as in the β phase. EDX measurement revealed that the β'-AlFeSi had a lower Si/Fe ratio than the β-AlFeSi. Westengen therefore concluded that the β' phase could be a low-Si modification of the β phase.

Al-Si-Fe is one of the most important commercial alloy systems. Unfortunately, the large number of metastable Fe-rich phases makes the study of these phases, particularly their phase selection very complicated.

2.3.1.2 Fe-rich IMCs in Al-Cu-Fe system

Al-Cu alloys containing 2-10 wt.% Cu, with other alloying additions, were one of the first and most widely used engineering Al alloys, now known as 2xx.x cast and 2xxx wrought alloys [144]. The presence of Fe impurity usually combines with Al and Cu and leads to the formation of coarse, insoluble and faceted Fe-rich IMCs during later stages of solidification. These IMC phases include Al_6(Fe,Cu) and Al_7Cu_2Fe, which can form at Fe concentration as low as 0.03 wt.% [145], well below the Fe concentration limit in most commercial Al alloys, including 2024 alloy (Fe limit 0.5 wt.%) that is widely used in the aerospace industry. As early as 1980s, Backerud *et al.* [145] observed Al_6(Fe,Cu) as the first IMC to form, which then transformed into Al_7Cu_2Fe in 206 cast Al with 0.03 wt.% Fe. Similar results have been reported [46, 146, 147] in cast Al-Cu alloys with Fe concentrations up to 0.3 wt.%, indicating only Al_7Cu_2Fe or co-existence of both Al_6(Fe,Cu) and Al_7Cu_2Fe in the final microstructure. In cast Al-Cu alloys with higher Fe concentrations (>0.3 wt.%), more diverse Fe-rich IMCs were reported [15, 148, 149] depending on the solidification conditions. These faceted insoluble

Phase	Status	Bravaise lattice	Lattice parameters	References
θ	Stable	Monoclinic	$a = 1.549\,nm$ $b = 0.808\,nm$ $c = 1.247\,nm$ $\beta = 107.69^o$	[110]
α (α_1)	Metastable	Cubic: BCC *or* primitive cubic	$a = 1.256\,nm$ (Im3) $a = 1.252\,nm$ (Pm3)	[105, 112, 115, 130, 131]
α' (α_2)	Stable	Hexagonal	$a = b = 1.23\,nm$ $c = 2.62\,nm$	[105, 112, 132]
α_v	Metastable	Monoclinic	$a = 0.89\,nm$ $b = 0.635\,nm$ $c = 0.632\,nm$ $\beta = 93.4°$	[132]
α_T	Metastable	Monoclinic	$a = 2.795\,nm$ $b = 3.062\,nm$ $c = 2.073\,nm$ $\beta = 97.74°$	[106, 132, 141]
α'' (q_1)	Metastable	Orthorhombic	$a = 1.27\,nm$ $b = 2.62\,nm$ $c = 1.27\,nm$	[106, 131, 142]
q_2	Monoclinic	Metastable	$a = 1.25\,nm$ $b = 1.23\,nm$ $c = 1.97\,nm$ $\beta = 111°$	[142]
α_R	Metastable	Rhombohedral superlattice	$a_{sup} = 3.076\,nm$ $c_{sup} = 3.623\,nm$	[143]
β	Stable	Monoclinic	$a = 0.612\,nm$ $b = 0.612\,nm$ $c = 4.15\,nm$ $\beta = 91°$	[106]
β'	Metastable	Monoclinic	$a = 0.89\,nm$ $b = 0.49\,nm$ $c = 4.16\,nm$ $\beta = 92°$	[106, 131]

Table 2.4: Crystallographic data for Fe-rich IMCs in Al-Si-Fe alloys.

IMCs can degrade the ductility and toughness by acting as stress raisers and crack initiators [149–151], and may also cause severe localised corrosion in high-end aerospace alloys [152–155].

In Al alloys with Cu concentration up to 40 wt.% and Fe concentration up to 3.5 wt.%, eutectic and peritectic reactions which form Fe-rich IMCs in equilibrium solidification are listed below [156], with equilibrium intermetallic phases being Al_3Fe (dissolving up to 0.5 wt.% Cu [108].), Al_6(Fe,Cu), Al_7Cu_2Fe and Al_2Cu

(Figure 2.25) [108, 157]:

- $L \rightarrow Al_3Fe + \alpha\text{-}Al$
- $L + Al_3Fe \rightarrow \alpha\text{-}Al_6(Fe,Cu) + \alpha\text{-}Al$
- $L \rightarrow \alpha\text{-}Al_6(Fe,Cu) + \alpha\text{-}Al$
- $L + \alpha\text{-}Al_6(Fe,Cu) \rightarrow \omega\text{-}Al_7Cu_2Fe + \alpha\text{-}Al$
- $L \rightarrow \omega\text{-}Al_7Cu_2Fe + \alpha\text{-}Al$
- $L \rightarrow \omega\text{-}Al_7Cu_2Fe + \alpha\text{-}Al + Al_2Cu$

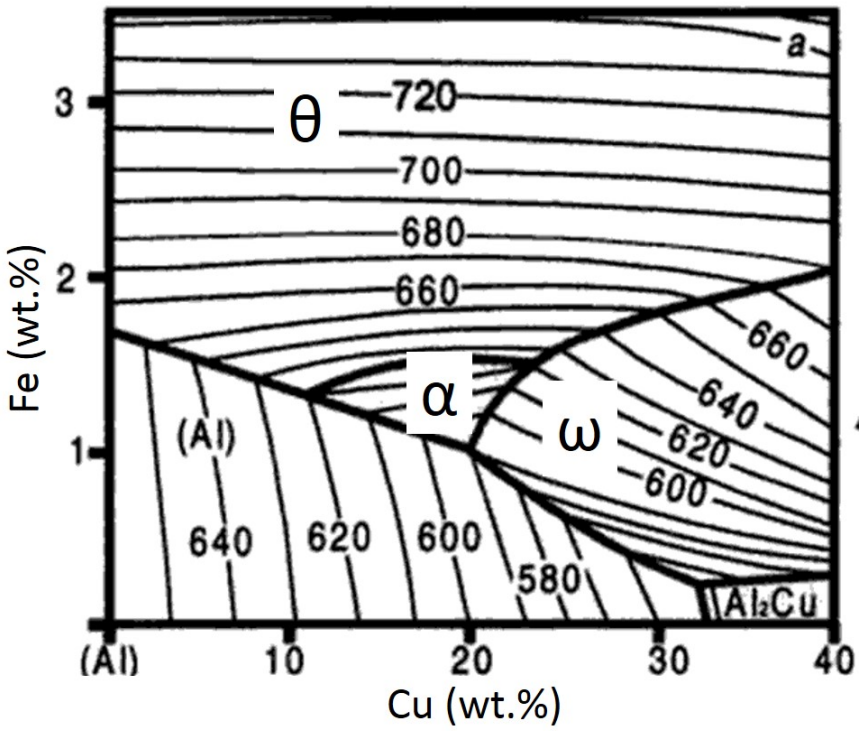


Figure 2.25: Liquidus projection of ternary Al-Cu-Fe phase diagram at Al-rich corner [156].

Orthorhombic α-Al_6(Fe,Cu) This orthorhombic phase (Table 2.5) was first found by Phragmen [115] and was assigned a formula of Al_6(Fe,Cu). The phase is also known as α-phase [158, 159] and $Al_{23}CuFe_4$ (τ_1) [160]. As the unit cell

dimension and the crystallographic symmetry were both very similar to those of the Al_6Fe [161], Phragmen therefore regarded the phase as a Cu-stabilised Al_6Fe, which is a metastable phase in binary Al-Fe. Further EDX measurements suggested a composition of 70 wt.% Al, 22 wt.% Fe, and 8 wt.% Cu. The work of Phragmen was then confirmed by Phillips [159], who studied the Al-rich corner of the ternary Al-Cu-Fe phase diagram, and established a primary field for the α-phase. The crystal structure was then further refined by Black *et al.* [162] using two-dimensional projections. Black *et al.* proposed that the α-phase has a centrosymmetric space group of $Ccmm$, but can undergo a symmetry debasement to the non-centrosymmetric space group of $Ccm2_1$ due to small atomic shifts.

Tetragonal ω-Al_7Cu_2Fe Bradley and Goldschmidt [163] found a ternary intermetallic phase in equilibrium with the Al-rich solid solution and assigned a formula of Al_7Cu_2Fe to the phase. This phase is also denoted as τ_2 [164, 165] and β [46, 166–168]. The ω-Al_7Cu_2Fe phase has a tetragonal structure (Table 2.5) with a space group of $P4/mnc$ [115]. The structure was then further refined by Bown and Brown [169]. In addition, the phase possesses a needle shape in 2D (Figure 2.26) [46] and has been reported to increase the susceptibility of alloys to localised corrosion [152, 153, 170].

Other ternary phases Other ternary Fe-rich phases, namely Al_6Cu_2Fe (i or Ψ) [163, 171] and $Al_{10}Cu_{10}Fe$ (φ or τ_3) [158, 160, 163, 171–173] are listed in Table 2.5.

Nonetheless, a complete understanding of the factors controlling nucleation, growth and how they vary with composition, solidification conditions, etc has yet to be developed, largely due to the restriction of inferring nucleation and growth behaviour from post-solidification microscopy and other qualitative techniques.

In terms of this thesis, the Al-Cu-Fe ternary system was selected as one of the model alloy systems. The smaller but sufficient number of Fe-rich phases in Al-

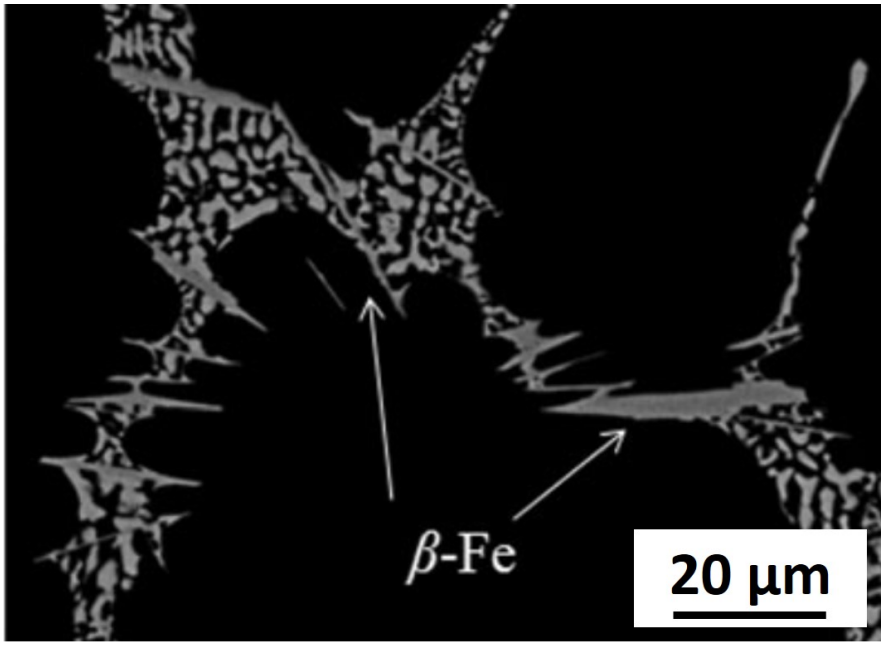


Figure 2.26: Backscattered electron image showing needle-like Al_7Cu_2Fe (β-Fe) in Al-4.5Cu-0.3Fe (wt.%) [46].

Cu-Fe makes the system more promising and feasible than the Al-Si-Fe system in studying the dynamics of Fe-rich IMC formation in solidification using *in-situ* synchrotron X-ray techniques, particularly in visualising the phase selection, where no dynamic study has been done.

Phase	**Status**	**Bravaise lattice**	**Lattice parameters**	**References**
α (τ_1)	Stable	Orthorhombic	$a = 0.644\,nm$ $b = 0.746\,nm$ $c = 0.878\,nm$	[115, 162]
ω (τ_2, β)	Stable	Tetragonal	$a = 0.633\,nm$ $c = 1.481\,nm$	[115, 169]
i (Ψ)	Stable	Icosahedral	$a_6 \approx 0.633\,nm$	[174]
φ (τ_3)	Stable	Orthorhombic	$a = 0.815\,nm$ $b = 1.414\,nm$ $c = 1.007\,nm$	[173]

Table 2.5: Crystallographic data for Fe-rich IMCs in Al-Cu-Fe alloys.

2.3.2 Modification of Fe-rich IMC phase selection

As discussed earlier, the presence of highly faceted Fe-rich IMCs causes various issues in terms of castability, mechanical properties (ductility in particular), fatigue life, and corrosion resistance. As it is very difficult to remove Fe impurities in an economical way, much effort has therefore been expended in understanding how to lessen their deleterious effects. Many researches are focusing on altering the harmful needle (platelet in 3D) morphology into less harmful forms, for instance, script (dendritic) morphology by trying to control phase selection. Current strategies of controlling the Fe-rich IMC morphology by modifying the phase selection are mainly realised via: (1) addition of "neutralisers" [13, 108, 146, 175–186] such as Mn, Co, Cr, Be, Mo, Ni, V, Ti, W, Cu, Sr, Zr, Y, Nd, La and Ce, with Mn being the most common addition, and (2) control of cooling rate [44, 48, 108, 116, 119, 126, 128, 135].

2.3.2.1 Neutralisers

Neutraliser	Neutraliser/Fe ratio	Reference
Mn	0.17-2	[13, 52, 116, 146, 177, 179]
Co	0.73-1.5	[177, 183, 187]
Cr	0.33-0.5	[177, 183, 188]
Be	0.2-0.54	[177, 189]
Sr	0.025-0.1	[55, 190]
Y	0.3	[191]
Ce	0.8	[192]

Table 2.6: A summary of major chemical neutralisers for β Fe-rich IMCs.

Table 2.6 summarises that major neutralisers. Despite that Mn by itself is deleterious to the mechanical properties of Al alloys, addition of Mn has been extensively used to neutralise the effect of Fe. In Al-Si-Fe ternary alloys and Al-Si-Mg-Fe quaternary alloys, sufficient addition of Mn can transform the needle-like β-Al_5FeSi into α-$Al_{15}(Mn,Fe)_3Si_2$ in a more compacted Chinese script or polyhedral morphology, giving rise to an improvement in ductility [108]. However,

the amount of Mn required to alter the morphology of the Fe-rich IMCs has not been well established and can be affected by various factors, such as cooling conditions and initial alloy compositions.

Kim et al. [179] studied the effect of Mn additions from 0.07 to 0.20 wt.% in Al-7Si-0.38Mg-0.2Fe (wt.%) with a fixed cooling rate. The original needle-like β-AlFeSi was replaced by rod-like α-Al(Mn,Fe)Si at Mn additions of 0.07 and 0.13 wt.%, and was eventually replaced by script-like α-Al(Mn,Fe)Si at Mn addition of 0.20 wt.% (Figure 2.27). Shabestari et al. [190] studied the effect of Mn additions in Al-13Si-2.5Fe (wt.%), and observed that Mn addition above 0.9 wt.% altered the phase selection from needle-like β-AlFeSi to more compacted polyhedral α-Al(Mn,Fe)Si. An approximate Mn/Fe (wt.%) ratio of 0.5 with Fe content exceeding 0.4 wt.% was proposed by the researchers [193] for conversion of the needle IMCs into polyhedral form at a cooling rate of 10°C/s. Cao and Campbell [52] observed that the conversion of needle intermetallics into Chinese script morphology at a much lower Mn/Fe ratio of 0.17 in Al-11.6Si-0.37Mg-1.16Fe (wt.%), given a cooling rate lower than 0.1°C/s.

Similarly, Mn additions to Al-Cu-Fe alloys also promote the formation of more compacted Chinese script phases while suppressing needle-like phases. Liu et al. [46] have reported replacement of needle-like Al_7Cu_2Fe by script-like α-$Al_{15}(Mn,Fe)_3(Si,Cu)_2$ in Al-4.5Cu-0.3Fe-0.3Si (wt.%) with Mn addtion of 0.3 wt.% at cooling rate of 0.2 °C/s. Tseng [146] observed that the Al_7Cu_2Fe needles at lower Mn concentration (0.29 wt.%) were replaced by script-like Mn-bearing IMCs at a higher Mn concentration (0.66 wt.%) in Al-4.5Cu-0.3Fe produced by permanent mould casting (cooling rate 2-3°C/s) (Figure 2.28).

However, Mn has a high redistribution coefficient of 0.95 in Al, which means that local Mn addition can easily exceed the eutectic concentration and lead to hypereutectic Al-Mn phases. In this case, the Mn modified Fe IMCs are formed as coarse primary α-phase, causing deterioration of mechanical properties [128].

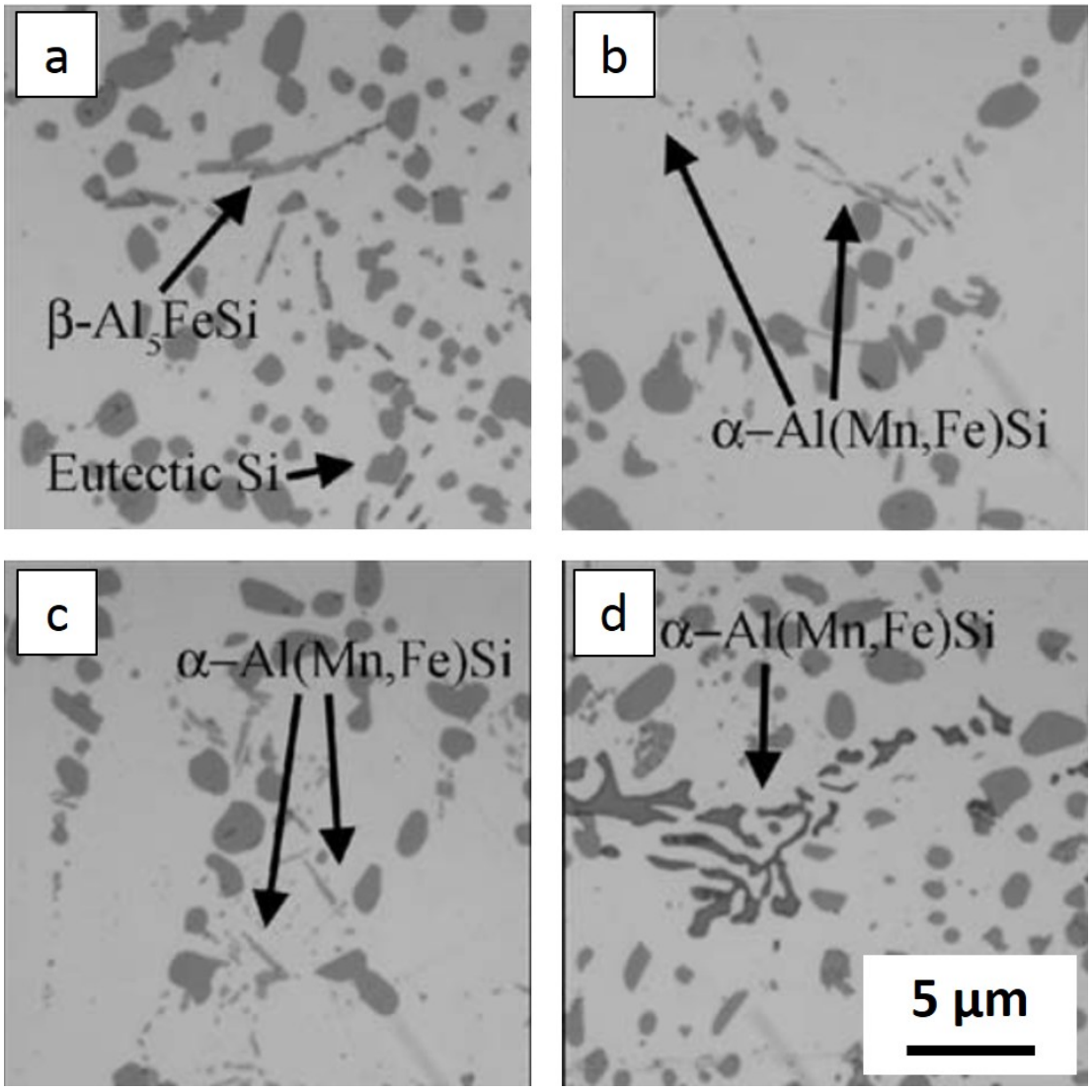


Figure 2.27: Different morphologies of Fe-rich IMCs in (a) Al-7Si-0.38Mg-0.2Fe, (b) Al-7Si-0.38Mg-0.2Fe-0.07Mn, (c) Al-7Si-0.38Mg-0.2Fe-0.13Mn, and (d) Al-7Si-0.38Mg-0.2Fe-0.2Mn [179].

A few studies [193, 194] have reported formation of primary α-$Al_{15}(Mn,Fe)_3Si_2$ when Mn was added or formation of primary α-$Al_{15}(Mn,Fe,Cr)_3Si_2$ when Mn and Cr were added. These primary IMCs, usually called "sludge", have high specific gravity, which causes them to settle towards the bottom of the melt and form hard agglomerates. These hard spots are detrimental to the overall properties of castings.

The other frequently reported neutralisers apart from Mn are Co and Cr, which have similar atomic radii to that of Fe. Mahta et al. [183] studied the

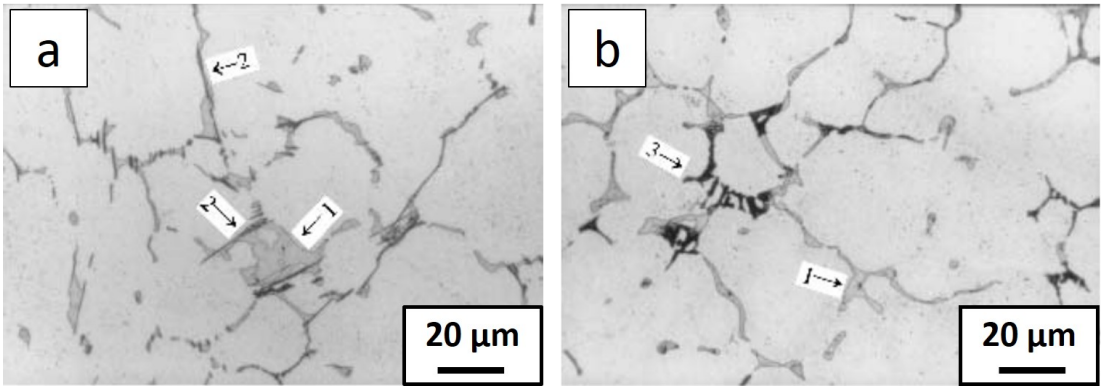


Figure 2.28: Optical micrographs showing the morphologies of Al_2Cu, Al_7Cu_2Fe and Mn-bearing IMCs in cast (a) Al-4.5Cu-0.3Fe-0.29Mn, (b) Al-4.5Cu-0.3Fe-0.66Mn (arrow 1: Al_2Cu, arrow 2: Al_7Cu_2Fe, arrow 3: Mn-bearing) [146].

effect of different amount of Co in alloy Al-11.7Si-0.6Cu-(1.2-2.4)Fe (wt.%), and suggested an optimum Co/Fe ratio of 1 to replace the β Fe-rich needles with an α Chinese script (dendritic) morphology. Figure 2.29a shows the microstructure of Al-11.7Si-0.6Cu-2.4Fe-2.4Co (wt.%) with script-like IMCs [183]. The composition of the α Chinese script phases was identified approximately as $Al_{15}(Fe,Co)_4Si_2$ using EDX [183]. Murali et al. [177] have reported similar findings in Al-7Si-0.3Mg-1Fe-1Co (wt.%) (Figure 2.29b). Further, almost all the Chinese script α-IMCs precipitate within primary Al dendrites (Figure 2.29a and b) [177, 183]. Thus, Co was thought to be better than Mn in terms of reducing the segregation tendency and preventing formation of coarse primary α-IMCs. Cr was believed to have a similar function to Co [183].

While addition of these neutralisers seemed to function to some extent in altering the IMC phase selection, little is known regarding the underlying mechanism leading to phase changes. It should be noted that some neutralisers reported to alter the Fe-rich IMC phase selection, such as Sr, Y, La and Ce were also reported as modifiers for growth of Si (as in the earlier section). In other words, it needs to be understood if this change in IMC phase selection was due to a growth competition where growth of the anisotropic β IMCs was restricted by these modifiers via a similar restricted TPRE mechanism or IIT mechanism as for Si. Hence,

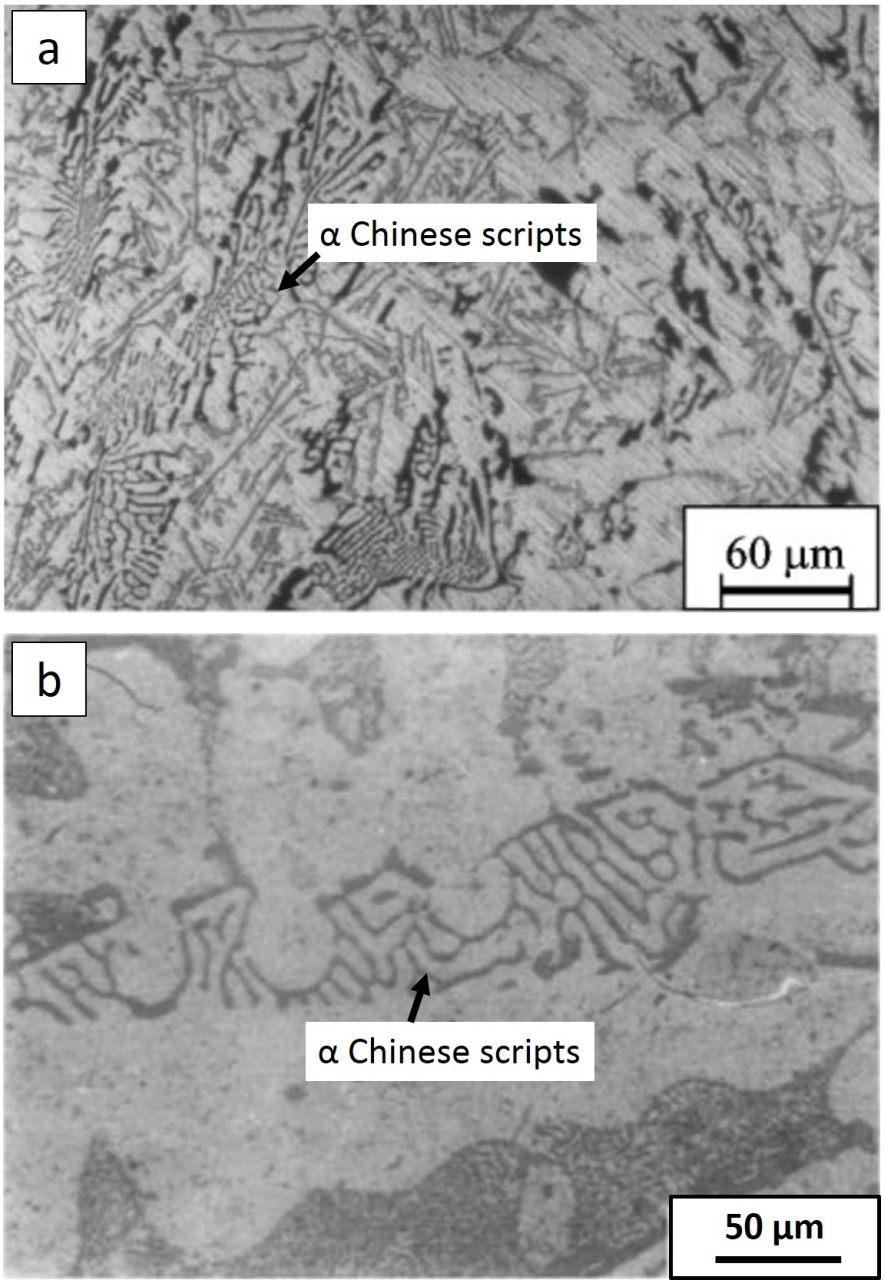


Figure 2.29: Optical micrographs showing Chinese script α-IMCs in (a) Al-11.7Si-0.6Cu-2.4Fe-2.4Co [183], and (b) Al-7Si-0.3Mg-1Fe-1Co [177].

in-situ X-ray radiography might be usefully employed to investigate the dynamic of IMC formation and growth with addition of these chemical modifiers.

2.3.2.2 Cooling rate

In Al-Si-Fe, β-Al_5FeSi is a stable phase under equilibrium conditions [108, 135]. Increasing the cooling rate has therefore been used to control the size and amount

of the needle-like β-phase. Effect of cooling rate can be viewed from different aspects. First, high cooling rates, for example in high pressure die casting, can suppress the segregation of Fe and therefore reduce the amount and also size of the β-phase [195]. Second, high cooling rate also promotes the formation of metastable Chinese script α-IMCs [44, 77]. Sha *et al.* [77] studied an Al-0.6Si-0.3Fe-0.8Mg (wt.%) alloy, which at a low solidification velocity of 0.5-1 mm/s selected needle-like β-IMCs, while at a higher solidification velocity of 2 mm/s selected the α-IMCs. Narayanan *et al.* [44] reported for A319 alloys (Al-6Si-3.5Cu-1.2Fe, wt.%) that the formation temperature of the needle β-phase kept decreasing with increasing cooling rate from 0.1 to 20°C/s, until the formation temperature merged into the Al-Si eutectic temperature. In this condition, the liquid composition favoured the formation of α-Al_8Fe_2Si. A similar phenomenon was also observed more recently by Castro-Roman et al. [116] in Al-7.5Si-0.65Fe-0.3Cu-0.2Mn (Figure 2.30). Increasing cooling rate from 0.1°C/s to 1°C/s promoted formation of Chinese script α-phase and reduced the amount of needle β-phase. This change in phase selection with increasing cooling rate likely results from kinetic issues. The α-phase is in a cubic structure and hence has a higher crystallographic symmetry than the monoclinic β-phase. Therefore, the cubic α-crystal, which has more fast-growing planes, is more able to grow in synchronisation with the rate of the heat extraction at higher cooling rates. Finally, a higher cooling rate reduces the dendrite arm spacing of the primary Al, and leads to a refinement of the interdendritic β-IMCs by restricting their growth [118, 124]. Liu *et al.* [118] performed a systematic study on the correlation between the dendrite arm spacing and the β-IMCs size in directionally solidified A356 and 319 alloys. There was a consistent decrease in size and increase in density of β-IMCs with decreasing dendrite arm spacing (i.e. increasing cooling rate) [118].

Similar effects of cooling rate on needle IMC modification has been observed in Al-Cu-Fe alloys. Kamguo *et al.* [166] reported for an Al-4.7Cu-0.3Fe-0.2Si-

0.2Mn (wt.%) that the fraction of needle-like Al_7Cu_2Fe dropped from 1.33% to 0.66% upon increasing the cooling rate from 1°C/s to 4°C/s, while formation of Chinese script $Al_{32}(Cu,Fe,Mn)_8(Al,Si)_4Si_2$ was promoted at the higher cooling rate of 4°C/s (Figure 2.31).

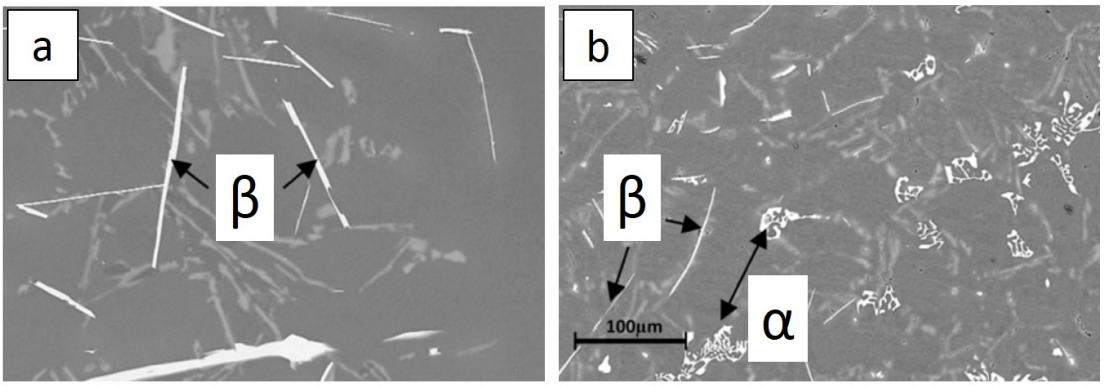


Figure 2.30: Distribution of Fe-rich IMCs in Al-7.5Si-0.65Fe-0.3Cu-0.2Mn at cooling rates of (a) 0.1°C/s, and (b) 1°C/s [116].

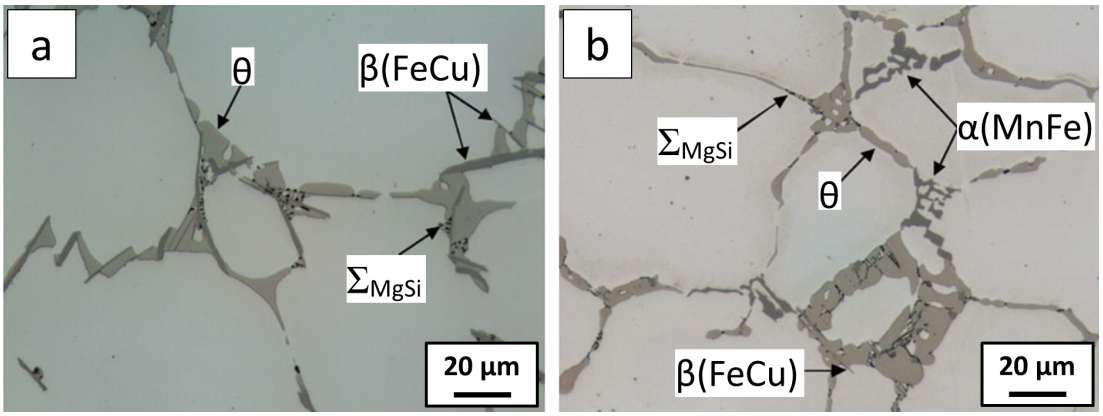


Figure 2.31: Microstructure of Al-4.7Cu-0.3Fe-0.2Si-0.2Mn at (a) 1°C/s, and (b) 4°C/s. Notice the decrease in the amount of Al_7Cu_2Fe (β(FeCu)) and the formation of $Al_{32}(Cu,Fe,Mn)_8(Al,Si)_4Si_2$ (α(MnFe)) at increasing cooling rate [166].

2.4 Summary

Studies concerning the nucleation, faceted growth and phase selection of Fe-rich IMCs in Al alloy solidification, and efforts to control or modify these behaviours to manipulate morphology, size and distribution have been reviewed.

Complex nucleation and growth dynamics and the low IMC volume fraction make it difficult to study the solidification of secondary Fe-rich IMCs, especially *in-situ* by X-ray radiography/tomography. Various combinations of alloy composition, casting condition, and external refiner or modifier have generally been used to try to gain more control over the morphology, size and distribution of Fe-rich IMCs, but have had limited effect.

The use of *in-situ* synchrotron X-ray imaging under contrived conditions where Fe-rich IMCs can be more easily studied might contribute to a more comprehensive understanding of Fe-rich IMC formation, growth and phase selection. Until now, only a handful of real-time *in-situ* studies have been conducted for Fe-rich IMCs, which have produced some new insights but have yet to be quantified and explored across a range of realistic conditions to influence technological properties.

Chapter 3

Experimental Methods

The overall aim of the thesis is to study the nucleation, growth and phase selection of Fe-rich IMCs and other similar faceted IMC crystals in Al alloy solidification. Three model alloy systems were investigated: Al-Cu-Fe, Al-Fe and Al-Pt-Er, and a combination of *in-situ* and *ex-situ* experimental techniques were employed. *In-situ* X-ray radiography was used to study the dynamics of the IMC formation and growth during solidification. Post-solidification microscopy was used for identification of IMC phases in solidified samples used in radiography experiments and in as-cast alloy ingots.

Four *in-situ* X-ray radiography campaigns were carried out including three at national synchrotron facilities: beamline B16, Diamond Light Source (DLS, experiment numbers MT8635 and MT9140), beamline ID19, European Synchrotron Radiation Facility (ESRF, experiment number MA4063) and beamline Psiche, SOLEIL (experiment number 20170765), together with one campaign using laboratory apparatus at Norwegian University of Science and Technology (NTNU, experiment number: NOR18).

3.1 Design of experiments

This section details the objectives, the design of experiments and selection of alloys. Fig. 3.1 shows a summary of the experiment focus, the alloys and the experimental campaigns.

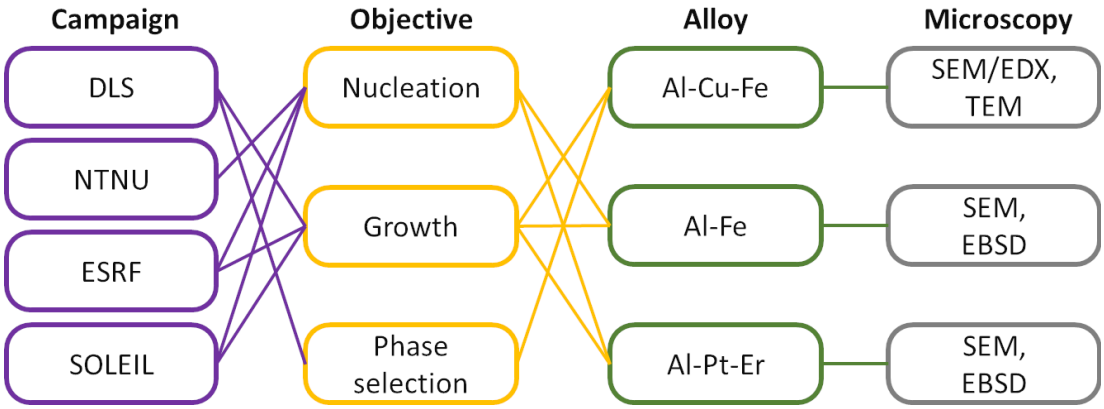


Figure 3.1: A diagram summarising the relationship between the *in-situ* experimental campaigns, their principal focus, the alloy used and post-solidification microscopy.

Initially, the focus was data acquired by prior group members at DLS on Al-Cu-Fe alloys, with campaign objectives to investigate the feasibility of imaging Fe-rich IMCs in Al alloys, and if so, to study the nucleation behaviour of these Fe-rich IMCs.

Model Al-Cu-Fe alloys were selected as an analogue to commercial 2xx series cast Al alloys, but with an intentionally higher Cu concentration of 10 wt.% and high Fe concentrations of 0.8 wt.% and 1.5 wt.% (maximum Fe concentration in 2xx Al cast alloy) for the purposes of: (a) forming a relatively high fraction of secondary Fe-rich IMCs, and (b) obtaining sufficient X-ray absorption contrast between the IMCs enriched in both Fe and Cu, the Al-rich primary phase, and the remaining Cu-rich liquid (as Cu is rejected into the liquid by the growing Al-rich phase).

The radiography data was analysed by the author, feasibility of IMC growth measurement was established, and new insights were gained regarding the mor-

phology and growth of secondary Fe-rich IMCs as a function of cooling rate and primary microstructure morphological changes via grain refiner addition. In addition, an *in-situ* method was developed to estimate the tip temperature and relationship to IMC phase selection directly from the radiography images, with phase selection supported by post-solidification microscopy.

Although good imaging contrast allowed insights on IMC growth in Al-Cu-Fe alloys to be gained, visualising IMC formation was not possible because of the obscuring presence of the majority phase of primary α-Al dendrites.

3.1.1 Nucleation and growth of primary IMCs in *binary* system

IMC extraction and microscopy suggested that TiB_2 in commercial Al-5Ti-1B grain refiners might be associated with nucleation of secondary platelet Fe-rich IMCs, evidenced by consistent observation of TiB_2 particles in physical contact with the IMC platelet after extraction [37, 39, 40]. However, an alternative interpretation of the co-location of the TiB_2 and IMCs may be simply due to physical impingement of growing IMCs with unused TiB_2 particles that are pushed into the inter-dendritic region by pre-formed α-Al dendrites in the final stages of solidification.

Accounting for this possibility and difficulties in studying secondary IMCs led to the idea of studying the formation of Fe-rich IMCs as a *primary* phase in a simple binary Al-Fe alloy. A hypereutectic Al-3Fe (wt%) alloy was therefore employed that formed platelet Fe-rich IMCs ($Al_{13}Fe_4$) as the *primary* phase i.e. it formed unconstrained geometrically in the liquid. Alloys with different inoculation conditions (no inoculation, TiB_2 and TiC) were prepared to study any effect of inoculant additions on formation of primary Fe-rich IMCs. The equilibrium partition coefficient was estimated to be $k = 12.3$ for an initial liquid composition of 3 wt% Fe from the equilibrium Al-Fe binary phase diagram (Fig. 1.3),

and so strong Fe segregation from the dilute liquid into the Fe-rich IMCs can be expected to provide strong X-ray absorption contrast between the liquid and the IMCs.

Radiography experiments with two typical set-ups were designed and performed. First, experiments were conducted at NTNU to investigate the feasibility and to assess what information might be gained by studying the formation of primary IMCs as a function of cooling rate and inoculant additions in a horizontal, near-isothermal solidification condition. Second, experiments were carried out at ESRF in vertical, directional conditions to further investigate the effect of thermal gradient on IMC formation. More details on these two different configurations are presented in Section 3.3.

3.1.2 Nucleation and growth of primary IMCs in *ternary* system

With new insights gained on IMC nucleation in the simple binary system, the next step was to investigate IMC nucleation and growth in a more complex multi-element alloy, particularly regarding the role of multi-solute diffusion, since commercial Al alloys are always composed of multiple elements. This work went on to become a significant part of a larger project in collaboration with Science and Technology Facilities Council (STFC) and the DLS, to study the potential of a new type of spectroscopic detector, known as "HEXITEC" [196–199], alongside conventional radiography, which aimed to provide direct, separate identification of each element in a multi-element alloy - not possible by conventional X-ray absorption radiography.

To explore this possibility and the capability of the HEXITEC prototype, an Al-Pt-Er model alloy system was chosen. The design criteria for the model alloy were:

1. To form a large fraction of highly faceted primary IMCs, morphologically closely related to $Al_{13}Fe_4$ and other β Fe-rich IMCs, in order to extend and generalise knowledge gained on primary Fe-rich IMCs.

2. To generate strong absorption contrast during micro-segregation of Pt and Er during solidification.

3. To have well-separated fluorescence peaks (in terms of energies) of the solute elements to facilitate their independent detection by the HEXITEC pixelated X-ray spectrometers.

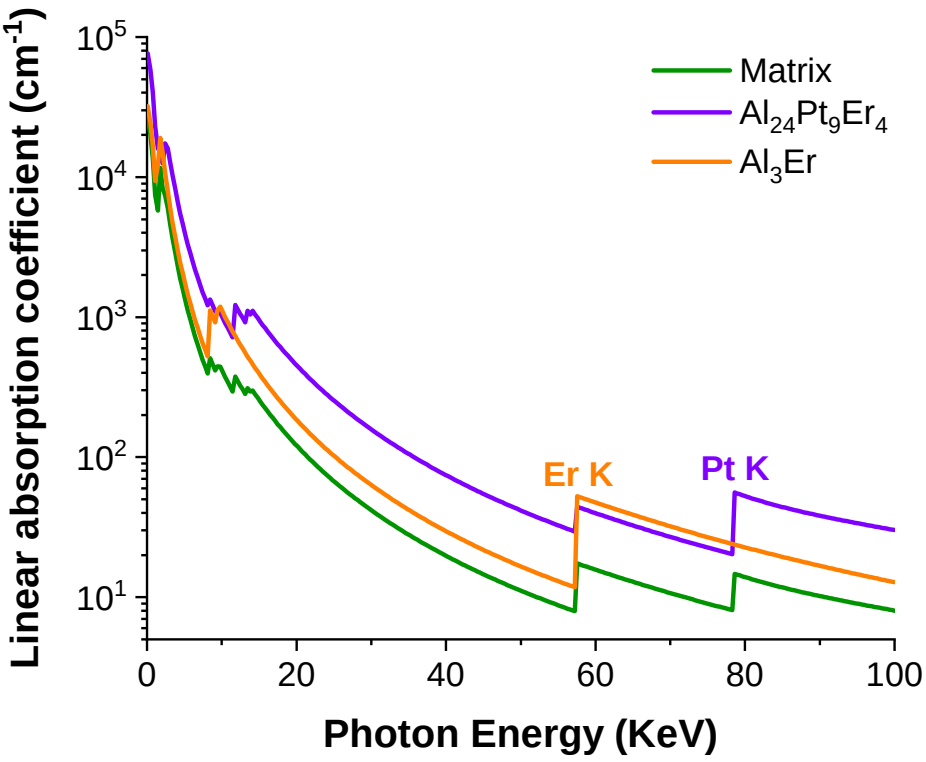


Figure 3.2: Linear absorption coefficient as a function of photon energy for $Al_{24}Pt_9Er_4$ (phase of interest in the work), the liquid matrix and Al_3Er, which was the other primary phase in the alloy.

Fig. 3.2 shows a graph of the linear absorption coefficient as a function of photon energy for the primary faceted IMC $Al_{24}Pt_9Er_4$ (phase of interest in the work), Al_3Er and the Al-rich liquid. The incident X-ray used in the synchrotron

radiography experiments was composed of a white beam peaking at 89 keV. Therefore, the high absorption K-edge of Pt of 78 keV together with the energy of the incident beam was expected to provide strong absorption contrast for the Pt-rich $Al_{24}Pt_9Er_4$ against the other two phases. In terms of assessing HEXITEC performance, Pt should only segregate into $Al_{24}Pt_9Er_4$ so it could be distinguished from Al_3Er.

3.2 Alloy and sample preparation

In general, preparation of radiography samples followed a three-step procedure. First, bulk alloy ingots were prepared by casting. Second, the bulk ingots were sectioned into thin slices, which were ground with SiC paper (800, 1200, 2500 and 4000 grit) and polished with diamond suspension (3 μm and 1 μm) to thickness of 200$\pm$5 μm with a final surface finish of $\pm$ 1 μm. For synchrotron experiments, the samples were approximately 20 $\times$ 8 mm. For laboratory experiments at NTNU, 50 $\times$ 5 mm samples were prepared [80, 200–203]. Finally, each polished "foil" sample was encapsulated into an X-ray transparent cell. Figs. 3.3(a) and (b) show examples of encapsulated radiography samples being prepared at NTNU and ESRF. For experiments at the DLS, sample cells were made of quartz; at NTNU and ESRF, 100 μm thick glassy carbon cells were used; and at SOLEIL, samples cells were made of 100 μm thick BN. The alloy casting, which differed across different alloy systems, is described below.

3.2.1 Al-Cu-Fe

Al-Cu-Fe alloys were prepared by prior group members as follows. Two alloy compositions were prepared: Al-10Cu-1.5Fe and Al-10Cu-0.8Fe (wt%), with and without TiB_2 additions (0.1 wt% Al-5Ti-1B master alloy). For convenience, the different alloy samples are named: 1.5Fe, 0.8Fe, 1.5Fe-GR and 0.8Fe-GR.

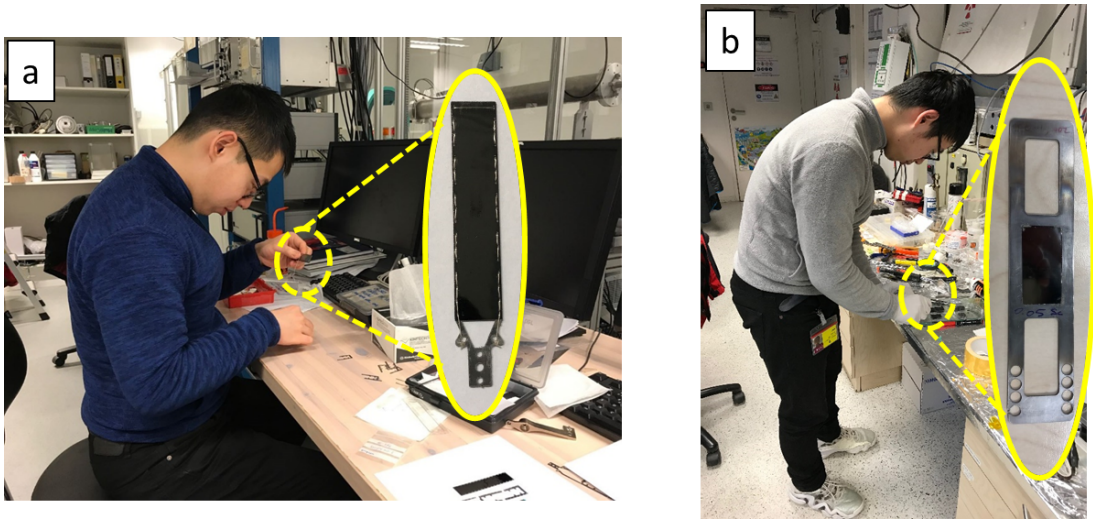


Figure 3.3: Photos of the author preparing samples for (a) laboratory X-ray radiography experiments at NTNU, and (b) synchrotron experiments at ID19, ESRF. Encapsulated samples are shown in the zoomed-in images.

First, an Al-10Cu (wt%) binary alloy was prepared by melting and mixing pure Al (99.999%) and pure Cu (99.999%) at 750°C. For grain refined samples, Al-5Ti-1B master alloy was added to the well-mixed melt. The alloy was then cast into a water-cooled Cu mould containing multiple cylindrical cavities of 30 mm diameter and 40 mm depth. Second, each of the grain refined or non-grain refined Al-10Cu alloy ingots was remelted separately at 780°C, and pure Fe tablets of approximately 3 mm in size were added into the melt to obtain Fe concentrations of 0.8 wt% and 1.5 wt%. Finally, each well-mixed melt was cast following the same method. The outcome of this step was 4 cylindrical ingots of 1.5Fe, 0.8Fe, 1.5Fe-GR and 0.8Fe-GR. The top part (∼10 mm) of each ingot was chopped off to remove oxides and/or other inclusions that usually floated during solidification. Foil samples were then sectioned from the ingot following Fig. 3.4.

3.2.2 Al-Fe

Al-3Fe alloys were prepared following a three-step procedure. First pure Al (99.999%) and an Al-75Fe (wt%) master alloy were fully melted and mixed by holding at 850°C for 30 min in an enclosed induction furnace with a controlled

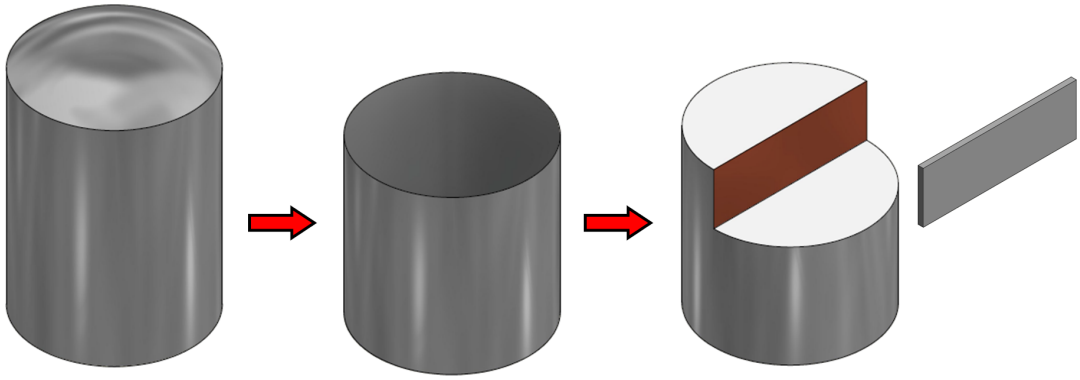


Figure 3.4: A schematic showing how foil samples were sectioned from a bulk Al-Cu-Fe ingot.

positive Ar pressure in the furnace chamber (to restrict evaporation and oxidation of Al) and then left to air cool in the furnace. Second, the "green" alloy obtained from the first step was remelted in a clay graphite crucible at 750°C, carefully stirred and cast into the same water-cooled Cu mould, to obtain 3 cylindrical ingots. This step was carried out before casting the alloy into the final shape in order to reduce possible macro-segregation caused by slower cooling in the first step. Third, each of the 3 cylindrical ingots were remelted again with addition of different inoculants: no addition, 0.5 wt% Al-5Ti-1B master alloy, and 0.5 wt% Al-5Ti-0.2C master alloy. The well-mixed melt was then poured into a rectangular copper mould with an internal cavity of 55×8×16 mm, following the design in [200]. The combination of small casting geometry and fast cooling effectively eliminated significant macro-segregation [200]. Fig. 3.5 shows a schematic of the casting arrangement, to promote rapid mould filling and how a foil sample was produced from the as-cast ingot. After the top structure and the bottom edge were chopped off, foil samples were produced using wire electro-discharge machining (wire EDM).

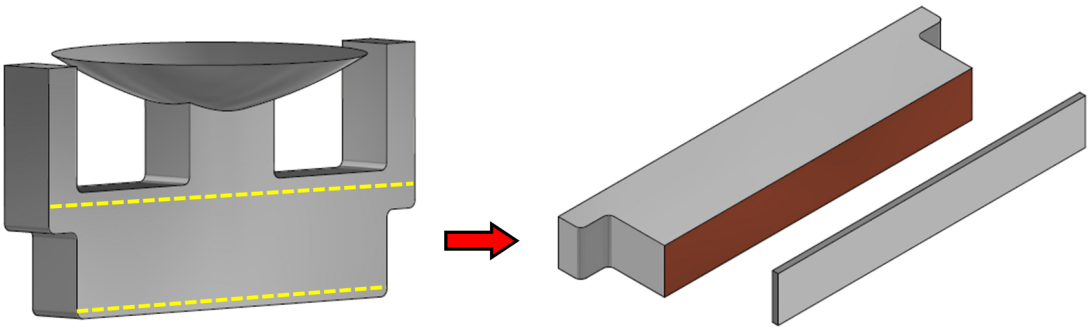


Figure 3.5: A schematic showing the casting arrangement and how foil samples were sectioned from the bulk Al-Fe ingot. The as-cast ingot was chopped as indicated by the yellow dashed lines, and sliced using wire electro-discharge machining (wire EDM) to produce foil samples.

3.2.3 Al-Pt-Er

Al-23Pt-20Er (wt%) alloys, both with and without TiB_2 additions (0.5 wt% Al-5Ti-1B master alloy) were prepared by vacuum arc melting due to the high melting points of Pt (1768°C) and Er (1529°C). First, for the samples with TiB_2 additions, TiB_2 was introduced by adding 0.9 wt% Al-5Ti-1B master alloy in pure Al using the same casting method as for Al-Cu-Fe. Then pure Al (or Al+0.9 wt% Al-5Ti-1B for the inoculated alloys), pure Er (99.9%, Sigma-Aldrich) and pure Pt (99.95%, Bullion By Post) were melted and mixed using vacuum arc melting. The total material mass for each batch was approximately 100 g. The solidified samples were flipped in the arc melting crucible and remelted after the first melting run to promote mixing. The outcome was an cap-shaped ingot with ∼50 mm diameter and ∼15 mm thickness, as shown in Fig. 3.6. The top surface was ground with SiC paper to remove the surface oxide, and the edges were chopped off where thick oxide films were often found. The ingot was then cut by water jet into four pieces (as denoted by the yellow dashed line). Foil samples were produced by sectioning using a diamond wheel blade.

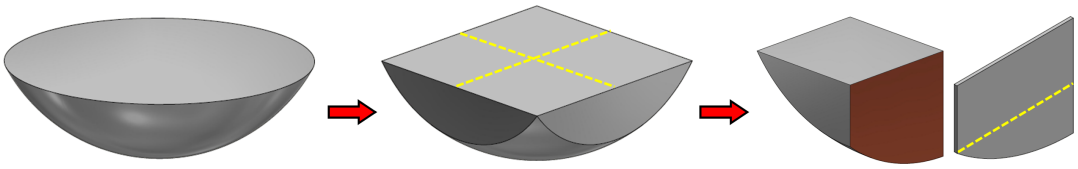


Figure 3.6: A schematic showing how foil samples were sectioned from a bulk Al-Pt-Er ingot. The as-cast ingot was cut by water jet as indicated by the yellow dashed lines, and sectioned using a diamond wheel blade to produce foil samples.

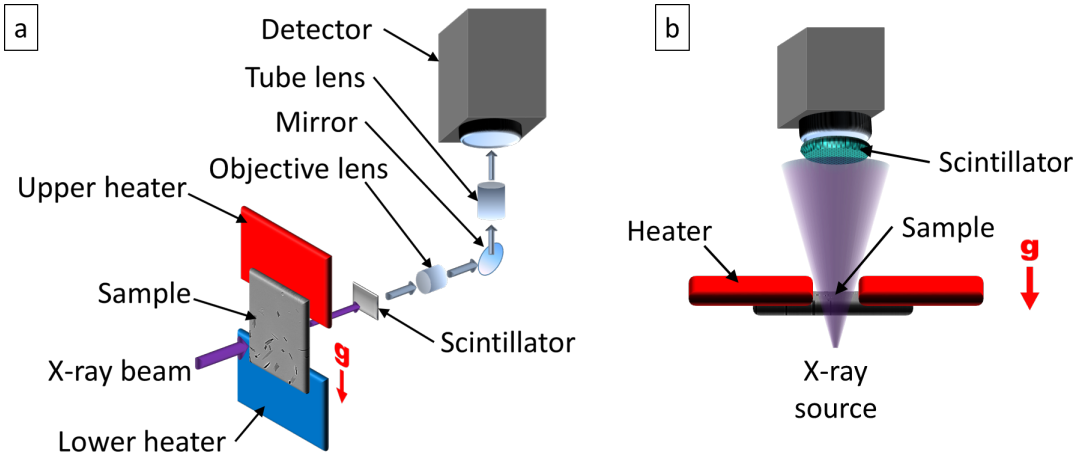


Figure 3.7: Schematic of experimental configurations for (a) synchrotron radiography experiments where gravity was parallel to the sample surface, and the incident X-ray was a parallel beam, and (b) laboratory radiography experiments where gravity was perpendicular to the sample surface, and the incident X-ray was a cone beam.

3.3 *In-situ* X-ray radiography

In-situ X-ray radiography experiments were conducted in two configurations: vertical solidification at synchrotrons and horizontal solidification using a laboratory apparatus, as shown in Figs. 3.7(a) and (b) respectively. Horizontal solidification offered the advantage of significantly reduced liquid convection, similar to micro-gravity conditions [80], and is a configuration generally not available at synchrotrons.

3.3.1 Solidification rigs

Two solidification rigs were designed and built in the group specially for *in-situ* X-ray radiography studies. Table 3.1 summarises the key technical information of the two rigs.

Rig	Furnace	Heating element	Maximum cooling rate (Ks^{-1})	Maximum temperature (°C)	Atmosphere
1st	Bridgman	Ni-Cr	2	850	Air
2nd	Bridgman	Poly graphite	28	1400	Controlled Ar

Table 3.1: A summary of key features of the two solidification rigs used for synchrotron X-ray radiography.

First generation rig

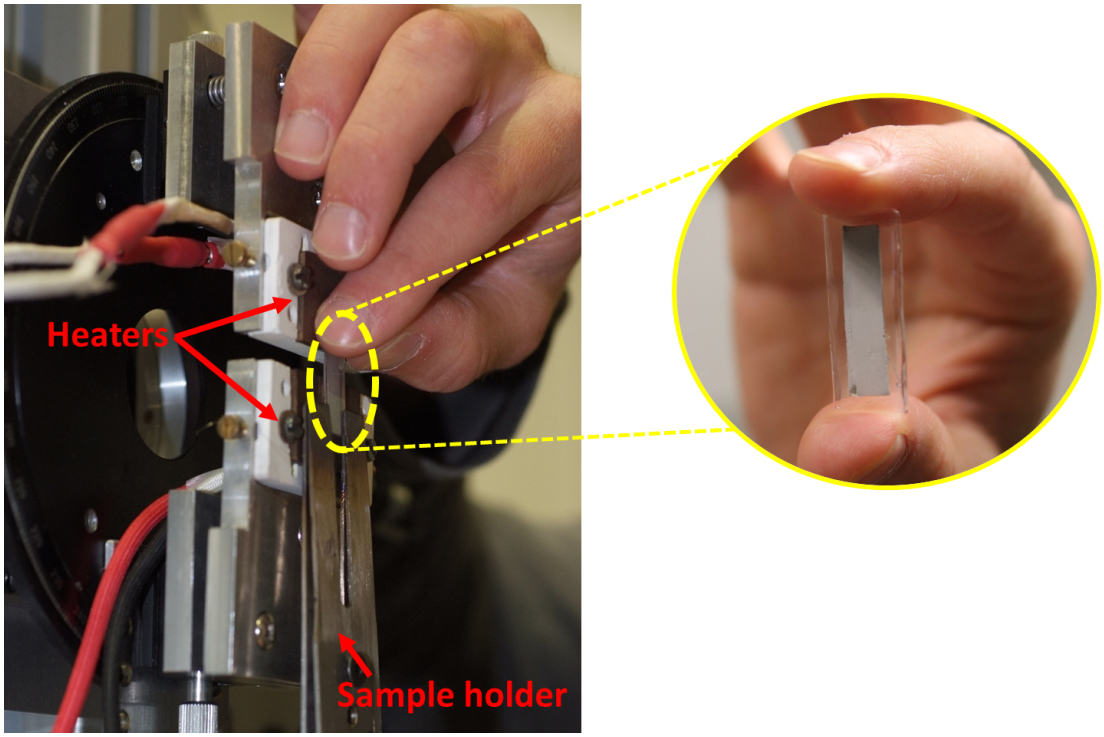


Figure 3.8: A photo of a sample being mounted onto the first-generation Bridgman solidification rig.

This solidification rig was used for synchrotron experiments carried out at beamline B16, DLS. A comprehensive description of the rig was given by Liotti *et al.* [95, 96]. Briefly, the rig consisted of a Bridgman furnace with two vertically

aligned resistance plate heaters with an adjustable gap through which the X-ray beam passes (Fig. 3.8). The heaters utilised Ni-Cr resistance wires as heating elements, which were embedded in a high-temperature cement substrate with a 1 mm bronze plate mounted on the top surface (to be in contact with the sample cell) to help provide a uniform heating zone. The encapsulated sample described in Section 3.2 was positioned in contact with both heaters so that heating and cooling of the sample was realised via thermal conduction from the heaters. During experiments, the entire rig was controlled remotely via a National Instruments module connected to a PC. The temperature of the two heaters was controlled independently by a PID algorithm. K-type thermocouples were embedded in the central heating zone of the heaters to serve as input for the PID temperature regulation. The maximum achievable cooling rate of the heaters was 2 Ks^{-1}, and the maximum achievable temperature was 850°C. The rig was operated in air.

Second generation

This solidification rig was used for synchrotron experiments at beamline ID19, ESRF, and at beamline Psiche, SOLEIL. The author participated in designing and building the rig as a member of a team of four people.

Fig. 3.9 shows a photo of the rig with the front lid removed to show the interior. The rig contained two vertically aligned poly graphite plate heaters encapsulated in poly BN, which were fabricated via chemical vapour deposition by Thermic Edge Ltd. Special care was taken when mounting the heaters in order to minimise heat loss. This included using ceramic bolts and ceramic spacers between the heater and the stainless steel support structure (on the back) to avoid direct contact. The gap between the two heaters through which the X-rays passed could be adjusted by rotating the knob at the top of the rig. Each sample cell was mounted onto a spring steel sample holder using high temperature cement

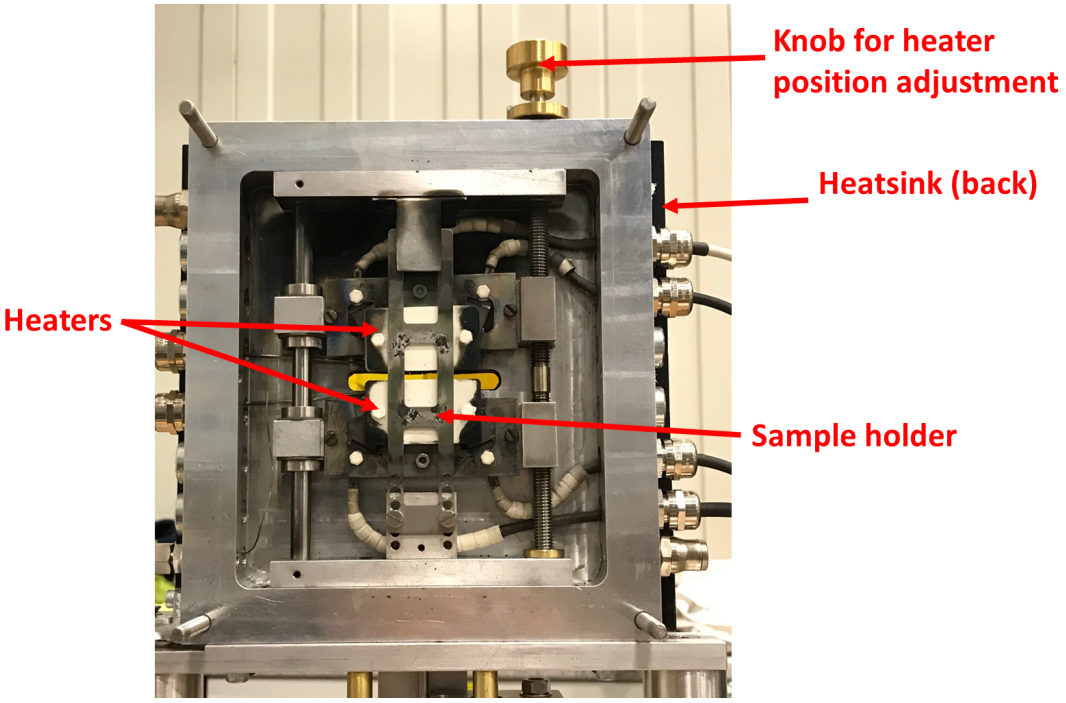


Figure 3.9: A photo of the second-generation Bridgman solidification rig for *in-situ* synchrotron X-ray radiography experiments. The front plate has been removed to show the interior.

and attached in close contact with both plate heaters. The chamber utilised a 25μm thick X-ray transparent Kapton thermal insulating film as the window material in the X-ray path. The solidification rig was controlled remotely by the same software as the first generation rig. The two heaters were also controlled separately by a PID algorithm, with temperature of each heater monitored by a K-type thermocouple mounted in the centre of the heating zone at the back of the heater. The maximum achievable cooling rate and temperature of the heaters were 28 Ks^{-1} and 1400°C respectively. The rig was operated with a controlled Ar atmosphere in the chamber, in order to protect the samples, glassy carbon sample cells and the heating elements from oxidation.

3.3.2 Experimental set-up

This section details the set-up of the four experimental campaigns in terms of the X-ray and solidification parameters. Table 3.2 summarises the key radiogra-

phy set-up of the four campaigns and Table 3.3 summarises all the solidification conditions and the number of repeat experiments in each condition.

Campaign	**NTNU**	**DLS**	**ESRF***	**ESRF****	**SOLEIL**
Source	Mo micro-focus	Bending magnets	Undulator	Wiggler	Wiggler
Beam	C, W	P, M	P, W	P, W	P, W
Peak energy (keV)	17.4	18	19	89	89
Scintillator	CsI	$CdWO_4$	LuAG:Ce	LuAG:Ce	LuAG:Ce
Camera	Vosskuhler DXI-11000	PCO.Edge	PCO.Edge	PCO.Edge	PCO.Edge
Temporal resolution (Hz)	2	7.5	10	10	Variable
Image pixel size (μm/pixel)	1.5	1.65	2.2	3.1×2.2	4.349×3.075
Sample-beam angle	90°	90°	90°	45°	45°
FoV (mm^2)	3×2	4×3	4×3	6×3	9×3

Table 3.2: A summary of radiography set-up of the four campaigns. C = cone beam, P = parallel beam, W = white beam, M = monochromatic beam. For experiments in SOLEIL, a variable temporal resolution of 10 HzK^{-1} (10 frames per degree of cooling, e.g. 1 Hz for cooling rate of 0.1 Ks^{-1}) was used to adapt to the wide range of cooling rate. * Al-3Fe alloys. ** Al-23Pt-20Er alloys.

Alloy			**Direction**	G_z	$\dot{T}$ (Ks^{-1})										**Campaign**
Name	Composition	Inoculation		($K\,mm^{-1}$)	0.1	0.2	0.5	0.6	1	2	4	8	15	28	
0.8Fe	Al-10Cu-0.8Fe	-	V	3	-	4	-	3	2	-	-	-	-	-	DLS
0.8Fe-GR	Al-10Cu-0.8Fe	TiB_2	V	3	-	4	-	2	2	-	-	-	-	-	
1.5Fe	Al-10Cu-1.5Fe	-	V	3	4	7	-	6	3	-	-	-	-	-	
1.5Fe-GR	Al-10Cu-1.5Fe	TiB_2	V	3	-	3	-	3	2	2	-	-	-	-	
AF	Al-3Fe	-	H	≈0	-	-	4	-	4	4	-	-	-	-	NTNU
AF-B	Al-3Fe	TiB_2	H	≈0	-	-	3	-	3	3	-	-	-	-	
AF-C	Al-3Fe	TiC	H	≈0	-	-	3	-	4	6	-	-	-	-	
AF	Al-3Fe	-	V	5	-	-	2	-	2	2	2	-	-	-	ESRF
AF-B	Al-3Fe	TiB_2	V	5	-	-	2	-	1	2	2	-	-	-	
AF-B	Al-3Fe	TiB_2	V	8	-	-	1	-	2	2	2	-	-	-	
APE	Al-23Pt-20Er	-	V	≈0	-	-	1	-	1	1	1	-	-	-	ESRF
APE-B	Al-23Pt-20Er	TiB_2	V	≈0	-	-	2	-	3	3	2	-	-	-	
APE	Al-23Pt-20Er	-	V	≈0	3	-	2	-	3	4	5	2	-	2	SOLEIL
APE-B	Al-23Pt-20Er	TiB_2	V	≈0	1	-	1	-	1	4	3	2	1	3	

Table 3.3: A summary of experimental conditions for all four radiography campaigns and the number of repeat experiments under each condition. Compositions are in wt%. G_z is the thermal gradient in the sample during solidification, and $\dot{T}$ is the cooling rate. In 0.8Fe-GR and 1.5Fe-GR, 0.1 wt% of Al-5Ti-1B was added to each bulk casting. In AF-B and APE-B, 0.5 wt% of Al-5Ti-1B was added to each bulk casting. In AF-C, 0.5 wt% of Al-5Ti-0.2C was added to the bulk casting.

NTNU

Fig. 3.10 shows photos of the laboratory apparatus. It comprises a micro-focus Mo-anode X-ray tube, a Bridgman solidification furnace (XRMON-GF), and a CCD camera (Vosskuhler DXI11000) with a Scint-X CsI scintillator. More

detailed description of the apparatus can be found in [79, 80, 200–203]. The tube voltage and tube current were adjusted to 50 kV and 100 μA for good absorption contrast between the Fe-rich IMC paricles and the Al-rich liquid, and the sample-source and sample-detector distance were also set accordingly for the best compromise between magnification and frame rate. Radiography videos were recorded at 2 Hz with an image pixel size of approximately 1.5 μm/pixel. The image pixel size was calculated by moving the sample up or down by an accurately known distance via the control module while counting its displacement in pixels from the radiography video. The ultimate spatial resolution (i.e. the smallest feature able to be resolved, calculated according to [79]) as a function of the source spot size, scintillator resolution and magnification was approximately 5 μm.

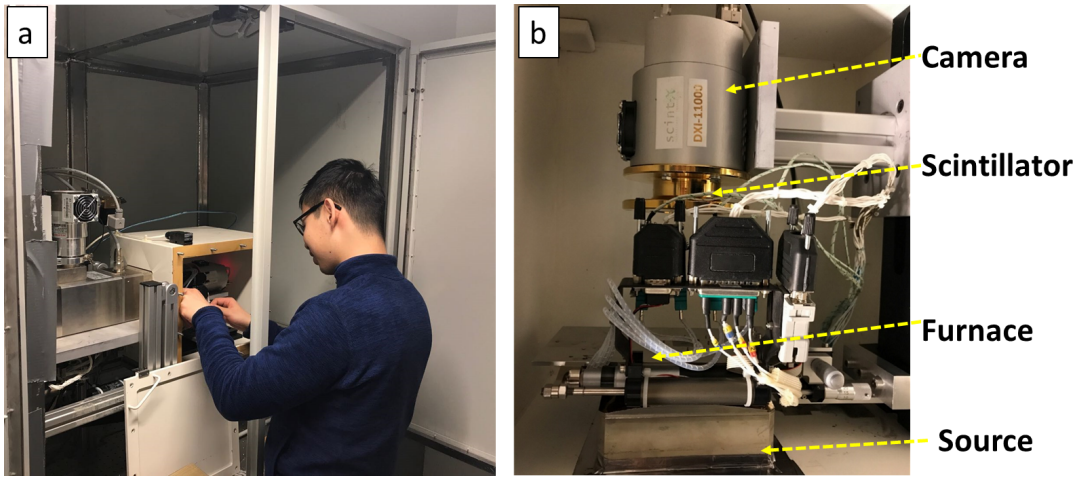


Figure 3.10: (a) A photo of the author adjusting the set-up of the laboratory apparatus for *in-situ* X-ray radiography of solidification at NTNU, Norway. (b) A photo of the XRMON-GF apparatus.

The *in-situ* radiography experiments on Al-3Fe (wt%) samples were performed in a N_2 atmosphere with the O_2 level measured consistently <1%, to protect both the sample and the glassy carbon cell from excessive oxidation. During the experiment, each sample was set in a horizontal position, i.e. with the flat surface of the sample perpendicular to gravity. Each sample was fully melted and held at 750°C for 3 min, following which it was cooled in a near-isothermal condition at

a constant cooling rate ranging from 0.5 Ks^{-1} to 2 Ks^{-1}. Overall, 34 experiments were carried out and in total 2725 IMC particles were studied.

Beamline B16, DLS

The incident X-ray was composed of a monochromatic beam of 18 keV, produced by bending magnets and a Ru/B_4C double multi-layer monochromator [204]. Transmitted X-rays through the sample were collected and converted into visible light by a 150 μm thick single crystalline $CdWO_4$ scintillator, following which the light was focused by a lens system onto a CMOS PCO.Edge camera. Radiography videos were recorded at a frame rate of 7.5 Hz with an image pixel size of 1.65 μm/pixel.

Each Al-Cu-Fe sample was fully melted and held isothermally at 750°C for 3 minutes, and then a constant pre-defined temperature gradient was applied by imposing a constant temperature difference between the two heaters, following which directional solidification from the bottom to the top was achieved by cooling both heaters at a constant rate (while maintaining the constant temperature difference between the heaters), through the alloy solidification temperature range. Fig. 3.11 shows an example of cooling curves of the two heaters during a typical solidification experiment.

Solidification experiments were performed on 1.5Fe, 0.8Fe, 1.5Fe-GR and 0.8Fe-GR alloys at cooling rates ranging from 0.1 Ks^{-1} to 2 Ks^{-1}. Overall, 203 IMC particles were studied in 47 experiments.

Beamline ID19, ESRF

Experiments at ID 19, ESRF were carried out on Al-Fe and Al-Pt-Er as specified in Fig. 3.1. Two sets of settings were employed.

For experiments using Al-3Fe (wt%), samples were illuminated with a white X-ray beam peaking sharply at 19 keV, produced by an X-ray undulator (U17.6, gap size 20 mm). The transmitted beam from the sample was collected by a

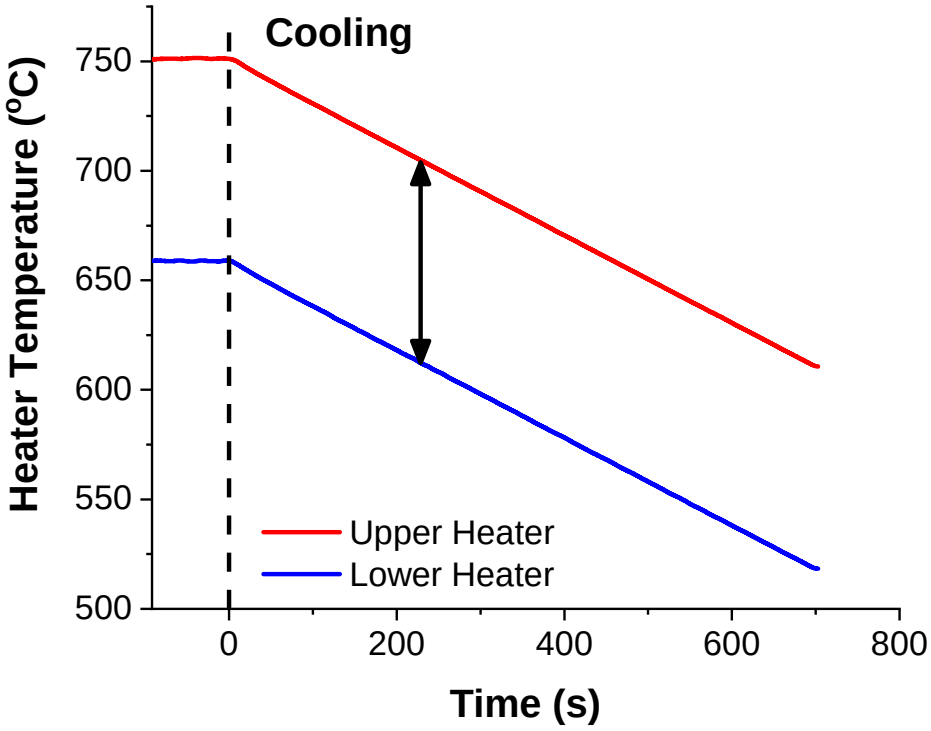


Figure 3.11: An example of cooling curves of the two heaters during a typical solidification experiment. A constant temperature difference was maintained between the two heaters while cooling both heater at a constant cooling rate to achieve directional solidification.

200 μm thick LuAG:Ce ($Lu_3Al_5O_{12}$:Ce) single crystal scintillator, which then projected the image onto a CMOS PCO.Edge 4.2 camera through a 3× objective lens system. Radiography videos were recorded at 10 Hz with an image pixel size of 2.2 μm/pixel.

Directional solidification from bottom to top was performed in a controlled Ar atmosphere at two different thermal gradients of $5\,\mathrm{K\,mm^{-1}}$ and $8\,\mathrm{K\,mm^{-1}}$, and four different cooling rates ranging from 0.5 $\mathrm{Ks^{-1}}$ to 4 $\mathrm{Ks^{-1}}$. Overall, 1893 IMC particles were studied in 22 experiments.

For experiments on the Al-Pt-Er alloys, the incident X-ray beam was a white beam peaking at 89 keV, generated via a wiggler at a gap size of 30 mm, while the scintillator, optics and the detector remained the same as above. In contrast to

the experiments on Al-Fe, where the incident X-ray beam was perpendicular to the sample surface, the Al-Pt-Er samples were positioned at 45° to the incident beam, to allow simultaneous collection of fluorescence signals alongside radiography. Radiography videos were recorded at 10 Hz with an image pixel size of 2.2 μm/pixel along vertical direction but an image pixel size of 3.1 μm/pixel along horizontal direction, because of the 45° angle between the incident beam and the sample.

Samples were heated to 1200°C when the alloy was fully melted and was held at the temperature for approximately 3 minutes. Solidification was then performed in an near isothermal condition, at cooling rates from 0.1 Ks^{-1} to 4 Ks^{-1}.

Psiche, SOLEIL

Investigation of the Al-Pt-Er alloys were repeated, following the same arrangements. The incident X-ray was a white beam peaking at the same energy of 89 keV. Radiography videos were recorded with an image pixel size of 3.075 μm/pixel along vertical direction and 4.349 μm/pixel along horizontal direction. A variable temporal resolution of 10 HzK^{-1} (10 frames per degree of cooling, e.g. 1 Hz for cooling rate of 0.1 Ks^{-1}) was used to adapt to the wide range of cooling rate. Solidification was again performed in a near-isothermal condition, but now at a wider range of cooling rates from 0.1 Ks^{-1} to 28 Ks^{-1}.

3.4 Data processing and data analysis

This section describes the procedure for processing the raw images from *in-situ* X-ray radiography and methods followed to analyse the radiographic images.

3.4.1 Image processing

Raw radiographic images obtained from both synchrotron and laboratory apparatus were often affected by sample surface defects and also variations in illuminating conditions arising from defects in the scintillator and/or optics. Therefore, the raw images were processed using Matlab scripts using a series of built-in functions. Table 3.4 summarises the steps of image processing for radiographic images from the four campaigns. The common steps included flat field correction, image filtering and normalisation of pixel intensity range. Figs. 3.12 to 3.16 present example radiographic images from each campaign to illustrate the image processing sequence.

Campaign	Image processing sequence
NTNU	**Flat fielding**, **Filtering**, **Intensity normalisation**
DLS	**Flat fielding**, De-banding, **Filtering**, **Intensity normalisation**
ESRF*	**Flat fielding**, **Filtering**, Image subtraction, **Intensity normalisation**
ESRF**	Image resize, **Flat fielding**, **Filtering**, **Intensity normalisation**
SOLEIL	Image resize, **Flat fielding**, **Filtering**, **Intensity normalisation**

Table 3.4: A summary of image processing sequences for radiographic images from the four campaigns. The bold text highlights the steps in common for all campaigns. * Al-3Fe alloys. ** Al-23Pt-20Er alloys.

Geometric correction

Geometric correction is the procedure to correct the distorted image given by the 45° sample-beam angle for radiographic images on the Al-Pt-Er from ESRF and SOLEIL. This step was performed by resizing the images along the horizontal axis, as shown in Fig. 3.15(b) and Fig. 3.16(b). This step was crucial for measurement of IMC growth.

Flat field correction

Variation in illumination was observed in radiographic images from all campaigns. Flat field correction was performed, where each image was divided by a

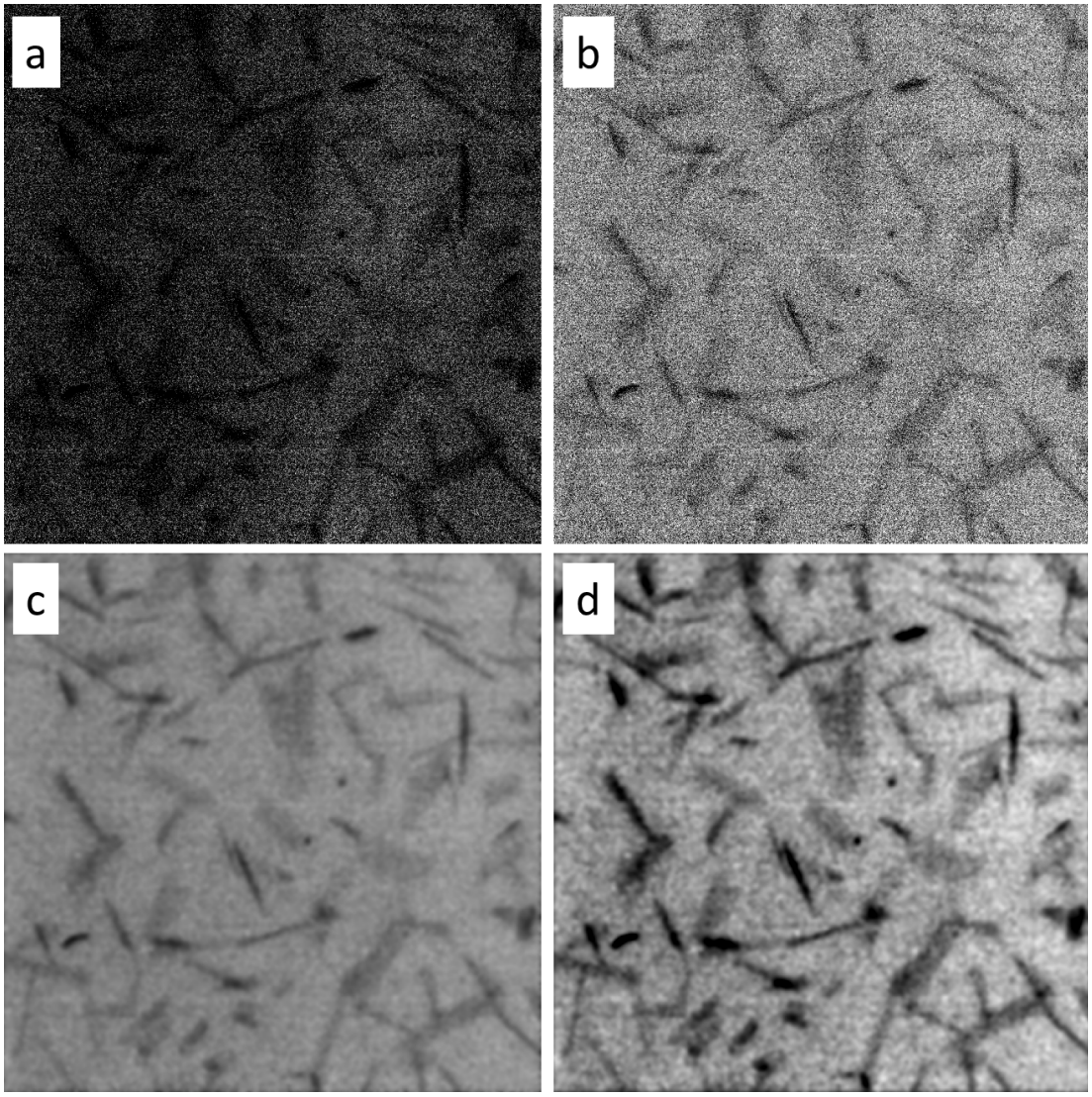


Figure 3.12: An example of image processing sequence for radiographic images from NTNU for Al-Fe. (a) Raw image. (b) Image after flat field correction. (c) Image after Wiener (11×11 pixels) filtering for noise reduction. (d) Image after normalisation of pixel intensity range.

flat image recorded when the sample was fully liquid. This step removed spatial variations in illumination that did not change with time and also static artefacts (Figs. 3.12(b), 3.14(b), 3.15(c) and Fig. 3.16(c)).

De-banding

While flat field correction successfully eliminated the variation in illumination on images from all the other three campaigns, it was not able to remove the inten-

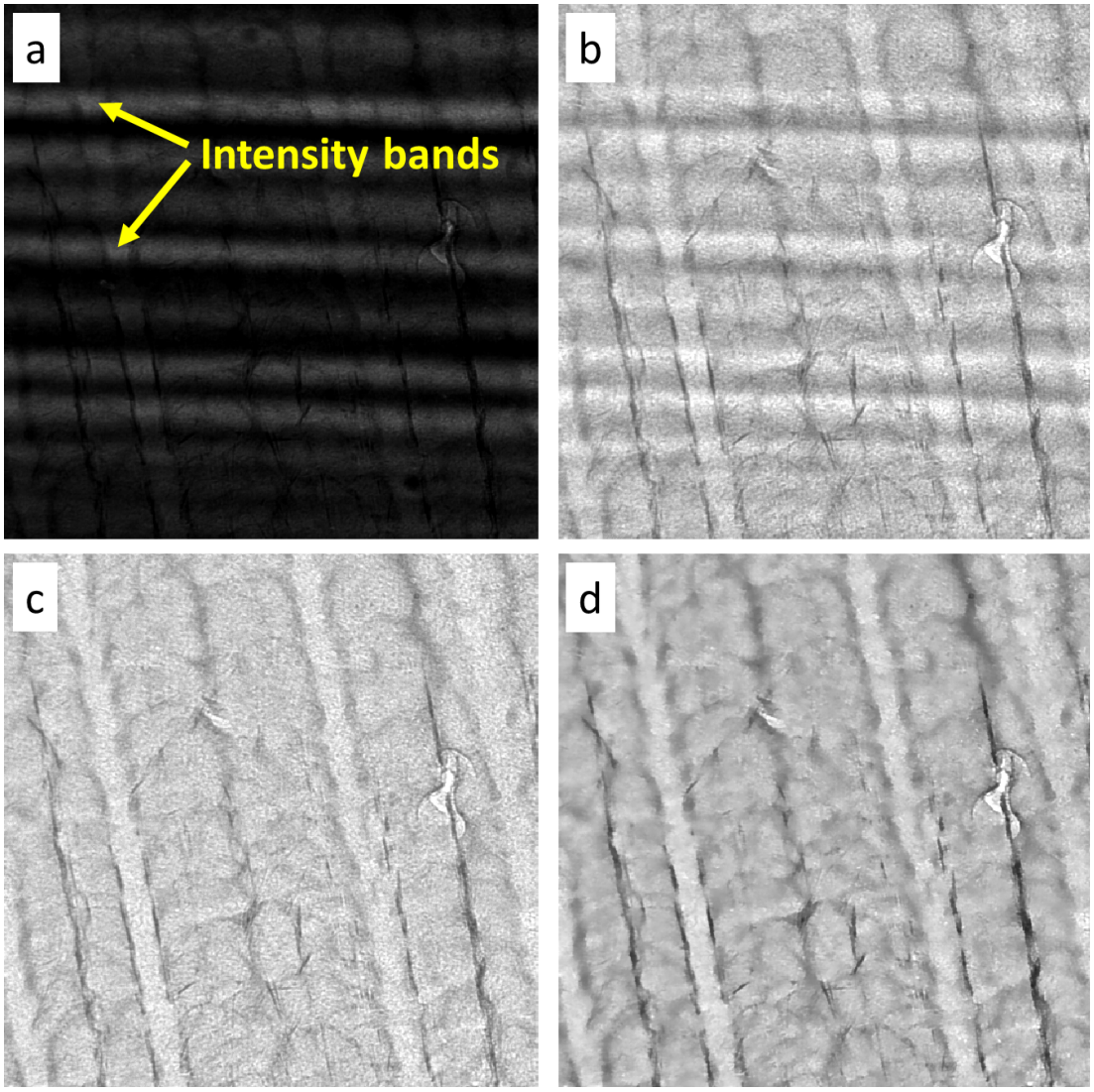


Figure 3.13: An example of image processing sequence for radiographic images from DLS for Al-Cu-Fe. (a) Raw image. (b) Image after flat field correction. (c) Image after de-banding codes were applied. (d) Final image after Wiener filtering (5×5 pixels) for noise reduction and normalisation of pixel intensity range.

sity bands present on the images from DLS (Fig. 3.13(b)). This was because these intensity bands were not static with time and they arose from irregular vibration of beam intensity due to irregular phase shifts in the reflected monochromatic beam caused by imperfections in the double multilayer monochromator [205]. To eliminate these irregular intensity bands, de-banding codes were applied on a per image basis (Fig. 3.13(c)), where each image frame was divided by its own background derived from a spatial Gaussian filter with a large rectangular kernel of

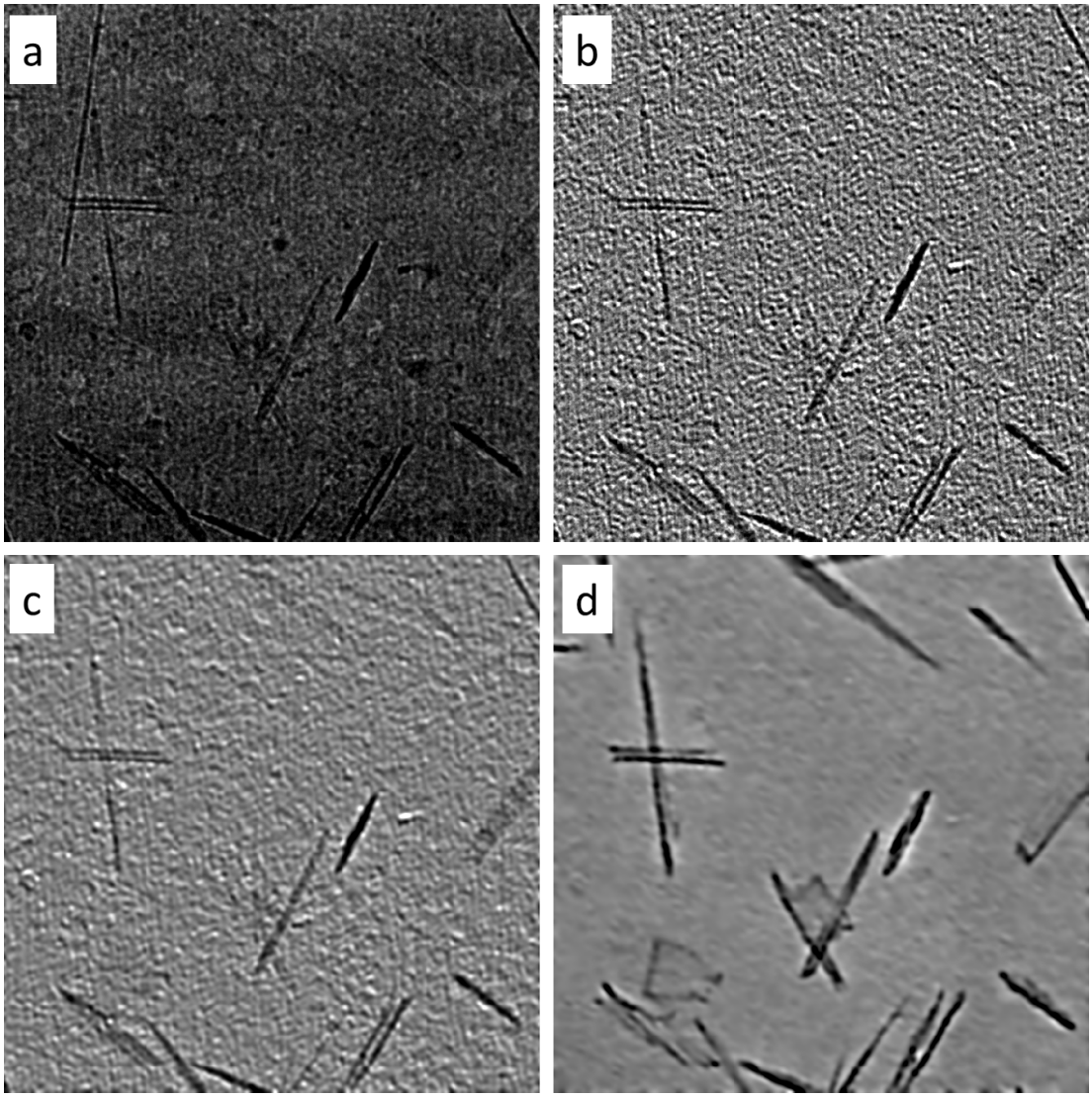


Figure 3.14: An example of image processing sequence for radiographic images from ESRF for Al-Fe. (a) Raw image. (b) Image after flat field correction. (c) Image after Wiener filtering (5×5 pixels) for noise reduction. (d) Final image after subtraction with the image 15 frames before it and normalisation of pixel intensity range to further enhance the image quality and the visibility of the IMCs.

approximately 5×200 pixels.

Image subtraction

In some image sequences from ESRF for Al-Fe, the image quality was degraded by the presence of phase contrast of the sample surface (Figs. 3.14(a) to (c)). Therefore, image subtraction was performed (Fig. 3.14(d)) on each frame of

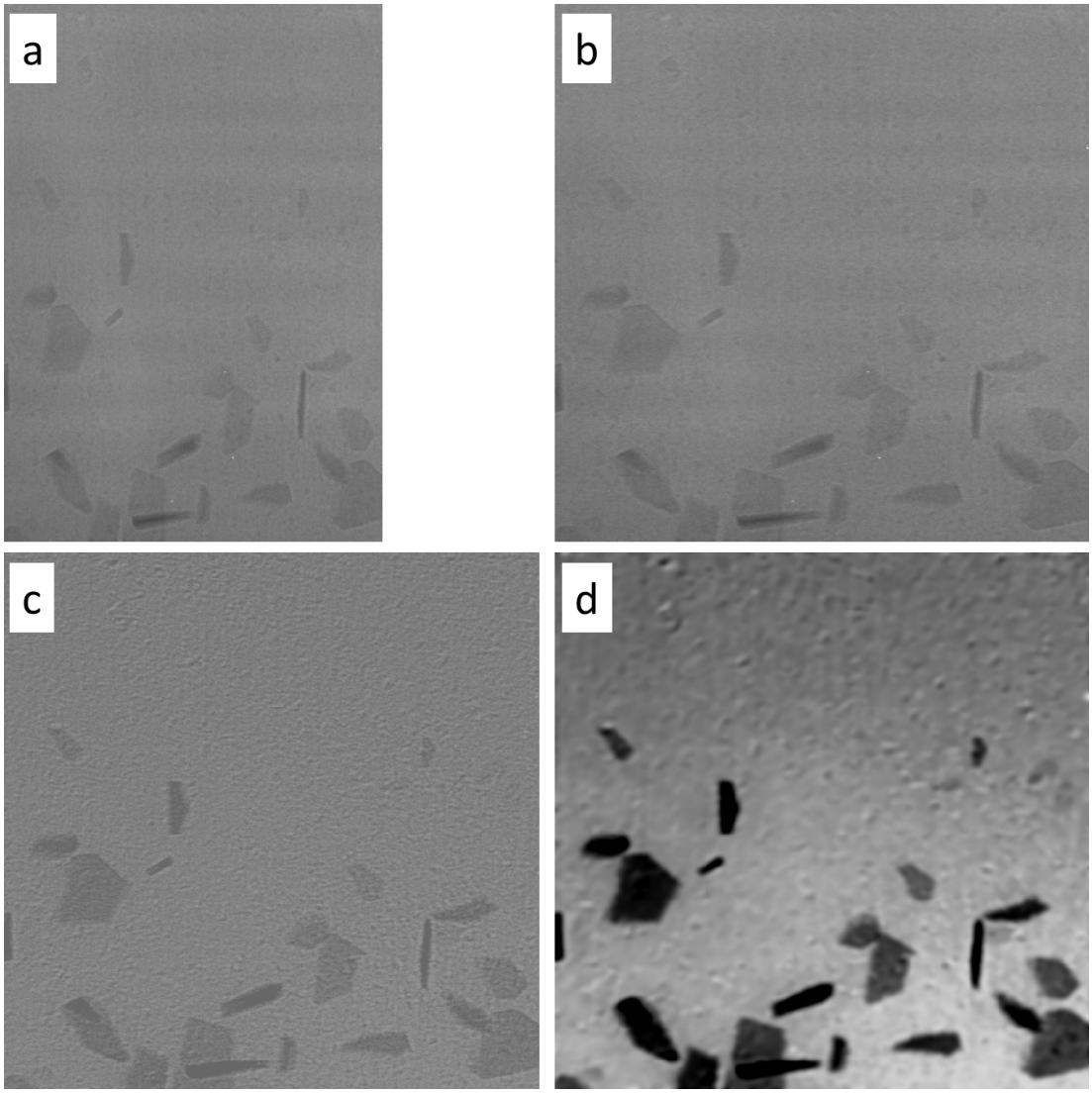


Figure 3.15: An example of image processing sequence for radiographic images from ESRF for Al-Pt-Er. (a) Raw image. (b) Image after geometrical correction was performed by resizing (a) along the horizontal axis to correct the distorted image pixel due to the 45° sample-beam angle. (c) Image after flat field correction. (d) Final image after Gaussian filtering (3×3 pixels) for noise reduction and normalisation of pixel intensity range.

these image sequences to facilitate time-resolved counting of IMC formation. In the example in Fig. 3.14, each frame was subtracted by an image 15 frames before it to enhance the image quality and the visibility of the IMCs.

Filtering and intensity normalisation

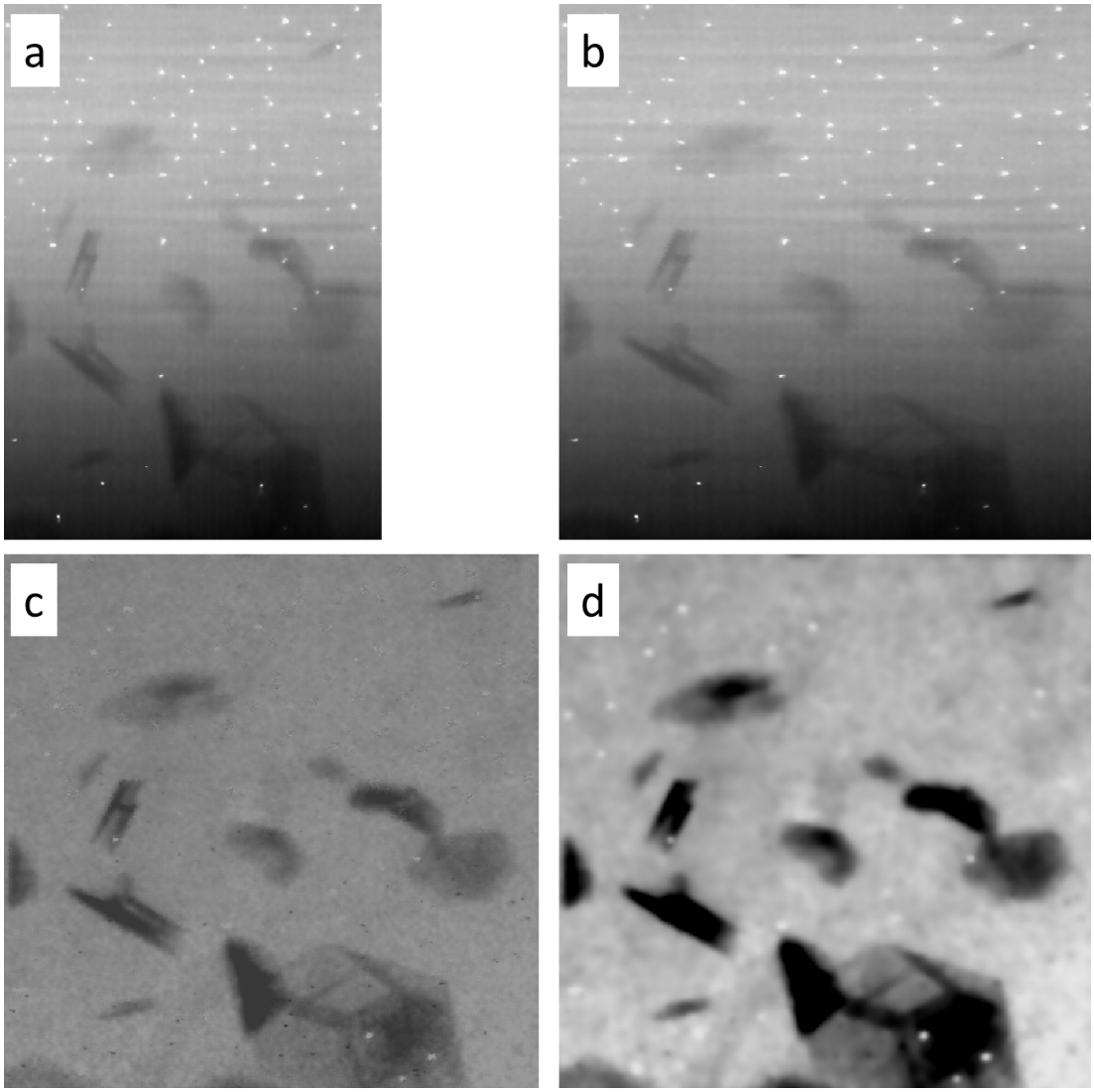


Figure 3.16: An example of image processing sequence for radiographic images from SOLEIL for Al-Pt-Er. (a) Raw image. (b) Image after geometrical correction. (c) Image after flat field correction. (d) Final image after Gaussian filtering (5×5 pixels) for noise reduction and normalisation of pixel intensity range.

Finally a spatial filter with a small square kernel was applied on images from all the campaigns for noise reduction, and the pixel intensity range in each image was normalised to enhance the image contrast.

3.4.2 Data analysis

Fig. 3.17 reproduces Fig. 3.1 and summarises the measurements and data analysis for each of the three alloy systems. These included tip temperature estimation

for secondary Fe-rich IMCs and estimation of number of branching points in inter-dendritic channels in Al-Cu-Fe, counting of formation events and estimation of formation temperature and formation undercooling of primary Fe-rich IMCs in Al-Fe, and measurement of growth of primary and secondary IMCs in all the alloys.

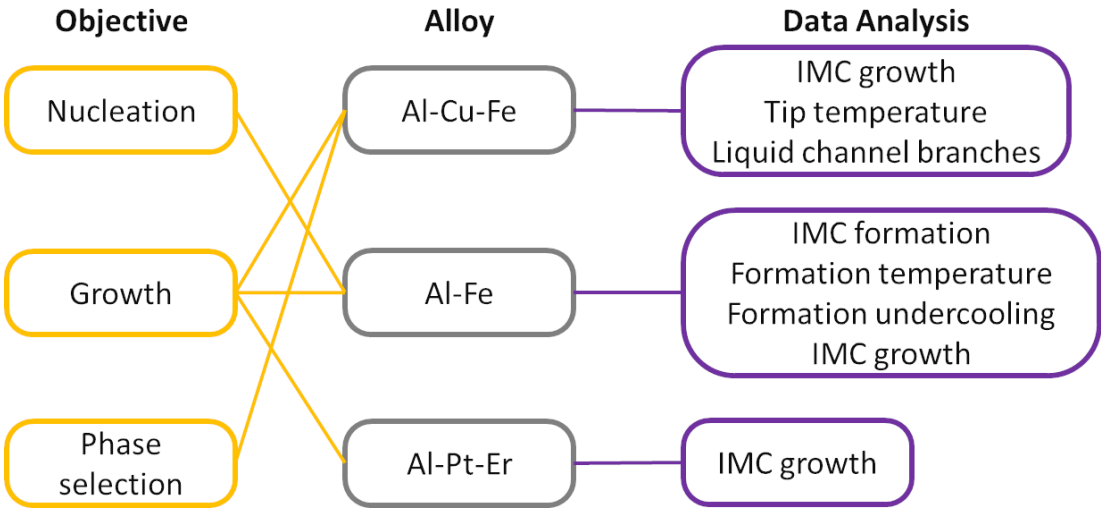


Figure 3.17: A diagram summarising the measurements and data analysis, relating to the overall research objectives and the different alloys.

3.4.2.1 Tip temperature estimation for secondary Fe-rich IMCs

During directional Al-Cu-Fe alloy solidification experiments, two K-type thermocouples were used to monitor the temperature of the two heaters. However the precise temperature in the sample itself was not available. Therefore, a method was developed that allowed estimation of the temperature at any point in the field of view [206]. It was assumed that for steady-state dendritic growth, constitutional supercooling at the dendrite tip was negligible. Thus, primary α-Al dendrite tips were considered always to be growing (from bottom to top) at the alloy liquidus temperature T_L. Therefore the α-Al dendrite tip with a well-defined front was used as an *in-situ* temperature reference.

Figs. 3.18(a) and 3.18(b) show two radiographs taken from the solidification

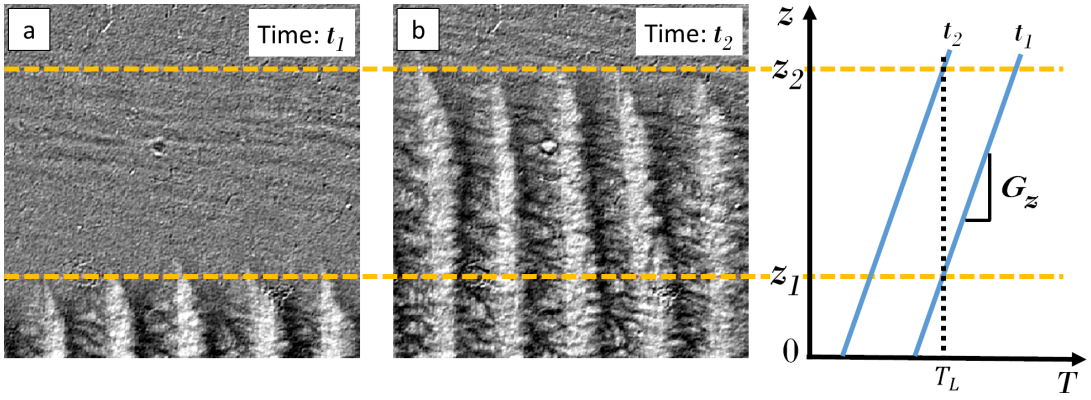


Figure 3.18: Radiographs of 0.8Fe at 0.2 Ks^{-1} and a schematic showing how the temperature field was estimated.

of 0.8Fe. Time $t = 0$ was set when the α-Al dendrite tips first appeared at the bottom of the field of view at vertical height $z = 0$. At time $t = t_1 > 0$, the α-Al dendrite tips were at position $z = z_1$ with a dendrite tip temperature of $T(z_1, t_1) = T_L$. At $t = t_2 > t_1$, the dendrite tips had grown upwards to position z_2, and the temperature at z_2 was $T(z_2, t_2) = T_L$, while the temperature at z_1 had reduced to $T(z_1, t_2) = T_L - \dot{T}(t_2 - t_1)$.

The 1-D temperature gradient in the z direction G_z, where G_z is positive along positive z direction, was therefore given by:

$$G_z = \frac{T(z_2, t_2) - T(z_1, t_2)}{z_2 - z_1} = \frac{T_L - \left[T_L - \dot{T}(t_2 - t_1)\right]}{z_2 - z_1} = \frac{\dot{T}(t_2 - t_1)}{z_2 - z_1} \tag{3.1}$$

Thus, the temperature $T(z, t)$ at any vertical distance z in the field of view at time t was estimated by:

$$T(z, t) = T_L - \dot{T}t + G_z z = T_L + \dot{T}\left[\frac{z}{z_2 - z_1}(t_2 - t_1) - t\right] \tag{3.2}$$

Consequently $T(z, t)$ was independent of the absolute heater temperatures, and dependent only on the differential of the temperature with respect to time i.e. the cooling rate, which was accurately controlled. By assuming there were

no temperature gradients in directions normal to the z direction, the positions of the IMC tip in each frame could directly be associated with an instantaneous temperature at that point. IMC tip position was tracked and recorded by eye directly from the radiographic image sequences for each of the different cooling rates in each of the alloy compositions using a mouse-click with a bespoke Matlab code. By tracking the position of individual IMC tips frame-by-frame this way and following the procedure of temperature calibration described above, the IMC tip temperature for every identified IMC tip in each image was estimated and recorded.

3.4.2.2 Estimation of branching points in interdendritic channels

The number of branching points in the inter-dendritic liquid channels in Al-Cu-Fe alloys was estimated to explore any correlation between the channel tortuosity and the tip temperature of secondary Fe-rich IMCs, and will be discussed in Chapter 4. The image (for example in Fig. 3.19(a)) was first binarised to separate the Al-rich dendrites and the Cu-rich inter-dendritic liquid channels, and an area opening function was then applied to compute the area (in pixels) of each component in the image and to remove small objects (e.g. artefacts) containing fewer than a defined number of pixels. This was followed by image skeletonisation which thinned the inter-dendritic channels to single pixel width inter-connected lines (Fig. 3.19(b)), and the branching points were counted (Fig. 3.19(c)). The only user defined variable in the code was the threshold of the number of pixels for the artefact-removal. This user defined threshold was varied to find the optimal setting, and this setting (30 pixels) was then applied across all image sequences. Thus, any systematic error would be applied equally to all images, and cross-comparisons, if not absolute quantification, could be usefully performed.

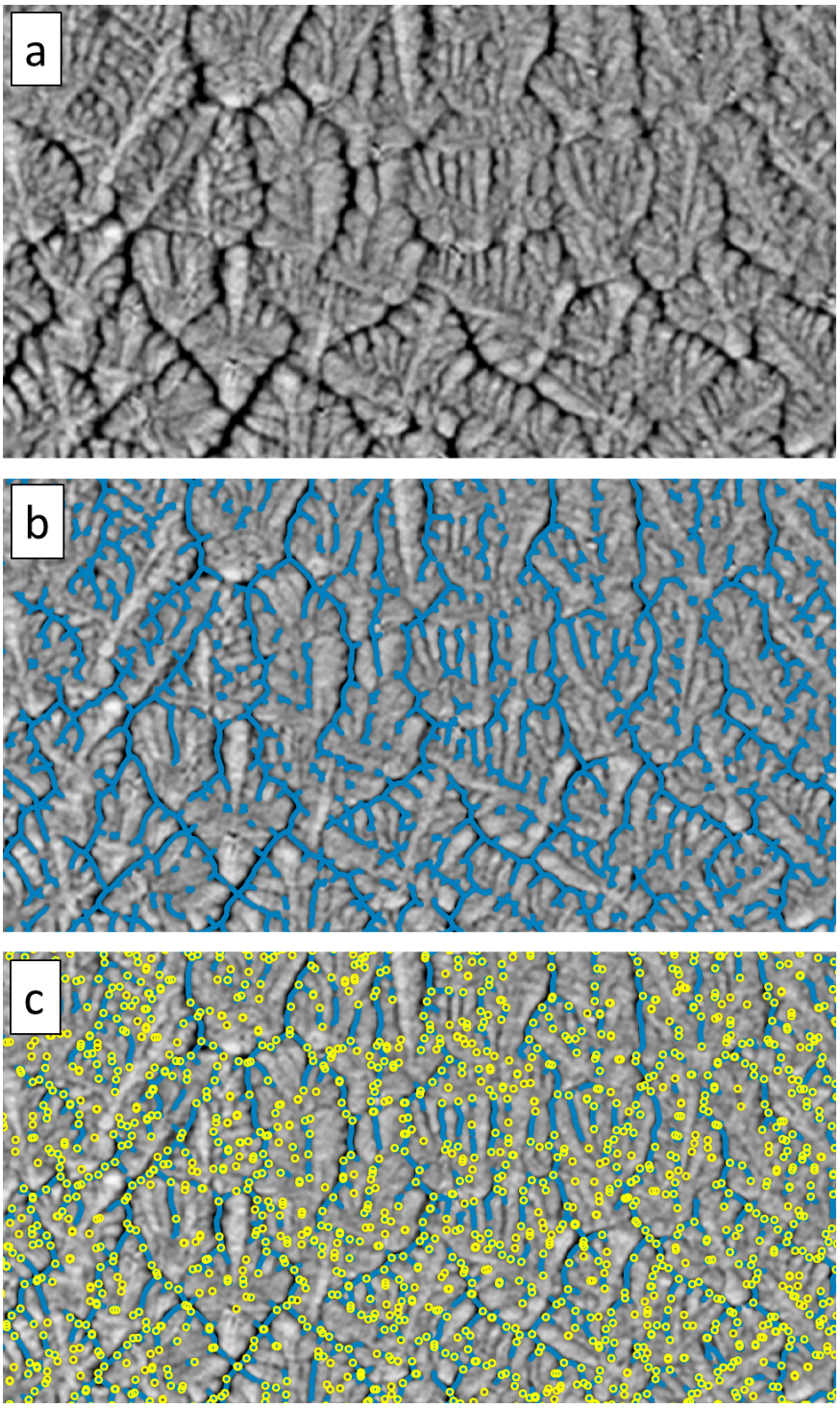


Figure 3.19: An example showing the key steps of the procedure to estimate the number of inter-dendritic channel branching points. (a) A radiograph of 0.8Fe-GR at the frame just before IMCs appeared. (b) Image after skeletonisation that thinned the inter-dendritic channels to single pixel inter-connected lines, superimposed on the radiograph. (c) Branching points were counted from (b) and superimposed on the image.

3.4.2.3 Formation of primary IMCs

By using a bespoke script in Matlab, the primary IMCs in Al-Fe alloys and Al-Pt-Er alloys in synchrotron radiography images were counted manually with a mouse-click frame by frame, from the instant they first appeared, and the positions in each frame were simultaneously recorded.

The total number of IMCs was obtained by summing the number of IMC formation events in each frame. By using this method, the total number of IMCs formed was not affected by any disappearance of the IMCs from the field of view due to settling. The number density of IMCs was calculated by dividing the total number of IMCs by the volume of the field of view in each experiment. Average IMC formation rate was therefore obtained by dividing the IMC number density by the duration of IMC formation (i.e. time between the first and last appearance of IMCs in the field of view).

For radiography images obtained from the lab apparatus at NTNU, due to the poorer image quality especially in the early stages of solidification (where contrast was poorer), it was not possible to measure time-resolved formation events. However as the samples were solidified horizontally, IMCs did not settle after formation. Therefore the total IMC formation events could be obtained by counting the final number of IMCs at the end of each solidification sequence. The total number density and the average formation rate were obtained following the same method.

3.4.2.4 Estimation of formation temperature of primary IMCs

Section 3.4.2.1 proposed the concept of estimating the secondary IMC tip temperature by using a well-defined solidification front with well-known equilibrium temperature as an *in-situ* reference. Based on this concept, a similar method was developed to allow estimation of formation temperature of primary IMCs in directional solidification of hypereutectic Al-3Fe (wt%), in this case by using the

eutectic front as a temperature reference.

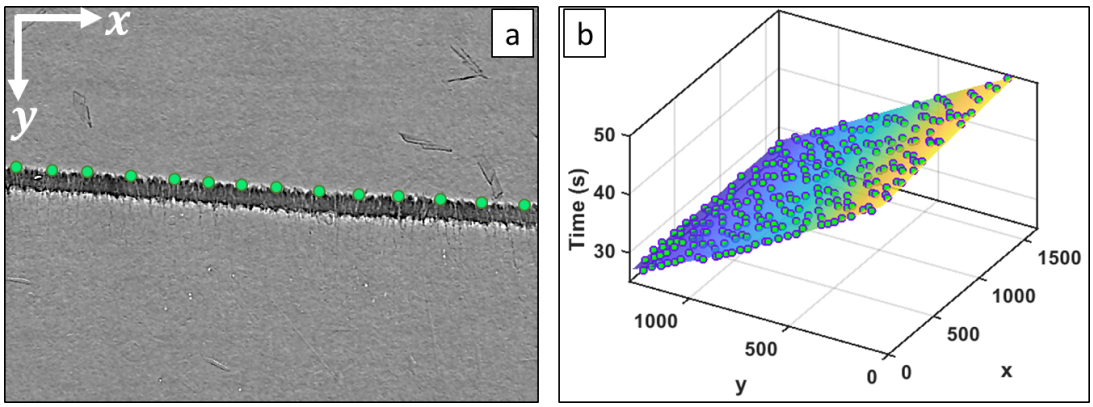


Figure 3.20: (a) A radiography image (subtracted from the image 8 frames before it) of AF-B at 1 Ks^{-1}, 8 $\mathrm{K\,mm}^{-1}$, showing the eutectic front near the middle of the field of view. Green markers were manually added frame by frame to track the position of this eutectic front. (b) A 3D scatter plot of time when eutectic appeared ($t = 0$ was set when primary IMC first appeared in the field of view) as a function of position (x, y), with a 2D surface best-fit, $R^2 = 0.999$.

First, the frame and position of first appearance of each IMC was recorded. Then, the eutectic front was employed as the *in-situ* temperature reference and its position was tracked frame by frame, by manually placing markers (10 to 15 markers per frame) by a mouse-click along the front (Fig. 3.20(a)). The coordinates (x, y) of each marker in each frame were recorded and a unique index number was assigned to each individual marker. Fig. 3.20(b) shows a 3D scatter plot of x, y and time of eutectic appearing at (x, y) ($t = 0$ was set when primary IMC first appeared in the field of view) of all the markers (average ~500 markers for each experiment). Following this a 2D surface best-fit was applied to the scatter plot (fitting quality of all 22 experiments was $R^2 > 0.99$), which gave a best-fit equation for time at which the eutectic appeared as a continuous function of position (x, y) in the field of view:

$$t(x, y) = ax + by + c \tag{3.3}$$

It was assumed that the undercooling at the eutectic front was negligible and

hence the eutectic front propagated at the equilibrium eutectic temperature of $T_E = 655°C$ (see the Al-Fe phase diagram in Fig. 1.3).

The position of first appearance of each IMC (X, Y) was then inputted into Eq. 3.3 which interpolated the time at which the eutectic front appeared at the same position (X, Y). The formation temperature of each IMC was therefore calculated by:

$$T_{IMC} = (t_E - t_{IMC}) \times \dot{T} + T_E \tag{3.4}$$

where $T_E = 655°C$ is the equilibrium eutectic temperature of the alloy, and t_{IMC} and t_E are the time at which the primary IMC and the eutectic appeared at the position (X, Y) respectively.

The error of this method was evaluated by calculating the maximum deviation between the interpolated time of eutectic appearance from Eq. 3.3 and the actual data (green dots in Fig. 3.20(b)), and converting this time error into a temperature error via the accurately known cooling rate. The resultant error in the estimated temperature was assessed to be within ± 1.6 K for all 22 experiments.

3.4.2.5 Estimation of formation undercooling for primary IMCs

If the temperature of formation can be estimated, then the formation undercooling might also be estimated. However, to calculate the formation undercooling of each individual IMC, one needs to know the instantaneous liquidus temperature i.e. the instantaneous liquid composition where each IMC was forming, because the liquid composition (and therefore the equilibrium liquidus temperature) changed with time as it became increasingly depleted of Fe as more and more primary IMCs formed i.e. the liquid composition tracks down the liquidus slope, as shown in Fig. 3.21. A speculative method was therefore developed that allowed an approximate estimation of the instantaneous liquidus temperature and therefore the formation undercooling of each primary IMC. The term

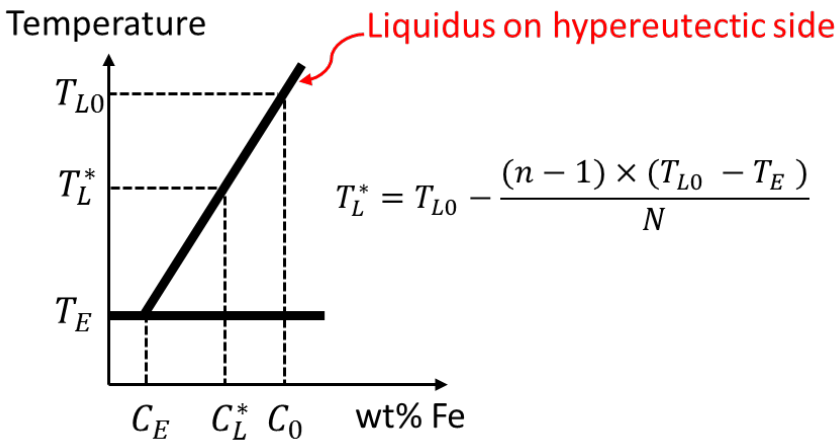


Figure 3.21: A schematic of the hypereutectic side of the Al-Fe phase diagram to illustrate the estimation of instantaneous liquidus temperature. C_0 is the initial alloy composition, C_E is the eutectic composition, and C_L^* is the instantaneous liquid composition when the nth IMC was forming. T_{L0}, T_E and T_L^* are the corresponding equilibrium (liquidus) temperature at C_0, C_E and C_L^* respectively. N is the total number of IMCs formed in the field of view in an experiment.

formation undercooling refers to the actual undercooling at which an IMC formed (presumably on a microscopic nucleant in the liquid).

First it was assumed that the liquid composition when the first IMC formed in the field of view was the initial alloy composition, corresponding to a liquidus temperature of T_{L0}, and that the liquid composition when the last IMC formed in the field of view was the eutectic composition, corresponding to a liquidus temperature of T_E (Fig. 3.21). Second by assuming that each IMC formation led to the same fractional decrease in Fe content in the liquid and thus a fractional change of the liquidus temperature of the remaining liquid, the instantaneous liquidus temperature when the nth IMC was forming could be estimated by:

$$T_L^* = T_{L0} - \frac{(n-1) \times (T_{L0} - T_E)}{N} \tag{3.5}$$

where $T_{L0} = 710°C$ is the equilibrium liquidus temperature of Al-3Fe, N is the total number of IMCs formed in the field of view in an experiment. Combining the estimated IMC formation temperature in Eq. 3.4 and the instantaneous liquidus

temperature in Eq. 3.5, the formation undercooling of each IMC was calculated by:

$$\begin{aligned}\Delta T_{IMC} &= T_L^* - \Big[(t_E - t_{IMC}) \times \dot{T} + T_E\Big] \\ &= T_{L0} - \frac{(n-1) \times (T_{L0} - T_E)}{N} - \Big[(t_E - t_{IMC}) \times \dot{T} + T_E\Big]\end{aligned} \tag{3.6}$$

The accuracy of the estimation method is therefore controlled by the validity of assumptions, and by the accuracy of determining the initial liquidus temperature of T_{L0}. This method implicitly assumes that the remaining liquid at any instant had a uniform composition. The extent to which the method gives useful insights is described following presentation of the results in Chapter 5.

3.4.2.6 Measurement of IMC growth

Growth of primary and secondary IMCs in all the alloys was measured by tracking the IMC tip (or the edge for primary IMCs) positions by eye, frame-by-frame using a mouse-click and a built-in Matlab function.

3.5 Electron microscopy

Scanning electron microscopy (SEM) in conjunction with energy dispersive X-ray spectroscopy (EDX), and transmission electron microscopy (TEM) were utilised to identify the different Fe-rich IMCs in solidified Al-Cu-Fe samples for each combination of: alloy composition, grain refiner additions and cooling rate, as obtained from *in-situ* radiography experiments at B16, DLS and/or prepared identically to the synchrotron solidification conditions. Electron backscatter diffraction (EBSD) was performed by collaborators at Imperial College London to identify growth twins in $Al_{13}Fe_4$ and $Al_{24}Pt_9Er_4$ crystals in solidified Al-Fe and Al-Pt-Er samples from synchrotron experiments.

3.5.1 SEM/EDX

To prepare samples for SEM and EDX, solidified foil samples were ground with SiC paper (1200, 2500 and 4000 grit) and subsequently polished with diamond suspension (3 μm and 1 μm). Each sample was then mounted on a standard 12.5 mm Al sample holder using an adhesive carbon disc.

SEM was performed in a JEOL JSM-5510 LV (Japan Electron Optics Ltd., Tokyo, Japan) at an acceleration voltage of 10 kV, beam spot diameter of 30 nm and working distance of 10 mm.

Composition measurements by EDX were performed at an acceleration voltage of 20 kV, beam spot diameter of 60 nm, working distance of 20 mm and live time of 100 s, using Kα fluorescence. Standardless K-line EDX analysis is generally accepted for major elements to have an accuracy of $\sim$1% [207].

3.5.2 TEM

To prepare the TEM samples, first discs of 3 mm diameter were punched from the SEM foil samples. The discs were then ground to $\sim$50 μm thick and polished to a surface finish of 1 μm. Precision ion polishing was then performed using a PIPS-II system (Gatan, Inc.) to further thin the sample down until a dimpled region was created and a small hole was generated in the centre with sufficiently thin edges for electrons to be able to penetrate.

TEM was performed in a JEOL-3000F (Japan Electron Optics Ltd., Tokyo, Japan) by a former group member. First bright field images were taken of IMCs and then high-resolution (HR-TEM) images of the lattice planes were acquired. HR-TEM images were analysed using Gatan Microscopy Suite (Gatan, Inc.), to fast Fourier transform (FFT) images to FFT patterns (reciprocal lattice). Then, inter-planar d-spacings were measured from the FFT patterns and compared with the d-spacings of the candidate IMCs as identified by SEM/EDX.

3.5.3 EBSD

To prepare samples for post-solidification EBSD, samples from synchrotron experiments were mounted in Struers VersoCit acrylic cold mounting resin and then ground to 4000 grit with SiC paper, followed by vibratory polishing on VibroMet^{TM} 2 with colloidal silica on a napped cloth.

For twinning identification, a Zeiss Sigma field emission scanning electron microscope fitted with a Bruker e-Flash high-resolution EBSD detector was used. The reference structures of $Al_{13}Fe_4$ [208] and $Al_{24}Pt_9Er_4$ [209] used for EBSD indexing are listed in Table 3.5. Bruker Esprit 2.0 software was utilised to analyse the orientations in twinned crystals. Unit cell wire frames were plotted from the Euler angles measured by EBSD.

Phase	**Space group**	**Pearson symbol**	**Lattice parameters**						**Ref.**
			a (Å)	b (Å)	c (Å)	α (°)	β (°)	γ (°)	
$Al_{13}Fe_4$	C2/m	mS102	15.492	8.078	12.471	90	108	90	[208]
$Al_{24}Pt_9Er_4$	$P\bar{1}$	aP37	7.475	7.475	13.067	101	95	60	[209]
	C2/m	mS25	7.462	4.313	13.044	90	101	90	

Table 3.5: Crystal structures and lattice parameters used to index the EBSD patterns for $Al_{13}Fe_4$ and $Al_{24}Pt_9Er_4$.

Chapter 4

Tip Temperature and Phase Selection of Secondary Fe-rich IMCs

4.1 Introduction

As seen in Chapter 2, X-ray radiography is used increasingly to study the solidification dynamics of Al alloys, for example to investigate crystal formation and fragmentation of primary α-Al dendrites [95, 96, 210], growth of secondary intermetallic compound (IMC) particles [49], growth [81] and fragmentation [99] of primary IMC particles, and bubble formation [211]. In all these studies, the temperature during the alloy solidification was measured indirectly by measuring the temperature of the heating element while the actual temperature in the sample was only inferred. While this issue may not be significant for qualitative studies of growth or fragmentation rate, it is crucial when studying strongly temperature-related phenomena such as nucleation, growth undercooling and phase transformations. In this chapter, the *in-situ* approach based on real-time X-ray radiography described in Chapter 3 was used to estimate the temperature at any time

and position in the radiography field of view and was applied to obtain tip temperatures of 203 secondary Fe-rich IMC particles during directional solidification of Al-Cu-Fe alloys, which showed significant tip undercoolings and different IMC phase selections.

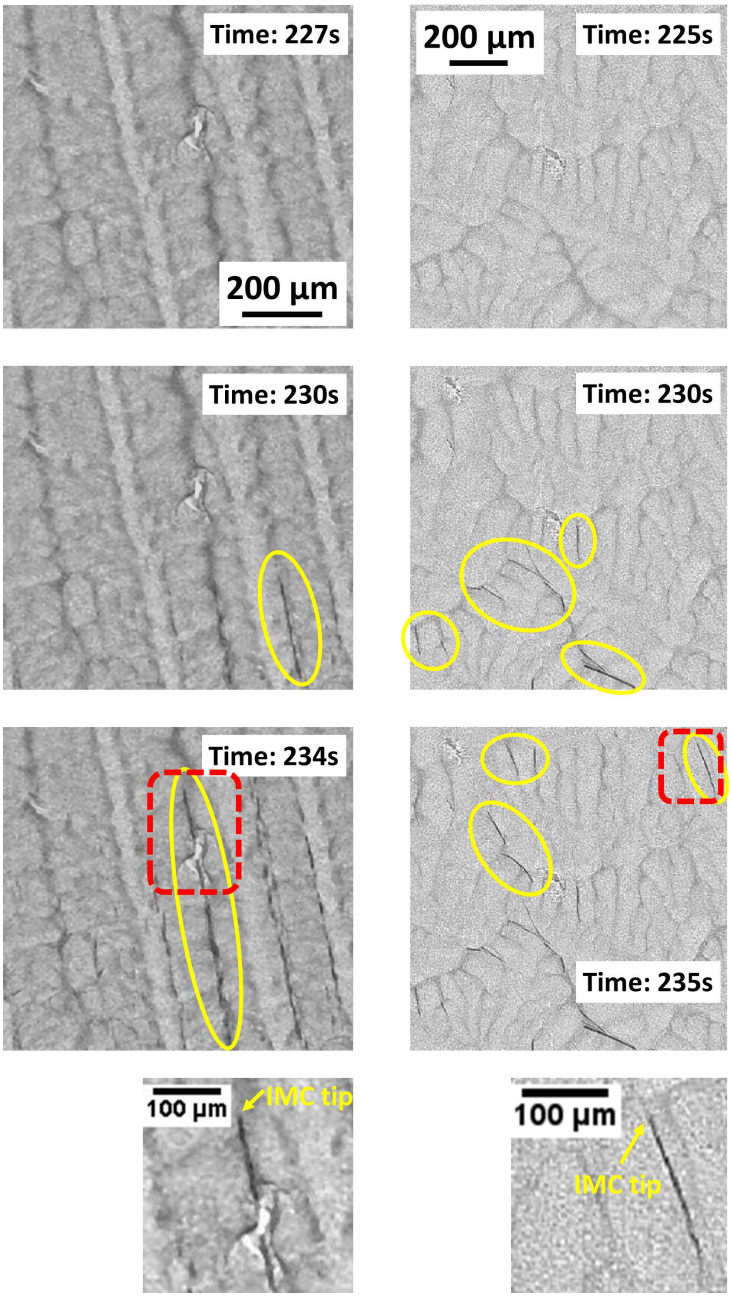
With real-time X-ray radiography and this *in-situ* temperature estimation approach, it will be shown how the different Fe-rich IMCs formed and grew at different tip undercoolings, the extent of which depended on cooling rate and grain refiner additions, which can affect the overall phase selection and final population of IMCs by affecting the inter-dendritic channel tortuosity.

4.2 Results

4.2.1 IMC tip temperature

Fig. 4.1(a) and 4.1(b) show representative example radiograph sequences of IMC growth in 0.8Fe and 0.8Fe-GR at 0.2 Ks^{-1} respectively. Without grain refiner in Fig. 4.1(a), the morphology of the α-Al primary phase was columnar because of the strong 1-D temperature gradient, growing bottom to top, and the IMCs grew along/in the inter-dendritic channels between columnar grains with a straight, needle-like morphology without branching. When grain refiners were added to the same alloy in Fig. 4.1(b), the α-Al primary phase became equiaxed (as intended) and the IMCs growing in the interdendritic channels necessarily branched to grow around grains, became shorter, and with IMC growth sometimes stopping and then re-nucleating nearby and continuing to grow.

Following the method described earlier in Section 3.4.2.1, Fig. 4.2 shows the IMC tip temperature versus cooling rate for 203 IMCs from all experiments. Non-grain refined 1.5Fe showed two clusters of IMC tip temperature at each cooling rate, suggesting the presence of two types of IMCs. The "high-T" IMC had a tip temperature of 614±6°C, 611±8°C, 614±5°C and 614±1°C, while the "low-



(a) Long IMCs **(b)** Short IMCs

Figure 4.1: Radiograph sequences of IMC growth at a cooling rate of 0.2 Ks^{-1} in (a) 0.8Fe and (b) 0.8Fe-GR, with zoomed-in images showing the IMC tips. Time $t = 0$ was set when the α-Al dendrite tips first appeared at the bottom of the field of view.

T" IMC had a tip temperature of 592±3°C, 589±5°C, 593±3°C and 592±2°C, as cooling rate increased from 0.1 Ks^{-1} to 1 Ks^{-1}. Thus within each of these populations, there was no significant variation in tip temperature with increasing

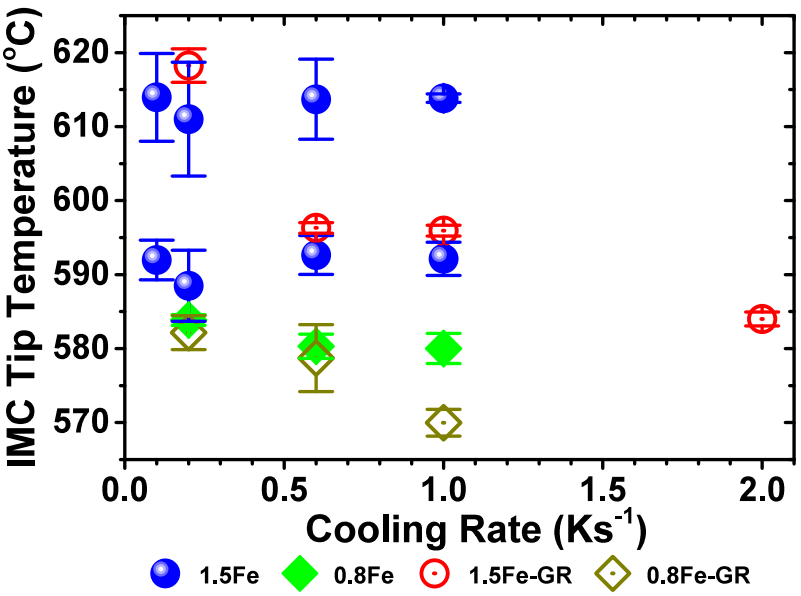


Figure 4.2: IMC tip temperature at different cooling rates for 1.5Fe, 0.8Fe, 1.5Fe-GR and 0.8Fe-GR.

cooling rate. The lower Fe concentration non-grain refined 0.8Fe showed a single range of IMC tip temperatures between 580°C and 585°C, regardless of cooling rate.

0.8Fe-GR showed an initial band of IMC tip temperatures in the range 580°C to 582°C at 0.2 Ks^{-1} and 0.6 Ks^{-1}, comparable with those of the non-grain refined 0.8Fe, but IMC tip temperatures then reduced to 570 °C when the cooling rate increased further to 1 Ks^{-1}. In contrast to its non-grain refined counterpart, which showed simultaneously two bands of IMC tip temperatures, 1.5Fe-GR showed only a narrow band of IMC tip temperatures at a given cooling rate, the mean of which decreased steadily with cooling rate, from ∼620 °C at 0.2 Ks^{-1} to ∼585 °C at 2 Ks^{-1}.

4.2.2 IMC identification

Because radiographic data could not provide sufficient contrast variations between IMCs to be used as a basis for phase identification, post-solidification microstructural analysis was conducted on samples prepared identically to those used in the

synchrotron experiments.

Table 4.1 summarises the number of IMC particles where EDX was performed and the number of EDX point measurements (in parenthesis) under each solidification condition.

Alloy	Cooling rate (Ks^{-1})				
	0.1	0.2	0.6	1	2
1.5Fe	4 (11)	6 (18)	5 (14)	5 (16)	-
1.5Fe-GR	-	5 (20)	4 (11)	4 (12)	5 (16)
0.8Fe	-	3 (8)	3 (7)	4 (9)	-
0.8Fe-GR	-	3 (5)	3 (5)	3 (7)	-

Table 4.1: A summary of the number of IMC particles identified using EDX and the number of EDX point measurements (in parenthesis) in each condition. Overall, 57 particles were analysed and 159 point measurements were performed.

In 1.5Fe, two different needle-like IMCs (A and B) formed at cooling rates between $0.2\,Ks^{-1}$ and $1\,Ks^{-1}$ (Fig. 4.3(a)), and these two populations correlated with the "high-T" and "low-T" IMCs in Fig. 4.2(b). Chemical composition measurements in Table 4.2 showed that high-T phase A contained 69 wt.% Al, 23 wt.% Fe and 8 wt.% Cu, corresponding to Al_6(Fe,Cu) (Al: 70 wt.%, Fe: 22 wt.%, Cu: 8 wt.%, Fe:Cu ratio: 2.8, [115, 159, 162]). Low-T phase B contained 54 wt.% Al, 14 wt.% Fe and 32 wt.% Cu corresponding to Al_7Cu_2Fe (Al: 51 wt.%, Fe: 15 wt.%, Cu: 34 wt.%, Fe:Cu ratio: 0.4). Composite particles of the two phases were also frequently observed in Al-10Cu-1.5Fe (Fig. 4.3(b)), with the lower temperature Al_7Cu_2Fe around the edge of the higher temperature Al_6(Fe,Cu) centre.

Phase	Element	Concentration (wt.%)	Fe:Cu ratio
A	Al	69	2.6-2.9
	Fe	23	
	Cu	8	
B	Al	54	0.4-0.5
	Fe	14	
	Cu	32	

Table 4.2: Chemical composition of IMC phases A and B. Standard deviation for each element concentration within ±1 wt.%.

1.5Fe-GR solidified at 0.2 to $1\,Ks^{-1}$ showed predominantly high-T Al_6(Fe,Cu),

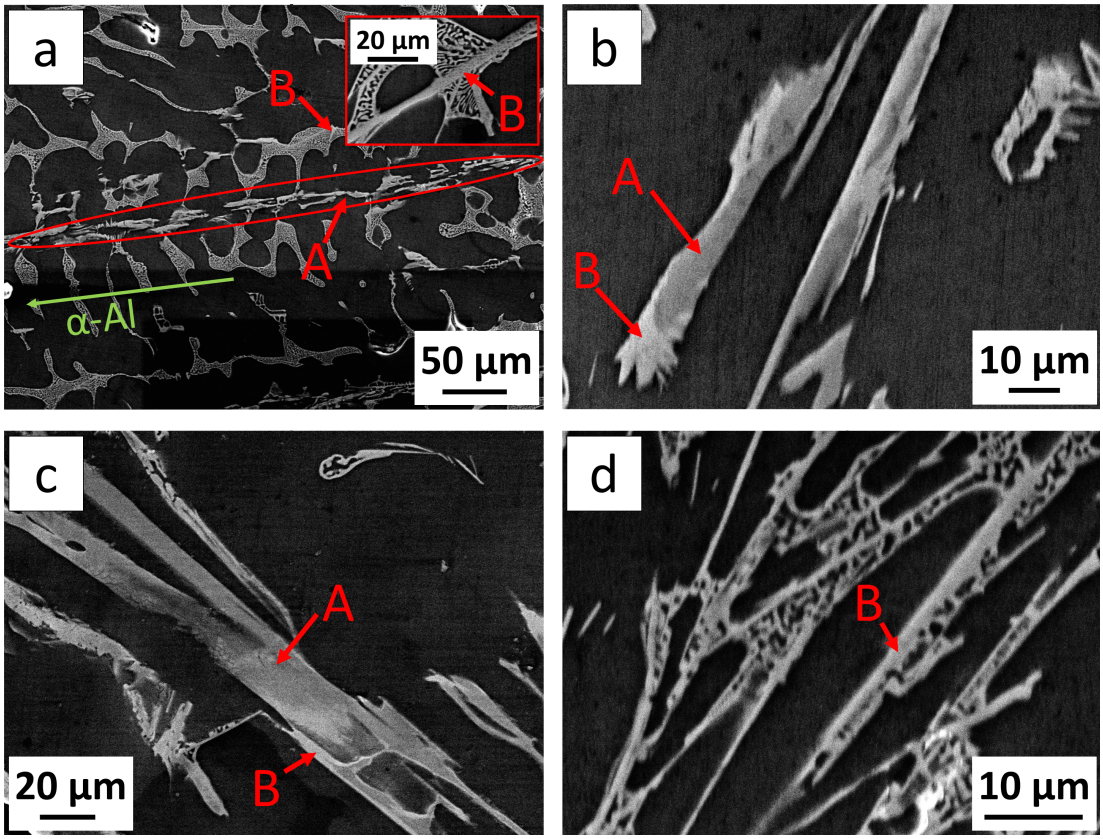


Figure 4.3: Secondary electron images of: (a) 1.5Fe showing presence of IMC A (in red ellipse), and IMC B (see inset image for detailed morphology) at $1\,\mathrm{Ks}^{-1}$, with green arrow indicating the orientation of the primary α-Al dendrites, (b) a composite IMC particle with IMC A in the centre and IMC B around the edge in 1.5Fe at $0.2\,\mathrm{Ks}^{-1}$, (c) IMC A particle with small regions near the edge transformed into IMC B in 1.5Fe-GR at $0.2\,\mathrm{Ks}^{-1}$, and (d) 1.5Fe-GR at $2\,\mathrm{Ks}^{-1}$ showing presence of IMC B only (IMC A: $Al_6(Fe,Cu)$; IMC B: Al_7Cu_2Fe).

with particles showing edge regions partially transformed or nucleating the low-T IMC Al_7Cu_2Fe (Fig. 4.3(c)). In contrast, the same 1.5Fe-GR solidified at the higher rate of $2\,\mathrm{Ks}^{-1}$ formed only low-T Al_7Cu_2Fe (Fig. 4.3(d)). By considering the tip temperature data in Fig. 4.2, this change in IMC phase population can be qualitatively correlated with the progressive decrease in the IMC tip temperature.

Figs. 4.4(a) and (c) show bright field TEM images of Al_7Cu_2Fe and $Al_6(Fe,Cu)$ respectively with yellow squares indicating the positions from which HR-TEM images in Figs. 4.4(b) and (d) were acquired respectively. Each of the HR-TEM images show the corresponding inset fast Fourier transform (FFT) patterns, and Table 4.3 lists the measured inter-planar d-spacings for the two IMCs, which were

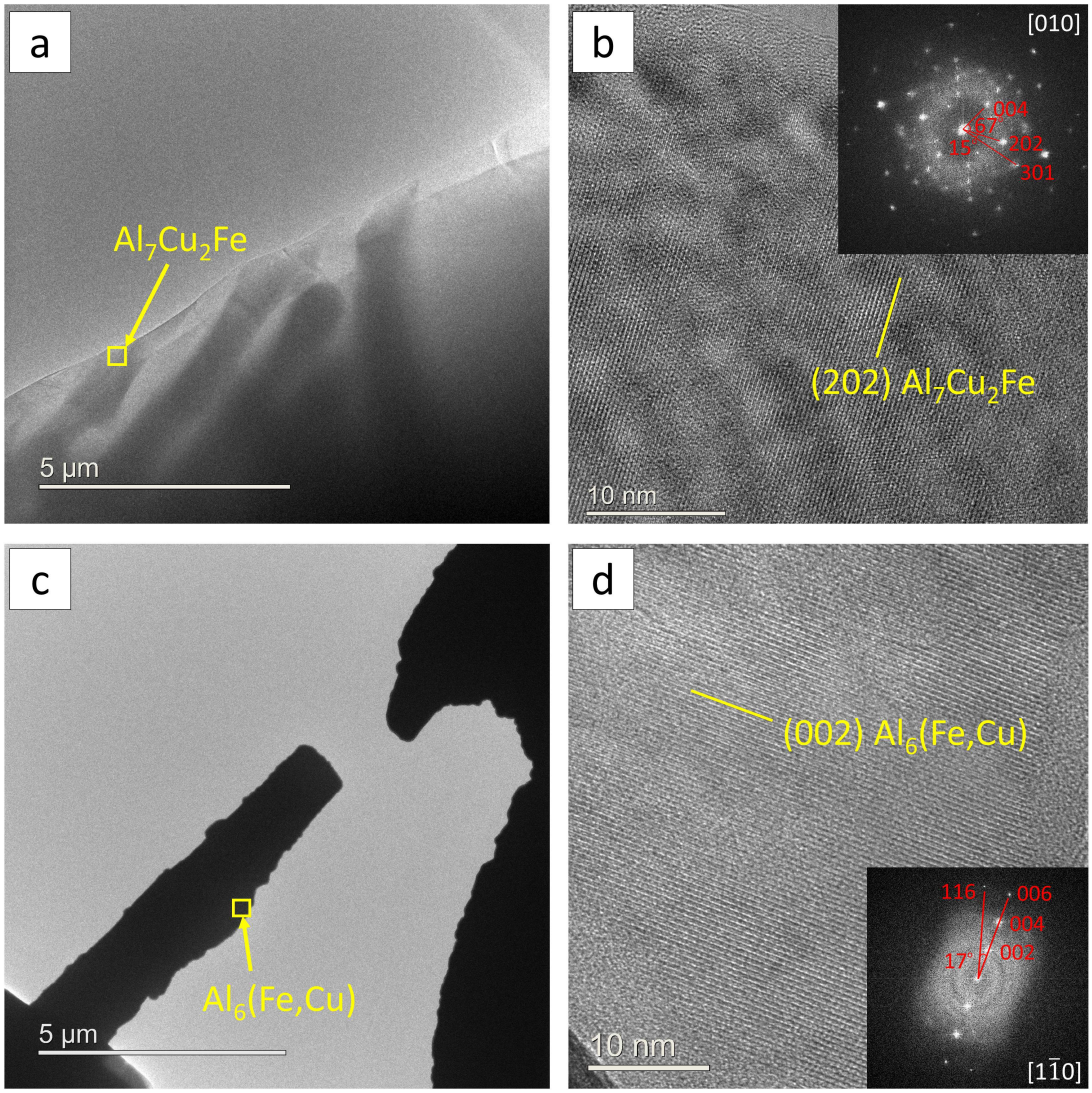


Figure 4.4: Bright field TEM images of (a) Al_7Cu_2Fe (dark needles) and (c) $Al_6(Fe,Cu)$ (yellow squares indicate the positions where HR-TEM images were acquired); HR-TEM images of (b) Al_7Cu_2Fe with FFT pattern along [010] direction and (d) $Al_6(Fe,Cu)$ with FFT pattern along [1$\bar{1}$0] direction.

in good agreement with the literature [115, 212].

Combining the SEM/EDX and HR-TEM findings, Table 4.4 summarises the predominant IMC populations for all experiments with respect to alloy composition, cooling rate and grain refiner addition.

Phase	Plane	Measured (nm)	Literature (nm)	Ref.
Al_7Cu_2Fe	004	0.372	0.370	[115]
	202	0.293	0.291	
	301	0.210	0.209	
Al_6(Fe,Cu)	002	0.449	0.439	[212]
	220	0.250	0.244	
	222	0.219	0.213	
	116	0.146	0.140	

Table 4.3: Measured and literature interplanar d-spacings for Al_7Cu_2Fe and Al_6(Fe,Cu).

Alloy	Refined	Cooling rate (Ks^{-1})				
		0.1	0.2	0.6	1	2
1.5Fe	-	Al_6+Al_7	Al_6+Al_7	Al_6+Al_7	Al_6+Al_7	-
1.5Fe-GR	TiB_2	-	Al_6	Al_6	Al_6	Al_7
0.8Fe	-	-	Al_7	Al_7	Al_7	-
0.8Fe-GR	TiB_2	-	Al_7	Al_7	Al_7	-

Table 4.4: Predominant Fe-rich IMC phases for the different alloy compositions, grain refiner additions and cooling rates (Al_6: Al_6(Fe,Cu), Al_7: Al_7Cu_2Fe).

4.3 Discussion

4.3.1 IMC phase selection

According to previous studies of the Al-Cu-Fe system using thermal analysis [46, 115, 159], the expected phase transformations in 1.5Fe are:

$$L \rightarrow \alpha\text{-Al} \tag{R1}$$

$$L \rightarrow \alpha\text{-Al} + Al_6(Fe,Cu) \tag{R2}$$

$$L + Al_6(Fe,Cu) \rightarrow \alpha\text{-Al} + Al_7Cu_2Fe \tag{R3}$$

$$L \rightarrow \alpha\text{-Al} + Al_7Cu_2Fe \tag{R4}$$

while in 0.8Fe alloy, only reactions R1 and R4 were expected because of the lower Fe concentration. Fig. 4.5 summaries the IMC phases, equilibrium formation temperatures and experimental measurement of IMC tip temperatures as a function of cooling rate. 1.5Fe formed both high-T Al_6(Fe,Cu) and low-T Al_7Cu_2Fe at all cooling rates from 0.1 Ks^{-1} to 1 Ks^{-1}. The estimated high-T Al_6(Fe,Cu) tip temperatures (Figs. 4.2 and 4.5) were in good agreement with the starting temperature of reaction R2 (i.e. the Al_6(Fe,Cu) formation temperature) of 620°C

determined by Phillips *et al.* [159] using thermal analysis at 0.08 Ks^{-1} for an alloy composition of 10 wt% Cu and 1.5 wt% Fe. Thus, Fig. 4.5 suggests an Al_6(Fe,Cu) tip undercooling of ∼5°C. The estimated tip temperatures for low-T Al_7Cu_2Fe showed good agreement with the equilibrium ternary peritectic (invariant) reaction temperature in Al-Cu-Fe of 595 °C [46]. Support for the peritectic reaction was provided by the frequent observation of Al_7Cu_2Fe formed around the edge of Al_6(Fe,Cu), such as that shown in Fig. 4.3(b). When grain refiner was added, high-T Al_6(Fe,Cu) was formed at all but the higher cooling rate of 2 Ks^{-1}, which instead formed Al_7Cu_2Fe. However, the Al_6(Fe,Cu) tip temperature became sensitive to cooling rate, decreasing with increasing cooling rate. For example, at the relatively high cooling rate of 1 Ks^{-1}, Al_6(Fe,Cu) grew at 597°C, and an undercooling of 23°C. Although this undercooling is large when compared with typical values of up to a few degrees for primary phases, IMCs undercoolings of up to 30°C have been measured by thermal analysis for various Fe-rich IMCs in grain refined Al-Cu-Fe alloys at similar cooling rates in the range 0.2 Ks^{-1} to 0.8 Ks^{-1} [148].

4.3.2 Inter-dendritic channel tortuosity

The constant IMC tip temperature in the non-grain refined alloys and by comparison the highly sensitive tip temperature to cooling rate in the grain refined alloys suggested that the primary microstructure played a role.

Fig. 4.5 shows that IMCs grew predominantly in two bands of temperature, and therefore primary solid fraction. Assuming the Scheil model of solidification may be applied (no diffusion in the solid, complete mixing in the liquid, solid/liquid interfacial equilibrium) and considering the two bands of IMC tip temperature, the solid fraction f_s of primary α-Al at each of the two temperatures was estimated using the Scheil model for the Al-Cu binary system according

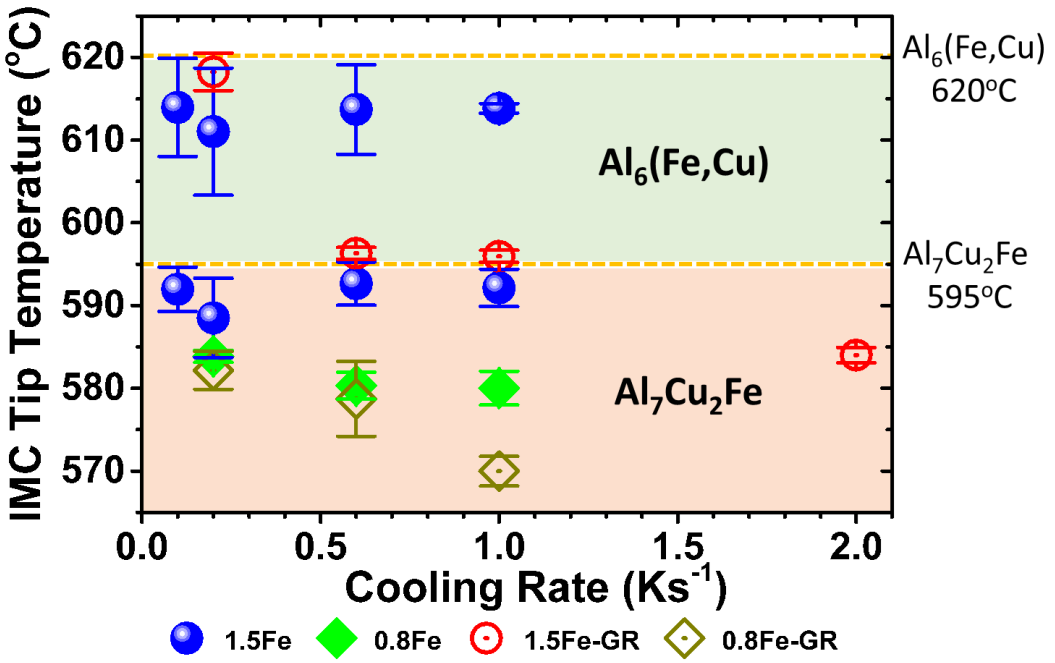


Figure 4.5: IMC tip temperature at different cooling rates for 1.5Fe, 0.8Fe, 1.5Fe-GR and 0.8Fe-GR, with labels indicating different IMC phase populations and literature values of $Al_6(Fe,Cu)$ [159] and Al_7Cu_2Fe [46] formation temperatures determined by thermal analysis.

to:

$$f_s = 1 - \left[\frac{T_m - T}{T_m - T_L}\right]^{\frac{1}{k-1}} \tag{4.1}$$

where $T_m = 660°C$ is the melting point of pure aluminium, $k = 0.17$ is the Al-Cu partition coefficient, and $T_L = 627°C$ is the liquidus temperature of the alloy. The resulting estimates of the solid fraction at each of the IMC growth temperatures (i.e. the measured tip temperature) are shown in Table 4.5.

	Alloy														
	1.5Fe				**1.5Fe-GR**				**0.8Fe**			**0.8Fe-GR**			
Cooling rate (Ks^{-1})	0.1	0.2	0.6	1	0.2	0.6	1	2	0.2	0.6	1	0.2	0.6	1	
Microstructure	Columnar				Equiaxed				Columnar			Equiaxed			
f_s	0.2-0.3	0.2-0.4	0.2-0.3	0.3	0.2-0.3	0.5	0.5	0.7	0.6-0.7	0.6-0.7	0.7	0.6-0.7	0.6-0.7	0.7	
Branched	No	No	No	No	No	Yes	Yes	Yes	No	No	No	Yes	Yes	Yes	

Table 4.5: Summary of the primary α-Al phase morphology, estimated solid fraction (f_s) at the IMC growth temperature and if IMCs were branched at each of the different cooling rates.

Combining Table 4.5 and Fig. 4.5, the tip temperature remained stable when the IMCs were non-branched whilst there was a reduced tip temperature in the conditions where IMCs appeared branched.

Comparing 1.5Fe and 0.8Fe shows that both alloys with columnar microstructures formed straight, non-branched IMCs regardless of the solid fraction, with IMCs growing along/in the straight inter-dendritic channels. Fig. 4.6(a) shows an image of a typical inter-dendritic channel morphology (highlighted in yellow) in 1.5Fe at the instant an IMC first appeared. The ratio of the channel length to the image height (1 mm) gives an estimate of the 2-D inter-dendritic channel tortuosity τ in the vertical direction according to:

$$\tau = L/L_0 \tag{4.2}$$

where $L = 1.02\,\text{mm}$ is the length of the path in Fig. 4.6a, and $L_0 = 1\,\text{mm}$ is the vertical distance between the bottom and top of the field of view, giving $\tau \sim 1$ for 1.5Fe.

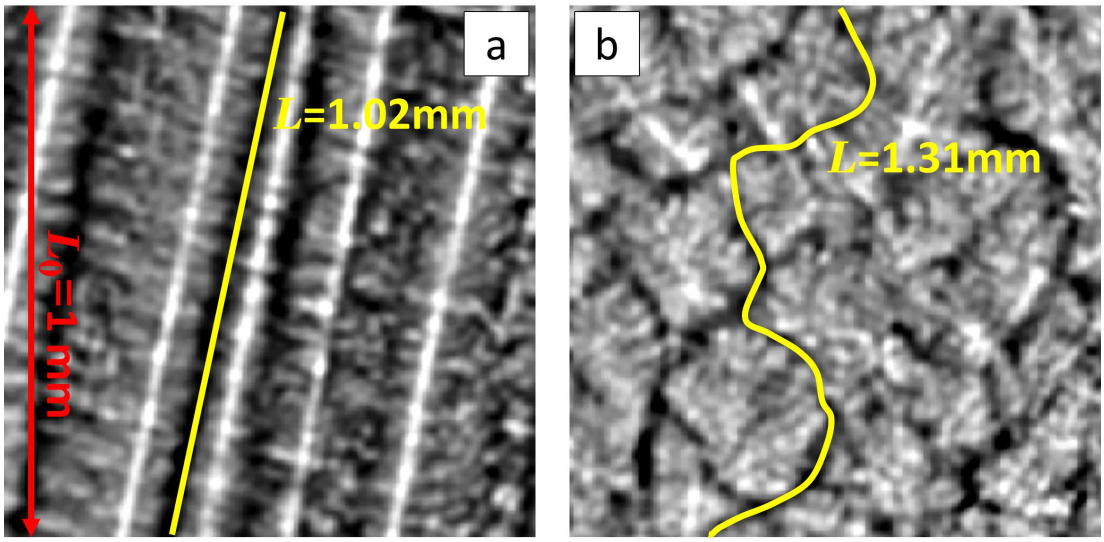


Figure 4.6: Radiographs showing inter-dendritic channel morphology in: (a) 1.5Fe and (b) 1.5Fe-GR at 1 Ks^{-1}. Yellow lines highlight a path in the inter-dendritic channel from bottom to top. The image height is 1 mm and the inter-dendritic channel length highlighted are 1.02 mm and 1.31 mm respectively.

Comparing equiaxed 1.5Fe-GR and 0.8Fe-GR shows that the IMC branching behaviour and the tip temperature were dependent on the solid fraction. In 1.5Fe-GR at 0.2 Ks^{-1} IMCs grew at a sufficiently low solid fraction of 0.2 to 0.3 that despite the equiaxed α-Al morphology, the liquid channels were still comparatively open and with low tortuosity. Thus, IMCs were able to grow with almost no branching and with a similar tip temperature to its non-grain refined counterpart. Examples of unbranched IMCs in 1.5Fe-GR at 0.2 Ks^{-1} are shown in Fig. 4.7(a). As the cooling rate increased to 0.6 and then 1 Ks^{-1}, IMCs were growing at an increased primary α-Al solid fraction and more tortuous liquid channels ($\tau \sim 1.3$ in Fig. 4.6(b)). Necessarily, branching became commonplace, as shown in Fig. 4.7(b). Although the branching appeared as a single IMC changing its growth direction, IMC growth also often stopped and a new IMC then formed nearby, giving the appearance of branching and this suggested more undercooling was therefore needed.

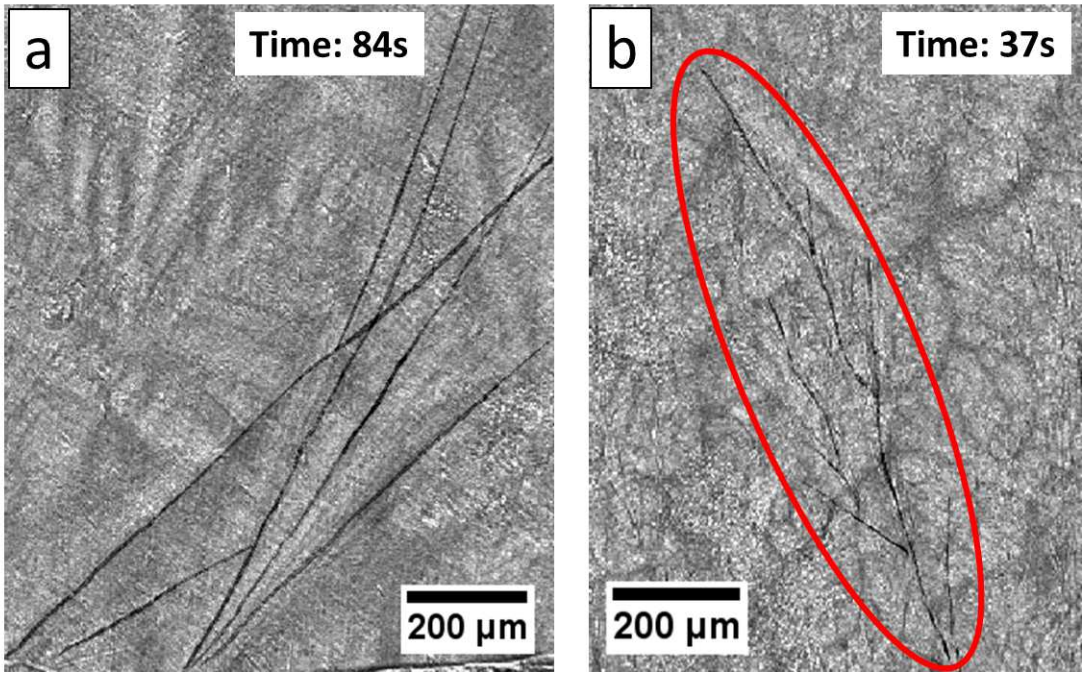


Figure 4.7: Radiographs of IMCs in 1.5Fe-GR at a cooling rate of: (a) 0.2 Ks^{-1} and (b) 1 Ks^{-1}.

The discussion above was made largely qualitatively. To further explore

the correlation between the IMC tip temperature, IMC branching/re-nucleation, and inter-dendritic channel morphology, the number of inter-dendritic channel branches per unit area was estimated in 0.8Fe, 0.8Fe-GR, 1.5Fe and 1.5Fe-GR (following the method detailed in Section 3.4.2.2), as shown in Fig. 4.8.

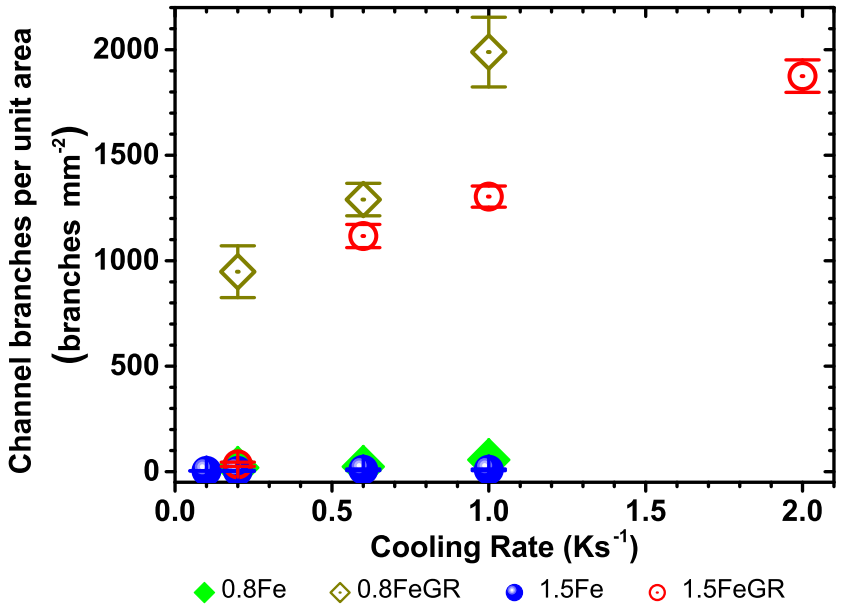


Figure 4.8: Estimation of inter-dendritic channel branches per unit area (mm^{-2}) in 0.8Fe, 0.8Fe-GR, 1.5Fe and 1.5Fe-GR at different cooling rates.

The non-grain refined alloys 1.5Fe and 0.8Fe both showed few branches in the inter-dendritic channels regardless of cooling rate. This was consistent with the constant tip temperature in Fig. 4.5. In contrast, their grain refined counterparts 1.5FeGR and 0.8FeGR showed a steady increase in the branch density, which also agreed with the increased IMC tip undercooling at increasing cooling rate (Fig. 4.5). At 0.2 Ks^{-1}, 1.5Fe-GR had few branches and a similar Al_6(Fe,Cu) tip undercooling to 1.5Fe. However, as the cooling rate increased to 0.6 Ks^{-1}, and then further to 1 Ks^{-1}, the channel branch density increased by two orders of magnitude. As a consequence, more frequent branching or re-nucleation of IMCs was required to follow the convoluted liquid channel, and therefore there was a progressive increase in IMC tip undercooling. Eventually at the higher cooling rate of 2 Ks^{-1}, the formation of high-T Al_6(Fe,Cu) (reaction R2) and the

subsequent peritectic reaction R3 were suppressed, and low-T Al_7Cu_2Fe formed from liquid via reaction R4, which was more kinetically realisable.

4.4 Summary

By using synchrotron X-ray radiography and a carefully controlled furnace, a method was developed to estimate the temperature at any time and any position in the field of view, and this method was applied to obtain data on the tip temperature and phase selection in directionally solidified Al-Cu-Fe alloys from 47 experiments and 203 IMCs. IMC tip temperatures indicated two Fe-rich IMCs that were identified by post-solidification microscopy as Al_6(Fe,Cu) and Al_7Cu_2Fe. Grain refiner additions increased the cooling rate sensitivity of the IMC tip temperature by increasing the tortuosity of inter-dendritic channels. Thus, by using grain refiner additions together with a higher cooling rate, IMC growth was delayed to significantly lower temperatures. Although developed for Al-Cu-Fe alloys in the present work, the *in-situ* thermal field calibration and temperature estimation method could find wide applicability in radiographic studies.

Chapter 5

Crystal formation and inoculation of primary Fe-rich IMCs

5.1 Introduction

As discussed in Chapter 2, a number of particles have been proposed to be associated with or to catalyse the nucleation of platelet Fe-rich IMCs, including oxides and commercial grain refiners TiB_2 and TiC, mostly based on microscopic observations of the physical contact between the IMCs and these particles. However, the detailed role (if any) of the different particles as nucleants, especially for Fe-rich IMCs, is somewhat unclear. In the experiments described subsequently, a hypereutectic Al-Fe alloy in which platelet Fe-rich IMCs ($Al_{13}Fe_4$) formed as primary phase was chosen. Formation of primary Fe-rich IMCs with different inoculation conditions (no inoculation, TiB_2 and TiC) was studied at a series of cooling rates and thermal gradients. As described below, strong evidence is provided from a large number of measurements (4618 IMCs in total) that inoculation directly enhanced the formation of primary Fe-rich IMCs, and under some

conditions, the oxide skin of the sample also catalysed nucleation. An increase in thermal gradient is shown to reduce significantly the number density and average formation rate of primary IMCs, and also decreased their formation temperature. A qualitative model to explain these trend-wise variations, accounting for the effect of thermal gradient and cooling rate, is proposed.

5.2 Results

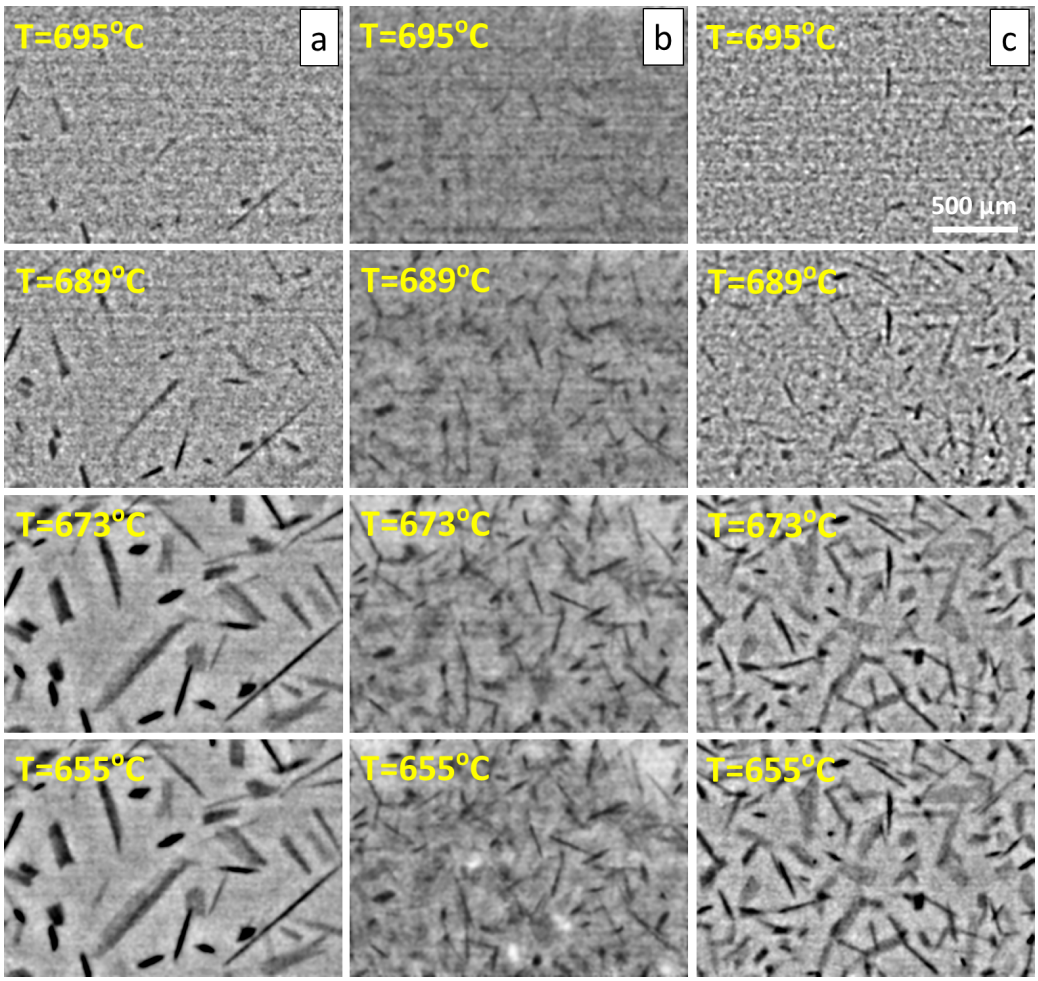


Figure 5.1: Radiography sequences showing primary IMC formation in near isothermal, horizontal solidification of alloys (a) AF, (b) AF-B and (c) AF-C, all at a cooling rate of 2 Ks^{-1}.

Fig. 5.1 shows image sequences from the solidification of alloys (a) AF, (b) AF-B and (c) AF-C, at 2 Ks^{-1} in a horizontal, near isothermal condition. In

this condition, the IMCs formed almost uniformly across the field of view, as expected from the absence of a thermal gradient, and they formed without noticeable movement (due to differential density) because of the horizontal arrangement. However, because of the relatively poor image quality at the early stages of solidification (where contrast due to Fe segregation was relatively low), the total number of IMC formation events could only be estimated by counting the IMCs at the end of the sequences (rather than frame by frame, as they appeared). The total number of IMCs was always significantly larger in the inoculated samples: 52 IMCs formed in AF (from the sequence shown in Fig. 5.1(a)), approximately 128 in AF-C (Fig. 5.1(c)) and 161 in AF-B (Fig. 5.1(b)).

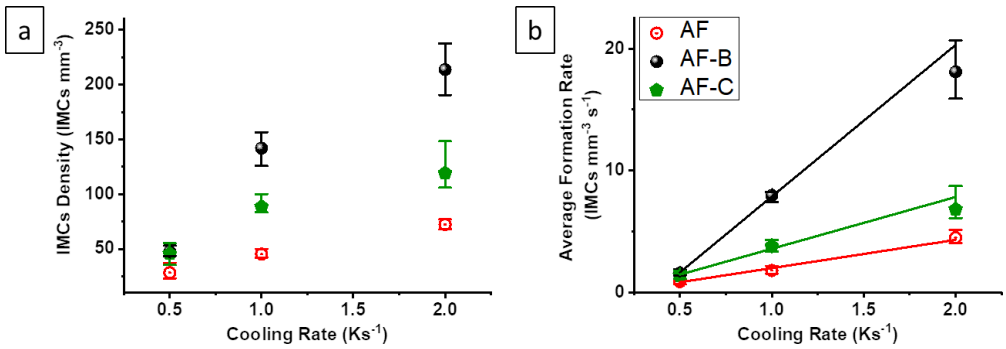


Figure 5.2: (a) Total IMC density (total number of IMCs divided by the volume of the field of view) and (b) average formation rate (total IMC density divided by the duration of IMC formation) in alloys AF, AF-B and AF-C at 0.5 - 2 Ks^{-1} in near isothermal, horizontal solidification. The solid lines in (b) indicate a linear best-fit to highlight the trend.

By dividing the total number of IMCs by the volume of the field of view in each experiment, Fig. 5.2(a) summarises the total IMC density in alloys AF, AF-B and AF-C as a function of cooling rate for 34 experiments in the near isothermal, horizontal arrangement. AF-B and AF-C both showed a higher IMC density than AF, particularly at higher cooling rates, whilst the AF-B alloy had the highest IMC density over the range of cooling rates. Dividing the IMC density by the duration of IMC formation (i.e. time between the first and last IMC appearing in the field of view), the average IMC formation rate in AF, AF-B and AF-C

increased steadily with cooling rate (Fig. 5.2(b)), and AF-B showed the greatest sensitivity to cooling rate (steepest gradient).

Fig. 5.3 shows three image sequences for the alternative vertical, directional solidification at $2\,\mathrm{Ks}^{-1}$ for (a) AF and (b) AF-B at a thermal gradient of $5\,\mathrm{K\,mm}^{-1}$ and (c) AF-B at a thermal gradient of $8\,\mathrm{K\,mm}^{-1}$.

The formation of IMCs started near the bottom of the field of view and continued upwards due to the vertical thermal gradient, and solidification finished with the appearance of the eutectic front at $T = 655\,^{\circ}\mathrm{C}$. The number of IMC formation events was counted manually frame-by-frame for each sequence and the total number of IMC formation events (i.e. total number of IMCs formed) in the base alloy (AF) was 66 compared with 97 in the TiB_2 inoculated sample (AF-B) at $5\,\mathrm{K\,mm}^{-1}$. Upon imposing a higher thermal gradient of $8\,\mathrm{K\,mm}^{-1}$, the total number of IMC formation events in the same AF-B alloy reduced sharply to 26. Figs. 5.3(d) and (e) show the evolution of the number of IMCs and the formation rate with time, respectively. For each experiment, $t = 0$ was set when an IMC first appeared in the field of view. IMC formation was generally in a pseudo-continuous manner (Fig. 5.3(e)) and the rate was the highest for AF-B at $5\,\mathrm{K\,mm}^{-1}$.

In contrast to the horizontal condition, there was frequent settling of IMCs in AF-B during vertical solidification because $Al_{13}Fe_4$ had higher density ($3.84\,\mathrm{g\,cm}^{-3}$) than the liquid ($2.75\,\mathrm{g\,cm}^{-3}$). The yellow circles in Figs. 5.3(b) and (c) highlight the white "shadow" left behind by settling IMCs due to the image subtraction algorithm. In contrast, all the IMCs remained static after formation in the alloy without inoculation. This will be discussed in more detail in the next section.

Figs. 5.4(a) and (b) summarise the total IMC density (total number of time-resolved formation events divided the volume of the field of view) and corresponding average formation rate in 22 directional, vertical solidification experiments of AF and AF-B respectively. In comparison with the near isothermal counterparts,

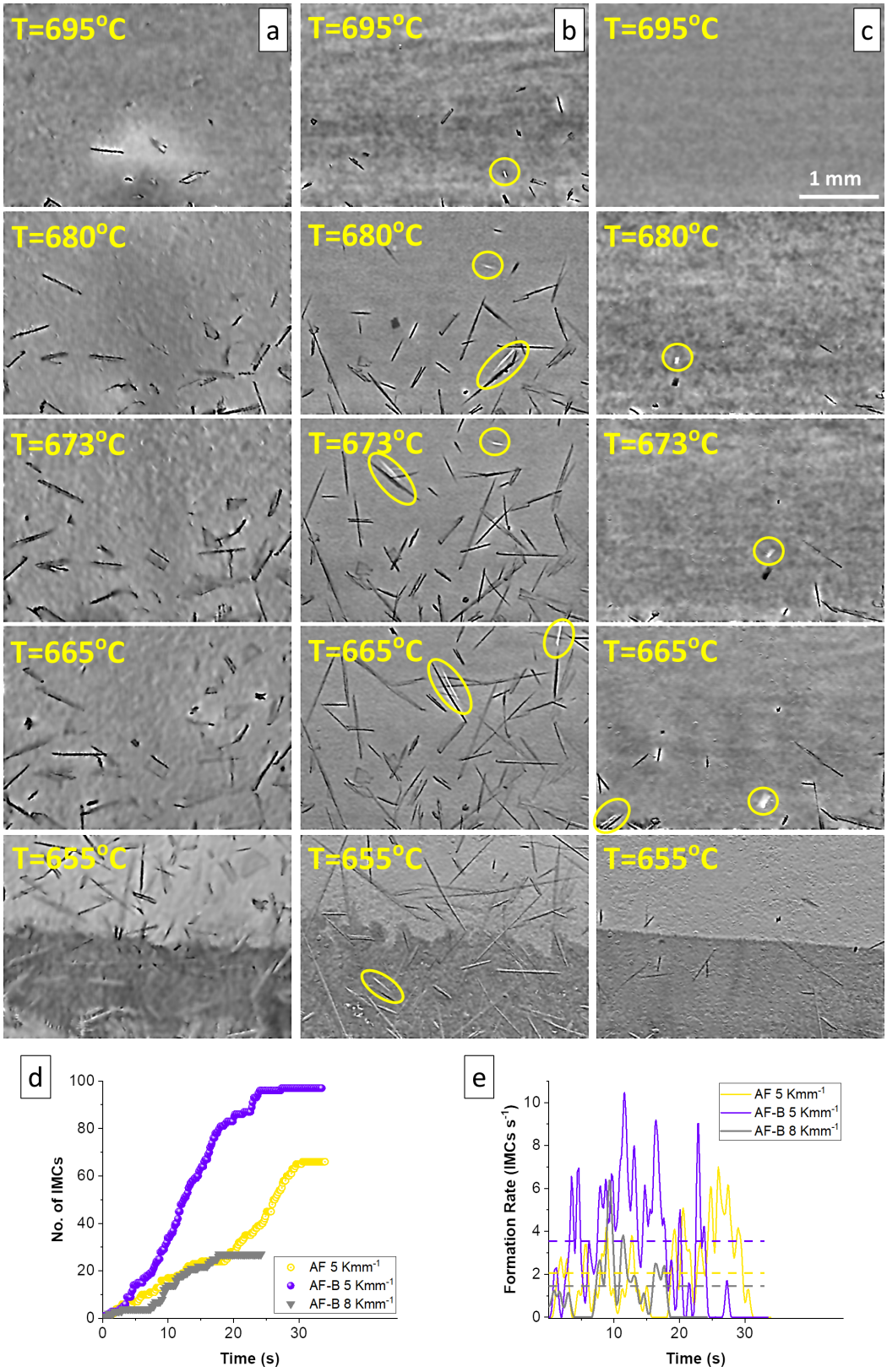


Figure 5.3: Radiographic sequences showing primary IMC formation in directional, vertical solidification at 2 Ks^{-1} of (a) AF and (b) AF-B at a thermal gradient of 5 $\mathrm{K\,mm}^{-1}$, and (c) AF-B at 8 $\mathrm{K\,mm}^{-1}$. Each image was obtained by subtracting frame f_n with frame f_{n-15}. In AF-B, settling of IMCs was frequently observed, and the yellow circles in (b) and (c) highlight the white "shadow" left behind by the settling IMCs upon image subtraction. (d) Corresponding evolution of the number of IMCs in the field of view, and (e) evolution of formation rate as a function of time. Dashed lines in (e) indicate the average formation rate. For each experiment, $t = 0$ was set when the first IMC appeared in the field of view.

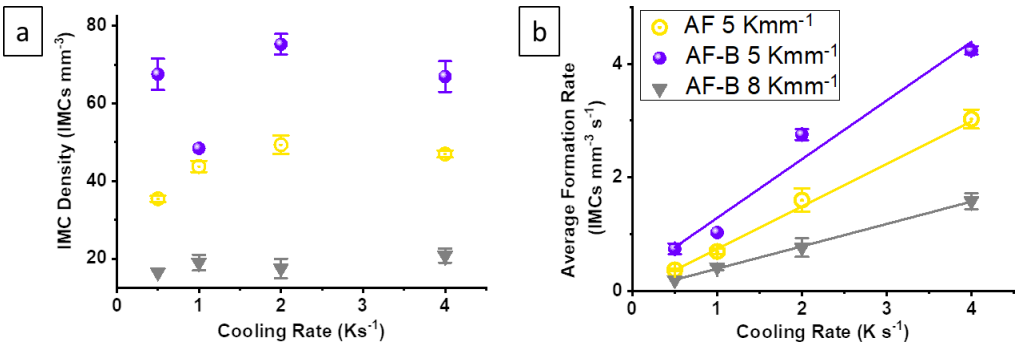


Figure 5.4: (a) Total IMC density (total number of time-resolved IMC formation events divided by the volume of the field of view) and (b) average formation rate in AF and AF-B at a thermal gradient of $5\,\mathrm{K\,mm^{-1}}$ and AF-B at a thermal gradient of $8\,\mathrm{K\,mm^{-1}}$, at cooling rates of 0.5 to 4 $\mathrm{Ks^{-1}}$ in directional, bottom-to-top solidification. The solid lines in (b) indicate a linear best-fit to highlight the trend.

solidification with a thermal gradient showed much weaker IMC density sensitivity to cooling rate (Fig. 5.4(a)), especially for inoculated alloys. Nonetheless, there was again a strong relationship between the average IMC formation rate and cooling rate (Fig. 5.4(b)). IMC density and average formation rate for AF-B were consistently higher than for AF at the same thermal gradient of $5\,\mathrm{K\,mm^{-1}}$. At an increased thermal gradient of $8\,\mathrm{K\,mm^{-1}}$, the IMC density in AF-B reduced from 70 IMCs $\mathrm{mm^{-3}}$ to <20 IMCs $\mathrm{mm^{-3}}$.

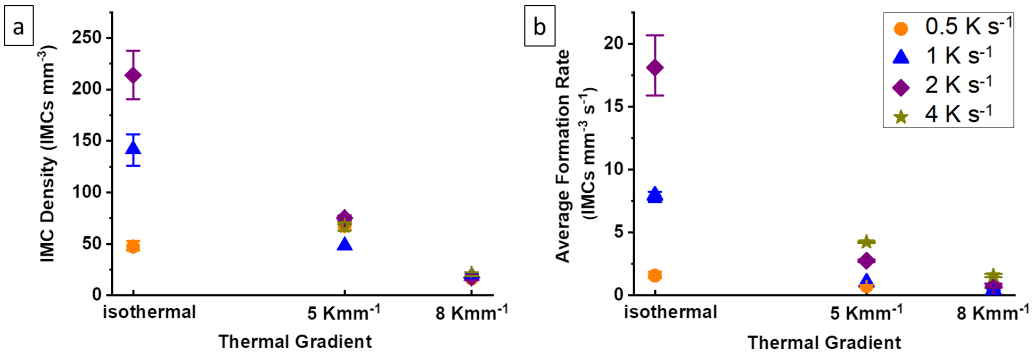


Figure 5.5: (a) IMC density as a function of thermal gradient for alloy AF-B. (b) Average IMC formation rate as a function of thermal gradient for alloy AF-B.

To further illustrate the effect of thermal gradient, Fig. 5.5 summarises the

IMC density and average formation rate data for near isothermal, $5\,\mathrm{K\,mm^{-1}}$ and $8\,\mathrm{K\,mm^{-1}}$ for AF-B. Increasing thermal gradient generally reduced both the IMC density and average formation rate, and the effect was more pronounced at higher cooling rate: at 2 $\mathrm{Ks^{-1}}$, the IMC density decreased from 214±24 IMCs $\mathrm{mm^{-3}}$ at near isothermal condition to 17±3 IMCs $\mathrm{mm^{-3}}$ at the highest thermal gradient of $8\,\mathrm{K\,mm^{-1}}$. The corresponding average formation rate was also significantly reduced from 18±3 IMCs $\mathrm{mm^{-3}s^{-1}}$ to 0.8±0.2 IMCs $\mathrm{mm^{-3}s^{-1}}$.

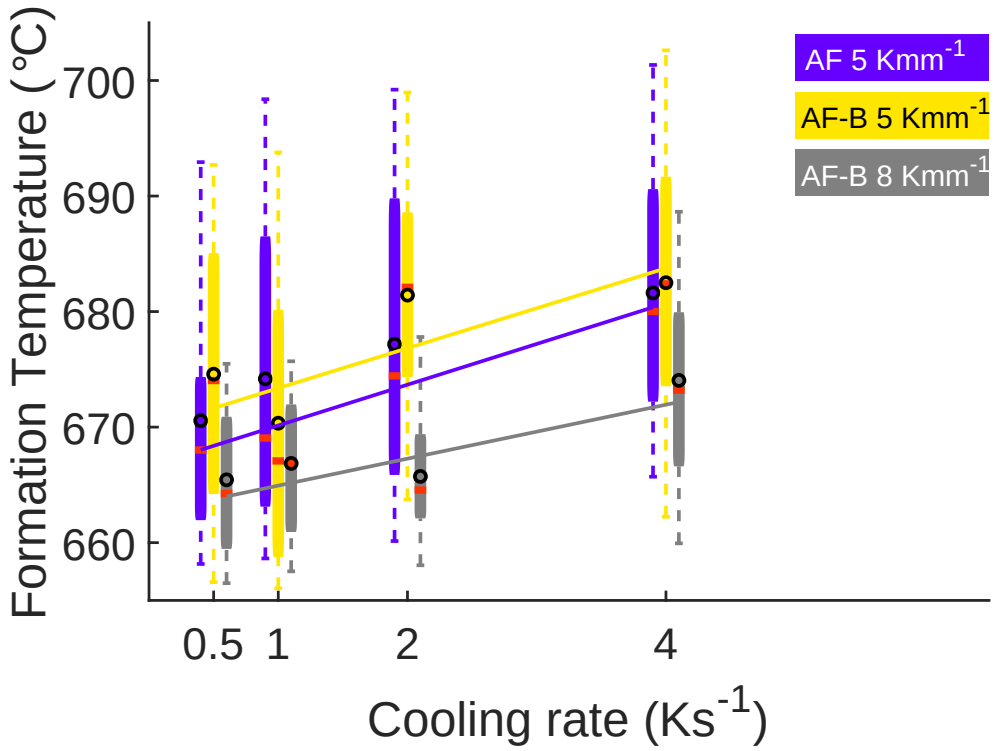


Figure 5.6: Estimated formation temperature of primary IMCs as a function of cooling rate for AF and AF-B at $5\,\mathrm{K\,mm^{-1}}$ and AF-B at $8\,\mathrm{K\,mm^{-1}}$. For each box plot, the red line denotes the median of the IMC formation temperature, the black circle denotes the mean, the top and bottom edges of the box indicate the 75% and 25% percentile, and the top and bottom whiskers indicate the 95% and 5% percentile. Solid lines with the same colour code represents a linear best-fit of the median formation temperature. The data set comprises 1893 measurements.

Following the method described in Section 3.4.2.4 in Chapter 3, the formation temperature of 1893 primary IMCs in 22 directional solidification experiments was estimated and is plotted as a function of cooling rate for AF and AF-B at

$5\,\mathrm{K\,mm^{-1}}$, and AF-B at $8\,\mathrm{K\,mm^{-1}}$ in Fig. 5.6. For each box plot, the red line denotes the median of the IMC formation temperature, the black circle denotes the mean, the top and bottom edges of the box indicate the 75% and 25% percentile, and the top and bottom whiskers indicate the 95% and 5% percentile. AF and AF-B at the same thermal gradient of $5\,\mathrm{K\,mm^{-1}}$ showed a similar wide range of primary IMC formation temperatures, in the range of 655°C to 700°C. As the thermal gradient increased to $8\,\mathrm{K\,mm^{-1}}$, there was a marked reduction in the maximum IMC formation temperature and a narrower range of formation temperatures, which were 15 to 20°C lower than at $5\,\mathrm{K\,mm^{-1}}$. In other words, primary IMC formation occurred at a lower temperature at increased thermal gradient, as can also be noticed from Fig. 5.3(c). In addition, both AF and AF-B displayed a trend of increasing median formation temperature with increasing cooling rate. This trend is highlighted in Fig. 5.6 by a linear best-fit of the median formation temperature to cooling rate.

5.3 Discussion

5.3.1 Nucleants for IMCs

In all conditions, inoculant additions increased the number of IMC formation events (Figs. 5.2 and 5.4), suggesting that TiB_2 and TiC catalysed the nucleation of IMCs. As pointed out previously in Figs. 5.3(b) and (c), when AF-B was solidified vertically, there was frequent settling of IMCs. By comparison, in AF all the IMCs remained static once formed, despite gravity, and this is interpreted as the IMCs in AF primarily nucleated on the interior side of the oxide skin of the sample. In contrast, frequent IMC settling in AF-B suggested that where TiB_2 was available, IMCs preferentially nucleated on the TiB_2 particles suspended in the melt. Therefore, settling of the IMCs helped distinguish IMCs nucleating on TiB_2 particles (that were largely mobile) and IMCs nucleating on the oxide skin

(that were largely immobile).

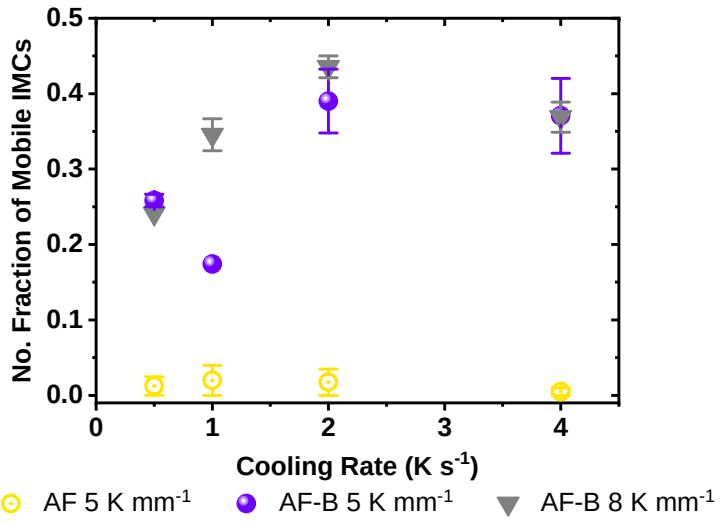


Figure 5.7: Number fraction of mobile primary IMCs as a function of cooling rate for AF and AF-B at $5\,\mathrm{K\,mm^{-1}}$ and AF-B at $8\,\mathrm{K\,mm^{-1}}$.

In either AF or AF-B, the number fraction of mobile IMCs shown in Fig. 5.7 had no obvious relationship with cooling rate. In AF nearly all IMCs remained static, because they nucleated on the oxide wall of the sample, consistent with previous observations by post-solidification microscopy [42, 43]. The minor fraction of mobile IMCs (∼2%) in AF could be a consequence of nucleation on minor inclusions in the liquid, or detachment from the oxide wall due to convection in the liquid. In AF-B, up to 45% of the primary IMCs were mobile regardless of thermal gradient or cooling rate, suggesting that they nucleated on TiB_2 particles. This provides strong evidence that TiB_2 can nucleate Fe-rich IMCs (at least as primary phase), as suggested by earlier researchers based on extraction and microscopy [37, 39, 40], and that it is a more efficient nucleant than oxide skins (or films), although finely dispersing the oxide (for example by melt shearing) might improve the oxide catalyst efficiency [213, 214].

5.3.2 IMC nucleation

IMC number density and average formation rate decreased as the thermal gradient increased, from the near isothermal condition to $5\,\mathrm{K\,mm^{-1}}$, and then further to $8\,\mathrm{K\,mm^{-1}}$ (Fig. 5.5). Similar observation of reducing grain formation events with increasing thermal gradient was reported by Xu *et al.* [202] for equiaxed α-Al dendrites in an Al-20Cu (wt%) alloy for near isothermal, $5\,\mathrm{K\,mm^{-1}}$ and $10\,\mathrm{K\,mm^{-1}}$ conditions. However, it was not very clearly stated whether the $5\,\mathrm{K\,mm^{-1}}$ and $10\,\mathrm{K\,mm^{-1}}$ were temperature gradients applied between the heaters, or the actual thermal gradients in the sample (which can be significantly different).

The difference in IMC formation behaviour under near isothermal and directional conditions can be explained by considering the undercooling conditions experienced by nucleants in the melt during cooling of the liquid. In the near isothermal condition, as temperature was reduced the liquid across the field of view became undercooled (approximately) simultaneously. In comparison, under directional solidification, only a proportion of the field of view was undercooled (the region closest to the colder, lower heater), and this region was then translated upwards across the sample as cooling proceeded. The extent of the undercooled regions and the distribution of undercooling within these regions is illustrated schematically in Fig. 5.8.

Fig. 5.8(a) shows a schematic of the solute concentration in the liquid ahead of a growing IMC. For hypereutectic composition, where the partition coefficient is $k > 1$, the solute segregates preferentially into the primary IMC, and there is a depletion of solute in the local liquid ahead of the solid/liquid interface. Solute diffuses down the concentration gradient from liquid further away, giving rise to a composition profile:

$$C_L = C_0 + \frac{C_0(1-k)}{k} exp(-\frac{x}{D_L/v}) \tag{5.1}$$

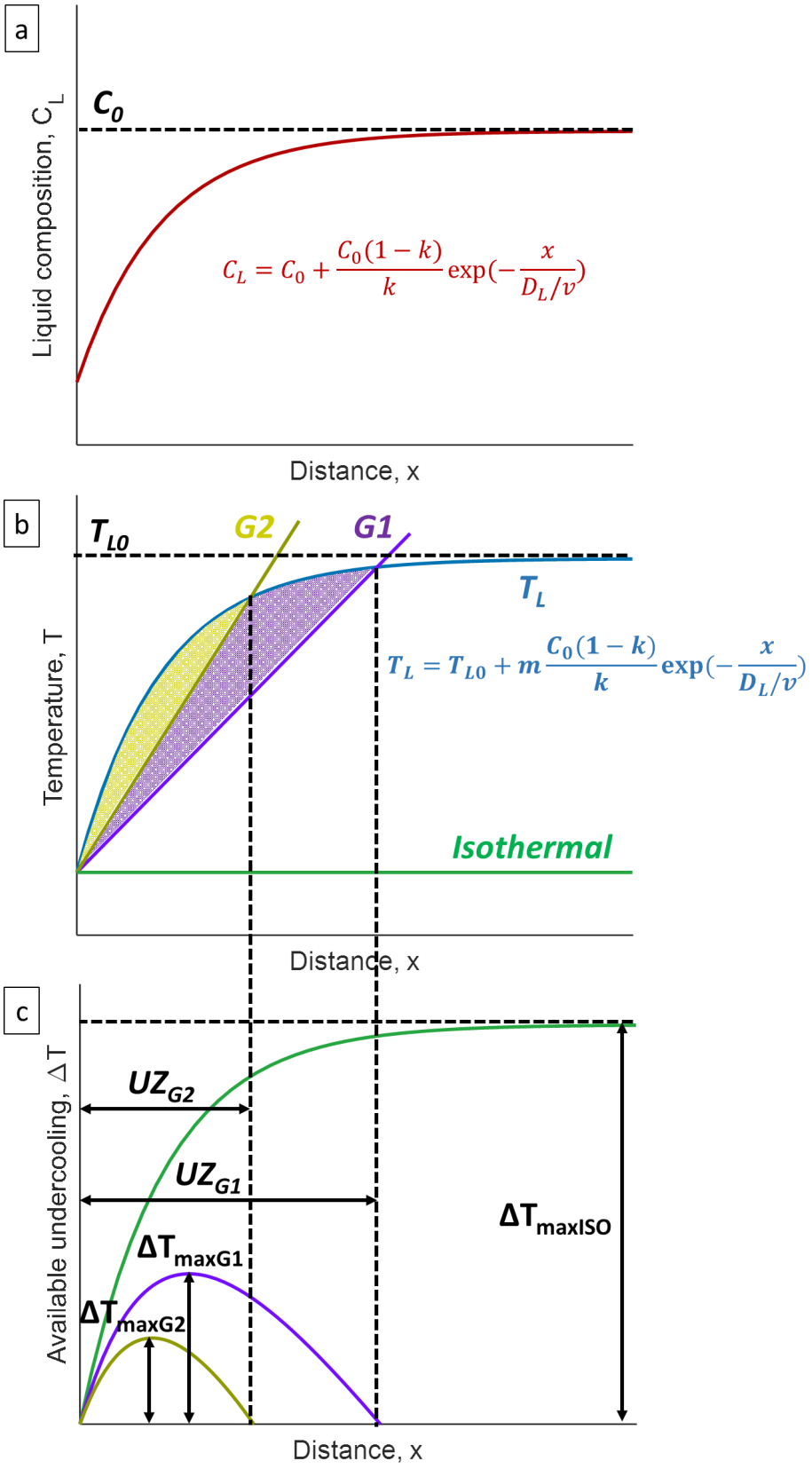


Figure 5.8: (a) A schematic of the liquid composition in front of a growing IMC. C_0 is the bulk liquid composition. (b) A schematic of the undercooled zone (UZ) in front of a growing IMC at isothermal condition, and thermal gradient of $G1$ and $G2$ ($G2 > G1$). T_L is the equilibrium liquidus temperature as a result of the liquid composition profile in (a). T_{L0} is the bulk liquidus. (c) Resultant available undercooling from (b), at isothermal condition, $G1$ and $G2$. UZ_{G1} and UZ_{G2} denote the extent of UZ at $G1$ and $G2$ respectively. ΔT_{maxISO}, ΔT_{maxG1} and ΔT_{maxG2} are the maximum available undercooling at isothermal condition, $G1$ and $G2$ respectively.

where C_L is the liquid composition ahead of the solid/liquid interface, C_0 is the bulk liquid composition, D_L is the solute diffusivity in the liquid, and v is the velocity of the solid/liquid interface. Fig. 5.8(b) shows the equilibrium liquidus temperature T_L in the liquid in front of the growing IMC for the L $\rightarrow$ $Al_{13}Fe_4$ + L reaction. T_L is not constant due to the solute re-distribution ahead of the solid/liquid interface and the resulting solute diffusion profile (Fig. 5.8(a)). The equilibrium liquidus temperature T_L is given by:

$$T_L = T_{L0} + m\frac{C_0(1-k)}{k}exp(-\frac{x}{D_L/v}) \tag{5.2}$$

where T_{L0} is the liquidus temperature at liquid composition C_0, and m ($m > 1$) is the slope of the liquidus on the hypereutectic side of the Al-Fe phase diagram. Fig. 5.8(b) also illustrates the undercooled zone (UZ, i.e. liquid where there was undercooling available) under isothermal conditions, and under conditions with thermal gradients $G1$ and $G2$ ($G2 > G1$). For ease of interpretation, the thermal gradient is shown horizontally although in experiments it was vertical. Under isothermal conditions, UZ is shown to extend across the entire volume of the melt. In contrast, UZ under directional solidification conditions occupies a region only adjacent to the growing IMC. As the thermal gradient is increased, the UZ width is reduced as shown in Fig. 5.8(b).

As well as changing the width of the UZ, the thermal gradient affects the distribution of available undercooling within the UZ, as shown in Fig. 5.8(c). The distribution of available undercooling under isothermal condition follows:

$$\Delta T_{ISO}(x) = m\frac{C_0(k-1)}{k} - m\frac{C_0(k-1)}{k}exp(-\frac{x}{D_L/v}) \tag{5.3}$$

and the distribution of available undercooling at thermal gradient of G follows

the equation of:

$$\Delta T_G(x,G) = m\frac{C_0(k-1)}{k} - m\frac{C_0(k-1)}{k}exp(-\frac{x}{D_L/v}) - Gx \qquad (5.4)$$

Fig. 5.8(c) assumes that the only non-thermal contribution to undercooling is that due to solute build-up ahead of the solid/liquid interface and that interfacial curvature undercooling due to the Gibbs-Thomson effect and kinetic attachment undercooling where there is relatively high entropy of fusion, are assumed negligible. For faceted, ordered phases, these assumptions might be considered arguable, but allow for a simple qualitative model for the effect of macro-cooling conditions to be considered. Within the melt, potential nucleants are assumed to be more or less uniformly distributed. However, the potential nucleants themselves have a distribution of efficiencies, related to their size (see the free growth model in Chapter 2). Therefore, as the arrangements in Figs. 5.8(b) and (c) are cooled, whether a new IMC is formed will thus depend on inter-acting factors: (i) thermodynamics - the size (or volume) of the UZ and the available undercooling, and (ii) kinetics - cooling rate and time.

5.3.2.1 Size of UZ and magnitude of available undercooling

The larger is the UZ, the greater is the possibility that it contains an efficient nucleant particle. Meantime, larger available undercoolings have a greater possibility of activating a nucleant. Isothermal cooling gives the widest UZ which is the entire liquid volume, and it also gives the highest maximum available undercooling of:

$$\Delta T_{maxISO} = m\frac{C_0(k-1)}{k} \qquad (5.5)$$

which is given by the difference between the actual melt temperature and the bulk liquidus of the melt. As a thermal gradient is introduced ($G1$) and is then

increased to $G2$, not only does the width of UZ reduces but so does the magnitude of available undercooling (ΔT_{max}) (Fig. 5.8(b)). Equation 5.4 is differentiated to obtain the position and the corresponding magnitude of the ΔT_{max} under gradient conditions:

$$\frac{\partial \Delta T_G}{\partial x} = \frac{mvC_0(k-1)}{D_L k} exp(-\frac{xv}{D_L}) - G \tag{5.6}$$

the maximum available undercooling at a thermal gradient of G is therefore given by:

$$\Delta T_{maxG} = m\frac{C_0(k-1)}{k} - \frac{GD_L}{v} + \frac{GD_L}{v} ln[\frac{GD_L k}{mvC_0(k-1)}] \tag{5.7}$$

Noting that for undercooling to be available G needs to be smaller than the gradient of T_L at the solid/liquid interface (i.e. at $x = 0$), the term $\frac{GD_L}{v} ln[\frac{GD_L k}{mvC_0(k-1)}]$ in Equation 5.7 must be negative. Therefore ΔT_{maxISO} (Equation 5.5) is always larger than ΔT_{maxG} (Equation 5.7). Then, the size of the UZ is determined by the x values at $\Delta T_G(x, G) = 0$:

$$m\frac{C_0(k-1)}{k} - m\frac{C_0(k-1)}{k} exp(-\frac{x}{D_L/v}) - Gx = 0 \tag{5.8}$$

Solving Equation 5.8 by Matlab, Fig. 5.9(a) shows the resultant plot of the size of UZ that is a strong non-linear function of thermal gradient G. The UZ extends towards maximum as G approaches zero (i.e. isothermal conditions). In contrast, UZ reduces to zero when G increases to $\frac{mvC_0(k-1)}{D_L k}$ that is the gradient of T_L at the solid/liquid interface. Fig. 5.9(b) illustrates the evolution of the magnitude of available undercooling ΔT_{maxG} with G (Equation 5.7). The maximum of ΔT_{maxG} is obtained at $G = 0$. Both the size of UZ and ΔT_{maxG} show a strong sensitivity to thermal gradient.

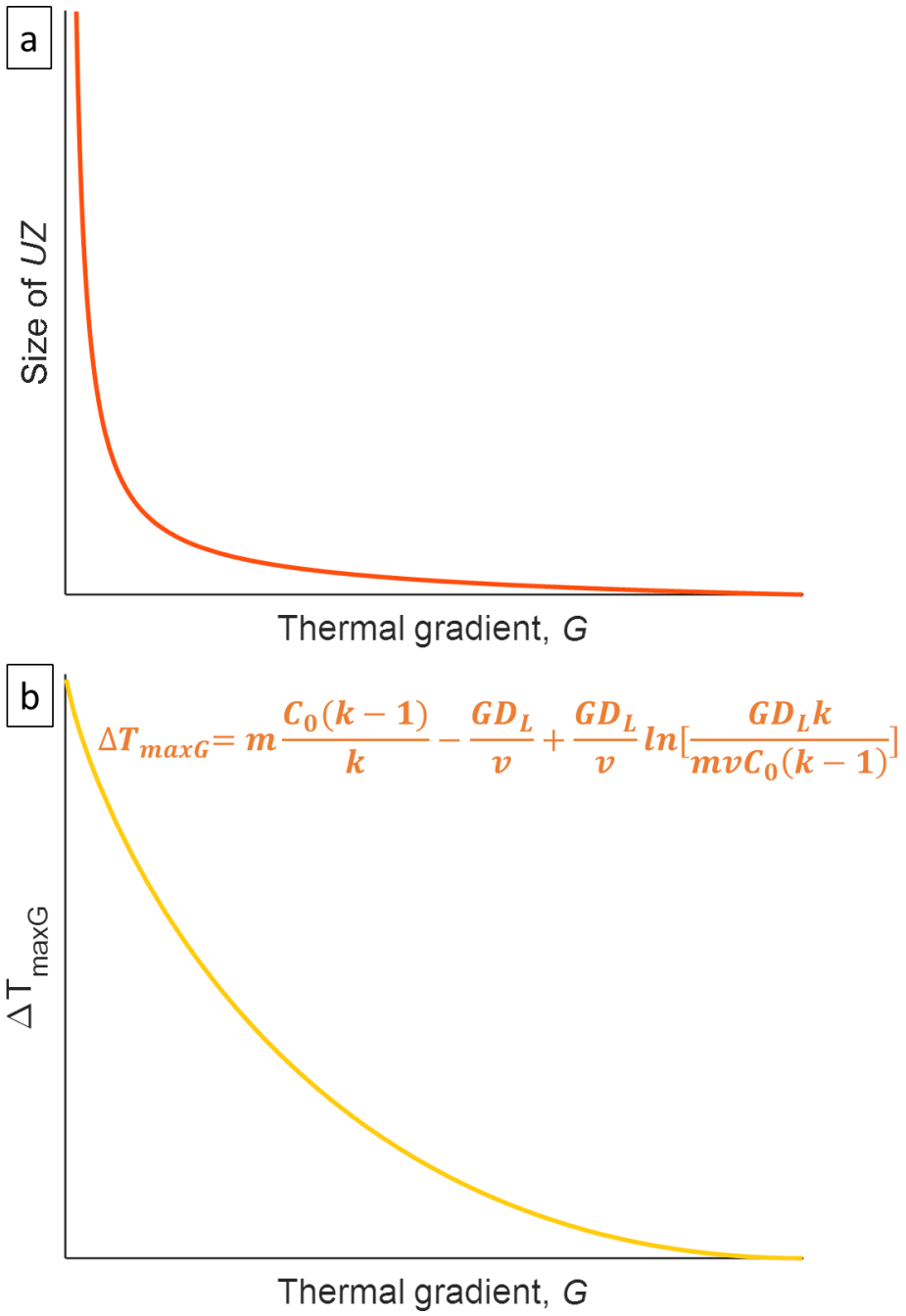


Figure 5.9: (a) A schematic illustrating the size of the undercooled region (UZ) as a function of thermal gradient. (b) A schematic illustrating the maximum available undercooling (ΔT_{maxG}) as a function of thermal gradient.

5.3.2.2 Cooling rate and time

Isothermal cooling

The nucleation rate is known to be a strong non-linear function of undercooling, as shown by Equation 2.3 and illustrated in Fig. 2.2 in Chapter 2. Under isothermal cooling, the size of UZ remains constant (i.e. the entire field of view) with time. According to the free growth model [31] and as shown by Equation 2.7 in Chapter 2, free growth of solid crystals starts preferentially on larger, more potent nucleant particles first as soon as the required undercooling is reached and then on progressively smaller particles as the undercooling available in the liquid is increased to meet a higher required undercooling. Stifling of further nucleation occurs when the undercooling in the liquid starts to reduce because: (i) soft impingement of thermal diffusion field - when the latent heat release becomes significant or (ii) soft impingement of solute diffusion field around growing crystals [31].

Taking into account the effect of latent heat release and soft impingement of solute diffusion field, the actual (net) undercooling achievable in the liquid during nucleation of IMCs will always be smaller than the ΔT_{maxISO} in Equation 5.5. Therefore, under isothermal conditions, it is the maximum of the net undercooling achievable (termed here as "achievable undercooling") before stifling of nucleation occurs that determines the total number of nucleant particles able to be activated for IMC nucleation and hence the final IMC density. By applying a higher cooling rate, a higher achievable undercooling can be reached and hence a larger number of nucleant particles are able to be activated for IMC nucleation, before the achievable undercooling starts to drop due to significant release of latent heat and soft impingement of solute diffusion field. This implies that more nucleating particles are involved, not just the most potent nucleants. Linking back to the free growth model, this is generally assumed to mean that progressively smaller particles are activated for IMC nucleation across the entire liquid volume. In contrast, a lower cooling rate leads to a lower achievable undercooling, which only allows the most potent particles (i.e. largest in size) to be activated for IMC

nucleation.

The probability of nucleation under isothermal cooling P_{ISO} is therefore a function that describes the interaction between the thermodynamic terms (ΔT_{maxISO} and UZ) and the kinetic terms (cooling rate $\dot{T}$ and time t):

$$P_{ISO} \propto f(\Delta T_{maxISO}) \times g(UZ) \times h(\dot{T}, t) \tag{5.9}$$

where f, g and h are unknown functions. Noting that under isothermal cooling, ΔT_{maxISO} (Equation 5.5) and UZ (the entire field of view) are both constant, the terms $f(\Delta T_{maxISO})$ and $g(UZ)$ should be constant. Therefore, the variable that determines the probability of nucleation under isothermal conditions is the cooling rate (and time), which determines the actual net undercooling achievable in the liquid before stifling of nucleation occurs.

Directional cooling

Under thermal gradient conditions, the UZ exists only adjacent to the growing IMC, and maximum available undercooling ΔT_{maxG} is at a specific distance from the solid/liquid interface given by the maximum difference between the local equilibrium liquidus temperature and the melt temperature (Figs. 5.8(b) and (c)). By applying a higher cooling rate, the gradient of the solute concentration profile increases, and so does the gradient of the equilibrium liquidus profile, as illustrated in Figs. 5.10(a) and (b). Fig. 5.10(c) shows the resultant distribution of the available undercooling at cooling rate $\dot{T}_1$ and $\dot{T}_2$ ($\dot{T}_2 > \dot{T}_1$)), at a thermal gradient of G_1. The black dashed line indicates the undercooling required for the most potent nucleants to be activated for nucleation of IMCs. As cooling rate increases from $\dot{T}_1$ to $\dot{T}_2$, there is a minor increase in the maximum available undercooling ΔT_{maxG} and a slight extension in the size of UZ, as a result of the change in the solute diffusion profile in Fig. 5.10(a). While the minor increase

in ΔT_{maxG} might not be sufficient to activate progressively smaller nucleants for more nucleation, the slight extension of the UZ increases the probability of involving a more potent (larger) nucleant.

As directional cooling proceeds, the UZ "sweeps" through the liquid volume from the colder side towards the hotter side, and this arrangement is illustrated in Fig. 5.11. The red dashed line in each graph indicates the boundary between the mushy zone (a mixture of solid and liquid) and full liquid. As time goes from $t = \Delta t$ to $t = 2\Delta t$, UZ moves progressively along positive x. At a higher cooling rate $\dot{T}_2$ (Figs. 5.11(b) and (d)), UZ moves faster and sweeps over a larger volume in the same amount of time Δt, and hence more potent nucleant particles are involved for IMC nucleation within the same amount of time, leading to a higher nucleation rate. However, as the ΔT_{maxG} is dominated by thermal gradient (Fig. 5.9(b)) and only has a weak sensitivity to cooling rate (Fig.5.10(c)), eventually the total number of nucleant particles able to catalyse nucleation (i.e. the smallest particles able to be activated) remained approximately constant against the cooling rate.

The probability of IMC nucleation under directional cooling P_G can therefore be written as a function of interactions between ΔT_{maxG}, which is a strong non-linear function of G (Fig. 5.9(b)) but only a weak function of $\dot{T}$ (Fig.5.10(c)), the UZ, which is also a strong non-linear function of G (Fig. 5.9(a)) but a weak function of $\dot{T}$ (Fig.5.10(c)), and the volume $V_{\Delta T}$ swept by the UZ in time t and at thermal gradient G, cooling rate $\dot{T}$:

$$P_G \propto J(\Delta T_{maxG}(G, \dot{T})) \times K(UZ(G, \dot{T})) \times W(V_{\Delta T}(G, \dot{T}, t)) \tag{5.10}$$

where J, K and W are unknown functions.

Linking back to the findings in the last section, the near isothermal cooling gave the highest IMC number density and average formation rate (Fig. 5.5),

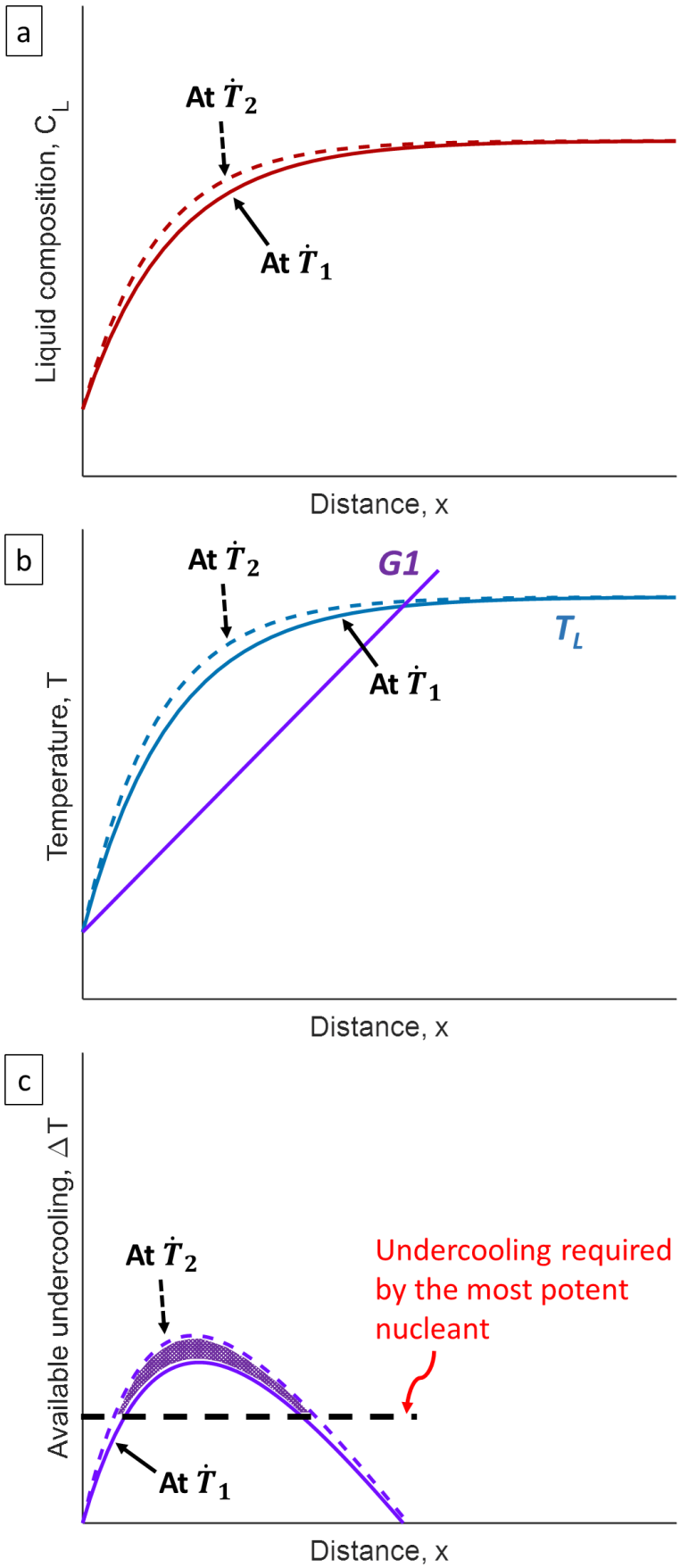


Figure 5.10: (a) A schematic of liquid composition profiles in front of a growing IMC at cooling rate $\dot{T}_1$ and $\dot{T}_2$ ($\dot{T}_2 > \dot{T}_1$)). (b) A schematic of equilibrium liquidus temperature profiles and the undercooled zones (UZ) at $\dot{T}_1$ and $\dot{T}_2$, at a thermal gradient of G_1. (c) Resultant distribution of available undercooling at $\dot{T}_1$ and $\dot{T}_2$, at G_1. The black dashed line indicates the undercooling required by the most potent nucleants to catalyse nucleation.

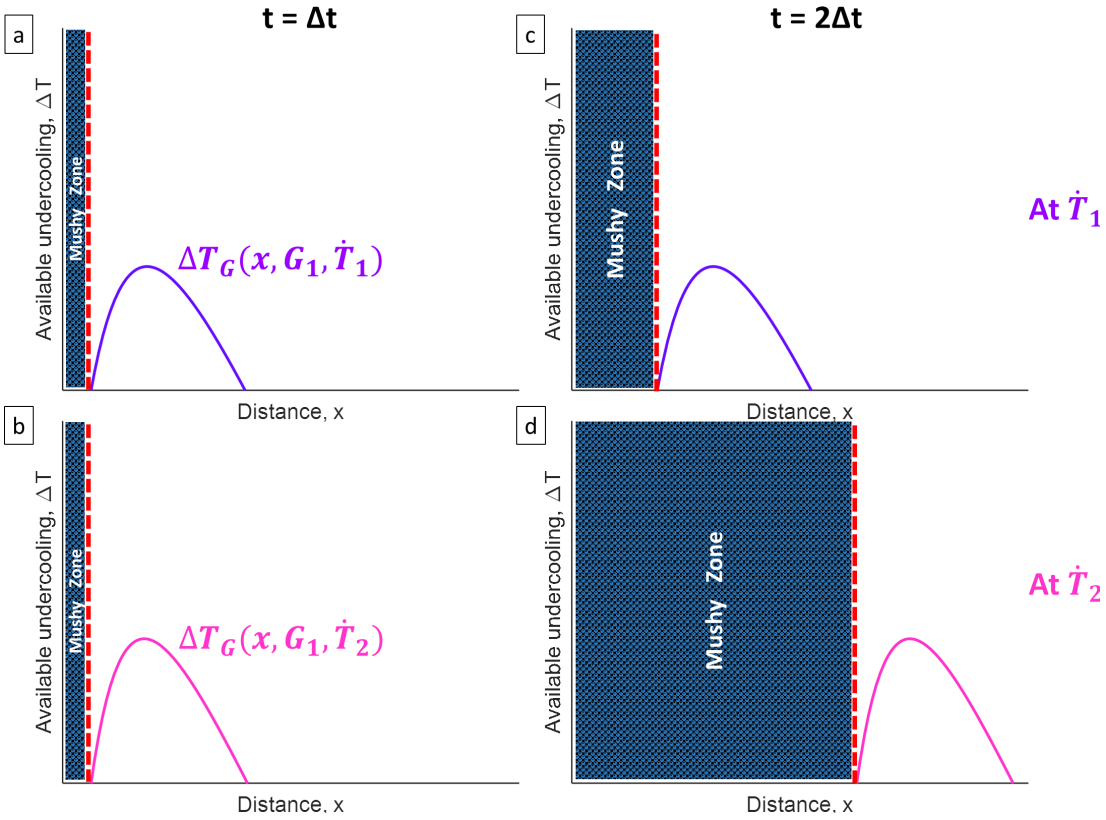


Figure 5.11: A schematic illustrating the translation of UZ with time, at two different cooling rates $\dot{T}_1$ and $\dot{T}_2$ ($\dot{T}_2 > \dot{T}_1$), at a thermal gradient of $G1$. The red dashed line in each graph indicates the boundary between the mushy zone (a mixture of solid and liquid) and full liquid.

because it possessed the largest UZ and highest available undercooling at any instant, and the directional cooling at $8\,\mathrm{K\,mm^{-1}}$ thereby gave the lowest IMC density and average formation rate. Under near isothermal cooling, both the IMC density and average formation rate increased with cooling rate (Fig. 5.2), because a higher cooling rate gave rise to a higher achievable undercooling that activated more nucleant particles for IMC nucleation i.e. not only the most potent nucleants but also the progressively less potent ones. Under directional cooling, only the average formation rate increased with cooling rate (Fig. 5.4(b)) whilst the IMC density had a weak cooling rate sensitivity (Fig. 5.4(a)), because cooling rate only strongly affected the speed at which the UZ swept through the liquid volume but had a weak effect on the magnitude of the available undercooling i.e. the total number of nucleants able to be activated for IMC nucleation was

dominated by the thermal gradient. The formation temperature under directional conditions increased with cooling rate (Fig. 5.6), and this can be explained by the slight extension of UZ at increasing cooling rate (Fig. 5.10(c)), which increased the probability of involving a potent nucleant for easier nucleation (i.e. at a higher temperature).

5.3.3 IMC formation undercooling

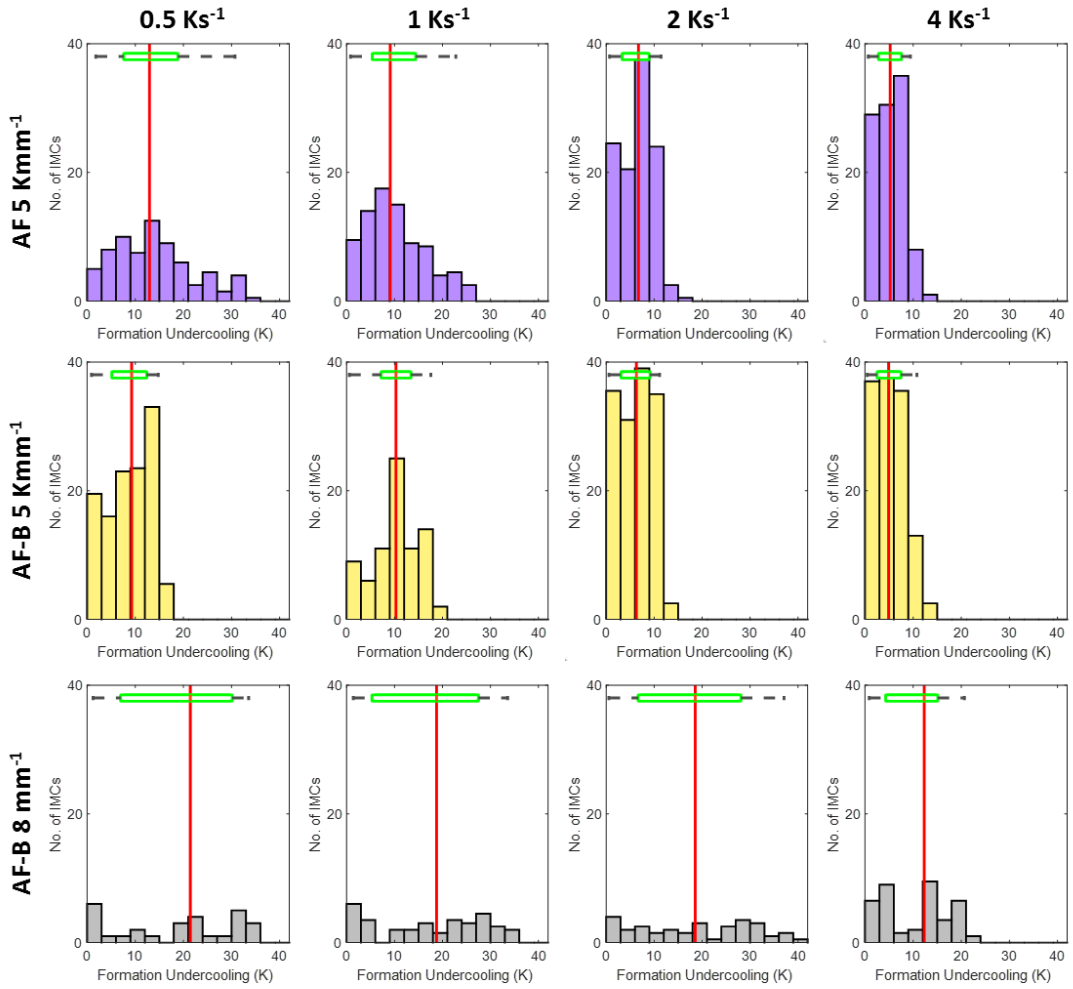


Figure 5.12: Histograms showing the distribution of estimated formation undercooling of primary IMCs for each of the 12 experimental conditions. The term formation undercooling refers to the actual undercooling at which an IMC forms on any potent nucleant. Each histogram was averaged against the number of repeat experiments. A box plot is superimposed at the top of each histogram to show the median undercooling (red line), the 25% and 75% percentile (green box), and the 5% and 95% percentile (the whiskers).

A method to estimate the formation undercooling of individual primary IMCs was described in Section 3.4.2.5 in Chapter 3. This formation undercooling should be distinguished from available undercooling in the liquid, and refers to the actual undercooling at which an IMC formed on any potent nucleant. The formation undercooling will always be less than the available undercooling. Fig. 5.6 showed a plot of the formation temperature of primary IMCs. However, to calculate the formation undercooling of each individual IMC, one needs to know the instantaneous liquidus temperature, i.e. the instantaneous liquid composition where each IMC was forming, as the remaining liquid became increasingly depleted in Fe concentration with the formation of more and more primary IMCs. A method was therefore developed that allowed an approximate estimation of the instantaneous liquidus temperature and the formation undercooling of each primary IMC. A full account of this method is given in Section 3.4.2.5 in Chapter 3.

Fig. 5.12 shows the distribution of estimated IMC formation undercooling for AF at $5\,\mathrm{K\,mm^{-1}}$, and AF-B at $5\,\mathrm{K\,mm^{-1}}$ and $8\,\mathrm{K\,mm^{-1}}$, at different cooling rates. AF and AF-B at $5\,\mathrm{K\,mm^{-1}}$ showed no apparent difference in the median value of the IMC formation undercooling at each cooling rate. In addition, both AF and AF-B displayed a mild trend of decreasing median formation undercooling with increasing cooling rate, from $\sim$10 K at 0.5 $\mathrm{Ks^{-1}}$ to $\sim$5 K at 4 $\mathrm{Ks^{-1}}$. The same trend with cooling rate was also maintained at the higher thermal gradient of $8\,\mathrm{K\,mm^{-1}}$, however with a marked increase in median formation undercooling. This general trend of slight decrease of median formation undercooling with increasing cooling rate is consistent with the finding proposed by Liotti *et al.* [210] on formation undercooling of equiaxed Al dendrites in Al-Cu alloys. This can be explained by the slight increase of UZ at higher cooling rate, as shown in Fig. 5.10(c), which increased the probability of involving a potent nucleant particle that required lower undercooling for IMC nucleation. Meanwhile, the increased formation undercooling at higher thermal gradient in the estimation can be ex-

plained as a result of the reduced UZ at increasing thermal gradient (Figs. 5.8(c) and 5.9(a)), which reduced the probability of a potent nucleant residing in the UZ.

It is also worth noting that - according to this approximate method - median IMC undercoolings spanned the range 5 to 20 K. These values are much greater than for primary Al, even when TiB_2 was added. This suggests that oxides, TiB_2 and TiC are all "poor" nucleants for $Al_{13}Fe_4$, or that this phase intrinsically has a high energy barrier to formation, highly related to a high entropy of fusion. These estimates of undercooling are consistent with those obtained by calorimetry, which showed a "nucleation undercooling" of 15 K at 0.7 Ks^{-1} [215]. However, attention needs to be drawn here that the "nucleation undercooling" measured by calorimetry is always a volumetric average value of the entire specimen (by assuming a good isothermal condition), i.e. when a release of latent heat arising from a liquid-solid phase transformation in the specimen is first detected by the calorimetry. In contrast, the approximate method in this work estimated the distribution of undercooling for individual IMCs.

5.4 Summary

The formation of primary $Al_{13}Fe_4$ IMCs and the effect of TiB_2 and TiC inoculation during solidification of a hypereutectic Al-3Fe alloy has been investigated systematically using *in-situ* laboratory and synchrotron X-ray arrangements. With 2725 IMCs studied in 34 near isothermal, horizontal experiments and 1893 IMCs studied in 22 directional, vertical experiments, the key findings are summarised as follows.

1. TiB_2 and TiC inoculation consistently increased the number density and average formation rate of primary Fe-rich IMCs under all conditions.

2. In vertical, directional cooling, IMCs primarily nucleated on the sample

oxide skins in the non-inoculated alloy, but nucleated preferentially on the TiB_2 particles when TiB_2 was added.

3. Near isothermal solidification showed the highest IMC number density and average formation rate, and both increased with increasing cooling rate. Under directional solidification, thermal gradient dominated the overall IMC density, whilst increase in cooling rate only enhanced the average formation rate.

4. A conceptual model for IMC nucleation was proposed to explain the effect of thermal gradient and cooling rate on the IMC number density and average formation rate. It concluded that: under isothermal cooling, the probability of IMC nucleation was controlled by the net achievable undercooling in the liquid, which was dominated by cooling rate (in competition with latent heat release and soft impingement of solute diffusion field); whilst under directional cooling, the probability of nucleation was controlled by the volume of undercooled liquid and the magnitude of the available undercooling within the volume, which were dominated by thermal gradient.

Chapter 6

Growth of faceted IMC crystals

6.1 Introduction

This chapter focuses on growth of faceted IMCs, including secondary Fe-rich IMCs in model Al-Cu-Fe alloys, primary Fe-rich IMCs in a model hypereutectic Al-Fe alloy and primary Pt-rich IMCs in a model Al-Pt-Er alloy. First, for the model Al-Cu-Fe alloys, secondary Al_7Cu_2Fe IMCs formed and grew in a constrained condition within inter-dendritic liquid channels, as in commercial Al alloys. Second, for the model Al-Fe hypereutectic alloy, $Al_{13}Fe_4$ IMCs formed as a primary phase and grew in a relatively unconstrained manner. Third, in order to obtain better absorption contrast to be able to investigate the growth of individual facets of anisotropic IMC crystals, a model Al-Pt-Er alloy was developed as described in Chapter 3, which formed highly faceted $Al_{24}Pt_9Er_4$ crystals as primary phase, directly from the liquid.

Time-resolved measurements of faceted growth of 106 IMCs in the three alloys suggested that the length and velocity evolution of both secondary IMCs in constrained liquid and primary IMCs in unconstrained liquid were governed by the solute field in the liquid, immediately ahead of the solid/liquid interface. With better image quality and the absence of primary Al dendrites in the

field of view, primary Fe-rich IMCs and Pt-rich IMCs with microscopic twins were revealed, and supported the hypothesis proposed by earlier researchers that anisotropic growth of elongated IMC crystals was facilitated by repeated twin plane re-entrant corners along the preferential growth direction, via a twin plane re-entrant edge (TPRE) mechanism [75]. In contrast, primary Fe-rich and Pt-rich IMCs with layered, parallel twin platelets were also observed, which reduced the crystal aspect ratio. Further work might explore chemical modifiers to "poison" the re-entrant corners to restrict the anisotropic TPRE mechanism in order to promote more isotropic crystal morphologies.

6.2 Results and Discussion

6.2.1 Growth of secondary IMCs

Secondary Fe-rich IMCs in the model Al-Cu-Fe alloys grew with one of two morphologies: relatively long needles or convoluted branched morphologies, depending if primary α-Al grain refiner (TiB_2) was added or not, as previously shown in Chapter 4. Fig. 6.1 shows again IMCs from two solidification sequences of 0.8Fe and 0.8Fe-GR. Without grain refiner in Fig. 6.1(a), the morphology of the α-Al primary phase was columnar because of the strong 1-D temperature gradient, growing bottom to top, and the IMCs grew along/in the inter-dendritic channels between columnar grains with a straight, needle-like morphology without branching. When grain refiner was added to the same alloy in Fig. 6.1(b), the α-Al primary phase became equiaxed (as intended) and the IMCs growing in the branched interdendritic channels were significantly shorter.

Fig. 6.2 shows the length and growth velocity of 6 long IMCs measured in the non-grain refined alloy and 15 short IMCs in the grain refined counterpart both at a cooling rate of 0.2 Ks^{-1}. All the long IMCs grew at an approximately constant velocity of $146 \pm 22\,\mu m\,s^{-1}$ across the field of view. The final length exceeded

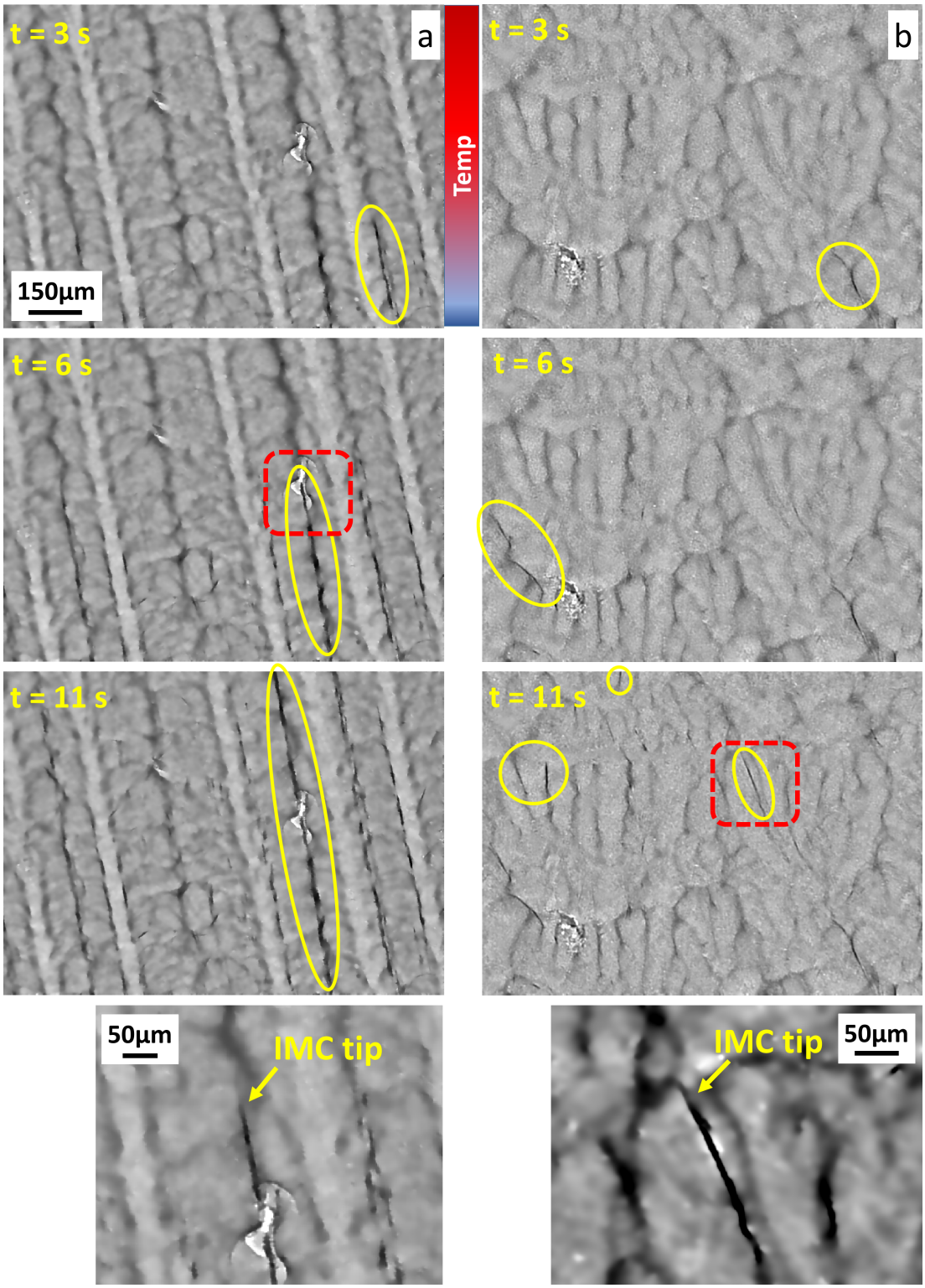


Figure 6.1: Radiograph sequences of IMC growth at a cooling rate of 0.2 Ks^{-1} in (a) 0.8Fe and (b) 0.8Fe-GR, with zoomed-in images showing the IMC tips. Time $t = 0$ was set when IMCs first appeared at the bottom of the field of view.

2000 µm, which was the typical size of the field of view. In contrast, growth of all the short IMCs in the grain refined alloy started with an initial velocity comparable to the long IMC, but velocity decreased rapidly towards zero. Two

hypotheses are therefore proposed here to account for the different IMC growth behaviour in the non-grain refined and grain refined alloys.

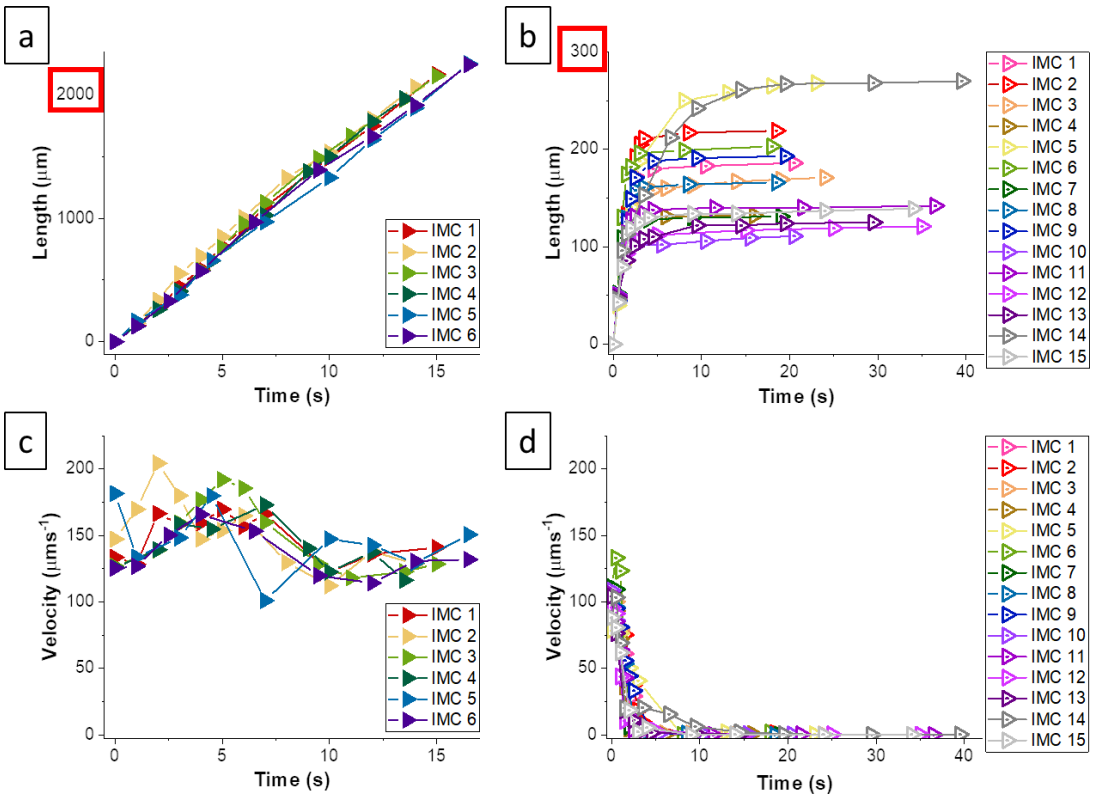


Figure 6.2: (a) Evolution of length of 6 long IMCs in 0.8Fe at 0.2 Ks^{-1}. (b) Evolution of length of 15 short IMCs in 0.8Fe-GR at 0.2 Ks^{-1}. The red rectangles highlight the difference in the length scale. (c) Velocity evolution of the long IMCs in 0.8Fe. (d) Velocity evolution of the short IMCs in 0.8Fe-GR.

Physical constraint and impingement In the non-grain refined alloy, the long and straight 1D inter-dendritic channels physically promoted continuous propagation of the IMCs, growing aligned to the principal temperature gradient direction. However in the grain refined alloy, the convoluted channels and the surrounding equiaxed Al grains physically restricted the growth of the IMCs and frequent re-nucleation was therefore necessary for IMCs to follow the liquid channels.

Solute constraint In the non-grain refined alloy, the straight channels collected solute rejected by Al dendrites that could be transported comparatively easily up/down the channels to feed the growth of the Cu and Fe rich IMCs continuously. Evidence to support this hypothesis is that the IMCs and the Al dendrites grew at very similar velocities: the columnar Al dendrites propagated at $164 \pm 24\,\mu m\,s^{-1}$, compared with $146 \pm 22\,\mu m\,s^{-1}$ for the IMCs. This may imply that the rate at which solute was rejected by Al dendrites was comparable with the rate at which the solute was consumed by the growing IMCs. In contrast, since the liquid channels were more convoluted in the grain refined alloy and inter-connectivity of the liquid reduced, each channel tended to act as a small solute reservoir that was either partially or entirely isolated from other regions of solute rich liquid, particularly in the final stages of solidification. Therefore a decay in growth velocity was observed due to depletion of the local solute in the local liquid channel.

6.2.2 Growth of primary IMCs

Manual time-resolved length and width measurement of primary Fe-rich IMC crystals was conducted from typically 5 frames (0.5 s) after the first appearance of an IMC until the terminal eutectic formed, which indicated the end of solidification.

Fig. 6.3(a) shows an example radiograph of solidifying Al-3Fe (wt%) where faceted Fe-rich crystals formed as primary phase. The yellow rectangle indicates the field of view of the radiograph sequence in Fig. 6.3(b). In the sequence, $t = 0$ was set at the beginning of the IMC size measurement. The IMC crystal grew in free liquid with no impingement against any neighbouring IMCs. Twin morphologies in many of the IMCs were suggested, and this is discussed in detail in the next section. Later, Al dendrites formed around the growing IMCs ($t = 64$ s), towards the end of solidification. Finally at $t = 67$ s, the remaining liquid

solidified via a eutectic reaction.

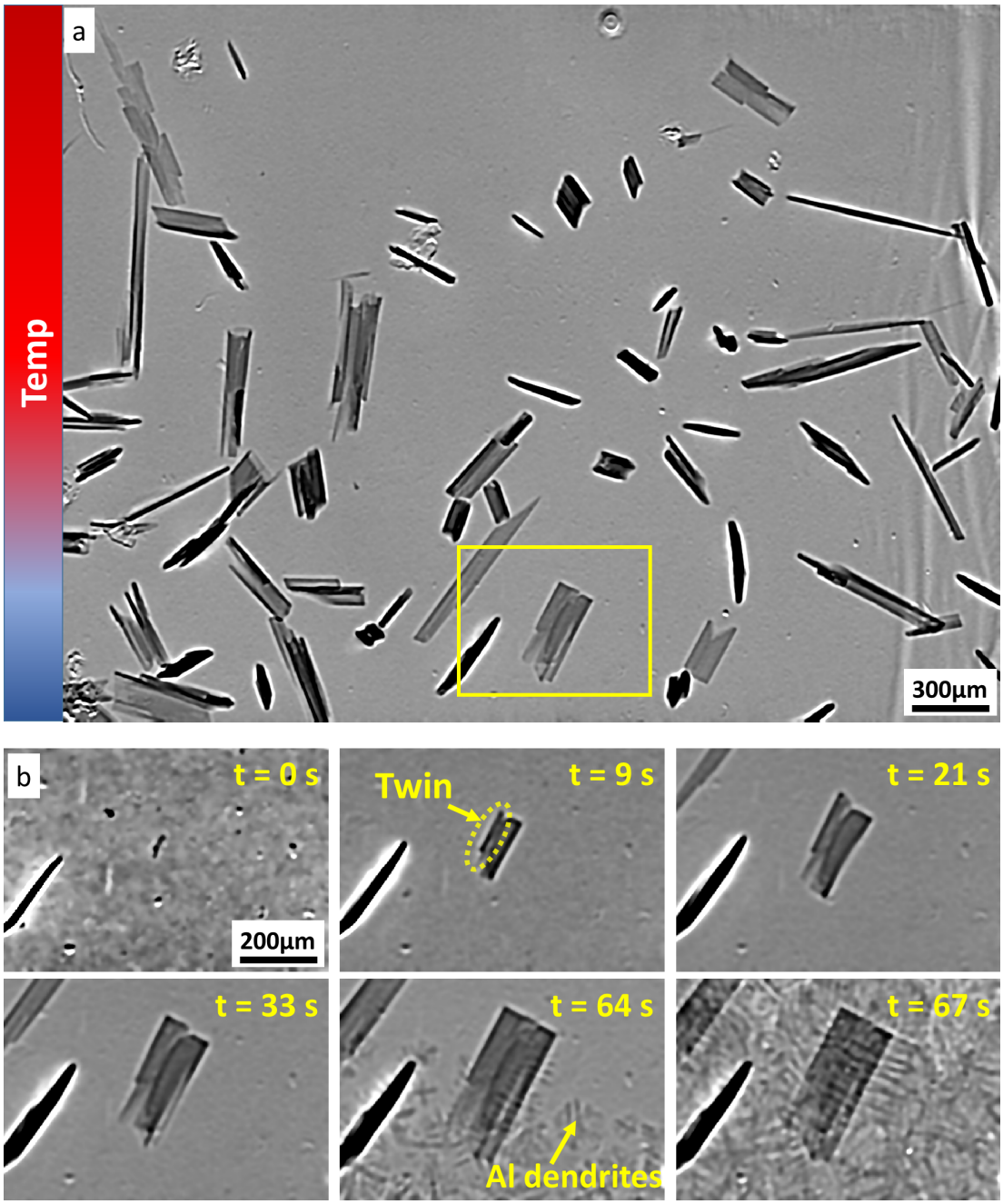


Figure 6.3: (a) An example radiograph showing primary Fe-rich IMCs in solidifying Al-3Fe (wt%) at 0.5 Ks^{-1}. The yellow rectangle indicates the field of view of the radiograph sequence in (b). (b) A radiograph sequence showing growth of a faceted Fe-rich crystal. $t = 0$ was set at the beginning of the size measurement.

Fig. 6.4(a) shows the evolution of length and width with time for the IMC in Fig. 6.3(b), and Fig. 6.4(b) shows the growth velocity along orthogonal directions aligned along the IMC length and width. A graph at finer scale is inset to show

in more detail the growth velocity of the IMC width at $0 < t < 20$ s. The length velocity was initially approximately 20 µm s^{-1} and then decayed to below 2 µm s^{-1} after 40 s, with some fluctuations between $t = 5$ s and $t = 40$ s. Although the IMCs formed as primary phase and grew without physical constraint in free liquid (in comparison with the secondary Fe-rich IMCs), the trend of a rapid decay in velocity was similar to the secondary IMCs in the grain refined Al-Cu-Fe alloy in Fig. 6.2(d). Referring back to the hypotheses proposed in Section 6.2.1, the rapid decrease in velocity may be explained as a result of depletion in local solute, as the Fe preferentially segregated into the IMCs and the composition of the surrounding liquid was shifted from hypereutectic towards eutectic composition. Qualitatively, the IMC has a narrow composition and it became progressively more difficult, i.e. slower, to provide Fe atoms from a progressively more dilute liquid to sustain the growth. It is also likely that reducing curvature of the IMC as it became larger may have contributed to a reducing driving force for growth.

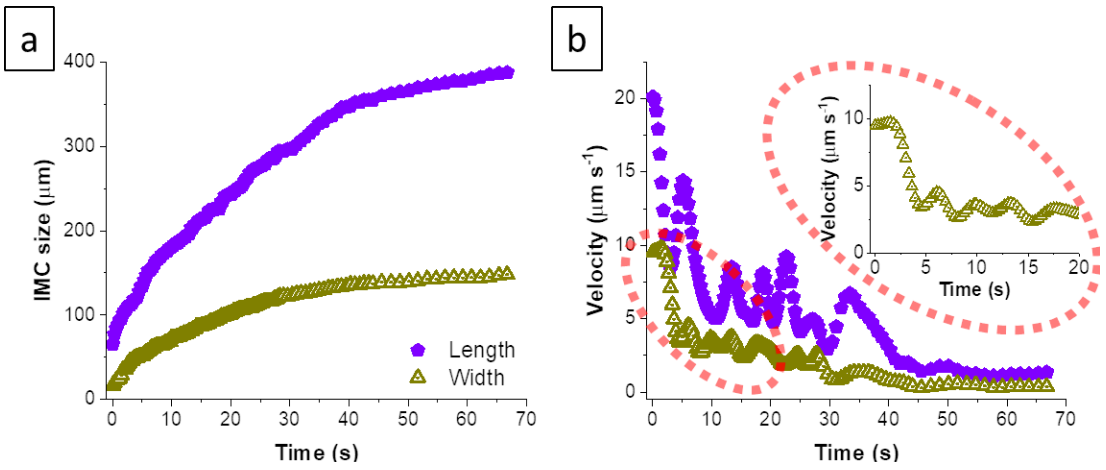


Figure 6.4: (a) Evolution of length and width with time for the IMC in Fig. 6.3(b). (b) Growth velocity of the length and width. $t = 0$ was set at the beginning of the size measurement. The inset shows detail of the growth velocity of the width at $0 < t < 20$ s.

Growth in the IMC width started at a velocity of approximately 10 µm s^{-1}, i.e. approximately half of the length velocity, which reflected the anisotropy of the $Al_{13}Fe_4$ crystal. There was then a similar decay of velocity as the length velocity.

At the earliest stage of width growth, there was a short period of approximately 2 s when the velocity was maintained at $\sim$10 µm s^{-1} (Fig. 6.4(b)). Assuming the hypothesis of solute constraint holds, this short period of nearly constant velocity may relate to relative abundance of Fe atoms close to the solid/liquid interface, before a significant diffusion profile in the liquid was established. The subsequent periodic fluctuations in velocity for both width and especially length are explained in the section below.

6.2.3 Twinning

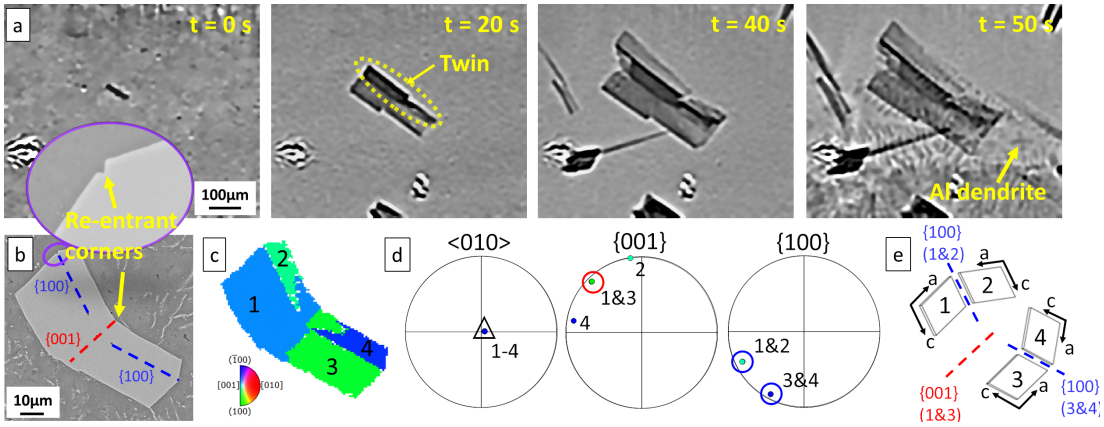


Figure 6.5: (a) A radiograph sequence of growth of a primary $Al_{13}Fe_4$ crystal, showing suspected twinning. (b) A secondary electron image of a twinned $Al_{13}Fe_4$ crystal in the solidified Al-Fe sample from synchrotron experiments. The dashed lines indicate the twin planes, which in this case are perpendicular to the paper, and the yellow arrows denote the re-entrant corners at the twin boundary. (c) An IPF-X map of the crystal in (b), showing four different orientations. (d) Pole figures of the crystal in (b). (e) Unit cell wire frames that illustrate the four different orientations.

Microscopic twinning was frequently suspected during growth of primary Fe-rich IMCs in Al-Fe (Figs. 6.3(b) and 6.5(a)) and growth of primary Pt-rich IMCs in the Al-Pt-Er alloy (Fig. 6.6(a)), on the slow growing facets of the crystals. The presence of twins was further investigated by EBSD on the solidified samples from the synchrotron experiments. Two types of twin were identified in $Al_{13}Fe_4$, as shown in Fig. 6.5(b) to (e). According to the IPF-X map (Fig. 6.5(c)), there

were four orientations in the $Al_{13}Fe_4$ crystal. The interface between 1 and 2 and between 1 and 3 coincided with the re-entrant corners on the facets, as highlighted in Fig. 6.5(b). Pole figures in Fig. 6.5(d) show that these four orientations shared the common monoclinic ⟨010⟩ direction. The common {001} plane (highlighted by a red circle in Fig. 6.5(d)) between 1 and 3 corresponded to the interface highlighted by a red dashed line in Fig. 6.5(b). The interface between 1 and 2 and between 3 and 4, is the {100} plane (highlighted by blue circles), corresponding to the blue dash lines in Fig. 6.5(b). The unit cell wire frames of these four orientations are plotted in Fig. 6.5(e). The twin type is identified as a 180° rotation along the common a-axis between 1 and 3 with {001} being the twin plane ({001} twinning), and a 180° rotation along the common c-axis between 1 and 2 (3 and 4) with {100} being the twin plane ({100} twinning).

According to [209], $Al_{24}Pt_9Er_4$ has a triclinic crystal structure with a monoclinic sub-cell that has the same space group as $Al_{13}Fe_4$. Similar to $Al_{13}Fe_4$, a re-entrant corner was observed (indicated by a yellow arrow in Figs. 6.6(a) and (b)). EBSD revealed two different orientations in the crystal: the Kikuchi patterns (Figs. 6.6(c) and (d)) of area 1 and 2 (as denoted in Fig. 6.6(b)) share some similarities but are nonetheless different. Superimposed Euler angle maps are plotted in Figs. 6.6(e) and (f), by indexing the crystal as a triclinic and monoclinic structure, respectively. For the triclinic unit cell, pole figures show that the two orientations shared a common {001} plane and a common ⟨010⟩ direction. The twin type is identified as a 180° rotation along the common ⟨010⟩ direction with {001} being the twin plane. When indexed with the monoclinic sub-cell, the two orientations show a common {001} plane and a common ⟨100⟩ direction, and the twin type is therefore identified as 180° rotation along ⟨100⟩ with {001} being the twin plane.

As discussed in Chapter 2, a twin plane re-entrant edge (TPRE) mechanism has been identified for the crystal growth of Ge and Si [61, 62], where anisotropic

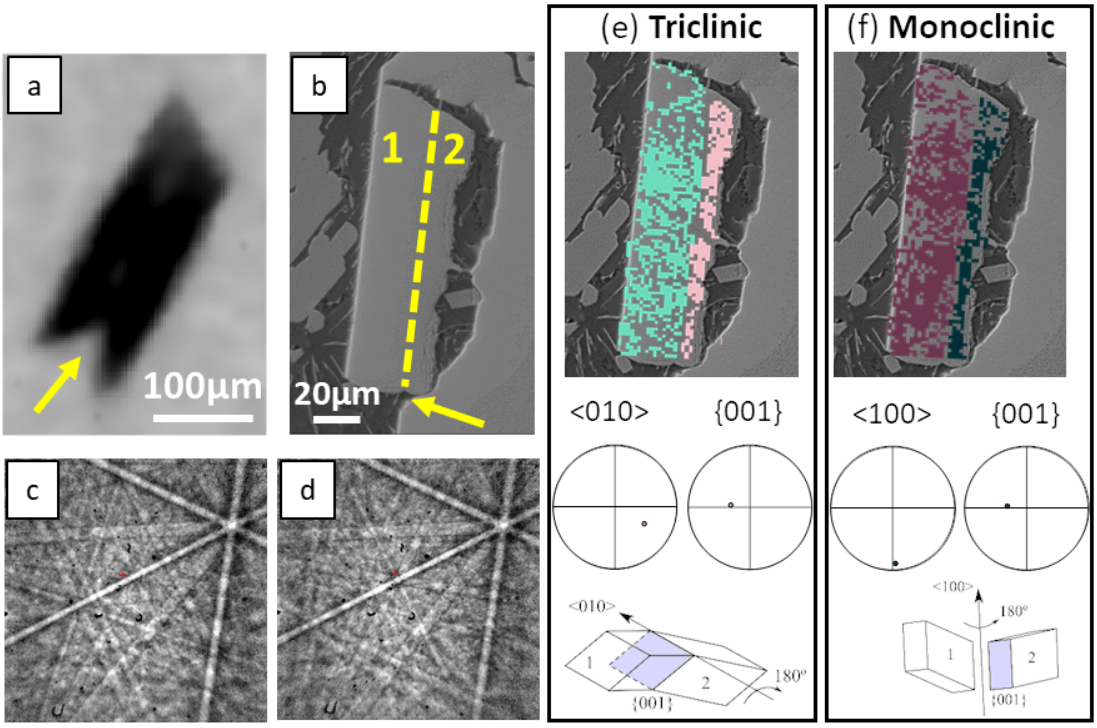


Figure 6.6: (a) A radiograph of a typical twinned primary $Al_{24}Pt_9Er_4$ crystal. (b) A secondary electron image of a twinned $Al_{24}Pt_9Er_4$ crystal in the solidified Al-Pt-Er sample from synchrotron experiments. The yellow dash line indicates the twin plane, which is perpendicular to the paper, and the yellow arrow denotes the re-entrant corner. (c) The Kikuchi pattern of area 1 in (b). (d) The Kikuchi pattern of area 2 in (b). (e) Superimposed Euler angle map, pole figures, and unit cell wire frames for the $Al_{24}Pt_9Er_4$ crystal, indexed as a triclinic structure. (f) Superimposed Euler angle map, pole figures, and unit cell wire frames for the same $Al_{24}Pt_9Er_4$ crystal, indexed as a monoclinic structure.

growth along the $\langle 11\bar{2} \rangle$ directions was facilitated by repeated formation of re-entrant corners (grooves in 3D) between the {111} twins, which were believed to provide low energy sites for the attachment of atoms during solidification. The same mechanism was also suggested to account for the growth of elongated platelet Fe-rich IMCs based on frequent microscopic observation of growth twins [73–75]. However to the best of the author's knowledge, there has been no prior *in-situ* solidification evidence focused on growth twins.

Fig. 6.7(a) is a radiograph sequence showing the growth of a millimetre-long primary Fe-rich IMC platelet, where suspected twin platelets appeared repeatedly along the preferential growth. This gave rise to the development of repeated re-

entrant corners, which perpetuated the anisotropic growth.

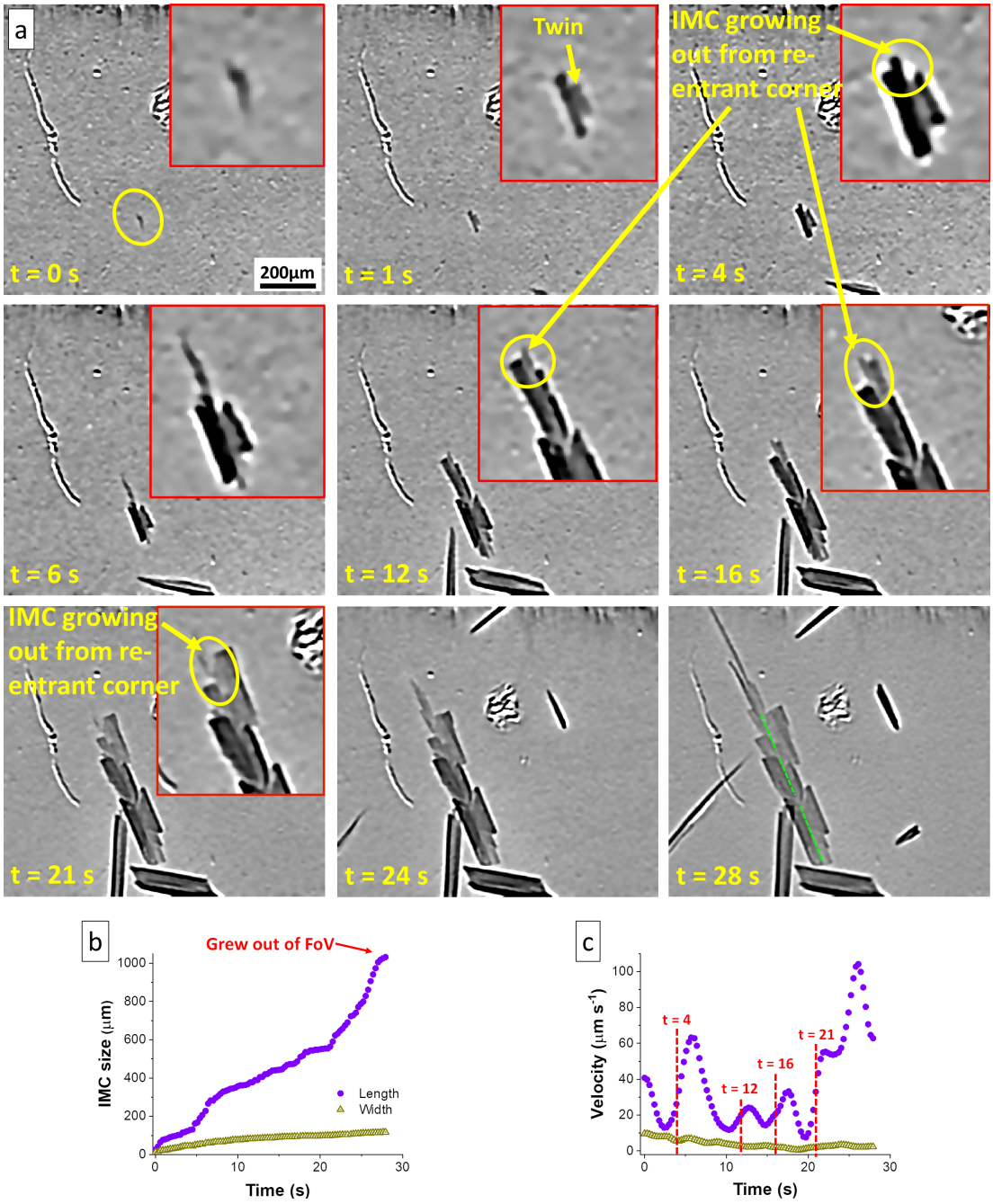


Figure 6.7: (a) A radiograph sequence of growth of an elongated $Al_{13}Fe_4$ crystal at 0.5 Ks^{-1}, showing repeated suspected twin platelets and re-entrant corners. $t = 0$ was set at the beginning of the size measurement. Inset images with red frames provided a zoomed-in view. The green dashed lines at $t = 28$ s highlight the boundaries between the suspected twin platelets. (b) Evolution of the length and width. The IMC grew out of the field of view after $t = 28$ s. (c) Evolution of growth velocities along the length and width. The time when a new plate appeared at the re-entrant corners ($t = 4$ s, $t = 12$ s, $t = 16$ s and $t = 21$ s) is labelled.

At time $t = 1$ s, a suspected twin platelet was observed on the slow growing facet of the crystal. At $t = 4$ s, a new plate was observed at the re-entrant corner (or groove) between the twin platelets and propagated rapidly along the original growth direction (see $t = 6$ s in Fig. 6.7(a)). A twin plate then appeared on this newly developed platelet and gave rise to another re-entrant corner, and the IMC continued to propagate from the new re-entrant corner ($t = 12$). The process repeated ($t = 12$ s, $t = 16$ s and $t = 21$ s), allowing the crystal to keep growing along its preferential direction, and gave rise to the highly elongated platelet crystal shown at $t = 28$ s. The crystal then continued to grow out of the field of view. The green dashed lines at $t = 28$ s in Fig. 6.7(a) highlight the boundaries between the suspected twin platelets.

Figs. 6.7(b) and (c) shows the evolution of the length, width and their velocities of the elongated IMC. The graphs are of the same types as shown earlier in Figs. 6.4(a) and (b). The velocity plot shows even more distinct periodic fluctuations than those in Fig. 6.4(b). Combining the radiograph sequence and the velocity profile of the IMC length, a peak velocity was always observed (Fig. 6.7(c)) following the development of each re-entrant corner (assessed as when a new plate first appeared at the re-entrant corners: $t = 4$ s, $t = 12$ s, $t = 16$ s and $t = 21$ s, as labelled in Fig. 6.7(c)).

Although the final length of the IMC was not able to be assessed, it grew up to 1046 μm by $t = 28$ s, corresponding to an average velocity of $37\,\mu\mathrm{m\,s^{-1}}$. The IMC in Fig. 6.4(b) had an average length velocity of $5\,\mu\mathrm{m\,s^{-1}}$. Despite the significant difference in crystal size and the magnitude of length growth velocity, qualitatively the plots in Fig. 6.4(b) and Fig. 6.7(c) are very similar, suggesting the same mechanism operated. The radiographs in Fig. 6.7(a) and the time-resolved measurements in Figs. 6.7(b) and (c) showed a link between the repeated formation of a re-entrant (TPRE) corner and the preferential anisotropic growth. This finding is in good qualitative agreement with the hypothesis proposed by Adam

and Hogan [75] that that growth of elongated $Al_{13}Fe_4$ platelets was facilitated by a TPRE mechanism as a result of repeated formation of re-entrant corners.

In contrast to this highly elongated IMC plate, crystals containing layered platelets were also observed, which had a much smaller aspect ratio. Fig. 6.8(a) shows an example, where the layered platelets observed were plausibly multiple parallel twins.

Growth of the crystal started with an initial velocity of $80\,\mu m\,s^{-1}$ in length (Fig. 6.8(c)) in the form of a thin plate. However, this velocity decayed rapidly to below $10\,\mu m\,s^{-1}$ in 3 seconds. In the meantime, a suspected twin platelet was observed on the slow growing facet of the crystal, increasing the crystal size along the non-preferential direction (i.e. the width). Following this, a new thin plate grew out from between the two platelets, leading to a peak velocity up to $35\,\mu m\,s^{-1}$ measured at $t = 10$ s. The yellow dashed line at $t = 10$ s in Fig. 6.8(a) highlights the boundary between the suspected twin platelets and the yellow circle highlights the thin plate growing between. Following this peak velocity, there was a long period of slow growth in length. Between $t = 23$ s and $t = 50$ s, the velocity along the preferential direction (i.e. the length) remained relatively low at 2 to $3\,\mu m\,s^{-1}$ (Fig. 6.8(c)), which was approximately equal to the velocity along the non-preferential direction. This period of "suppression" of the preferential growth probably resulted from solute constraint due to the presence of other IMCs either "below" or "above" it, as shown in the field of view in Fig. 6.8(a). Towards the later stage of the growth (i.e. later stage of solidification), a thin IMC platelet shot out and overgrew the other platelets in the crystal, as highlighed by a yellow dashed rectangle at $t = 72$ in Fig. 6.8(a). However, because of the presence of a pre-existing crystal in the path, growth of this thin plate stopped on impingement. Compared with the elongated IMC in Fig. 6.7(a) where there was no IMCs above it to constrain its preferential growth, the crystal in Fig. 6.8(a) possessed a reduced length of 825 μm (compared with 1046 μm),

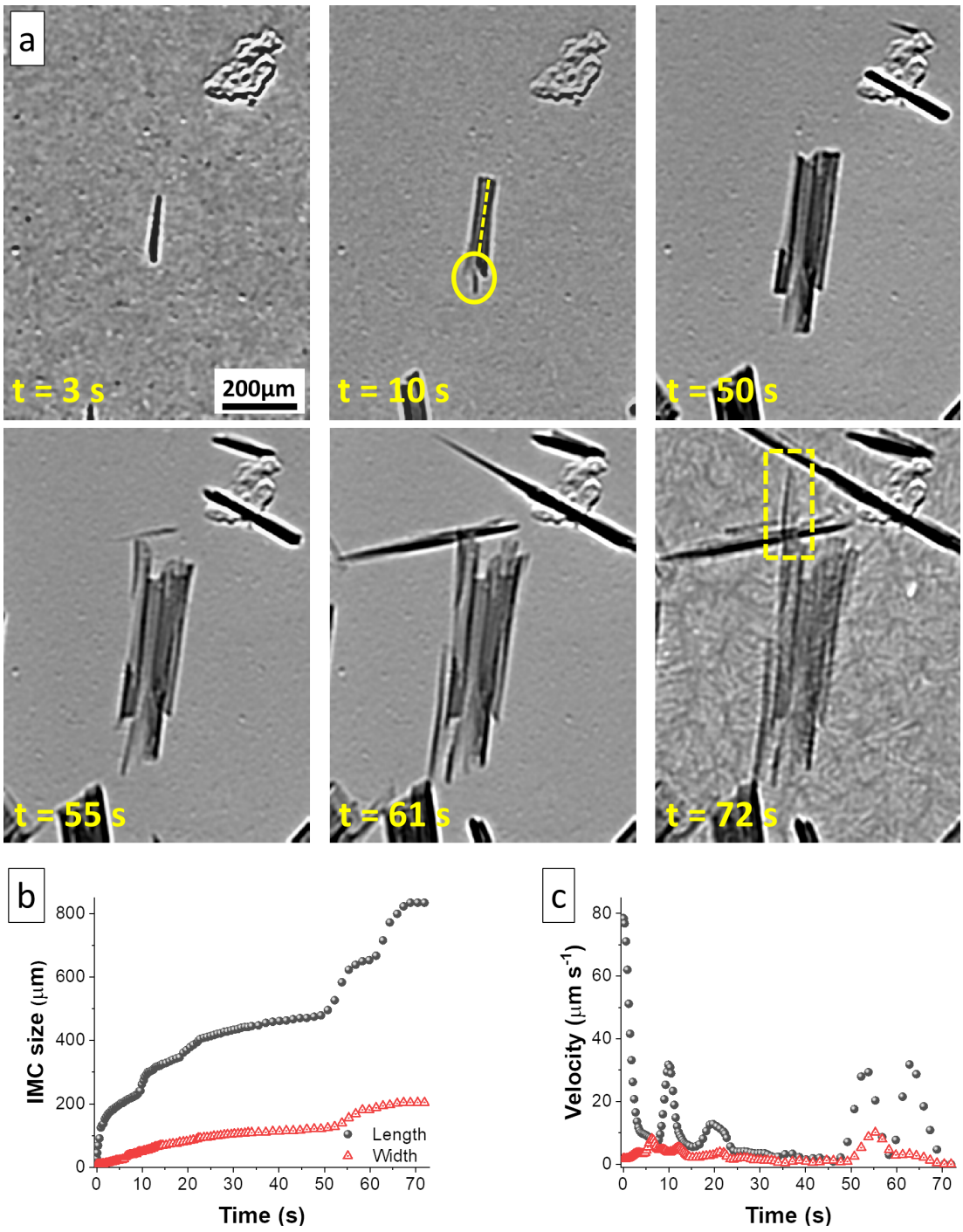


Figure 6.8: (a) A radiograph sequence showing growth of a primary $Al_{13}Fe_4$ crystal containing layered platelets perpendicular to its preferential growth direction at 0.5 Ks^{-1}. The yellow dashed line at $t = 10$ s highlights the boundary between two suspected twin platelets, and the circle highlights a new thin plate growing between the two platelets. The dashed rectangle at $t = 72$ highlights a thin IMC plate that overgrew the other platelets of the crystal but eventually was stopped by a pre-existing crystal above it. (b) Evolution of the length and width of the crystal. (c) Evolution of growth velocities of the crystal.

an increased width of 205 μm (compared with 112 μm) and hence a lower aspect ratio of 4 in contrast to an aspect ratio of 9. Furthermore, the crystal showed a reduced average growth velocity of $11\,\mu m\,s^{-1}$ along its preferential direction, compared with $37\,\mu m\,s^{-1}$ for the elongated IMC platelet in Fig. 6.7(a).

Fig. 6.9(a) shows another crystal containing layered microscopic twin platelets, where the preferential growth was constrained by other surrounding IMCs at an earlier stage, resulting in a shorter length of 410 μm and a smaller aspect ratio of 3.4. The length velocity (Fig. 6.9(c)) follows a very similar trend to that in Fig. 6.8(c), however with a much lower initial velocity of $30\,\mu m\,s^{-1}$ (compared with $80\,\mu m\,s^{-1}$) and a lower average velocity of $5\,\mu m\,s^{-1}$ (compared with $11\,\mu m\,s^{-1}$). The reduced preferential growth velocity was probably because the crystal was aligned horizontally so that its preferential direction was easily constrained by other IMCs that formed in adjacent regions (Fig. 6.9(a)) and competed with it for solute. While the preferential growth was constrained, the width of the crystal, where relatively less constraint was experienced, started to grow via the formation of layered microscopic twin platelets. While these twin platelets might not be very noticeable at the earlier stage, because the crystal in this case was significantly smaller than those in Figs. 6.7(a) and 6.8(a), they became more recognisable as growth proceeded. The green dashed lines at $t = 50$ s highlight the boundaries between the microscopic twin platelets, and the green arrow indicates a re-entrant corner.

Comparing Figs. 6.7(c), 6.8(c) and 6.9(c), a significant re-acceleration along the preferential direction was commonly observed towards the end of crystal growth (just before the appearance of the eutectic), where a thin platelet grew out from the bulk crystal (likely from a re-entrant corner). This final-stage re-acceleration might be related to the formation of the Al dendrites towards the later stage of solidification (as denoted at $t = 57$ s in Fig. 6.9(a)). The formation and growth of the Al dendrites rejected Fe into the surrounding liquid, resulting

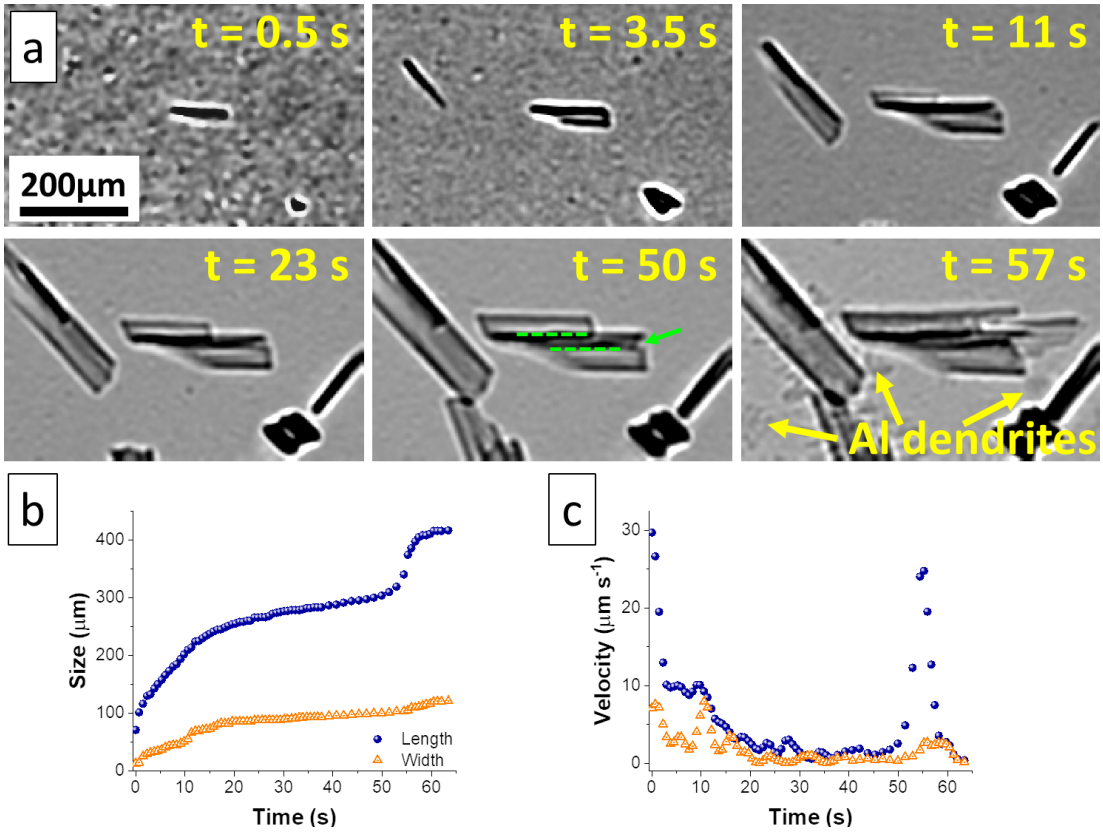


Figure 6.9: (a) A radiograph sequence showing growth of a primary $Al_{13}Fe_4$ crystal containing layered platelets at 0.5 Ks^{-1}. The green dashed lines at $t = 50$ s highlight the boundaries between the microscopic twin platelets, and the green arrow denotes a re-entrant corner. (b) Evolution of crystal length and width. (c) Evolution of growth velocities.

in a Fe-rich liquid environment to feed the growth of primary $Al_{13}Fe_4$ crystals (while also providing driving force for eutectic $Al_{13}Fe_4$).

Layered twins were also frequently observed in $Al_{24}Pt_9Er_4$ in the Al-Pt-Er alloy. The strong X-ray absorption contrast between the Pt-rich IMCs and the liquid facilitated easier identification of this microscopic twin type, as shown in Fig. 6.10(a). In this case, facets were hexagonal and grew "layer upon layer" while maintaining an aspect ratio of ∼1. Growth velocity along the length and width was initially ∼6 μm/s and decayed rapidly to near zero (Fig. 6.10(c)). "Layered" twins, stacked in the plane of the page suggested that growth out of the page occurred via formation of these stacked twin layers. A similar phenomenon has been reported for modified Si crystals [216] and $MgAl_2O_4$ crystals [217].

Recalling that in modified Al-Si alloys (as mentioned in Chapter 2), addition of chemical modifiers such as Sr and Na suppresses the otherwise preferential growth of Si along $\langle 11\bar{2} \rangle$ directions so that layered {111} twins are instead promoted [66, 67, 83, 90, 93]. This contributes to thickening of the platelet crystals via a combination of restricted-TPRE mechanism [66] and the impurity-induced-twinning (IIT) mechanism [67, 93]. This provides an inspiration that analogous chemical modifiers might exist to provide some level of control over the growth morphology of otherwise highly faceted and elongated IMCs due to Fe pick-up in Al alloys. Such modifiers must poison the re-entrant corners and deactivate the anisotropic TPRE growth, and meantime promote layered parallel twins along the thickness, giving rise to a lower and more uniform crystal aspect ratio.

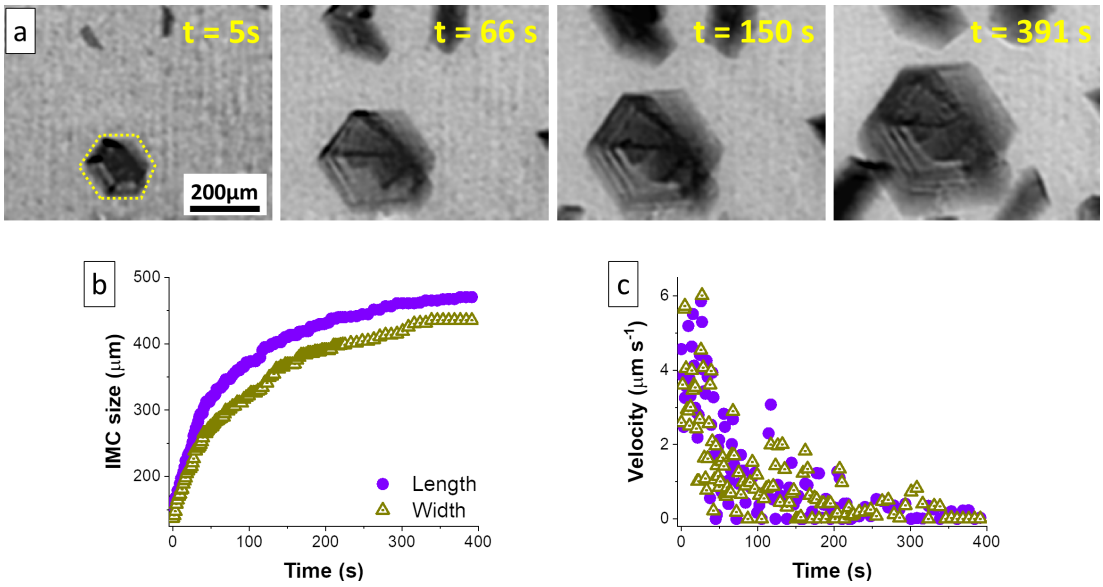


Figure 6.10: (a) A radiograph sequence showing growth of a primary $Al_{24}Pt_9Er_4$ crystal, comprising layered twin platelets, in an Al-Pt-Er alloy at 0.5 Ks^{-1}. (b) Evolution of the length and width of the crystal in (a). (c) Evolution of the length and width growth velocity of the IMC crystal.

6.3 Summary

Faceted growth of primary and secondary IMCs was investigated systematically during the solidification of a series of faceted-IMC-forming model Al alloys, by

using *in-situ* X-ray radiography. The growth of 106 IMCs was tracked and measured frame-by-frame, and the key findings are summarised as follows.

1. Secondary Al_7Cu_2Fe in a non-grain refined Al-Cu-Fe alloy with long and straight inter-dendritic channels grew at a constant velocity, whilst the same IMCs growing in grain-refined alloy counterparts, with convoluted inter-dendritic channels, started with a similar initial velocity but the velocity decayed rapidly towards zero.

2. In the absence of physical constraint, growth of primary $Al_{13}Fe_4$ in the Al-Fe and primary $Al_{24}Pt_9Er_4$ in the Al-Pt-Er showed a decay in velocity similar to the secondary IMCs in the grain refined Al-Cu-Fe. This similar decay in growth velocity for both secondary and primary IMCs suggested that growth in both cases was likely controlled by solute diffusion effects in the liquid immediately ahead of the solid/liquid interface rather than physical constraint or mechanical impingement. Reducing interfacial curvature as IMCs became larger may have also played a role.

3. Microscopic twins during the growth of faceted IMCs were frequently observed in radiography and validated by post-solidification EBSD. Repeated formation of twin plane re-entrant (TPRE) corners were shown to strongly promote the anisotropic growth and the formation of platelet crystals with a high aspect ratio of up to 10. In contrast, for some IMCs where preferential growth was constrained by surrounding crystals, formation of layered, parallel twin platelets perpendicular to the preferential direction promoted thickening of the IMCs and resulted in a much lower aspect ratio.

4. The study provokes thinking that chemical modifiers could be explored that poison the re-entrant corners at an early stage of IMC growth, to restrict the anisotropic TPRE mechanism, and growth may then become facilitated by a less energetically favourable layered twin mechanism, which results in lower

aspect ratio IMCs. Ultimately, more isotropic (and finer scale) IMCs should ameliorate some of the undermining effects of Fe pick-up on commercial Al alloy toughness and tensile ductility.

Chapter 7

Conclusions

The thesis has described investigations of the nucleation, growth and phase selection of Fe-rich IMCs and other related faceted IMC crystals in Al alloy solidification, by using *in-situ* X-ray radiography in combination with post-solidification microscopy. The aim was new insights that could ultimately be used to manage the morphology, size and distribution of IMCs in order to produce more Fe-tolerant Al alloys and/or processing routes.

A method was developed to estimate directly from X-ray radiography videos the temperature at any time and position in the field of view, and this method was then applied to estimate the IMC tip temperatures during growth and the effect on phase selection of 203 secondary Fe-rich IMCs during directional solidification of Al-Cu-Fe alloys across 47 experiments. The estimated IMC tip temperatures show two thermal regimes for Fe-rich IMC formation that were identified by post-solidification SEM/EDX and HR-TEM as Al_6(Fe,Cu) and Al_7Cu_2Fe. TiB_2 grain refiner additions indirectly increased the sensitivity of the IMC tip temperature to cooling rate by increasing the tortuosity of the inter-dendritic liquid channels. By using grain refiner additions together with a higher cooling rate, IMC growth could be delayed to significantly lower temperatures. With grain refiner additions, the size of the IMCs was also significantly reduced from over 2000 µm to below

300 µm.

Nucleation of primary $Al_{13}Fe_4$ and the effect of TiB_2 and TiC inoculation were investigated during solidification of a hypereutectic Al-3Fe alloy, using *in-situ* laboratory and synchrotron arrangements. 2725 IMCs were studied in 34 near isothermal, horizontal solidification experiments, and 1893 IMCs were studied in 22 directional, vertical experiments. TiB_2 and TiC inoculation consistently increased the number density and average formation rate of primary $Al_{13}Fe_4$ IMCs under all solidification conditions studied. In vertical solidification, approximately all the IMCs remained static after formation in the non-inoculated alloy, while frequent settling of IMCs was observed when TiB_2 was added. This indicates that the IMCs nucleated preferentially on the TiB_2 particles when present, and on the "inside" of the sample oxide skin when TiB_2 was absent. For a given cooling rate, near isothermal solidification gave the highest IMC density and average formation rate, both of which decreased when a thermal gradient was applied, and increased. Under near isothermal cooling, both IMC density and average formation rate increased with cooling rate. Under directional cooling, while a higher cooling rate promoted a higher average formation rate, the IMC density had a relative weak sensitivity to cooling rate, and was instead dominated by the effects of the thermal gradient. A conceptual model for IMC nucleation was proposed to explain qualitatively the effect of thermal gradient and cooling rate. It was concluded that the probability of primary IMC nucleation was controlled by the volume of the undercooled liquid and the magnitude of the available undercooling within the volume, and showed how these were both related to the imposed thermal gradient.

Faceted growth of secondary Al_7Cu_2Fe in Al-Cu-Fe alloys, primary $Al_{13}Fe_4$ in an Al-Fe alloy, and $Al_{24}Pt_9Er_4$ (morphologically related to $Al_{13}Fe_4$) in an Al-Pt-Er model alloy, were investigated during solidification. Secondary Fe-rich IMCs in a columnar Al-Cu-Fe alloys without grain refiner addition grew along/within the

long and straight inter-dendritic liquid channels at a constant velocity, whilst the same IMCs, growing in the grain refined equiaxed counterparts with convoluted inter-dendritic channels, started with a similar initial velocity but growth velocity decayed rapidly towards zero. In the absence of physical constraint, growth of primary $Al_{13}Fe_4$ in the Al-Fe and primary $Al_{24}Pt_9Er_4$ in the Al-Pt-Er showed a decay in velocity similar to the secondary IMCs in the grain refined Al-Cu-Fe. This similar decay in growth velocity for both secondary and primary IMCs suggested that growth in both cases was likely controlled by solute diffusion effects in the liquid immediately ahead of the solid/liquid interface rather than physical constraint or mechanical impingement. Meantime, reducing interfacial curvature as IMCs became larger may have also played a role.

Microscopic twins during the growth of faceted IMCs were frequently observed in radiography and validated by post-solidification EBSD. Repeated formation of twin plane re-entrant (TPRE) corners were shown to strongly promote the anisotropic growth and the formation of platelet crystals with a high aspect ratio of up to 10. In contrast, for some IMCs where preferential growth was constrained by surrounding crystals, formation of layered, parallel twin platelets perpendicular to the preferential direction promoted thickening of the IMCs and resulted in a much lower aspect ratio. The study provokes thinking that chemical modifiers could be explored that poison the re-entrant corners at early stage of growth to restrict the anisotropic TPRE mechanism, and growth may then become facilitated by a less energetically favourable layered twin mechanism, which promotes lower aspect ratio IMCs. Ultimately, more isotropic (and finer scale) IMCs should ameliorate some of the undermining effects of Fe pick-up on commercial Al alloy toughness and tensile ductility.

Chapter 8

A look to the future

As mentioned in Chapter 3, the investigation of the Al-Pt-Er alloy was part of a larger project in collaboration with STFC and DLS, aiming to study and understand the role of multi-solute diffusion in the nucleation and growth of faceted IMC crystals in multi-element Al alloys, by utilising the HEXITEC X-ray spectrometer alongside radiography. This chapter briefly outlines some further, preliminary research on *in-situ* multi-element mapping using a combination of the HEXITEC detector and the model Al-Pt-Er alloy, and the future work now planned. The results do not yet provide meaningful new insights relating to nucleation and growth of IMCs in Al alloys, but the results are original, and so far are of interest from a technique and instrumentation perspective. They also suggest the exciting potential for future work more directly relating to solidification theory.

8.1 Multi-element mapping using synchrotron X-ray fluorescence

8.1.1 Experimental set-up

As mentioned in Chapter 3, simultaneous *in-situ* radiography-fluorescence experiments were used to investigate the solidification behaviour of Al-Pt-Er alloys at ESRF and SOLEIL synchrotrons. Fig. 8.1 shows a schematic of the experimental set-up. Samples were positioned at 45° to the incident beam, and two HEXITEC spectrometers were positioned perpendicularly to the incident X-ray beam (one on each side) to collect the fluorescence signals, whilst the transmitted signal was collected by a PCO.Edge detector positioned at the end of the X-ray path. A 50 μm diameter pinhole was positioned between the sample and each detector with careful alignment to generate magnification (Fig. 8.1). The magnification (i.e. image pixel size) of each detector was determined by the ratio between the pinhole-to-detector and sample-to-pinhole distance. Both detectors provided an image pixel size of approximately 40 μm/pixel.

8.1.2 Preliminary results

Fig. 8.2(a) shows a radiograph of a solidifying Al-Pt-Er alloy at 0.1 Ks^{-1}, and Figs. 8.2(b) and (c) show the simultaneous HEXITEC fluorescence map of the distribution of Er and Pt respectively. Fig. 8.2(c) shows that Pt preferentially segregated into the particulate IMC crystals, which were $Al_{24}Pt_9Er_4$. In contrast, Fig. 8.2(b) shows that the long "ribbon" IMC crystal was enriched only in Er, and was primary Al_3Er. Meantime, Fig. 8.2(a) provides strong X-ray absorption contrast between the two phases and details of crystal morphology. While data analysis is still ongoing, simultaneous *in-situ* X-ray radiography and fluorescence shows the potential in studying the multi-solute redistribution during formation

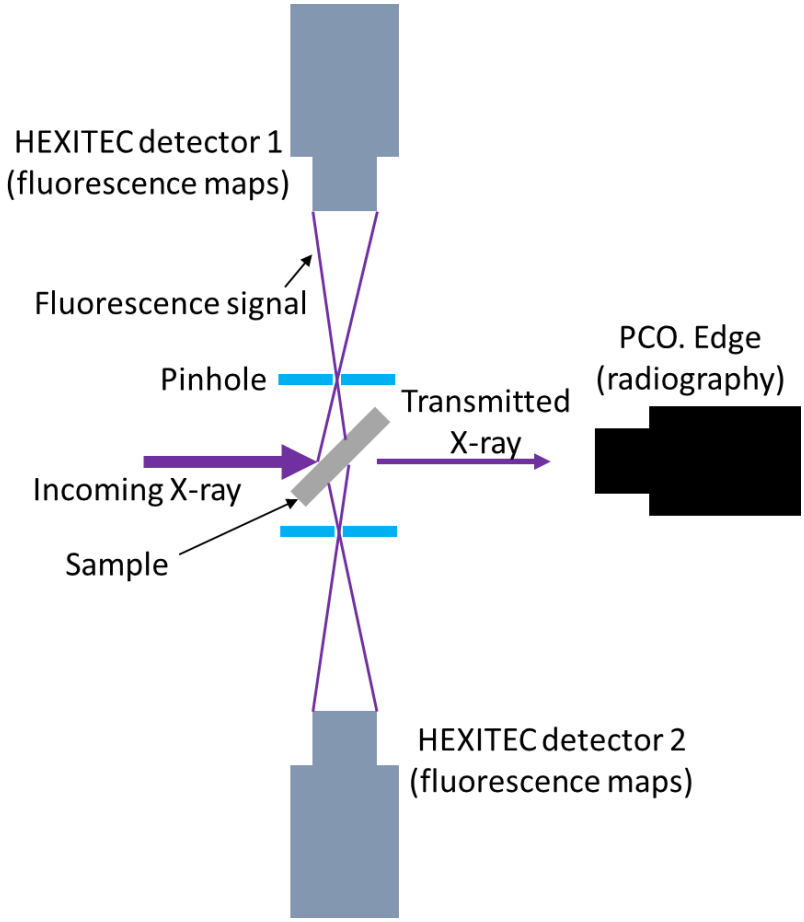


Figure 8.1: A schematic of simultaneous radiography-fluorescence set-up.

and growth of multi-element crystals, and may be the one of the first discriminations between three phases (liquid, $Al_{24}Pt_9Er_4$ and Al_3Er) during real-time solidification.

8.2 Multi-element mapping using laboratory X-ray transmission

8.2.1 Experimental set-up

A study was undertaken to assess if the HEXITEC detector could have any useful role in more convenient laboratory studies, without recourse to the restrictions of synchrotron access. Solid-state HEXITEC mapping of elements in the Al-Pt-Er

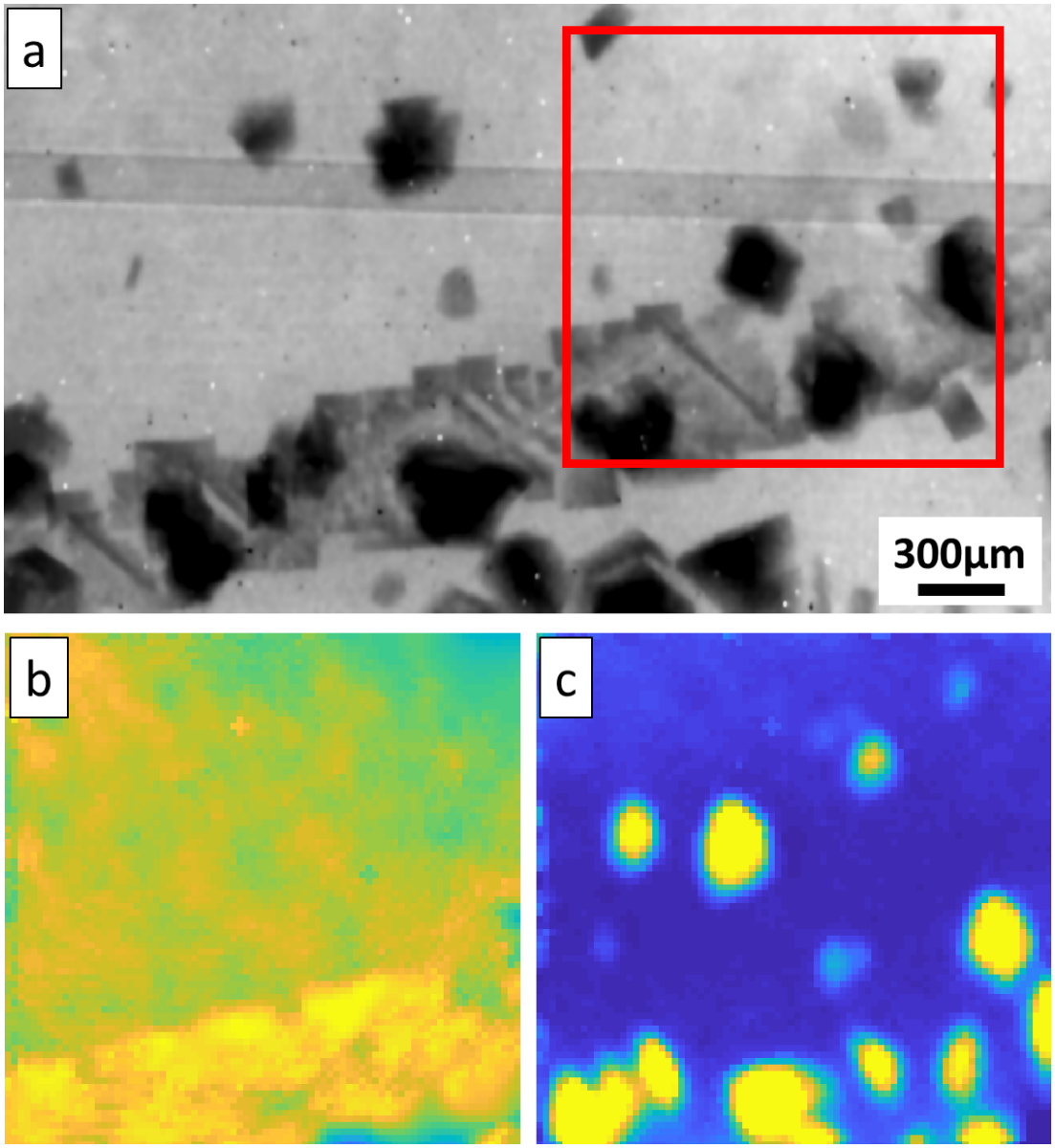


Figure 8.2: (a) A radiograph of a solidifying Al-Pt-Er alloy at 0.1 Ks^{-1}. (b) Simultaneous HEXITEC fluorescence map of the Er distribution. (c) Simultaneous HEXITEC fluorescence map of the Pt distribution. The red square in (a) indicates the field of view of the HEXITEC maps.

alloy was conducted using modified laboratory North Star X-ray Imaging (NSI) apparatus, readily available in the department. To assess detector performance and overall set-up, there was no need to melt/solidify the alloy. Should the arrangement show promise, then a compact furnace suitable for safe integration into the NSI equipment could be developed.

Fig. 8.3 shows the NSI apparatus and the experimental set-up, comprising a

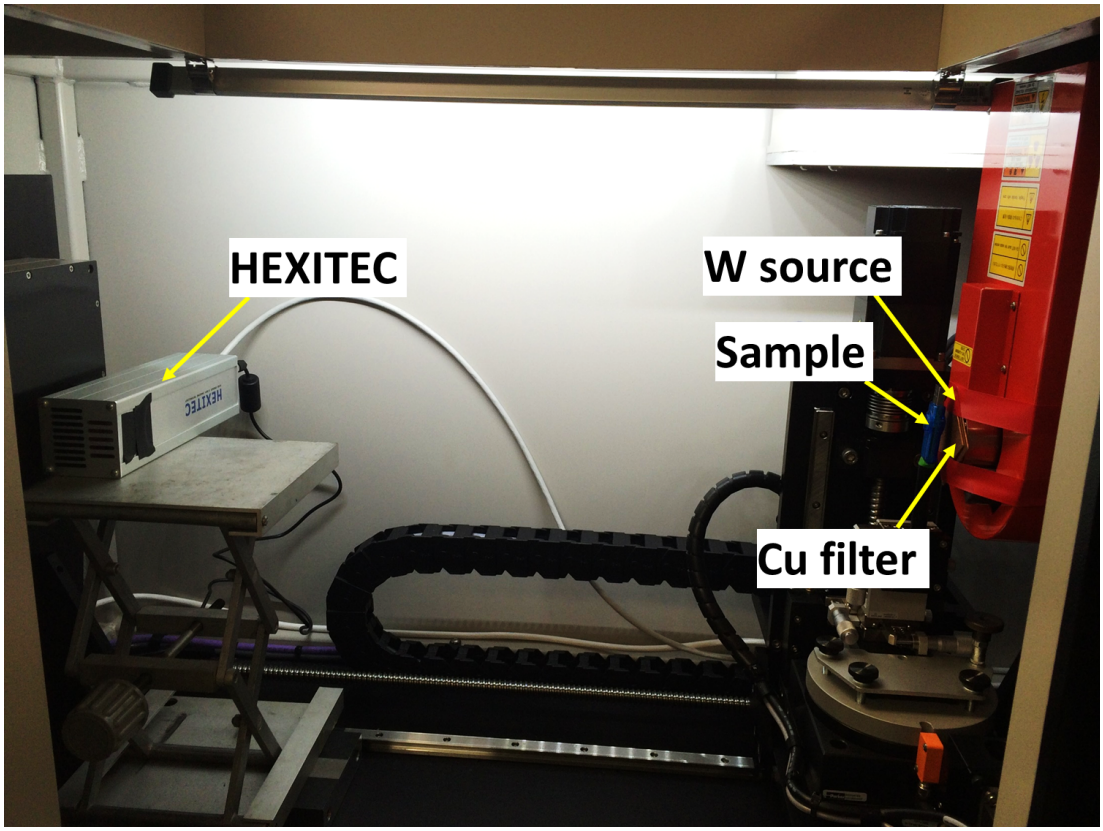


Figure 8.3: A photo of the laboratory NSI apparatus and set-up for solid-sate HEXITEC mapping.

W-anode X-ray source, a specimen positioned in the X-ray path and a HEXITEC detector to collect the transmitted signal. SpekCalc [218] was used to calculate the emission profiles of the W X-ray source at different combinations of tube voltage, filter material and filter thickness to estimate the optimum combination so that peak emission was located closest to the K-edges of elements of interest. A tube voltage of 100 keV and a filter comprising a 1 mm thick Cu disc were selected, which gave rise to a peak emission between the Er K-edge of 57.5 keV and Pt K-edge of 78.4 keV, whilst eliminating the lower energy photons ($<$ 40 keV) that could saturate the detector. Table 8.1 summarises the key settings of the apparatus.

Tube voltage (keV)	**Tube current** (μA)	**Cu filter** (mm)	**Image pixel size** (μm/pixel)	**Acquisition time** (s)
100	15	1	10.3	180

Table 8.1: A summary of key apparatus settings for laboratory HEXITIC mapping.

8.2.2 Data processing

Each experiment was composed of two acquisition runs using exactly the same settings, where the first run collected the flat field signal (without a specimen) and the second run collected the transmitted signal through the specimen. The acquisition time of each run was 180 s for a high signal-noise ratio. According to the Beer-Lambert equation, the relationship between the incident beam and the transmitted beam can be expressed by:

$$\ln(\frac{I_0}{I}) = \mu_{Al}t_{Al} + \mu_{Er}t_{Er} + \mu_{Pt}t_{Pt} \tag{8.1}$$

where I_0 is the intensity of the incident beam, I is the intensity of the transmitted beam, μ_{Al}, μ_{Er} and μ_{Pt} are the linear absorption coefficients of pure Al, Er and Pt respectively, and t_{Al}, t_{Er} and t_{Pt} are the equivalent thickness of Al, Er and Pt in the specimen along the X-ray path assuming they were in the form of pure elements. By assuming that the source was stable throughout the two acquisition runs, then for a given pixel in the HEXITEC array detector, the incident beam intensity I_0 was obtained from the flat field acquisition, while the second acquisition provided the corresponding transmitted intensity I. For a given pixel the resultant spectrum, i.e. $\ln(\frac{I_0}{I})$ as a function of photon energy, is shown in Fig. 8.4. The outcome by processing the data pixel-by-pixel this way was 6400 (given by the 80×80 pixel array of the HEXITEC) energy dispersive spectra.

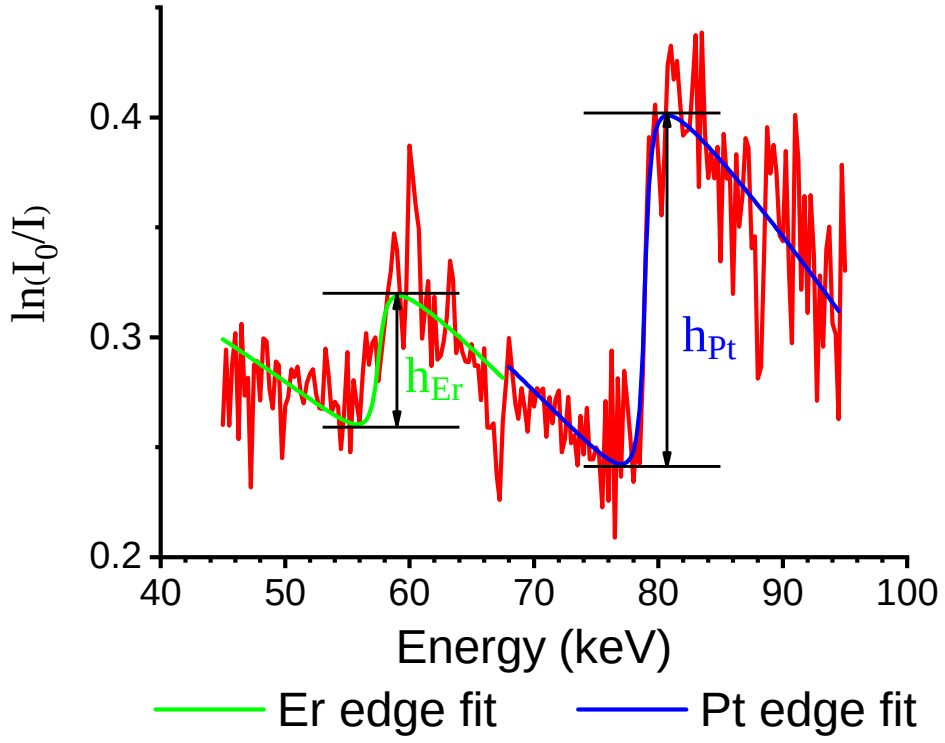


Figure 8.4: An example spectrum of $\ln(\frac{I_0}{I})$ as a function of photon energy from one pixel of the HEXITEC. h_{Er} and h_{Pt} are the sizes of the Er and Pt K-edges in the spectrum. The green and blue curves are the best-fit curves of the Er and Pt edges respectively.

8.2.3 Results

The spectrum in Fig. 8.4 contains two distinct edges, which corresponded to the Er and Pt absorption K-edges. First, qualitative mapping was used to show the relative enrichment of Er and Pt in the field of view, by using the local maxima above each edge in the spectrum. Practically, due to presence of noise in the spectrum, the local "maxima" was taken by averaging the $\ln(\frac{I_0}{I})$ values along a small energy interval of 2 keV above the Er and Pt edges respectively. Figs. 8.5(b) and (c) show a qualitative map of Er and Pt in an Al-Pt-Er alloy prepared by arc melting, while Fig. 8.5(a) shows a radiograph of the sample with a red square indicating the field of view of the HEXITEC. The Er and Pt maps were qualitatively in good agreement with findings from EDX, where Er was present in both the faceted IMCs ($Al_{24}Pt_9Er_4$) and the "matrix" (containing primary and

eutectic Al_3Er), while Pt preferentially segregated into the $Al_{24}Pt_9Er_4$.

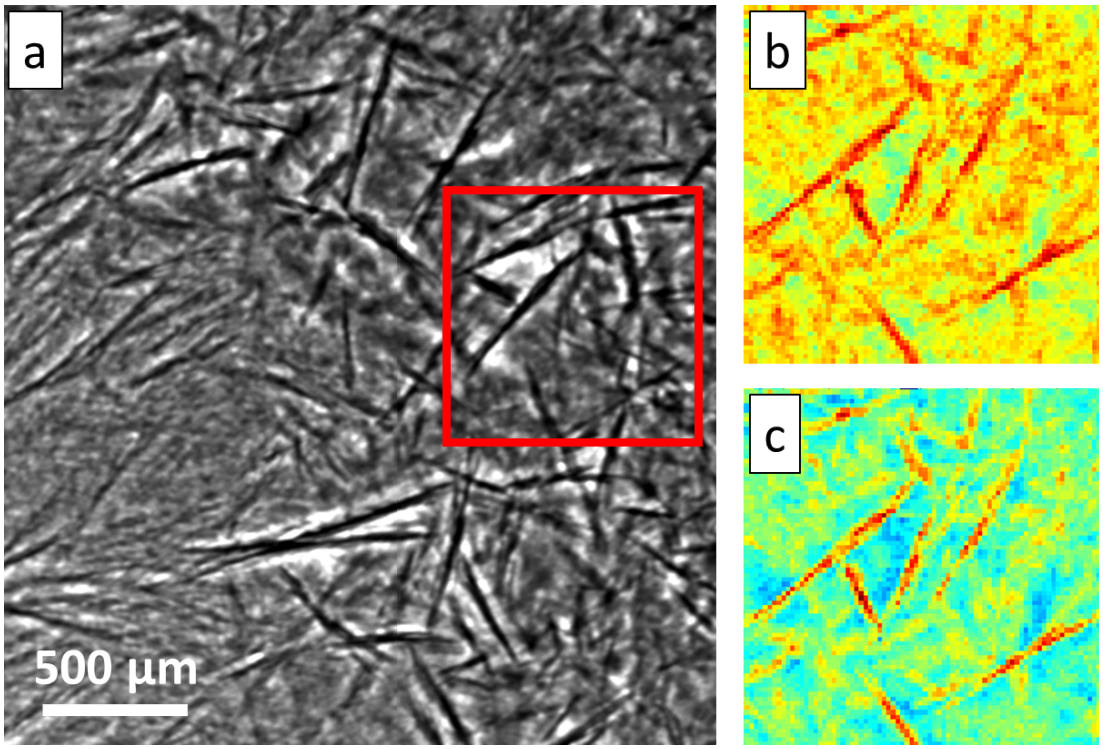


Figure 8.5: (a) A radiograph of an Al-Pt-Er alloy as prepared by arc melting, using the NSI apparatus. The red square indicates the field of view in the HEXITEC in (b) and (c). (b) Qualitative HEXITIC map of Er. (c) Qualitative HEXITEC map of Pt.

Second, by associating the Er and Pt edge sizes h_{Er} and h_{Pt} in Fig. 8.4 with Equation 8.1, it was investigated if it would be possible to quantify the weight percentage of Er and Pt in each pixel. Fig. 8.6 shows the linear absorption coefficient as a function of photon energy for Al, Pt and Er. At the Er K-edge, there was a discrete jump in the Er linear absorption coefficient μ_{Er}, while μ_{Al} and μ_{Pt} remained continuous. The same applied to μ_{Pt} at the Pt K-edge. The edge size h_{Er} in Fig. 8.4 was therefore dependent only on the amount of Er and independent of Pt and Al:

$$h_{Er} = (\mu^{+}_{Er} - \mu^{-}_{Er}) \times t_{Er} = (\frac{\mu^{+}_{Er}}{\rho_{Er}} - \frac{\mu^{-}_{Er}}{\rho_{Er}}) \times \frac{m_{Er}}{A} \tag{8.2}$$

where μ^{+}_{Er} and μ^{-}_{Er} are the Er linear absorption coefficients above and below the

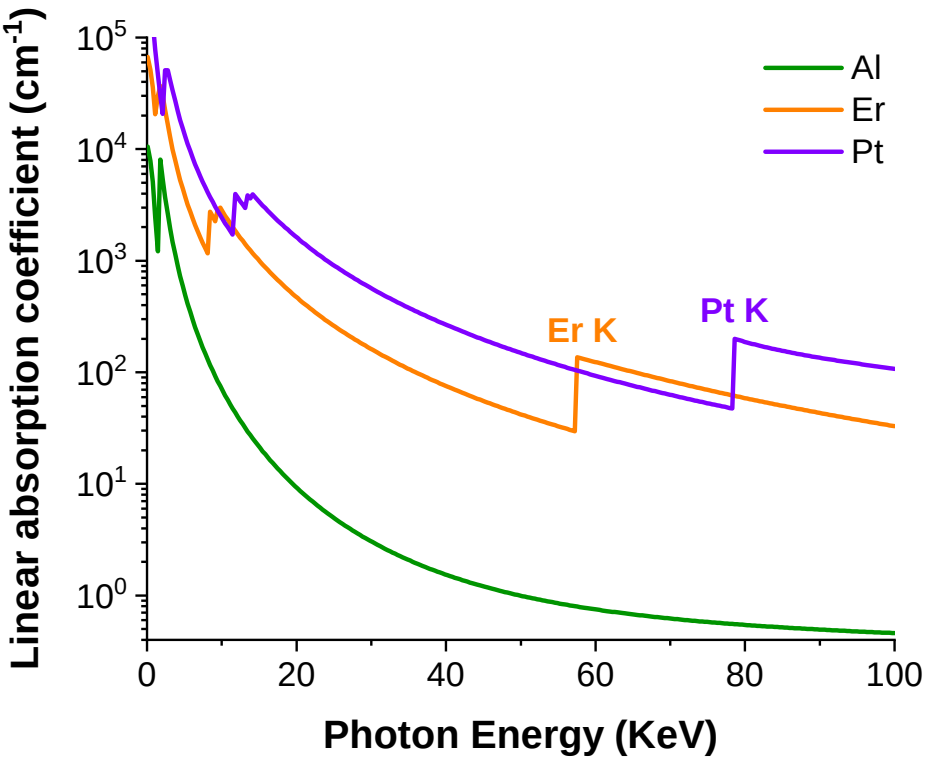


Figure 8.6: Linear absorption coefficients of Al, Er and Pt as a function of photon energy.

Er K-edge respectively, ρ_{Er} is the density of pure Er, $\frac{\mu^+_{Er}}{\rho_{Er}}$ and $\frac{\mu^-_{Er}}{\rho_{Er}}$ are the mass absorption coefficients, t_{Er} is the equivalent thickness of Er along the X-ray path assuming the form of pure element, m_{Er} is the mass of Er in the given pixel, and A is the pixel area. The ratio between the Pt and Er weight percentage at any point in the field of view can therefore be calculated by:

$$\frac{c_{Pt}}{c_{Er}} = \frac{h_{Pt}\rho_{Pt}(\mu^+_{Er} - \mu^-_{Er})}{h_{Er}\rho_{Er}(\mu^+_{Pt} - \mu^-_{Pt})} \tag{8.3}$$

where c_{Pt} and c_{Er} are the weight percentage of Pt and Er at a given point (pixel) in the field of view.

To obtain the edge sizes h_{Er} and h_{Pt} from all the 6400 $\ln(\frac{I_0}{I})$ spectra, fitting was conducted on each edge independently in each spectrum, with an example shown in Fig. 8.4. The fitting function was composed of a quadratic function for

the spectrum background and an arctangent function to fit the edge:

$$f(x) = ax^2 + bx + c + m\,tan^{-1}[n(x-p)] \tag{8.4}$$

The edge size was then obtained by calculating the difference between the local maxima and minima of each fitted curve. Combining the extracted edge sizes h_{Er} and h_{Pt} and Equation 8.3, Fig. 8.7 shows the resultant map of $\frac{c_{Pt}}{c_{Er}}$ ratio for the same experiment as Fig. 8.5. The IMC "needles" in the map typically showed an $\frac{c_{Pt}}{c_{Er}}$ ratio of 3 to 3.5, whilst the same IMCs measured by EDX showed an $\frac{c_{Pt}}{c_{Er}}$ ratio of ∼3.5. While the map quality needs improvement, particularly regarding noise reduction, it shows promise of the arrangement towards an *in-situ* multi-element mapping capability.

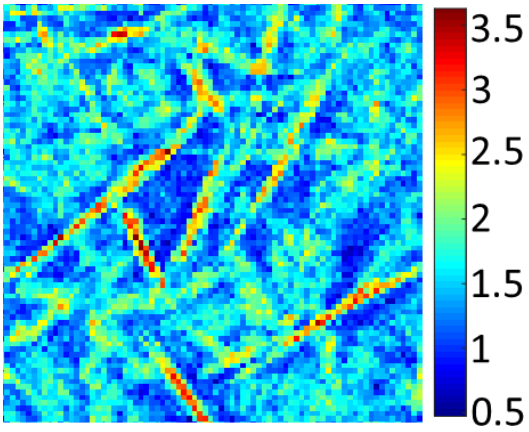


Figure 8.7: A map of $\frac{c_{Pt}}{c_{Er}}$ ratio for the Al-Pt-Er alloy, using the same data as Fig. 8.5b and 8.5c.

8.3 Further work

Based on the findings in the thesis, future work will likely involve:

- The role of multi-solute diffusion in nucleation and growth of the $Al_{24}Pt_9Er_4$ by linking the radiography counting and size measurement with the simul-

taneous HEXITEC fluorescence mapping.

- Calculation and modelling to estimate potential growth modifying elements for $Al_{13}Fe_4$.

- *In-situ* studies on the effect of chemical modifiers on twinning-mediated growth of $Al_{13}Fe_4$ crystals.

- Investigation on the faceted-nonfaceted transition behaviour observed in primary Al_3Er in the Al-Pt-Er alloy as a function of cooling rate, combining *in-situ* radiography and post-solidification EBSD.

Bibliography

[1] J. Hirsch. *Mater. Trans.*, 52(5):818–824, 2011.

[2] European Aluminium Association, 2014.

[3] World Aluminium Market, 2017. URL `https://www.aluminiumleader.com`.

[4] R. MacLachlan, C. Clark, and C. M. Harris. Belconnen, ACT Industry Commission, 1998.

[5] G. E. Totten and S. D. MacKenzie. CRC Press, 2003.

[6] E.A. Starke and J.T. Staley. *Prog. Aerosp. Sci.*, 32(2):131–172, 1996.

[7] V. Kevorkijan. *Mater. Tehnol.*, 47(1):13–23, 2013.

[8] D. Paraskevas, K. Kellens, A. Van de Voorde, W. Dewulf, and J. R. Duflou. *Procedia CIRP*, 40:209–213, 2016.

[9] G. Liu, C. E. Bangs, and D. B. Muller. *Nat. Clim. Chang.*, 3(4):338–342, 2012.

[10] J. M. Cubero-Sesin and Z. Horita. *J. Mater. Sci.*, 48(13):4713–4722, 2013.

[11] H. W. L. Phillips. London : Aluminium Development Association, 1961.

[12] C. H. Caceres, I. L. Svensson, and J. A. Taylor. *Int. J. Cast Met. Res.*, 15 (5):531–543, 2003.

[13] L. Ceschini, I. Boromei, A. Morri, S. Seifeddine, and I. L. Svensson. *J. Mater. Process. Technol.*, 209(15-16):5669–5679, 2009.

[14] S. Ji, W. Yang, F. Gao, D. Watson, and Z. Fan. *Light Met. 2013*, 2013.

[15] W. Zhang, B. Lin, D. Zhang, and Y. Li. *Mater. Des.*, 52:225–233, 2013.

[16] J. Z. Yi, Y. X. Gao, P. D. Lee, and T. C. Lindley. *Mater. Sci. Eng. A*, 386 (1-2):396–407, 2004.

[17] J. O. Park, C. H. Paik, Y. H. Huang, and R. C. Alkire. *J. Electrochem. Soc.*, 146(2):517, 1999.

[18] K. A. Yasakau, M. L. Zheludkevich, S. V. Lamaka, and M. G.S. Ferreira. *Electrochim. Acta*, 52(27):7651–7659, 2007.

[19] J. A. Taylor, G. B. Schaffer, and D. H. StJohn. *Metall. Mater. Trans. A*, 30(6):1643–1650, 1999.

[20] J. A. Taylor, G. B. Schaffer, and D. H. StJohn. *Metall. Mater. Trans. A*, 30(6):1651–1655, 1999.

[21] J. A. Taylor, G. B. Schaffer, and D. H. StJohn. *Metall. Mater. Trans. A*, 30(6):1657–1662, 1999.

[22] C. M. Dinnis, J. A. Taylor, and A. K. Dahle. *Mater. Sci. Eng. A*, 425(1-2): 286–296, 2006.

[23] L. Sweet, M. A. Easton, J. A. Taylor, J. F. Grandfield, C. J. Davidson, L. Lu, M. J. Couper, and D. H. StJohn. *Metall. Mater. Trans. A*, 44(12): 5396–5407, 2013.

[24] C. Puncreobutr, P. D. Lee, K. M. Kareh, T. Connolley, J. L. Fife, and A. B. Phillion. *Acta Mater.*, 68:42–51, 2014.

[25] C. M. Allen, K. A. Q. O'Reilly, B. Cantor, and P. V. Evans. *Prog. Mater. Sci.*, 43(2):89–170, 1998.

[26] L. A. Narayanan, F. H. Samuel, and J. E. Gruzleski. *Metall. Mater. Trans. A*, 26(8):2161–2174, 1995.

[27] Q. G Wang, D Apelian, and D. A Lados. *J. Light Met.*, 1(1):85–97, 2001.

[28] D Zhang, L Zheng, and D. H. StJohn. *J. Light Met.*, 2(1):27–36, 2002.

[29] C. J. Davidson, J. R. Griffiths, and A. S. Machin. *Fatigue Fract. Eng. Mater. Struct.*, 25(2):223–230, 2002.

[30] J. A. Dantzig and M. Rappaz. EPFL Press, 2009.

[31] A. L. Greer, A. M. Bunn, A. Tronche, P. V. Evans, and D. J. Bristow. *Acta Mater.*, 48(11):2823–2835, 2000.

[32] D. A. Porter, K. E. Easterling, and M. Y. Sherif. CRC Press, 2009.

[33] B. Cantor and R.D. Doherty. *Acta Metall.*, 27(1):33–46, 1979.

[34] W. T. Kim and B. Cantor. *Acta Metallurgica et Materialia*, 40(12):3339–3347, 1992.

[35] W. T. Kim and B. Cantor. *Acta Metall. Mater.*, 42(9):3115–3127, 1994.

[36] T. E. Quested and A. L. Greer. *Acta Mater.*, 53(9):2683–2692, 2005.

[37] G. Sha, K. O'Reilly, B. Cantor, R. Hamerton, and J. Worth. *Mater. Sci. Forum*, 331-337:253–258, 2000.

[38] W. Khalifa, F. H. Samuel, J. E. Gruzleski, H. W. Doty, and S. Valtierra. *Metall. Mater. Trans. A*, 36(4):1017–1032, 2005.

[39] A. Lui. PhD thesis, University of Oxford, 2009.

[40] J. Rakhmonov, G. Timelli, and F. Bonollo. *Metall. Mater. Trans. A Phys. Metall. Mater. Sci.*, 47(11):5510–5521, 2016.

[41] J. Rakhmonov, G. Timelli, F. Bonollo, and L. Arnberg. *International Journal of Metalcasting*, 11(2):294–304, 2017.

[42] X. Cao and J. Campbell. *Metall. Mater. Trans. A*, 34(7):1409–1420, 2003.

[43] D. N. Miller, L. Lu, and A. K. Dahle. *Metall. Mater. Trans. B Process Metall. Mater. Process. Sci.*, 37(6):873–878, 2006.

[44] L. A. Narayanan, F. H. Samuel, and J. E. Gruzleski. *Metall. Mater. Trans. A*, 25(8):1761–1773, 1994.

[45] S. Terzi, J. A. Taylor, Y. H. Cho, L. Salvo, M. Suery, E. Boller, and A. K. Dahle. *Acta Mater.*, 58(16):5370–5380, 2010.

[46] K. Liu, X. Cao, and X. G. Chen. *Metall. Mater. Trans. A Phys. Metall. Mater. Sci.*, 42(7):2004–2016, 2011.

[47] G. K. Sigworth. *Int. J. Met.*, 2(2):19–40, 2008.

[48] A. M. Samuel, A. Pennors, C. Villeneuve, F. H. Samuel, H. W. Doty, and S. Valtierra. *Int. J. Cast Met. Res.*, 13(4):231–253, 2000.

[49] B. Kim, S. Lee, S. Lee, and H. Yasuda. *Mater. Trans.*, 53(2):374–379, 2012.

[50] C. Puncreobutr, A. B. Phillion, J. L. Fife, P. Rockett, A. P. Horsfield, and P. D. Lee. *Acta Mater.*, 79:292–303, 2014.

[51] J. Campbell. Saint Louis : Elsevier Science, 2011.

[52] X. Cao and J. Campbell. *Metall. Mater. Trans. A*, 35(5):1425–1435, 2004.

[53] P. Orozco-Gonzalez, M. Castro-Roman, S. Maldonado-Ruiz, S. Haro-Rodriguez, F. Equihua-Guillen, R. Muniz-Valdez, S. Luna-Alvarez,

M. Montoya-Davila, and A. Hernandez-Rodriguez. *J. Miner. Mater. Charact. Eng.*, 03(01):15–25, 2015.

[54] B. L. Bramfitt. *Metall. Trans.*, 1(7):1987–1995, 1970.

[55] L. Lu and A. K. Dahle. *Metall. Mater. Trans. A*, 36(13):819–835, 2005.

[56] W. Khalifa, A. M. Samuel, F. H. Samuel, H. W. Doty, and S. Valtierra. *Int. J. Cast Met. Res.*, 19(3):156–166, 2006.

[57] G. Sha, K. A. Q. O'Reilly, B. Cantor, J. M. Titchmarsh, and R.G. Hamerton. *Acta Mater.*, 51(7):1883–1897, 2003.

[58] K. A. Jackson. *Asm, Cleveland*, 174, 1958.

[59] K. A. Jackson. In *Proc. of the Intern. Conf. on Crystal Growth at Coopertown, NY*, 1958.

[60] J. W. Cahn. *Acta Metallurgica*, 8(8):554–562, 1960.

[61] R. S. Wagner. *Acta Metallurgica*, 8(1):57–60, 1960.

[62] D. R. Hamilton and R. G. Seidensticker. *Journal of Applied Physics*, 31(7): 1165–1168, 1960.

[63] A. Hellawell. *Progress in Materials Science*, 15(1):3–78, 1970.

[64] K. Kobayashi and L. M. Hogan. *Philosophical Magazine A*, 40(3):399–407, 1979.

[65] O. A. Atasoy, F. Yilmaz, and R. Elliott. *Journal of Crystal Growth*, 66(1): 137–146, 1984.

[66] K. F. Kobayashi and L. M. Hogan. *Journal of Materials Science*, 20(6): 1961–1975, 1985.

[67] S. Lu and A. Hellawell. *Journal of Crystal Growth*, 73(2):316–328, 1985.

[68] M. Shamsuzzoha and L. M. Hogan. *Journal of Crystal Growth*, 76(2):429–439, 1986.

[69] R. Wang, W. Lu, and L. M. Hogan. *Journal of Crystal Growth*, 207(1-2): 43–54, 1999.

[70] S. Hegde and K. N. Prabhu. *Journal of Materials Science*, 43(9):3009–3027, 2008.

[71] K. Fujiwara. *International Journal of Photoenergy*, 2012:1–16, 2012.

[72] J. Wang, Z. Guo, and S. M. Xiong. *Materials Characterization*, 123:354–359, 2017.

[73] G. Sha, K. O'Reilly, and B. Cantor. *Mater. Sci. Forum*, 519-521:1721–1726, 2006.

[74] M. H. Mulazimoglu, A. Zaluska, J. E. Gruzleski, and F. Paray. *Metall. Mater. Trans. A*, 27(4):929–936, 1996.

[75] C. M. Adam and L. M. Hogan. *Acta Metall.*, 23(3):345–354, 1975.

[76] V. Hansen, B. Hauback, M. Sundberg, C. Romming, and J. Gjonnes. *Acta Crystallogr. Sect. B Struct. Sci.*, 54(4):351–357, 1998.

[77] G. Sha, K. O'Reilly, B. Cantor, J. Worth, and R. Hamerton. *Mater. Sci. Eng. A*, 304-306:612–616, 2001.

[78] J. Wang, P. D. Lee, R. W. Hamilton, M. Li, and J. Allison. *Scr. Mater.*, 60(7):516–519, 2009.

[79] C. Rakete, C. Baumbach, A. Goldschmidt, D. Samberg, C. G. Schroer, F. Breede, C. Stenzel, G. Zimmermann, C. Pickmann, Y. Houltz, C. Lockowandt, O. Svenonius, P. Wiklund, and R. H. Mathiesen. *Rev. Sci. Instrum.*, 82(10), 2011.

[80] H. Nguyen-Thi, G. Reinhart, G. Salloum Abou Jaoude, R. H. Mathiesen, G. Zimmermann, Y. Houltz, D. Voss, A. Verga, D. J. Browne, and A. G. Murphy. *J. Cryst. Growth*, 374:23–30, 2013.

[81] A. Bjurenstedt, D. Casari, S. Seifeddine, R. H. Mathiesen, and A. K. Dahle. *Acta Mater.*, 130:1–9, 2017.

[82] J. Barrirero, M. Engstler, N. Ghafoor, N. Jonge, M. Oden, and F. Mucklich. *Journal of Alloys and Compounds*, 611:410–421, 2014.

[83] X. Liu, Y. Zhang, B. Beausir, F. Liu, C. Esling, F. Yu, X. Zhao, and L. Zuo. *Acta Materialia*, 97:338–347, 2015.

[84] Z. M. Shi, Q. Wang, G. Zhao, and R. Y. Zhang. *Materials Science and Engineering A*, 626:102–107, 2015.

[85] P. Xing, B. Gao, Y. Zhuang, K. Liu, and G. Tu. *Acta Metallurgica Sinica (English Letters)*, 23(5):327–333, 2010.

[86] J. H. Li, X. D. Wang, T. H. Ludwig, Y. Tsunekawa, L. Arnberg, J. Z. Jiang, and P. Schumacher. *Acta Materialia*, 84:153–163, 2015.

[87] E. M. Elgallad, H. W. Doty, S. A. Alkahtani, and F. H. Samuel. *Advances in Materials Science and Engineering*, 2016:1–13, 2016.

[88] M. DeGiovanni, J. A. Kaduk, and P. Srirangam. *JOM*, 71(1):426–434, 2019.

[89] K. Nogita, S. D. McDonald, and A. K. Dahle. *Materials Transactions*, 45 (2):323–326, 2005.

[90] M. Timpel, N. Wanderka, R. Schlesiger, T. Yamamoto, N. Lazarev, D. Isheim, G. Schmitz, S. Matsumura, and J. Banhart. *Acta Materialia*, 60 (9):3920–3928, 2012.

[91] K. Nogita, J. Drennan, and A. K. Dahle. *Materials Transactions*, 44(4): 625–628, 2005.

[92] M. DeGiovanni, T. Alam, R. Banerjee, and P. Srirangam. *JOM*, 70(9): 1765–1770, 2018.

[93] S. Lu and A. Hellawell. *Metallurgical Transactions A*, 18(10):1721–1733, 1987.

[94] E. Aerts, P. Delavignette, R. Siems, and S. Amelinckx. *Journal of Applied Physics*, 33(10):3078–3080, 1962.

[95] E. Liotti, A. Lui, R. Vincent, S. Kumar, Z. Guo, T. Connolley, I. P. Dolbnya, M. Hart, L. Arnberg, R. H. Mathiesen, and P. S. Grant. *Acta Mater.*, 70: 228–239, 2014.

[96] E. Liotti, A. Lui, S. Kumar, Z. Guo, C. Bi, T. Connolley, and P. S. Grant. *Acta Mater.*, 121:384–395, 2016.

[97] D. Ruvalcaba, R. H. Mathiesen, D. G. Eskin, L. Arnberg, and L. Katgerman. *Acta Mater.*, 55(13):4287–4292, 2007.

[98] R. H. Mathiesen, L. Arnberg, P. Bleuet, and A. Somogyi. *Metall. Mater. Trans. A*, 37(8):2515–2524, 2006.

[99] F. Wang, D. Eskin, J. Mi, C. Wang, B. Koe, A. King, C. Reinhard, and T. Connolley. *Acta Mater.*, 141:142–153, 2017.

[100] M. W. Zandbergen, Q. Xu, A. Cerezo, and G. D. W. Smith. *Acta Mater.*, 101:136–148, 2015.

[101] M. W. Zandbergen, A. Cerezo, and G. D. W. Smith. *Acta Mater.*, 101: 149–158, 2015.

[102] R. Ramesh, R. Bhattacharya, and G. Williams. *Mater. Sci. Eng. A*, 541: 128–134, 2012.

[103] V. Stefaniay, A. Griger, and T. Turmezey. *J. Mater. Sci.*, 22(2):539–546, 1987.

[104] G. V. Raynor and V. G. Rivlin. *Inst. Met.*, 2(1):143–145, 1988.

[105] C. Y. Sun and L. F. Mondolfo. *J. Inst. Met.*, 95:384, 1967.

[106] P. Skjerpe. *Metall. Trans. A*, 18(2):189–200, 1987.

[107] S. Kumar, P. S. Grant, and K. A. Q. O'Reilly. *Metall. Mater. Trans. A*, 47 (6):3000–3014, 2016.

[108] L. F. Mondolfo. Butterworths, 1976.

[109] C. Freiburg and B. Grushko. *J. Alloys Compd.*, 210(1-2):149–152, 1994.

[110] J. Grin, U. Burkhardt, M. Ellner, and K. Peters. *Zeitschrift fuer Krist.*, 209(6):479–487, 1994.

[111] P. Skjerpe. *J. Microsc.*, 148(1):33–50, 1987.

[112] D. Munson. *J. Inst. Met.*, 95:217–219, 1967.

[113] K. Robinson and P. J. Black. *London, Edinburgh, Dublin Philos. Mag. J. Sci.*, 44(359):1392–1397, 1953.

[114] H. Tanihata, T. Sugawara, K. Matsuda, and S. Ikeno. *J. Mater. Sci.*, 34 (6):1205–1210, 1999.

[115] G. Phragmnn. *J. Inst. Met.*, 77(6):489–551, 1950.

[116] M. J. Castro-Roman, I. Aguilera-Luna, A. A. Gaona-Coronado, M. Herrera-Trejo, and J. Torres. *Trans. Indian Inst. Met.*, 68(6):1193–1197, 2015.

[117] S. Terzi, J. Taylor, Y. Cho, L. Salvo, M. Suery, E. Boller, and A. K. Dahle, 2010.

[118] L. Liu, A. M. A. Mohamed, A. M. Samuel, F. H. Samuel, H. W. Doty, and S. Valtierra. *Metall. Mater. Trans. A*, 40(10):2457–2469, 2009.

[119] S. Belmares-Perales, M. Castro-Roman, M. Herrera-Trejo, and L. E. Ramirez-Vidaurri. *Met. Mater. Int.*, 14(3):307–314, 2008.

[120] A. M. Samuel, F. H. Samuel, and H. W. Doty. *J. Mater. Sci.*, 31(20): 5529–5539, 1996.

[121] P. Ashtari, H. Tezuka, and T. Sato. *Scr. Mater.*, 53(8):937–942, 2005.

[122] D. Li, C. Cui, X. Wang, Q. Wang, C. Chen, and S. Liu. *Mater. Des.*, 90: 820–828, 2016.

[123] Z. Li, A. M. Samuel, F. H. Samuel, C. Ravindran, H. W. Doty, and S. Valtierra. *Mater. Sci. Eng. A*, 367(1):111–122, 2004.

[124] Z. Li, A. M. Samuel, F. H. Samuel, C. Ravindran, S. Valtierra, and H. W. Doty. *Mater. Sci. Eng. A*, 367(1):96–110, 2004.

[125] C. Puncreobutr, A. B. Phillion, J. L. Fife, and P. D. Lee. *Acta Mater.*, 64: 316–325, 2014.

[126] Y. Liu, L. Luo, C. Han, L. Ou, J. Wang, and C. Liu. *J. Mater. Sci. Technol.*, 32(4):305–312, 2016.

[127] G. B. Winkelman, Z. W. Chen, D. H. St John, and M. Z. Jahedi. *J. Mater. Sci.*, 39(2):519–528, 2004.

[128] Y. Liu, G. Huang, Y. Sun, L. Zhang, Z. Huang, J. Wang, and C. Liu. *Materials (Basel).*, 9(2):88, 2016.

[129] G. Mrowka-Nowotnik, J. Sieniawski, and A. Nowotnik. *J. Microsc.*, 237(3): 407–10, 2010.

[130] M. Cooper. *Acta Crystallogr.*, 23(6):1106–1107, 1967.

[131] H. Westengen. *Zeitschrift fur Met.*, 73(6):360–368, 1982.

[132] A. L. Dons. *Zeitschrift fur Met.*, 75(2):170–174, 1984.

[133] A. Griger, V. Stefaniay, E. Kovacs-Csetenyi, and T. Turmezey. *Key Eng. Mater.*, 44-45:17–30, 1990.

[134] J. M. Yu, N. Wanderka, G. Miehe, and J. Banhart. *Intermetallics*, 72: 53–61, 2016.

[135] W. Khalifa, F. H. Samuel, and J. E. Gruzleski. *Metall. Mater. Trans. A*, 34(13):807–825, 2003.

[136] G. Timelli, S. Capuzzi, and A. Fabrizi. *J. Therm. Anal. Calorim.*, 123(1): 249–262, 2015.

[137] E. Tillova, M. Chalupova, and L. Hurtalova. *Scan. Electron Microsc.*, pages 411–438, 2012.

[138] M. Dash and M. Makhlouf. *J. Light Met.*, 1(4):251–265, 2001.

[139] J. A. Taylor. *Procedia Mater. Sci.*, 1:19–33, 2012.

[140] V. G. Rivlin and G. V. Raynor. *Int. Met. Rev.*, 26(1):133–152, 1981.

[141] C. L. Jensen and R. K. Wyss. *Metall. Trans. A*, 19(4):893–898, 1988.

[142] P. Liu, T. Thorvaldsson, and G. L. Dunlop. *Mater. Sci. Technol.*, 2(10): 1009–1018, 1986.

[143] P. Liu and G. L. Dunlop. *J. Mater. Sci.*, 23(4):1419–1424, 1988.

[144] ASM International Handbook. volume 2. 1990.

[145] L. Backerud, E. Krol, and J. Tamminen. *Solidification characteristics of aluminium alloys*. Skanaluminium, Universitetsforlaget AS, 1986.

[146] C. Tseng, S. Lee, S. Tsai, and C. Cheng. *J. Mater. Res.*, 17(09):2243–2250, 2002.

[147] M. A. Talamantes-Silva, A. Rodriguez, J. Talamantes-Silva, S. Valtierra, and R. Colas. *Mater. Charact.*, 59(10):1434–1439, 2008.

[148] K. Liu, X. Cao, and X. Chen. *Metall. Mater. Trans. A*, 44(2):682–695, 2012.

[149] S. C. Wang and M. J. Starink. *Int. Mater. Rev.*, 50(4):193–215, 2005.

[150] C. Tseng, S. Lee, T. Wu, and J. Lin. *Mater. Trans. JIM*, 41(6):708–713, 2000.

[151] A. Bolouri, K. Liu, and X. G. Chen. *Metall. Mater. Trans. A Phys. Metall. Mater. Sci.*, 47(12):6466–6480, 2016.

[152] N. Birbilis, M. K. Cavanaugh, and R. G. Buchheit. *Corros. Sci.*, 48(12): 4202–4215, 2006.

[153] A. Chemin, D. Marques, L. Bisanha, A. Motheo, W. Bose Filho, and C. Ruchert. *Mater. Des.*, 53:118–123, 2014.

[154] S. Lebouil, J. Tardelli, E. Rocca, P. Volovitch, and K. Ogle. *Mater. Corros.*, 65(4):416–424, 2014.

[155] A. Chemin, D. Spinelli, W. Bose Filho, and C. Ruchert. *Procedia Eng.*, 101 (C):85–92, 2015.

[156] N. A. Belov, A. A. Aksenov, and D. G. Eskin. *Iron in aluminum alloys : impurity and alloying element*. Taylor & Francis, 2002.

[157] M. E. Drits. *Phase Diagrams of the Aluminum and Magnesium Systems*. Moscow, 1977.

[158] V. Raghavan. *J. Phase Equilibria Diffus.*, 31(5):449–452, 2010.

[159] H. W. L. Phillips. *J. Inst. Met.*, 82(5):197, 1954.

[160] V. Raghavan. *J. Phase Equilibria Diffus.*, 26(1):59–64, 2005.

[161] J. G. Barlock and L. F. Mondolfo. *Zeitschrift fur Met.*, 66(10):605–611, 1975.

[162] P. J. Black, O. S. Edwards, and J. B. Forsyth. *Acta Crystallogr.*, 14(9): 993–998, 1961.

[163] A. J. Bradley and H. J. Goldschmidt. *J. Inst. Met.*, 6:157–210, 1939.

[164] N. Saadi, M. Harmelin, F. Faudot, and B. Legendre. *J. Non. Cryst. Solids*, 153:500–503, 1993.

[165] G. Rosas and R. Perez. *Mater. Sci. Eng. A*, 298(1):79–83, 2001.

[166] H. Kamguo-Kamga, D. Larouche, M. Bournane, and A. Rahem. Solidification of Aluminum-Copper B206 Alloys with Iron and Silicon Additions. *Metall. Mater. Trans. A*, 41(11), 2010.

[167] B. Lin, W. Zhang, Y. Zhao, and Y. Li. *Mater. Charact.*, 104:124–131, 2015.

[168] B. Binesh and M. Aghaie-Khafri. *Metals (Basel).*, 6(3):42, 2016.

[169] M. G. Bown and P. J. Brown. *Acta Crystallogr.*, 9(11):911–914, 1956.

[170] Y. Liu, X. M. Zhang, and H. Zhang. *Mater. Res. Innov.*, 17(sup1):83–88, 2013.

[171] Prevarsk, A. P. *Russ. Metall.*, 4:154, 1971.

[172] H. Chen, Y. Du, H. Xu, and W. Xiong. *J. Mater. Res.*, 24(10):3154–3164, 2009.

[173] L. Zhang, J. Schneider, and R. Luck. *Intermetallics*, 13(11):1195–1206, 2005.

[174] Y. Calvayrac, A. Quivy, M. Bessiere, S. Lefebvre, M. Cornier-Quiquandon, and D. Gratias. *J. Phys. Paris*, 51(5):417–431, 1990.

[175] J. E Hatch. *Aluminum properties and physical metallurgy.* Metals Park, OH : American Society for Metals, 1984.

[176] C. M. Dinnis, J. A. Taylor, and A. K. Dahle. *Metall. Mater. Trans. A*, 37 (11):3283–3291, 2006.

[177] S. Murali, K. S. Raman, and K. S. S. Murthy. *Mater. Charact.*, 33(2): 99–112, 1994.

[178] P. Ashtari, H. Tezuka, and T. Sato. *Mater. Trans.*, 44(12):2611–2616, 2003.

[179] H. Kim, T. Park, S. Han, and H. Lee. *J. Cryst. Growth*, 291(1):207–211, 2006.

[180] S. S. Sreeja-Kumari, R. M. Pillai, T. P. D. Rajan, and B. C. Pai. *Mater. Sci. Eng. A*, 460:561–573, 2007.

[181] C. Bidmeshki, V. Abouei, H. Saghafian, S. Shabestari, and M. Noghani. *J. Mater. Res. Technol.*, 5(3):250–258, 2016.

[182] S. K. Shaha, F. Czerwinski, W. Kasprzak, J. Friedman, and D. L. Chen. *Metall. Mater. Trans. A*, 47(5):2396–2409, 2016.

[183] M. Mahta, M. Emamy, A. Daman, A. Keyvani, and J. Campbell. *Int. J. Cast Met. Res.*, 18(2):73–79, 2005.

[184] S. Murali, S. Muthukkaruppan, K. S. Raman, and K. S. S. Murthy. *Mater. Sci. Technol.*, 13(4):337–342, 1997.

[185] F. H. Samuel, A. M. Samuel, H. W. Doty, and S. Valtierra. *Metall. Mater. Trans. A*, 34(1):115–129, 2003.

[186] S. Yie, S.and Lee, Y. Lin, and J. Lin. *Mater. Trans. JIM*, 40(4):294–300, 1999.

[187] M. Sha, S. Wu, X. Wang, and L. Wan. *Journal of Alloys and Compounds*, 551:468–474, 2013.

[188] G. Timelli, A. Fabrizi, S. Capuzzi, F. Bonollo, and S. Ferraro. *Materials Science and Engineering: A*, 603:58–68, 2014.

[189] S. Murali, K. S. Raman, and K. S. S. Murthy. *Mater. Sci. Eng. A*, 190(1): 165–172, 1995.

[190] S. G. Shabestari, T. Mahmudi, M. Emamy, and T. Campbell. *Int. J. Cast Met. Res.*, 15(1):17–24, 2002.

[191] B. Wan, W. Chen, L. Liu, X. Cao, L. Zhou, and Z. Fu. *Mater. Sci. Eng. A*, 666:165–175, 2016.

[192] N. Nordin, S. Farahany, T. Abu-Bakar, E. Hamzah, and A. Ourdjini. *Journal of Alloys and Compounds*, 650:821–834, 2015.

[193] S. G. Shabestari. *Mater. Sci. Eng. A*, 383(2):289–298, 2004.

[194] A. M. Samuel and F. H. Samuel. *J. Mater. Sci.*, 30(7):1698–1708, 1995.

[195] T. O. Mbuya, B. O. Odera, and S. P. Nganga. *Int. J. Cast Met. Res.*, 16 (5):451–465, 2003.

[196] M. D. Wilson, R. Cernik, H. Chen, C. Hansson, K. Iniewski, L. L. Jones, P. Seller, and M. C. Veale. *Nuclear Instruments and Methods in Physics*

Research, Section A: Accelerators, Spectrometers, Detectors and Associated Equipment, 652(1):158–161, 2011.

[197] P. Seller, S. Bell, R. J. Cernik, C. Christodoulou, C. K. Egan, J. A. Gaskin, S. Jacques, S. Pani, B. D. Ramsey, C. Reid, P. J. Sellin, J. W. Scuffham, R. D. Speller, M. D. Wilson, and M. C. Veale. *J. Instrum.*, 6(12):12009–12009, 2011.

[198] M. C. Veale, S. J. Bell, D. D. Duarte, A. Schneider, P. Seller, M. D. Wilson, and K. Iniewski. *Nucl. Instruments Methods Phys. Res. Sect. A Accel. Spectrometers, Detect. Assoc. Equip.*, 767:218–226, 2014.

[199] E. Liotti, A. Lui, T. Connolley, I. P. Dolbnya, K. J. S. Sawhney, A. Malandain, M. D. Wilson, M. C. Veale, P. Seller, and P. S. Grant. *Sci. Rep.*, 5:6, 2015.

[200] A. G. Murphy, D. J. Browne, W. U. Mirihanage, and R. H. Mathiesen. *Acta Mater.*, 61(12):4559–4571, 2013.

[201] A. G. Murphy, W. U. Mirihanage, D. J. Browne, and R. H. Mathiesen. *Acta Mater.*, 95:83–89, 2015.

[202] Y. Xu, D. Casari, R. H. Mathiesen, and Y. Li. *Acta Mater.*, 149:312–325, 2018.

[203] Y. Xu, D. Casari, Q. Du, R. H. Mathiesen, L. Arnberg, and Y. Li. *Acta Mater.*, 140:224–239, 2017.

[204] K. J. S. Sawhney, I. P. Dolbnya, M. K. Tiwari, L. Alianelli, S. M. Scott, G. M. Preece, U. K. Pedersen, and R. D. Walton. *AIP Conf. Proc.*, 1234: 387–390, 2010.

[205] A. Rack, T. Weitkamp, M. Riotte, D. Grigoriev, T. Rack, L. Helfen, T. Baumbach, R. Dietsch, T. Holz, M. Kramer, F. Siewert, M. Meduna,

P. Cloetens, and E. Ziegler. *Journal of Synchrotron Radiation*, 17(4):496–510, 2010.

[206] S. Feng, E. Liotti, A. Lui, S. Kumar, A. Mahadevegowda, K. A. Q. O'Reilly, and P. S. Grant. *Scr. Mater.*, 149:44–48, 2018.

[207] J. Pouchou. *Mikrochim. Acta*, 114-115(1):33–52, 1994.

[208] K. Peters. *Zeitschrift fuer Kristallographie*, 209:479–487, 1994.

[209] V. M. T. Thiede, B. Fehrmann, and W. Jeitschko. *Zeitschrift fur Anorg. und Allg. Chemie*, 625(9):1417–1425, 1999.

[210] E. Liotti, C. Arteta, A. Zisserman, A. Lui, V. Lempitsky, and P. S. Grant. *Sci. Adv.*, 4(4):eaar4004, 2018.

[211] W. W. Xu, I. Tzanakis, P. Srirangam, W. U. Mirihanage, D. G. Eskin, A. J. Bodey, and P. D. Lee. *Ultrason. Sonochem.*, 31:355–361, 2016.

[212] L. K. Walford. *Acta Crystallogr.*, 18(2):287–291, 1965.

[213] H. T. Li, Y. Wang, and Z. Fan. *Acta Mater.*, 60(4):1528–1537, 2012.

[214] Y. Zhang, J. B. Patel, J. Lazaro-Nebreda, and Z. Fan. *JOM*, 70(11):2726–2730, 2018.

[215] Z. P. Que, Y. P. Zhou, Y. Wang, and Z. Fan. In *Proc. of the 6th Decennial Intern. Conf. on Solidification Processing at Old Windsor, UK*, 2017.

[216] J. Wang, Z. Guo, J. L. Song, W. X. Hu, J. C. Li, and S. M. Xiong. *Scientific Reports*, 7(1):14994, 2017.

[217] S. Drev, A. Recnik, and N. Daneu. *CrystEngComm*, 15(14):2640–2647, 2013.

[218] G. Poludniowski, G. Landry, F. Deblois, P. M. Evans, and F. Verhaegen. *Phys. Med. Biol.*, 54(19):N433–N438, 2009.